Controlled Molecules for X-ray Diffraction Experiments at Free-Electron Lasers

Dissertation

zur Erlangung des Doktorgrades
des Department Physik
der Universität Hamburg

vorgelegt von

Stephan Stern

aus Magdeburg

Hamburg
2013

Gutachter der Dissertation:	Prof. Dr. Henry N. Chapman Prof. Dr. Jochen Küpper
Gutachter der Disputation:	Prof. Dr. Jochen Küpper PD Dr. Tim Laarmann
Datum der Disputation:	18. November 2013
Vorsitzender des Prüfungsausschusses:	PD Dr. Michael Martins
Vorsitzender des Promotionsausschusses:	Prof. Dr. Peter Hauschildt
Dekan der Fakultät für Mathematik, Informatik und Naturwissenschaften:	Prof. Dr. Heinrich Graener

Abstract

X-ray diffractive imaging is at the very heart of materials science and has been utilized for decades to solve unknown molecular structures. Nowadays, it serves as the key method of structural biology to solve molecular structures of large biological molecules comprising several thousand or even millions of atoms. However, x-ray diffraction from isolated molecules is very weak. Therefore, the regular and periodic arrangement of a huge number of identical copies of a certain molecule of interest within a crystal lattice has been a necessary condition in order to exploit Bragg diffraction of x-rays. This results in a huge increase in scattered signal and a strongly improved signal-to-noise ratio compared to diffraction from non-crystalline samples. The major bottleneck of structural biology is that many of biologically interesting molecules refuse to form crystals of sufficient size to be used at synchrotron x-ray lightsources. However, novel x-ray free-electron lasers (XFELs), which became operational very recently, promise to address this issue.

X-ray pulses provided by XFELs are many orders of magnitude more intense than x-ray pulses from a synchrotron source and at the same time as short as only several tens of femtoseconds. Combined with wavelengths in the nm–pm range, XFELs are well-suited to study ultrafast atomic and molecular dynamics. Additionally, the ultrashort pulses can be utilized to circumvent the damage threshold which set a limit to the incident intensity in x-ray diffraction experiments before. At XFELs, though eventually destroying the investigated sample, no significant sample deterioration happens on the ultrashort timescale of the XFEL pulse and the measured diffraction pattern is due to an (almost) unharmed sample.

In the framework of this thesis, the approach of utilizing the highly intense XFEL pulses for x-ray diffraction of weakly-scattering non-crystalline samples was taken to the limit of small isolated molecules. X-ray diffraction was performed on a gas-phase ensemble of the prototypical molecule 2,5-diiodobenzonitrile ($C_7H_3I_2N$, DIBN) at the x-ray free-electron laser LCLS. The target molecules were laser-aligned along a common axis in the laboratory frame by a Nd:YAG laser. Reaching a strong degree of molecular alignment,

was an important step in this experiment. Therefore, a significant part of the work was dedicated to gaining control of the molecular degrees of freedom. In order to reach a high degree of alignment, the target molecules were prepared in low rotational quantum states by means of efficient cooling in a supersonic expansion from a pulsed valve followed by spatial quantum-state selection in an electrostatic deflector. Utilization of the deflector significantly improved alignment of the DIBN molecules. Further applications of the deflection technique such as, e. g., the spatial separation of several species of molecular complexes/clusters are presented in this thesis as well.

The quantum-state selected and strongly laser-aligned samples were probed by the x-ray pulses of LCLS and the obtained diffraction patterns show a significant difference when comparing diffraction from aligned and isotropically-distributed DIBN which agrees well with theory. The results represent an important step in the effort of pushing diffractive imaging of non-crystalline samples at XFELs towards the single-molecule limit. Concepts and experimental requirements for future experiments of this kind are discussed, involving, e. g., the step towards imaging of laser-aligned large (bio)macromolecules or imaging of ultrafast fragmentation dynamics in femtosecond pump-probe experiments at XFELs.

Zusammenfassung

Bildgebung durch Röntgenbeugung ist eine wichtige experimentelle Methode der Materialwissenschaften und wird bereits seit vielen Jahrzehnten erfolgreich zur Strukturbestimmung unbekannter molekularer Proben angewendet. Röntgenbeugung stellt die wichtigste Methode der Strukturbiologie dar, um unbekannte molekulare Strukturen großer Biomoleküle zu bestimmen, welche üblicherweise viele Tausend bis einige Millionen Atome umfassen können. An einzelnen Molekülen durchgeführte Röntgenbeugungsexperimente liefern jedoch nur ein sehr schwaches Streusignal. Daher ist die periodische Anordnung vieler identischer Exemplare des zu untersuchenden Moleküls innerhalb eines strikt periodischen Kristallgitters eine notwendige Voraussetzung für die Messung eines stark verbesserten Streusignals durch sog. Bragg-Streuung. Der dafür notwendige Schritt der Kristallisation ausreichend grosser Kristalle einer molekularen Probe stellt heutzutage jedoch das größte Hindernis der Strukturbiologie dar. Neuartige Röntgenquellen wie sog. "X-ray Freie-Elektronen Laser" (XFELs) stellen jedoch einen neuartigen Ansatz dar, dieses Hindernis zu umgehen.

Röntgenpulse von XFELs besitzen eine um mehrere Größenordnungen höhere Intensität als die Pulse eines Synchrotrons, können aber gleichzeitig nur wenige Femtosekunden (fs) lang sein; kombiniert mit Wellenlängen im nm–pm-Bereich sind sie somit perfekt zur Untersuchung schneller dynamischer Prozesse im atomaren und molekularen Bereich geeignet. Die Verwendung dieser Ultrakurzzeitpulse erlaubt weiterhin die Umgehung der sonst üblicherweise zu beachtenden Begrenzung der Intensität in Röntgenbeugungsexperimenten; durch die "Ultrakurzzeitbelichtung" im Zeitbereich weniger fs kann das Streubild eine intakten Probe erhalten werden bevor die unweigerlich erfolgende, in der hohen Eingangsintensiät begründete, Zerstörung zu einem nennenswerten Zerfall der Probe führt.

Im Rahmen dieser Arbeit wurde dieser Ansatz bis zum Limit kleiner isolierter einzelner Moleküle verfolgt. In einem am Freie-Elektronen Laser LCLS durchgeführten Experiment wurde ein Ensemble von 2,5-Diiodobenzonitril-Molekülen in der Gasphase durch einen Nd:YAG-Laser ausgerichtet sowie anschliessend Röntgenbeugung an diesen ausgerichteten

Molekülen durchgeführt. Die starke Ausrichtung der DIBN-Moleüle erforderte eine gute Präparation der Moleüle in möglichst niedrigen Quantenzuständen, was durch Kühlung innerhalb einer supersonischen Expansion sowie folgende Selektion der niedrigsten Quantenzustände mittels eines elektrostatischen Deflektors erreicht wurde. Die Verbesserung der Ausrichtung der Moleküle nach erfolgter Quantenzustandsselektion konnte nachgewiesen werden. Quantenzustandsselektion im Deflektor kann auch zur räumlichen Trennung verschiedener Komplexe, bestehend aus mehreren Molekülen, gebraucht werden, was ebenfalls in dieser Arbeit dargestellt ist.

Im folgenden Röntgenbeugungsexperiment konnte schließlich ein signifikanter Unterschied des Signals ausgerichteter gegenüber isotrop-verteilter Moleküle nachgewiesen werden, der durch die theoretische Berechnung von Röntgenstreuintensitäten bestätigt wurde. Die Resultate stellen damit einen wichtigen Schritt hin zu Röntgenbeugungsexperimenten an einzelnen Molekülen an XFELs dar. Aufbauend auf den Resultaten dieser Arbeit werden erforderliche Voraussetzungen für folgende Experimente dieser Art behandelt. Hierbei wird ausdrücklich auch die Durchführbarkeit derartiger Experimente für grössere Biomakromoleküle sowie die Voraussetzungen der Beobachtung ultraschneller dynamischer Prozesse mittels Röntgenbeugungsexperimenten an XFELs diskutiert.

Contents

1. Introduction

1.1. X-ray Diffraction

When Wilhelm Conrad Röntgen reported in 1895, to speak, in his words, "on a new kind of radiation" [1] the importance of his discovery most likely couldn't have been foreseen by him at this time. The new type of electromagnetic radiation, named "x-rays" by Röntgen, had a huge impact in science throughout the following century and its importance for many scientific areas within materials science, condensed matter physics, and many other scientific areas such as medical, chemical, biological, atomic and molecular physics can hardly be overestimated.

X-rays are electromagnetic waves. With their wavelengths in the range of the interatomic and intermolecular distances (nm–pm range) in molecules or bulk condensed matter samples (e. g., metals and alloys, liquid/solid crystal phases), x-rays permit structure determination at (inter)atomic resolution by means of x-ray diffraction experiments. Due to the diffraction limit, this cannot be achieved by imaging experiments utilizing radiation in the optical regime such as, e. g., optical microscopy: wavelengths in the optical regime are in the range of 400–780 nm, i. e., exceeding interatomic lengthscales by 2–3 orders of magnitude. In addition to structure determination by diffraction experiments, x-rays are also well suited to study absorption/ionization processes of matter upon interaction with x-ray photons. Since wavelengths in the nm–pm range correspond to photon energies of several 100 to 1000 eV, x-rays are able to probe inner shell electrons of heavy atoms and big molecules with binding energies in the keV-range. Hence, experiments involving x-rays

allow interesting insights into, e. g., Auger decay processes, photoelectron spectroscopy, and photoelectron angular distributions of inner-shell electrons.

1.1.1. Structure Determination by X-ray Diffraction

This thesis is concerned with the development of a new approach in structure determination by x-ray diffraction experiments. Therefore, it is useful to recall the concept of structure determination by x-rays. Röntgen observed absorption rather than scattering/diffraction of x-rays by matter. However, it was Max von Laue who paved the way towards x-ray crystallography. In his experiment, a copper-sulfate crystal ($CuSO_4$) was irradiated by x-ray radiation. Then, von Laue recorded well-defined narrow peaks of high intensity on a photographic plate in forward scattering direction. Von Laue was awarded the Nobel Prize in physics for his pioneering research [2]. His experiment was explained by W.L. Bragg [3], who, together with his father W.H. Bragg, continued reasearch of x-ray diffraction by crystals and developed the important formula which is nowadays known as Bragg's law, relating the appearance of sharp spots in the diffraction pattern to interference of x-ray waves reflected at distinct crystallographic planes within the crystal [4].

In general, a diffraction pattern obtained in a x-ray diffraction measurement represents the square modulus of the complex structure factor at a certain set of scattering vectors covered by the detector. Structure factors are proportional to Fourier components of the electron density of the sample, as will be shown in chapter 2. Maxima/minima in the diffracted wave are due to constructive/destructive interference of waves scattered from different sites of the sample. Measuring the diffracted wave (in far-field), i. e., its intensity and phase for a sufficient set of scattering vectors by a detector would enable determination of the original sample structure (in real space) simply by means of Fourier transformation. However, at each point on the detector, the intensity of the diffracted wave is measured but the phase information is lost. This is known as the so-called "phase problem" in x-ray crystallography, which prohibits a simple inversion of the recorded diffraction data in order to obtain the sample structure of interest [5]. An important step in the beginning of utilizing crystallography for structure determination were the first reports about solutions to the phase problem, reported by Harker and Kasper [6], shortly followed by Sayre [7]. Following this, x-ray crystallography became more and more important in the subsequent years and many scientific breakthroughs were achieved in experiments involving x-ray crystallography such as the confirmation of the helical structure of DNA by Franklin and Gosling [8], which was proposed shortly before by Watson and Crick [9].

Since scattering of electromagnetic waves by matter is relatively weak when, e. g., compared to electron scattering [10], structure determination by evaluation of x-ray diffraction data relies heavily on work taking place already prior to the actual x-ray diffraction experiment, namely on growing crystals of sufficient size in order to obtain a reasonable strong scattering intensity via Bragg diffraction. In Bragg diffraction, the regular and periodic arrangement of many identical copies of the molecule of interest within a crystal lattice results in a huge increase of the diffracted signal scattered into sharp so-called "Bragg spots" of high intensity. In case the molecules are not assembled in a regular crystal lattice, the scattered intensity is very weak compared to the case of Bragg diffraction and the poor signal-to-noise ratio becomes a serious issue for every experiment. Unfortunately, many molecules which are of fundamental interest in biology refuse to assemble to crystals of a size sufficient for structure determination by x-ray crystallography and especially the majority of membrane proteins show this behaviour. Membrane proteins are a class of proteins which are located in cell membranes. They mediate signal and transport processes between different cells in a living organism and therefore are of fundamental interest in understanding inter-cell processes. Furthermore, they are the target for many synthetical drugs. Understanding the structure of this important class of biomolecules would serve as the first step in understanding their function and would give access to sophicticated tailoring of new drugs designed to target specific sites and hence initiate only specific and well-defined processes with preferably negligible side effects. As mentioned above, cristallization of such molecules nowadays is the major bottleneck and an approach that allows structure determination from small crystals (which consist only of a few unit cells) or even single isolated molecules would be very beneficial [11].

1.1.2. X-ray Free-Electron Lasers

Weakly scattering non-crystalline samples require high incident x-ray intensities in order to collect a sufficient amount of scattering intensity from this sample. However, high incident intensities lead to significant radiation damage and subsequent sample deterioration which could severely affect the diffraction data. The concept to overcome radiation damage limits in structure determination of non-crystalline molecular samples by using ultrashort x-ray pulses was proposed by Neutze et al. [12], based on the idea of Solem [13, 14]. It has been strongly driven by the development of a new class of x-ray lightsources, namely the x-ray free-electron lasers (XFELs). The idea was to irradiate a non-crystalline (molecular) sample by an x-ray pulse of very high intensity, i. e., by far exceeding the damage threshold. Eventually, the high intensity of the pulse destroys the sample, but since the x-ray pulse length is in the fs-range, no remarkable deterioration of

the sample has happened during the pulse and the diffraction pattern will be the diffraction pattern of an intact sample. This is the so-called "diffract-before-destruct" approach. The very high incident intensity accounts for the tradeoff of not being able to exploit the strong amplification of the scattering signal due to Bragg diffraction, since the sample is non-crystalline. Novel XFELs in the hard x-ray regime have been designed and promise to address these issues by providing ultrashort pulses with single-pulse intensities some orders of magnitude larger than 3rd generation synchrotron sources [15].

X-ray free-electron lasers utilize the emission of free electrons, accelerated to high kinetic energies (in the GeV range), travelling through a periodic magnetic array, i. e., a so-called undulator. The original concept of using this undulator radiation was examined theoretically by Motz in 1951 [16] and the first incoherent undulator radiation in the visible and millimeter range was experimentally achieved by Motz, Thon and Whitehurst shortly thereafter [17]. Experiments performed by Phillips [18] on an undulator microwave source (the "ubitron") demonstrated for the first time two effects which are of great importance of todays x-ray free-electron lasers, namely the Doppler up-shift of the undulator radiation and the spatial modulation of the electron bunch into small slices, an effect which is known as "microbunching" in an FEL [15]. Using undulator radiation to create coherent x-rays was then proposed by Madey in 1971 [19]. However, x-ray free electrons lasers demand large-scale accelerators in order to accelerate the electron bunches to high relativistic energies, which is a prerequisite for the necessary Doppler-shift for creation of coherent emission in the x-ray region [15]. The first FEL in the XUV/ soft x-ray range has been the "Free-Electron Laser in Hamburg" (FLASH), which became operational in 2005. It was followed by the opening of the Linac Coherent Light Source (LCLS) at the SLAC National Accelerator Laboratory in 2009, which is able to provide ultrashort (fs-range) highly intense coherent x-ray pulses in the range of 270 eV – 9.5 keV [20] and hence is considered to be the first x-ray FEL.

A general overview of the working principle of x-ray free electron lasers was given, e. g., by McNeil and Thompson [21]. The properties of the x-ray pulses provided by the XFELs are distinctively different from the radiation at synchrotron sources. XFELs are able to provide ultrashort coherent x-ray pulses (in the fs-range) of very high intensity (10^{12} – 10^{13} photons/shot) and the response of atoms and molecules to this pulses can be severely different compared to synchrotron radiation. Indeed, recent studies have proven the creation of almost "hollow atoms" of Neon by stripping off nearly all of the electrons from Neon, which is ascribed to the high fluence of XFEL pulses [22]. However, the ionization mechanism at these high intensities might be quite distinctive, as was shown by Rudek

et al. [23]: The authors observed very high charge states in Xenon (up to Xe^{36+}), which is argued to be due to a multi-photon process in Xenon, but unlike resonance-enhanced multi-photon ionization (REMPI) in the optical regime, is driven by a strong increase of x-ray absorption cross-sections by ionization during the x-ray pulse. This enhanced cross-sections in the following lead to a significant increase in photoabsorption by the Xenon atoms.

Considering imaging of non-crystalline molecular samples, single-shot pulse intensities of XFELs by far exceed the damage limit of individual (bio)molecules. This results in significant photoionization and subsequently fast Coulomb explosion of the samples. In order to collect sufficient diffraction signal, identical samples have to be provided in a reproducible manner to collect many single-shot diffraction patterns. Since Coulomb explosion of highly ionized samples happens fast (on a sub-ps timescale), the exposure time (i. e., the x-ray pulse length) of the sample to the x-ray pulse must be short enough that the fragments of the sample haven't moved significantly from their equilibrium positions (which would result in significant blurring of the single-shot diffraction pattern) during the whole pulse.

This so-called "diffract-before-destruct" approach to circumvent the influence of radiation damage of the sample on the diffraction pattern was introduced by Solem in 1982 [13, 14] and was revived by Neutze et al. to be utilized with the novel upcoming XFELs [12]. It was successfully tested experimentally at the x-ray free-electron laser FLASH on an artificial sample placed on top of a silicon nitride membrane [24]. The relatively large sample provided sufficient diffraction signal to reconstruct the original sample structure from only a single-shot diffraction pattern. A follow-up experiment utilized a pump-probe scheme to investigate the fast sample degradation due to the intense radiation [25]. However, the first experiments on biological samples applying the "diffract-before-destruct" approach were performed at the x-ray free-electron laser LCLS in late 2009. Using the fs-pulses from LCLS and a sophisticated liquid-jet sample-delivery system [26], diffraction data from non-crystalline virus particles [27] and nano-crystals of the protein photosystem-I [28] was measured. The virus particles have no periodicity at all (and hence show no Bragg diffraction), whereas the nano-crystals are small crystals comprising just a few tens of unit cells and hence the diffraction patterns contain Bragg and non-Bragg features. In both cases, the sample structure was succesfully obtained from the analysis of many single-shot diffraction patterns. Recently, the first unknown biological structure of an inhibitor of a protein was already solved by this method [29]. An overview of utilizing XFELs for structural biology, comprising recent achievements and future opportunities, is given by Spence, Weierstall, and Chapman [30].

1.1.3. Imaging of Single Molecules

The steps mentioned above pave the way towards the ambitious goal to ultimatively collect diffraction data from even single molecules with sufficient signal-to-noise for structure determination. Single-molecule imaging is of particular concern for structure determination of membrane proteins which are of major interest in biology. The difficulty is based in the fact, that crystallization of membrane proteins can be tedious, may take years, or may not be achieved at all at a level sufficient for x-ray crystallography experiment as discussed by Spence and Doak [11]. XFELs with their ultrashort coherent x-ray pulses of high intensity hold the promise to determine atomically resolved structures and to trace structural dynamics of individual molecules at fs-timescales. The generally proposed approach is to deliver a stream of identical individual molecules to the focus of an XFEL and to collect single molecule diffraction patterns similar to the method mentioned above. In principle, the three-dimensional diffraction volume from the various random orientations of the molecules can be computed, allowing the reconstruction of a three-dimensional structure of the object in case the diffraction signal is above noise and enough single-shot diffraction patterns are recorded. The major problem of this approach is the low scattering signal expected from individual molecules. Therefore, it is necessary to record very large numbers of single-molecule diffraction patterns, which then need to be classified and assembled into a diffraction volume that will enable the reconstruction of a three-dimensional structure.

The option of extracting the orientation of a single molecule by inspection of its diffraction pattern on a shot-to-shot basis is discussed, e. g., in ref. 31–36. However, these approaches still rely on the assumption of being able to measure at least some 1000 scattered photons per shot, a condition which is by far not met in the experiment described in this thesis, where count rates of ≈ 0.20 scattered x-ray photons/shot were measured by the detector. This, of course, is due to the small number of constituent atoms of the prototypical molecule 2,5-diiodobenzonitrile ($C_7H_3I_2N$, DIBN). While count rates of photons scattered by small single molecules, such as DIBN, are too low this might be achieved with envisioned stronger and shorter x-ray pulses. In contrast, application of this kind of single-shot imaging to large biomolecules might be achievable. However, further complication of this approach is given by the fact, that complex macromolecules typically come in various structural isomers, or shapes, which must also be sorted, averaged, and analyzed separately.

An alternative approach is to spatially separate various shapes [37] or even isomers [38, 39] before delivery to the interaction point and to orient the molecules and particles in space [11, 40]. This controlled-delivery approach would allow for the averaging of many iden-

tical patterns and a controlled variation of the molecular alignment and orientation in space would allow to tomographically build up the complete three-dimensional diffraction volume of individual isomers. The upcoming European XFEL facility [41] will give the opportunity to collect single shot diffraction patterns at repetition rates much higher than the repetition rates currently achieved at LCLS, and data acquisition following the controlled-delivery approach will only limited by the repetition rates of the alignment laser system and the repetitive read-out of the detectors.

In the experimental work carried out for this thesis, a modification of the controlled-delivery approach was followed, in which x-ray diffraction patterns of controlled ensembles of identical, quantum-state selected and strongly aligned 2,5-diiodobenzonitrile ($C_7H_3I_2N$, DIBN) molecules in the gas phase were recorded. The strongly aligned samples [42] allow to simply average the continuous diffraction patterns from a very large number of isolated molecules [40]. In contrast to a single molecule diffraction pattern, the ensemble of many molecules aligned in the laboratory frame provides signal enhancement through incoherent superposition of single-molecule diffraction intensities, i. e., the diffraction pattern from an ensemble of aligned, but isolated gas-phase molecules is simply the sum of single-molecule diffraction intensities.

Ultrafast x-ray diffraction on non-crystalline samples was experimentally carried out, e. g., by Ihee et al. [43], using ps-pulses from a synchrotron. In a time-resolved pump-probe experiment, an iodine atom was dissociated from the haloethane molecule ($C_2H_4I_2$) dissolved in methanol, and the subsequent process of forming a new species was followed, giving evidence of intermediate structures during the process with 100 ps time-resolution. In contrast to x-ray diffraction, such structure intermediates were also studied exploiting ultrafast electron diffraction in similar experiments [44, 45]. However, these experiments have not made use of molecular alignment and are therefore comparable to powder-diffraction experiments. Recently, in an approach similar to the one carried out for the work of this thesis, ultrafast electron diffraction of a laser-aligned ensemble of the small symmetric top molecule CF_3I in the gas-phase was conducted by Hensley et al. [46], and the succesful reconstruction of the molecules' electron density solely based on the diffraction pattern was confirmed by the authors. However, the approach of using an ensemble of quantum-state selected and strongly aligned gas-phase molecules in an x-ray diffraction experiment has not been followed up to now.

A short note on complementary methods of structure determination should be given here. In contrast to the application imaging techniques such as x-ray or electron diffraction, molecular structures can be solved by utilizing spectroscopic methods, such as rotational [47–49] or NMR spectroscopy [50, 51], since the spectrum of the quantized molecular en-

ergy levels is determined by the molecular structure and is an almost "unique fingerprint" of the latter.

In rotational spectroscopy, energies of transitions between quantized rotational states (i. e., in the microwave region) are measured. It should be mentioned, that pure rotational spectroscopy does not work for completely unpolar molecules, i. e., molecules without any dipole moment such as, e. g., N_2. The characteristic transition frequencies of the rotational spectrum are due to the principal moments of inertia of the molecule and hence to the molecular structure. Thereby, the molecular structure, i. e., the relative bond lengths and -angles of the atomic constituents of a certain molecule, can be deduced from rotationally resolved spectroscopy. An important step has been the development of the analysis of the distinct spectra of a molecule when different isotopic species of the same chemical element are utilized in the target molecule, as described by Kraitchman [52]. Additional effects like tunneling splitting, shifts of spectral lines due to centrifugal distortion, and hyperfine spectral structure contain further information and thereby improve molecular structure determination by rotational spectroscopy [49]. In general, the larger the molecule of interest, the more complicated is its rotational spectrum, and the number of transitions grows enormously with increasing size of the molecule. Information about larger molecular systems is more easily obtained by, e. g., pump-probe rotational coherence spectroscopy (RCS). In RCS, which is a time-domain type of spectroscopy, a pump-laser initiates a transient alignment of an ensemble of gas-phase molecules by creation of a wave packet based on the coherent superposition of rotational states. Dephasing and subsequent rephasing of the transient alignment at characteristic timescales allows for determination of the molecular rotational constants. RCS was introduced by Felker in 1992 [53] and a review of possible experimental implementations is given, e. g., by Riehn [54]. In general, advances in experimental methods such as, e. g., exploiting rapid cooling in pulsed and seeded molecular beams [55], the recent invention of new methods such as, e. g., combining conventional rotational spectrocopy with mass spectrometry [56], and improved signal-to-noise and data acquisition, e. g., by utilizing novel broadband Fourier transform microwave spectrometers with chirped pulses [57], have greatly enhanced the possibilities of rotational spectroscopy and the range of molecular systems accessible by this method. As an example, the chirped-pulse microwave spectrometer [57] allows for investigation of fast isomerization kinetics on ps-timescales via examination of the frequency separation of rotational spectra of the reactant and the product [58, 59]. However, exploiting the possibilities of XFELs will allow to study structural dynamics on a even shorter, i. e., fs-timescale.

NMR spectroscopy, on the other hand, is especially interesting for structure determination of somewhat bigger molecules than can be adressed by rotational spectroscopy. In

NMR spectroscopy, transitions between spin states of NMR-active nuclei in a strong static magnetic field are measured [50, 51]. NMR-active nuclei are nuclei with unpaired neutrons and/or protons, hence with net spin $S \neq 0$. Examples are certain isotopes such as, e. g., ^{1}H, ^{13}C, and ^{19}F. For all of these, $S = 1/2$. The ratio of the naturally occuring amounts of an NMR-active vs. the (usually much more abundant) -inactive ($S = 0$) isotope of a certain element determines whether NMR spectroscopy with sufficient signal levels can be performed for this element. The resonance frequencies of NMR-active nuclei mainly depend on the isotope and the field strength of the static magnetic field. A slight shift (the so-called chemical shift) of these frequencies due to couplings of the nuclear spin with the chemical environment (i. e., the arrangement and type of the adjacent atoms) is the main feature to be exploited for structure determination by NMR spectroscopy. During the last decade, NMR spectroscopy became an important tool in structure determination and the major achievements were summarized by Emsley and Feeney [60]. In particular, NMR became a valuable tool for structure determination of biological macromolecules such as proteins, RNA, and DNA, as pointed out by nobel laureate Kurt Wüthrich [61], one of the pioneers of this field. On the one hand, one of the key advances of structure determination by NMR is that NMR data can be recorded in solution, i. e., under physiological natural conditions of, e. g., (bio)macromolecules of living organisms. Therefore, solvents can be used which closely mimic physiological conditions (in terms of, e. g., temperature, pH and salt concentration) and the molecule of interest can be studied in its "natural environment". On the other hand, NMR-based structure determination, even by multi-dimensional NMR-methods, faces several limitations, such as, e. g., an upper size limit of the sample size of $\approx$ 30 kDa [62]. Recent improvements of the sensitivity by the invention of new techniques such as transverse relaxation-optimized spectroscopy (TROSY) [63], which results in better spectral resolution, i. e., less line-broadening in larger structures, combined with optimized magnetization transfer techniques [64] challenge this size limit and push NMR structure determination methods towards molecular weights up to 870 kDa, which means that structure determination of larger molecules such as, e. g., membrane proteins becomes possible [62]. However, as pointed out by Wüthrich and co-workers, even today no standardized systematic procedures for data evaluation and production of solutions for the proteins were established, at least not as standardized in the sense such as in the x-ray crystallography community [65]. The authors fear NMR-based structure determination might only be considered in the case when crystallization attempts have failed. With the new approach of data collection in diffraction-before-destruction-type experiments at XFELs, even the demand for sufficient crystallization attempts is softened, which most likely results in structure determination being strongly in favour of x-ray diffraction at XFELs in the near future.

1.2. Controlled Molecules

Getting back to the idea of coherent x-ray diffraction of an ensemble of isolated and laser-aligned molecules in the gas-phase at the new XFELs, a key feature of this approach is gaining control of the orientation of the molecules in the gas-phase ensemble with respect to the laboratory frame. For many purposes in molecular physics it is advantageous to gain some degree of control over the molecular degrees of freedom (including the quantum-state) of the molecule whose properties are subject of an experiment. Furthermore, control of molecular motion and orientation with respect to a space fixed axis connects the laboratory to the molecular frame and hence allows to measure molecular properties directly in the molecular frame. In particular, laser-alignment of molecules was applied for the tomographic imaging of molecular orbitals [66] and investigations of photoelectron-angular distributions [67] and time-resolved dynamics [68] in the molecular frame. Many other experiments have been envisioned to exploit alignment and control of molecules at XFEL lightsources 69.

In the following, a brief overview of the development of the experimental tools for controlling molecular degrees of freedom is given, starting with the concept of quantum-state selection which is followed by an explanation of laser-alignment.

1.2.1. Quantum-State Selection

The famous Stern-Gerlach experiment in 1922 can be regarded as the first experiment involing spatial quantum-state selection of gas-phase atoms. The alteration of the trajectory of Ag-atoms in dependence of their spin quantum-state by passing an inhomogenous magnetic field was first proposed by Stern [70] and experimentally proven by Stern and Gerlach soon afterwards [71]. The deflection of polar molecules using static inhomogenous electric rather than magnetic fields was developed at the same time. It was theoretically described in 1921 [72] and proven experimentally soon afterwards [73]. Even in 1926, Stern envisioned the deflection technique to be suitable for spatial quantum-state selection of small molecules at low temperatures [74].

In addition to the deflection technique, spatial quantum-state selection by focussing of distinct quantum states was developed and lead to a famous experiment performed by Gordon, Zeiger, and Townes in 1954 [75]. By using a quadrupole focussing field, a population inversion in a microwave cavity was achieved by focussing a single quantum state of ammonia. The population inversion was used for “microwave amplification by stimulated emission of radiation”, i. e., the creation of the first MASER which paved the way towards “light amplification by stimulated emission of radiation” in a laser by Maiman in 1960 [76].

While deflection and focussing techniques only concern the transverse motion of molecular beams, the longitudinal motion can be affected by using, e. g., a Stark decelerator, which was realized first in 1999 [77]. The Stark decelerator makes it feasable to slow down molecules, initially travelling at high speed (depending on the carrier gas) in a molecular beam, to standstill, allowing for trapping or loading into "molecular storage rings" for a variety of experiments [78]. However, static electric fields in multipole focussing and the Stark decelerator work only for molecules in low-field seeking (lfs) quantum states. Large molecules with small rotational constants have a high density of states. Stark interaction coupling of closely-spaced mixed (pendular) states of the same symmetry in large molecules turn any low-field seeking state into a high-field seeking (hfs) state, already at relatively weak electric field strength. While deflection of hfs states in a electrostatic deflector is feasable, focussing of hfs states using only static fields is not possible, since a minimum of the field-strength by static fields is not allowed by the electromagnetic theory. Therefore, alternating gradient (AG) focussing was developed. In AG focussing [79, 80], an array of electrostatic lenses along the molecular beam path is used to focus molecules along one transversal coordinate while defocussing them on the perpendicular transverse coordinate. By switching the direction of the focussing/defocussing fields at a certain frequency, a net focussing along both transversal directions can be achieved for molecules in hfs states. AG focussing was applied to, e. g., the prototypical molecule benzonitrile (C_6H_5CN) [81] and to the benzonitrile-argon complex [82], demonstrating its feasibility for large asymmetric top molecules in hfs states.

1.2.2. Laser Alignment

As pointed out above, a high level of control of the internal and external degrees of freedom of a molecule is very beneficial for a large variety of applications in chemistry and physics. This includes control of the population of the distinct quantum-states of a molecule as well as the control of a molecule's orientation with respect to the laboratory frame, allowing for measuring molecular properties directly in the molecular frame. Molecules that exhibit order with respect to a space fixed axis (an axis in the laboratory frame) are said to be aligned. Furthermore, if the molecules also exhibit order with respect to the direction of this axis the molecules are said to be oriented [83]. While alignment and orientation of molecules can be obtained with relative ease in the condensed phase (due to strong intermolecular interactions, which are of present in solids and even in liquids, such as, e. g., in liquid crystal phases [84]), alignment of neutral molecules in in the gas phase is a challenging goal. The techniques demonstrated so far comprise collisional processes [85–87], static electric fields [88] and rapidly changing electrical fields like (optical) laser fields

[83, 88–90]. The degree of alignment obtained in collisional processes of molecules in the gas phase is relatively weak. Using strong dc electric fields ("brute force orientation") is only applicable to cold samples of molecules possessing a large dipole moment and which can be strongly cooled in the molecular beam [83]. An alternative for achieving molecular alignment is using the strong ac electric field of a laser.

First experiments on laser-induced alignment made use of the selective photoabsorption of light by molecules in dependence of their orientation [91, 92], by which molecules in certain orientations are removed from the sample, leaving an anisotropic distribution. While this technique is rather general and applicable to many molecules, only a few percent of the original molecular sample is left for further investigations [83]. A different approach is the laser alignment of molecules at non-resonant frequencies, which exploits the interaction of a molecules anisotropic polarizability and a strong laser field. The situation is similar to brute-force orientation, but the dc electric field is replaced by the rapidly varying ac electric field of a laser and the alignment is not governed by interaction of the laser field with the permanent dipole moment but rather by the interaction with the molecular polarizability. The molecule gets aligned by feeling a torque and rotating into a preferred direction in space given by the axis of highest polarizability anisotropy being parallel to the laser polarization. The first theoretical treatment of the influence of a non-resonant laser field on the rotational spectrum of a molecule was given by Zon and Katsnel'son [93], but they didn't consider the spatial effect of the hybrid rotational states.

In 1991, Friedrich et al. considered laser alignment of non-polar molecules, governed by the interaction of the polarizability of the molecule with an external laser field [94]. In 1992, Normand et al. reported results of an experiment exploiting strong-field ionization of CO molecules by two time-delayed and linearly polarized short pulses (ps-range) of an off-resonant Nd:YAG laser. Beside ionization, the strong laser pulses also cause laser-induced aligment of the CO molecules, as can be explained by the ionization yields under different laser-polarization conditions [95]. This experimental work was followed by detailed derivations of the properties of the hybrid rotational wave functions for linear and symmetric top molecules [89, 96]. In the strong field of the laser, the field-free wavefunctions of a molecule become hybridized, i. e., states of different J mix and the spatial distribution of molecules is these mixed states (the "pendular states") becomes non-isotropic. The experimental demonstration of this concept was achieved in 1996 by Kim and Felkner [97] and was followed by the experimental work of Sakai et al. [98] and Larsen et al. [99]. As pointed out by Friedrich and Herschbach in 1999, by the combination of a non-resonant laser field and a dc electric, alignment as well as orientation of molecules could be achieved with the degree of orientation being enhanced compared to

brute-force orientation even at quite modest dc electric fields [100]. The combination of dc and ac electric fields was named mixed-field orientation.

In general, non-resonant laser alignment is divided into two regimes, which are called adiabatic and non-adiabatic (or: impulsive) alignment. In adiabatic alignment, the time-envelope of the alignment laser pulse is slowly varying and the alignment pulse is long compared to the rotational period of the molecule. On the other hand, there is "impulsive" or "non-adiabatic" alignment: a very short laser pulse (fs-regime) is interacting with the molecule, creating a time-dependent coherent superposition of molecular rotational states (a "rotational wave-packet"), where an ensemble of molecules exhibits some initial degree-of-alignment, which then slowly decays with time but then increases again at some point in time. These "revivals" happen again at determined times long after the laser pulse is over, but the degree of alignment achieved decreases as the coherence is lost after some revival periods. Nevertheless, molecular alignment under external field-free conditions can only be achieved during these revivals of impulsive alignment. Non-adiabatic alignment was first treated theoretically by Seidemann [101] and demonstrated experimentally by Rosca-Pruna and Vrakking [102, 103]

Of particular concern is the idea of extending laser alignment of gas-phase molecules to alignment of molecules in solution, which might be an interesting route to follow in the case of large biomolecules. Within the group of Stapelfeld, adiabatic and non-adiabatic alignment experiments on iodobenzene dissolved in liquid helium droplets was investigated in the framework of a PhD thesis [104]. It is shown, that the adiabatic alignment of iodobenzene in liquid helium droplets is close to the alignment achieved in a supersonic jet expansion. More intriguing, however, is the behaviour of alignment achieved in the non-adiabatic regime. The alignment seems to be significantly different from the alignment observed in a molecular beam, indicating a distinct interaction between the molecules and the environment of the helium droplet. The field-free alignment is quite modest ($\langle \cos^2 \theta_{2D} \rangle = 0.76$) but extends over a long period of several tens of ps, reaching the isotropic distribution after ≈ 80 ps. As pointed out by Nielsen [104], the cause of this is not fully understood, but may be a significant improvement for envisioned pump-probe experiments of molecules under (laser)field-free conditions as the period of alignment is much enhanced compared to non-adiabatic alignment of gas-phase molecules. Recently, qualitative similar results were obtained for methyliodide (CH_3I) as well [105] and may pave the way towards new experiments on cold (cooled by the liquid helium droplet), non-adiabatically aligned molecules in future experiments.

1.3. Outline of this thesis

This thesis is concerned with the demonstration of the feasibility of using XFELs for coherent diffraction experiments on single molecules and hence pave the way towards structure determination by diffraction without exploiting the huge signal increase by Bragg diffraction from crystals. As mentioned above, the majority of, e. g., membrane proteins refuses to assemble to crystals of sufficient size to be used in crystallography diffraction experiments at synchrotrons and hence diffraction experiments exploiting non-Bragg diffraction will be of growing interest.

For the proof-of-principle diffraction experiment, the results of which are presented in this thesis, the prototypical molecule 2,5-diiodobenzonitrile ($C_7H_3I_2N$, DIBN) was used. In DIBN, the two heavy iodine atoms serve as the main scattering centers. In order to compensate for the very weak scattering signals expected from single molecules, a modification to the diffract-before-destruct approach was applied: Instead of using single molecules, an ensemble of isolated molecules in the gas-phase was provided on a shot-to-shot basis. By applying spatial quantum-state selection via electrostatic deflection of DIBN molecules in different quantum states, molecules residing preferably in the lowest quantum-states were selected, as these will be best suited for laser alignment. Laser alignment of molecules was applied in order to increase the scattered signal of a single molecule by incoherent superposition of single-molecule diffraction patterns of the same orientation in a linear way, i. e., the intensity scales linearly with the number of molecules in the interaction region.

The theoretical concepts of spatial quantum-state selection, laser alignment and x-ray diffraction will be explained in chapter 2. The first part of that chapter describes, how neutral but polar molecules can be quantum-state selected by exploiting the Stark effect in an inhomogenous dc electric field. The second part of this chapter is concerned with the theory of laser alignment and why molecules residing in preferably the lowest quantum states will be best suited for laser alignment. The third part outlines the theory of x-ray diffraction of single molecules which is a prerequisite for quantitative calculations of x-ray diffraction intensities from DIBN.

Chapter 3 introduces the experimental setup. The first part describes the molecular beam setup, which was used for spatial quantum-state selection of DIBN at LCLS as well as for a deflection experiment on indole-water clusters at DESY. The second part explains the setup used at LCLS. It gives an explanation of the x-ray free-electron laser LCLS and outlines the experimental endstation CAMP, the laser setup, and data acquisition by the CFEL-ASG-Software-Suite (CASS).

Chapter 4 presents the results of deflection experiments on two distinct molecular systems. The first part is concerned with electrostatic deflection of the prototypical molecule indole and indole-water clusters. It is shown, that cooling of indole-water clusters to rotational temperatures of a few K can be achieved in a supersonic expansion of a molecular beam and that the spatial dispersion of clusters in distinct quantum states can be well simulated by applying the theory outlined in chapter 2. The second part presents results of the deflection of DIBN, measured at DESY and during the x-ray diffraction experiment at the free-electron laser facility LCLS.

Chapter 5 presents the results obtained by probing the alignment of DIBN at LCLS. Strong adiabatic laser alignment of DIBN was achieved by using a far-off resonant NIR laser. It is shown that laser alignment benefits from spatial quantum-state selection explained in chapter 4, as the degree-of-alignment obtained for colder molecules is significantly higher than the one obtained for molecules at higher rotational temperatures.

In chapter 6, the concept of quantitative simulations of x-ray diffraction intensities of DIBN and the backing gas Helium is explained, based on the theory derived in the third part of chapter 2. By considering various experimental parameters like the molecular densities, number of photons per shot, degree of alignment of DIBN, etc., the expected numbers of photons, scattered by DIBN and the backing gas Helium to the detector, are simulated in a quantitative way. The results of these simulations will be utilized for fitting the experimentally obtained diffraction data.

Chapter 7 presents the results of the coherent x-ray diffraction experiment on the ensemble of quantum-state selected and strongly-aligned DIBN molecules. As the scattering signal from isolated molecules is very weak, a huge amount of single-shot diffraction data was measured from which single scattered x-ray photons were extracted after the single-shot data was cleaned thouroughly for several significant artifacts and backgrounds. An average count rate of ≈ 0.20 x-ray photons/shot scattered to the detector was obtained from the cleaned diffraction data. Diffraction data was obtained for aligned and not-aligned DIBN molecules in order to subtract isotropic background scattering and confirm the observation of x-ray diffraction signal from aligned molecules clearly above the noise level. The issue of radiation damage and its effect on diffraction data is discussed as well.

Finally, the results are summarized and possible improvements for future diffraction experiments on single-molecules are discussed in chapter 8.

A detailed description of the steps involved in cleaning of the single-shot diffraction data and counting of single photons is given in appendix A. Appendix B briefly summarizes the molecular properties of 2,5-diiodobenzonitrile, the target molecule for the diffraction experiment. Following the bibliography, the most important results are given in a summary.

2. Controlled Molecules for X-ray Diffraction – Theoretical Description

This chapter deals with the theoretical aspects concerning x-ray diffraction experiments of controlled asymmetric top rotor molecules. An important feature of the method presented here is that the molecules to be investigated are not assembled into a crystal but rather provided to the experiment via a supersonic expansion of a gaseous mixture together with a backing gas. As scattering from isolated molecules is very weak compared to Bragg scattering, improved scattering signals are obtained by measuring the incoherent superposition of multiple single-molecule diffraction patterns, all of them aligned along a common axis in the laboratory frame. This is achieved by laser-alignment of the ensemble of target molecules in the interaction volume.

In general, for a large variety of applications in chemistry and physics, a high level of control of the internal and external degrees of freedom of a molecular sample in the gas phase is very beneficial and for the x-ray diffraction experiment presented in this thesis it is even mandatory. Control of molecular degrees of freedom includes spatial selection of molecules residing in (a small set of) distinct quantum states as well as the control of the spatial orientation of the molecules with respect to the laboratory frame. This allows for measuring molecular properties directly in the molecular frame and, in the case of the x-ray diffraction experiment presented here, serves as a means to obtain the single-molecule diffraction pattern with improved signal as explained above.

This chapter follows the route of the presentation of the results in chapter 4–chapter 7. It starts with explaining theoretical aspects concerning the control of gas-phase molecules, followed by the theory to describe x-ray diffraction quantitatively.

The first section outlines the theory of quantum state-selection of single neutral molecules in the gas phase by using strong inhomogenous dc electric fields in order to spatially separate molecules in lower-lying rotational quantum states from those in higher-lying rotational quantum states. This allows to prepare molecular ensembles in preferably low-lying states, as these will be best suited for laser alignment. The section sketches the derivation of the field-free energy levels of asymmetric top rotor molecules followed by the explanation of the alteration of these energy levels in an electric field due to the Stark effect. This Stark shift of molecular energy levels allows for spatial deflection of molecules in an inhomogenous dc electric field and the calculation of the quantum-state specific spatial deflection will be outlined.

The second section is concerned with laser alignment and how it can be achieved experimentally exploiting the strong ac electric field of an off-resonant laser. From the theory, it will be clear why pre-selection of molecules in preferably lowest-lying rotational quantum states (as is achieved by electrostatic deflection) significantly enhances the degree of alignment (i. e., the angular confinement of the molecules) in the experiment.

In the third section, the theoretical framework necessary for quantitative calculations of x-ray diffraction intensities of laser-aligned isolated molecules in the gas phase will be explained, derived from basic principles.

2.1. Quantum-State Selection by Electrostatic Deflection

This section outlines the basic principles of calculating energies of rotational quantum states of cold ($\approx$ 1 K) molecules in a molecular beam in the presence of an external electric field using the CMIstark software package [106]. The obtained energies are used for calculations of rotational quantum-state dependent molecular beam deflection profiles using the libcoldmol software package [107].

2.1.1. The Field-Free Asymmetric Rotor

The energy W of a molecule, according to quantum mechanics, can be calculated from the Schrödinger equation

$$H\Psi = W\Psi \tag{2.1}$$

where H is the Hamiltonian in the center-of-mass frame of the molecule while Ψ is the internal wave function of the molecule. The equation is an eigenvalue problem, with H being an operator and W being the eigenvalues of this operator. When the Born-Oppenheimer approximation [108] is valid, stating that the motion of the nuclei and

the motion of the electrons are decoupled, the complete internal wavefunction can be expressed as the product of the electronic (Ψ_{el}), vibrational (Ψ_{vib}), rotational (Ψ_{rot}) and nuclear spin (Ψ_{ns}) wave functions [109].

$$\Psi = \Psi_{\mathrm{el}}\Psi_{\mathrm{vib}}\Psi_{\mathrm{rot}}\Psi_{\mathrm{ns}} \tag{2.2}$$

Then, the total energy W of the molecule is the sum of the individual energies W_{el}, W_{vib}, W_{rot} and W_{ns} [109].

$$W = W_{\mathrm{el}} + W_{\mathrm{vib}} + W_{\mathrm{rot}} + W_{\mathrm{ns}} \tag{2.3}$$

The temperatures of the molecules in the molecular beam in the experiments presented here are in the order of a few Kelvin, thanks to the cooling of the target molecules by collisions with the buffer gas during the supersonic expansion. Hence, the molecules are in their respective electronic and vibrational ground state, but they still remain distributed over a range of rotational states. Field-free energies and Stark-shifts for these states have to be calculated in order to simulate spatial quantum-state selection by electrostatic deflection. Couplings of nuclear rotation to electronic and nuclear spins (which contribute to fine and hyperfine structure) were not taken into account in the calculation of the Stark energies by CMIstark. W_{ns} can safely be neglected for molecules like indole (which comprises only relatively light atoms), since it is usually some orders of magnitude smaller than W_{rot} and doesn't contribute considerably to the Stark shifts. However, W_{ns} may be considerably larger for molecules comprising heavy atoms. In particular, the energy shift of the molecule 2,5-diiodobenzonitrile (DIBN) based on nuclear quadrupole coupling is expected to be huge as will be explained in chapter 4. Since W_{ns} was not taken into account in CMIstark, deflection of DIBN was not simulated.

The rotational Hamiltonian can be simplified to the Hamiltonian $H_{\mathrm{rot}}^{\mathrm{rigid}}$ of the rigid rotor model and calculation of the field-free energies (and later Stark shifts) of the rotational states is achieved by solving the Schrödinger equation with the $H_{\mathrm{rot}}^{\mathrm{rigid}}$ [49, 109]

$$H_{\mathrm{rot}}^{\mathrm{rigid}} = \frac{P_a^2}{2I_a} + \frac{P_b^2}{2I_b} + \frac{P_c^2}{2I_c} = \frac{4c\pi^2}{h}(AP_a^2 + BP_b^2 + CP_c^2) \tag{2.4}$$

where P_a, P_b, and P_c are the components of the quantum-mechanical operator of the angular momentum and I_a ,I_b , and I_c are the components of the moment of inertia with respect to the principal axes a, b, and c. For the most general case of a molecule, the so-called asymmetric top molecule, all moments of inertia are non-equal and non-zero. By convention, the axes a, b, and c in a molecule are labelled such, that $I_a < I_b < I_c$.

Moments-of-Inertia	Rotational Constants	Rotor Type	Example
$I_a = 0,\ I_b = I_c$	$A = \infty,\ B = C$	linear top	CO, OCS
$I_a = I_b = I_c$	$A = B = C$	spherical top	C_{60}, CH_4, SF_6
$I_a < I_b = I_c$	$A > B = C$	prolate symmetric top	$CClH_3$
$I_a = I_b < I_c$	$A = B > C$	oblate symmetric top	C_6H_6 (benzene)
$I_a \neq I_b \neq I_c \neq I_a$	$A \neq B \neq C \neq A$	asymmetric top	2,5-diiodoben-zonitrile,indole

Table 2.1.: Types of rotors according their to moments-of-inertia

Depending on the arrangement of atoms in a molecule, a given molecule can be classified according to its moments of inertia. As can be seen in table 2.1, the molecules dealt with in this thesis (2,5-diiodobenzonitrile, indole) are asymmetric tops. Instead of using the moments of inertia, often the rotational constants A, B, and C are used, most notably in molecular spectroscopy. Their explicit form differs throughout the literature, depending on the units they are expressed in. If expressed in units of wavenumbers (cm^{-1}), the rotational constants are [49]

$$A = \frac{h}{8c\pi^2 I_a}, \qquad B = \frac{h}{8c\pi^2 I_b}, \qquad C = \frac{h}{8c\pi^2 I_c} \tag{2.5}$$

where h is Plancks constant and c the speed of light in vacuum. While an analytical solution of the Schrödinger equation can be found for the linear and symmetric tops (its explicit form is given, e. g., in ref. 49), no closed analytic solution for the asymmetric tops exists. However, if the difference of two of the three moments of inertia is small (compared to the third one), the molecule is close to the limiting cases “prolate symmetric top” or “oblate symmetric top”. An asymmetry parameter κ, proposed by Ray [110] , is introduced to classify the asymmetry.

$$\kappa = \frac{2B - A - C}{A - C} \tag{2.6}$$

For the limiting cases, κ takes the values of $\kappa = 1$ (oblate) an $\kappa = -1$ (prolate) while the “degree-of-asymmetry” is most pronounced with $\kappa = 0$. The ansatz (explained, e. g., in [49] to solve eq. (2.1) is to expand the asymmetric top wavefunctions $\Psi_{\text{asym}} = |J_{K_a K_c} M\rangle$ in terms of the symmetric top wavefunctions $\Psi_{\text{sym}} = |JKM\rangle$

$$|J_{K_a K_c} M\rangle = \sum_{J,K,M} a_{JKM} |JKM\rangle \tag{2.7}$$

where a_{JKM} are coefficients and J, K, and M are the quantum numbers for the total

angular momentum, the projection of the total angular momentum onto the figure axis (z-axis), and the the projection of the total angular momentum onto a space fixed axis (Z-axis) respectively [1]. While all these quantum numbers are "good" quantum numbers for the symmetric top (meaning that the operators P^2 and its components P_z and P_Z commute with $H_{\mathrm{rot}}^{\mathrm{rigid}}$), for the asymmetric top K is not a "good" quantum number anymore, since the projection of the total angular momentum onto the figure axis is not constant, because in an asymmetric top there is no internal component of the angular momentum that is a constant of motion [49]. Instead, the distinct sublevels of the asymmetric top can be described by the K quantum numbers of the limiting cases of the symmetric top levels (prolate/oblate) and written as subscripts K_a and K_c to the J quantum number of the respective level. This method was introduced by King et al. [111]. It is noted, that K_a and K_c are no real quantum numbers anymore, instead they are called "pseudo quantum numbers".

Figure 2.1 shows the graph of the connected sublevels (correlation diagram). It sketches the qualitative behaviour of the energy eigenvalues of the asymmetric top wavefunctions as a function of κ and it is visible, that the degeneracy of two symmetric top states with $|J, K, M\rangle$ and $|J, -K, M\rangle$ with $K \neq 0$ is raised and each symmetric top level for $K \neq 0$ connects to two asymmetric top levels. Hence, while the symmetric rotor has only $J + 1$ distinct sublevels, the asymmetric rotor has $2J + 1$ distinct sublevels for each value of J. While fig. 2.1 gives a qualitative behaviour of the levels of the asymmetric top, it is also useful to derive selection rules from it, because it gives the symmetry of the levels.

By setting up the Hamiltonian in the basis of symmetric top wavefunctions, one can solve the Schrödinger equation (the procedure is comprehensively described in [49]) and derive the eigenenergies of the distinct states of the asymmetric top rotor. It is necessary, to identify the a, b, and c axes (assigned to the distinct rotational constants) with the molecular axes x, y, and z, which are given by symmetry operations (and z by convention being the figure axis, i. e., the "axis of highest symmetry" in the molecule). For reference, see [49, table 7.3]. When using the I^l representation (x$\hat{=}$c, y$\hat{=}$b, z$\hat{=}$a), the non-vanishing matrix elements are [111]:

$$\langle JKM|H_{\mathrm{rot}}^{\mathrm{rigid}}|JKM\rangle = \frac{B+C}{2}\left[J(J+1) - K^2\right] + AK^2 \tag{2.8}$$

$$\begin{aligned}\langle JKM|H_{\mathrm{rot}}^{\mathrm{rigid}}|JK \pm 2M\rangle = \frac{C-B}{4}&\left[J(J+1) - (K \pm 1)(K \pm 2)\right]^{\frac{1}{2}} \\ &\times \left[J(J+1) - K(K \pm 1)\right]^{\frac{1}{2}}\end{aligned} \tag{2.9}$$

[1] By convention, coordinates in the molecular frame are given by lower case letters whereas coordinates in the space-fixed (i. e., "laboratory") frame are given by capital letters.

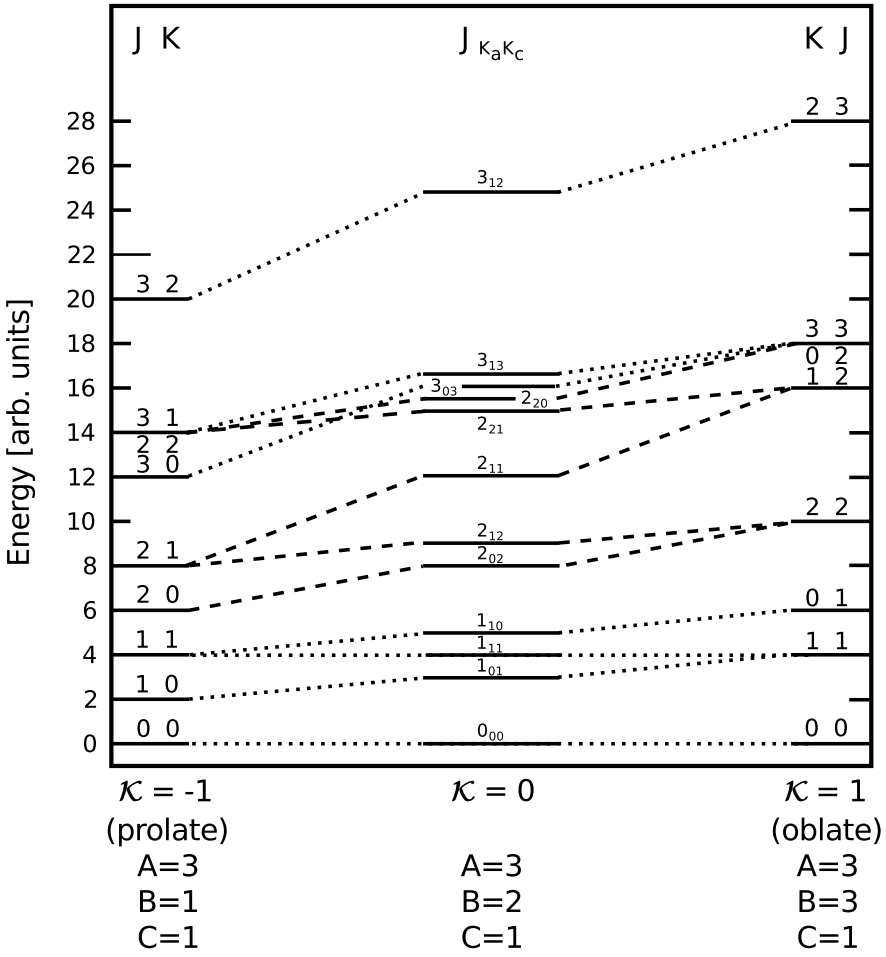

Figure 2.1.: Relation of the energy levels of the asymmetric top rotor to the limiting cases of the prolate and oblate symmetric top rotor levels in dependence of κ. Note: Sublevels of a given J never cross while sublevels of different J may cross (see sublevels in the center of the image, for better illustration: dashed lines are $J = 2$, dotted lines are $J = 1, 3$). Figure adopted from [49]

While this is valid for a strictly rigid molecule, centrifugal forces of the rotating molecule lead to distortions of this molecule which are known as centrifugal distortions. In general, centrifugal distortion increases the moments-of-inertia, thereby decreasing the rotational constants, leading to slightly lower energy levels compared to the rigid rotor model. The resulting Hamiltonian H_{rot} can be written as the sum of $H_{\mathrm{rot}}^{\mathrm{rigid}}$ and a Hamiltonian $H_{\mathrm{rot}}^{\mathrm{cd}}$, the latter comprising the centrifugal distortions.

$$H_{\mathrm{rot}} = H_{\mathrm{rot}}^{\mathrm{rigid}} + H_{\mathrm{rot}}^{\mathrm{cd}} \tag{2.10}$$

The matrix elements of $H_{\mathrm{rot}}^{\mathrm{cd}}$ were given by Watson [112].

In principle, the problem of finding the asymmetric top energy levels is achieved by solving the eigenvalue problem corresponding to eq. (2.1) by applying eqs. (2.8) and (2.9). However, considering symmetry properties of the Hamiltonian results in a further simplification of the problem and it is a prerequisite to determine real or avoided crossings between two certain rotational states when the molecule is exposed to an electric field (which the next subsection will be concerned with). The symmetric top wavefunctions which are used used as the basis functions, see eq. (2.7), can be symmetrized by applying the Wang transformation [113] in order to make them belong to one of the four species of the Four-group. For details on the Four-group and the Wang transformation see, e. g., ref. 49.

The Wang transformation is applied to the symmetric top wavefunctions and results in a factorization (which means a further simplification of the matrix diagonalization task) of the Hamiltonian into four sub-matrices

$$H_{\mathrm{rot}}^{\mathrm{Wang}} = \mathbf{E}^{+}(K_a, K_c) + \mathbf{O}^{+}(K_a, K_c) + \mathbf{E}^{-}(K_a, K_c) + \mathbf{O}^{-}(K_a, K_c) \tag{2.11}$$

The classification of an asymmetric top wavefunction into one of these four classes is obtained by simply looking at the evenness/oddness of the J and K values of the limiting prolate (K_a) and oblate (K_c) symmetric top levels for a certain asymmetric top level. For the I^l representation it is given in table 2.2, where A, B_a, B_b, and B_c represent the four symmetry species of the Four-group, see ref. 49.

Submatrix	K	γ	$\mathrm{J}_{\mathrm{even}}$	$\mathrm{J}_{\mathrm{odd}}$
$\mathbf{E}^{+}$	e	e	A(ee)	B_a(eo)
$\mathbf{E}^{-}$	e	o	B_a(eo)	A(ee)
$\mathbf{O}^{+}$	o	e	B_b(oo)	B_c(oe)
$\mathbf{O}^{-}$	o	o	B_c(oe)	B_b(oo)

Table 2.2.: Classification of the four submatrices in dependence of the evenness/oddness of J, and the evenness/oddness (abbreviated e/o) of K_a, and K_c (in parentheses like (ee), (eo),...) of the limiting prolate and oblate symmetric top levels of a certain asymmetric top level. γ is either 0 (for symmetric Wang functions) or 1 (for antisymmetric Wang functions); table taken from [49]

2.1.2. Stark Effect

When a molecule is exposed to an external electric field, shifting and splitting of the energy levels is observed, an effect first described by Stark [114] and nowadays known as the Stark effect. The interaction energy of a molecule, possessing the permanent dipole moment μ, in an external electric field $\mathbf{E}$ is $-\mu \cdot \mathbf{E}$. We now consider an external electric field along the fixed-in-space Z-axis ($|\mathbf{E}| = E_Z = E$). Then, the Stark contribution to the field-free Hamiltonian H_{rot} is

$$H_{\mathrm{Stark}} = -\mu\mathbf{E} = -E \sum_{g=a,b,c} \mu_g \Phi_{Zg} \tag{2.12}$$

where Φ_{Zg} are the direction cosines or projection of the molecular axes onto the field direction Z [49]. With $-E\mu_g\Phi_{Zg}$ being the contribution H^g_{Stark} to H_{Stark}, it is valid to say $H_{\mathrm{Stark}} = \sum_{g=a,b,c} H^g_{\mathrm{Stark}}$. The eigenvalues of the Hamiltonian $H_{\mathrm{rot,E}} = H_{\mathrm{rot}} + H_{\mathrm{Stark}}$ are found by matrix diagonalization in the basis of the symmetric-top wavefunctions. The Stark effect couples rotational states with $\Delta M = 0$ and $\Delta J = 0, \pm 1$ and hence M remains the only good quantum number in the presence of the external electric field. The non-vanishing eigenvalues of H_{Stark} are given in ref. 115 and ref. 116 respectively.

In practice, calculation of the Stark energies by the CMIstark software is done by setting up $H_{\mathrm{rot,E}}$ for each M individually for all states $|JKM\rangle$ and restricting the number of states to be calculated to a maximum J value J_{max}. The Wang transformation is applied to these states, thereby reducing the computation time for the matrix diagonalization. First, the calculation of the field-free energies is performed and these are sorted by energy. Then, the calculation of Stark energies W_{Stark} is performed for a number of electric field strengths typically achieved in the electrostatic deflector (several 100 kV/cm) in steps of 1 kV/cm. The correct assignment of energies in presence of the electric field to the field-free states is done for each set of states of the same symmetry: Since states of the same symmetry never cross, the ordering must be the same as in the field-free case.

The resulting energies are stored in a file for later application in trajectory simulations using the libcoldmol software package [107]. It is noted, that for decent simulation of molecular trajectories, the calculation of Stark energies must not only be performed for states up to a J_{max}, which are populated in the supersonic expansion, but also for a decent number of higher J states, as the energies of lower lying J states are affected by the higher J states.

Molecular states for which the total energy in an electric field is decreased (compared to the field-free case) are called high-field-seeking (hfs) states, i. e., molecules residing in

these states feel a force towards higher electric field strengths. A so-called effective dipole moment μ_{eff} is introduced as being the gradient of the Stark curve

$$\mu_{\text{eff}} = -\frac{\partial W_{Stark}}{\partial E} \tag{2.13}$$

and molecular states for which $\mu_{\text{eff}} > 0$ are high-field-seeking states. While the behaviour (i. e., whether a state is high- or low-field-seeking) depends on the electric field strength, for the field strengths applied in the experiments described within this thesis, all states are high-field-seeking.

2.1.3. Simulation of Electric Field Induced Deflection

Simulation of electric field induced deflection of molecules using the calculated rotational energies from CMIstark is described in detail in ref. 79. Here, it will be outlined briefly.

First, the electric field strength inside the deflector was calculated with a spatial resolution of 0.1 mm using COMSOL multiphysics [117]. The results were stored in a file to be read by the libcoldmol software.

Single-molecule trajectories were calculated for individual rotational quantum states up to $J_{\text{max}} = 30$. Therefore, molecular packets, each consisting of 10,000 molecules, were used. The molecules were chosen randomly from a initial phase-space distribution. The initial distribution of the transverse coordinates (y, z; x is the propagation axis of the molecular beam) was described by mean values and width of circularly uniform distributions. The velocity coordinates were given by Gaussian distributions, characterized by mean and FWHM values and the initial spread of the starting time (corresponding to the opening time of the Even-Lavie molecular beam valve) was characterized by a Gaussian as well.

After a single-molecule was chosen from this phase-space distribution, its trajectory was calculated by solving the 3d-equations-of-motion using a Runge-Kutta algorithm. The mechanical apertures of the first beam skimmer and the deflector were taken into account and molecules hitting either the skimmer or the deflector electrodes were removed from the simulation. Inside the deflector, the beampath is altered according to the quantum-state dependent dipole moment of the molecule, its mass and the electric field at a given point (the latter was obtained from the COMSOL simulations, see above). Fringe fields at the entrance and exit of the deflector were neglected and the electric field were taken to be constant along the molecular beam propagation direction. After passing the deflector, the molecule is propagated in field-free space to the interaction region. By histogramming the number of molecules in the interaction region in terms of the transverse positions, eventually single-quantum-state molecular beam profiles are obtained.

The single-quantum-state intensities have to be weighted according to the relative contributions of each J-state which is determined by the relative population of theses states at a given temperature. If a single-quantum-state intensity distribution in the interaction region is given by I_s, the total intensity distribution $I(T_{\mathrm{rot}})$ at a given rotational temperature T_{rot} is given by

$$I(T_{\mathrm{rot}}) = \frac{1}{w} \sum_{s=1}^{N} w_s(T_{rot}) I_s \tag{2.14}$$

with N being the number of quantum states used in the simulations, including only states with $M \geq 0$ and $w_s(T_{\mathrm{rot}})$ being the weighting factor for the population

$$w_s(T_{\mathrm{rot}}) = g_M g_{\mathrm{ns}} e^{\frac{W_0 - W_s}{k_B T_{\mathrm{rot}}}} \tag{2.15}$$

g_{ns} is the weighting factor based on the nuclear spin statistical weight of the current state. $g_M = 1$ for $M = 0$ and $g_M = 2$ otherwise (states with $M > 0$ are doubly degenerate). The exponential term accounts for a temperature dependent Boltzmann distribution of the population of the specific state. W_0 is the energy of the field-free ground state and W_s the energy of the specific state s.

2.2. Laser Alignment

2.2.1. Introduction

Laser alignment of gas-phase molecules can be achieved by exploiting the anisotropic interaction of the molecular polarizability with a strong polarized laser field. During the experiment performed in the framework of this thesis, only adiabatic laser-alignment (where the laser pulse is long compared to the rotational period of the molecule) by a near-infrared (NIR) laser with pulses in the ns-regime was utilized and will be described in the following. In general, due to quantum mechanics the spatial confinement of a coordinate (here: the polar angle θ decribing the relative orientation of molecule with respect to the laser polarization) requires an uncertainty in the conjugate coordinate, which in the case of the polar angle θ is the angular momentum. Thus, a superposition of states of different angular momentum is required for spatial confinement, i. e., alignment of θ. By interaction of the polarized laser field with the anisotropic polarizability of the target molecule, eventually the molecule gets aligned along a preferred direction in space given by the most polarizable axis of the molecule [83].

2.2.2. Qualitative Description of Laser Alignment

To be more precise, consider an electric field of the laser at a fixed point in space (i. e., the position of the molecule) given by

$$\mathbf{E}(t) = \epsilon(t)\mathbf{E}_0 \cos(\omega t) \tag{2.16}$$

The interaction energy of a molecule with an electric field $\mathbf{E}(t)$ can be described in terms of the interaction of the electric field with the permanent (μ) and induced ($\alpha \cdot \mathbf{E}(t)$) dipole moments of the molecule. The additional potential $V(t)$ to the field-free Hamiltonian H_{rot} of the molecule is given by

$$V(t) = -\sum_i \mu_i E_i - \frac{1}{2}\sum_{i,j} E_i(t)\alpha_{ij}E_j^*(t) \tag{2.17}$$

where the first term can be easily identified as the Stark interaction term from eq. (2.12). When exploiting the electric field of a strong, but non-ionizing, off-resonant laser for molecular alignment, interaction of a molecule with the rapidly varying electric field of the laser forces the time-average of the term comprising the permanent dipole moment to be zero when averaged over a cycle of the laser pulse [2]. Since the first term on the right side of eq. (2.17) can be neglected, laser alignment of molecules in first approximation is governed by the interaction of the polarizability α_{ij} of the molecule with the electric field of the laser, which does not average to zero upon reversal of the electric field, since the induced dipole follows the reversal of the electric field [118]. It should be mentioned, that the expansion of the potential $V(t)$ in terms of the electric field E in principle also includes higher moments of the order of E^3, E^4, ..., which, for simplicity, are neglected in eq. (2.17). In general, laser alignment is governed by all (hyper-) polarizabilities connected to even powers of E (i. e., the terms proportional to E^2, E^4, E^6, ...). In the following, only the term proportional to E^2 is considered.

In the general case of an asymmetric top molecule, the polarizability is a 3×3 tensor, given by the components α_{ij} with respect to a certain coordinate system. It is always possible to achieve a representation where α_{ij} is diagonal, containing the three distinct components α_{xx}, α_{yy}, and α_{zz}. The distinct components represent the fact that polarization of the molecule by external electric fields is in favor of some directions in the molecule, hence the interaction is anisotropic. As a consequence, the interaction of the molecule and the electric field of the laser depends on the relative orientation of the fields and the field exerts a torque on molecules, which are residing in "not favorable" orientation at the

[2] For the fundamental of an Nd:YAG laser with $\lambda = 1064$ nm, the field direction is reversed after each half-cycle of the laser pulse, where a half-cycle is 1.77 fs.

time of interaction between the laser field and the molecule. The components of α_{ii} (the diagonal representation) are not necessarily along the a,b,c-axes (i. e., the principal axes which are given by the principal moments of inertia of the molecule) nor along a space-fixed axis. A transformation from one system to another can be performed by applying the direction cosine matrices, given in, e. g., ref. 119.

For determination of the degree of alignment achievable by an induced potential given by the laser field, the solutions of the Hamiltonian

$$H = H_{\mathrm{rot}} + V(t) \tag{2.18}$$

have to be found. It should be noted, that non-perturbative methods must be applied, as the interaction term, caused by the induced potential, exceeds the field-free rotational energies by some orders of magnitude. The eigenstates in the presence of a strong external electric field are called "pendular states", since they correspond to a molecule librating in a potential well, similar to the motion of a pendulum. While the second term in eq. (2.17) depicts the most general case of an induced potential $V(t)$, for linearly polarized laser light interacting with a linear molecule, the potential can be written as

$$V = -\frac{E_0^2}{4}(\Delta\alpha \cos^2\theta + \alpha_\perp) \tag{2.19}$$

with $\Delta\alpha = \alpha_\parallel - \alpha_\perp$ being the polarizability anisotropy, i. e., the difference of the polarizabilities along and perpendicular to the internuclear axis and θ being the polar angle between the linear polarization of the laser and the internuclear axis of the molecule. It should be noted, that the potential for the symmetric top molecule looks the same and θ in that case is the angle between the laser polarization and the axis of highest symmetry of the molecule. The additional factor of $1/2$ accounts for the fact that the time scale of molecular rotation is much longer than one optical half-cycle, hence the time-average of the term $\cos^2(\omega t)$ is equal to $1/2$. With $\Delta\alpha > 0$, the energy is minimized for $\theta = 0, \pi$, i. e., alignment along the internuclear axis. For an asymmetric top with α_{ij} being diagonal in the principal axes frame of the molecule, $V(t)$ can be written as

$$V = -\frac{1}{4}E_0^2 \left[\sin^2\theta(\alpha_{xx}\cos^2\chi + \alpha_{yy}\sin^2\chi) + \alpha_{zz}\cos^2\theta\right] \tag{2.20}$$

introducing the new angle χ which is the angle of rotation around the axis of the laser polarization. Though not completely unhindered when using linearly polarized laser light, the potential in this χ-direction is usually small and asymmetric tops almost freely rotate about this axis if the two smaller components of α_{ij} are almost equal [83]. A numerical solution to the Schrödinger equation involving the matrix elements of the trigonometric

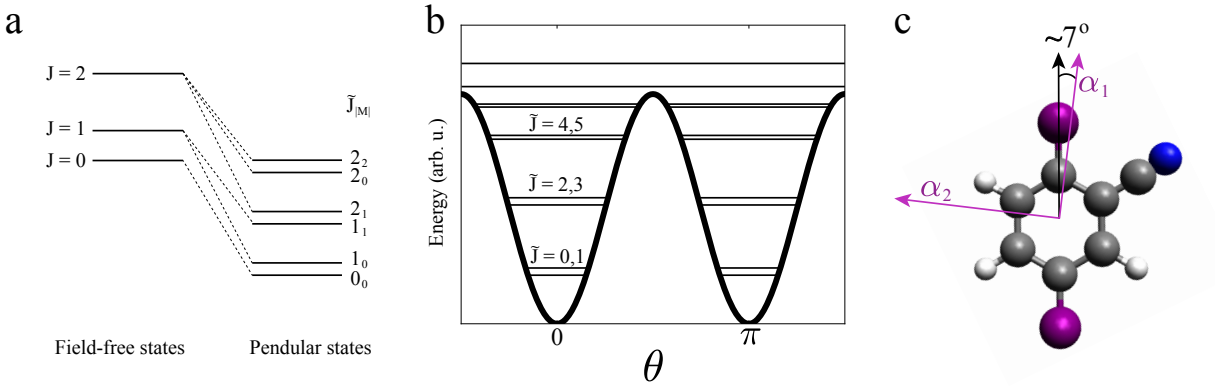

Figure 2.2.: Schematic illustration of the relation of field-free states to the corresponding pendular states (a) and the pendular states in the laser potential for $|M| = 0$ (b) for a linear molecule. Figures derived from [89, 118, 123]. The tunneling splitting is exaggerated for illustrative purposes. (c) shows the molecule 2,5-diiodobenzonitrile (DIBN). The highest component of the polarizability is inclined by $\approx 7°$ with respect to the iodine-iodine axis.

functions given above is outlined, e. g., in ref. 120. In a qualitative view, from the shape of the potential V, involving the angles χ and θ, it is immediately seen, that V gives rise to a wave packet in J and K-space while M remains a good quantum number and is unaltered by V in the case of a linearly polarized laser. Using elliptically polarized laser light enables to achieve 3d-alignment of molecules with the axis of second-highest polarizability pointing along the smaller axis of the laser-polarization ellipse [121]. The potential involving elliptically polarized laser light is much more involved and is given, e. g., in ref. 122.

Equations (2.19) and (2.20) predict a double-well potential with respect to the angle θ and the eigenfunctions of the potential in presence of a strong laser field are the pendular states. In case of a linear molecule with just two distinct components of the polarizability, the relation of the pendular states to the adiabatically corresponding field free-states and the double-well potential can be drawn easily and this gives a good qualitative view of laser alignment. Figure 2.2 (a) shows the correlation of the field-free eigenstates to the pendular states in presence of the laser field and (b) sketches the double-well potential in dependence of the angle θ for states with $|M| = 0$. In the latter case, the states appear as closely-spaced (in terms of energy) doublets with each doublet consisting of two parity eigenstates with positive and negative parity [96]. The spacing between the two states of each doublet is given by the tunneling frequency which depends on the height and width of the potential. The calculation of the energies of the pendular states, even without knowing the wavefunctions explicitely, can be achieved in a way similar to the

calculation of the energies of the field-free asymmetric top, which was described above, namely by projecting the Hamiltonian on the symmetric top eigenstates as is described, e. g., in ref. 118.

For DIBN, the polarizabilities were obtained using ab-initio calculations (GAMESS-US MP2/6-311G** [124]). The most-polarizable axis (with $\alpha_1 = 30.81$ Å^3) lies in the plane of the benzene ring, inclined by $\approx 7°$ to the iodine–iodine axis. Therefore, DIBN will align almost along the iodine-iodine axis. The second highest polarizability ($\alpha_2 = 18.91$ Å^3) lies in the molecular plane, perpendicular to α_1 and the smallest component ($\alpha_3 = 9.57$ Å^3) lies normal to the molecular plane. A detailed picure of the polarizability components is also given in appendix B.

A short note on the state population concludes this section: In adiabatic alignment, each initial state is transferred adiabatically to the corresponding pendular state as the pulse envelope $\epsilon(t)$ slowly (i. e., long compared to the rotational period of the molecule) increases with time [96]. Hence, the presence of the field does not change the initial population of the states. In order to achieve a good degree of alignment, the molecules should already be in the lowest states prior to interaction with the laser potential, because, as can be seen in fig. 2.2 (a), the lower states are spatially (i. e., with respect to θ) confined to a more narrow range than the higher states. Therefore, spatial quantum-state selection of the lowest rotational states will be a highly-valued prequisite in order to achieve strong laser alignment as was confirmed experimentally, see, e. g., ref. 42.

2.3. X-ray Diffraction from Isolated Molecules

2.3.1. Introduction

The study of the structure of matter, i. e., the spatial arrangement of individual atoms almost always serves as the first step of understanding the physical properties of matter and its behaviour when undergoing dynamical processes. As pointed out in before, molecular structures can be obtained by imaging, i. e., optical methods or spectroscopic methods respectively. Spectroscopic methods such as rotational or NMR spectroscopy were outlined before in chapter 1 and will not be dealt with any longer. Structure determination by optical methods with spatial resolution in the range of interatomic distances requires electromagnetic wavelengths in the x-ray regime, hence wavelengths in the nm – pm range. The far-field wavefield of the x-rays, scattered from atoms or molecules, in principle contains all the information necessary for reconstruction of the structure, i. e., the electron density (x-rays scatter primarily at electrons) of the sample under investiga-

tion. If the wavefields intensity and phase could be measured simultaneously, an image of the sample could be obtained by a simple Fourier transform. Optical devices like lenses can be used to "perform the Fourier transformation", i. e., produce an image of the sample in real space). However, this approach doesn't work for x-ray diffraction since no optical devices like lenses exist for x-ray radiation (though zone plates may be used as dispersive elements in the UV/soft x-ray regime). Furthermore, only the diffracted intensities can be measured in an experiment and the information about the phase of the scattered wave is lost. This is known as the "phase problem" in the x-ray imaging community. Prior knowledge about the sample size, complementary measurements (e. g., involving absorption or inelastic scattering processes) and/or mathematical algorithms may be used to perform the retrieval of the phase and eventually, a reconstruction of the unknown sample structure [5, 125].

Other kinds of radiation, such as, e. g., particle radiation made up by accelerated electrons, or neutrons, maybe used for imaging at the atomic lengthscales, too, as their de-Broglie wavelengths are typically also within the necessary pm-range when accelerated to high kinetic energies. The theoretical description of the scattering and imaging by these particle beams is in many respects very similar to the description of diffraction and imaging by x-rays. However, this thesis deals with electromagnetic radiation in the x-ray region only. In the following, the theoretical framework to understand x-ray diffraction by molecules is derived and necessary formulas are given. The theory outlined here will be utilized again in chapter 6 in order to quantitatively simulate x-ray diffraction intensities.

2.3.2. Photon Scattering from an Electron

The theory of x-ray diffraction presented here is either explicitly given in ref. 125 or derived from there. X-rays are electromagnetic waves and the electric field of a linearly polarized monochromatic electromagnetic wave at a certain point $\mathbf{r}$ in space at a given time t can be written as

$$\mathbf{E}(\mathbf{r}, t) = \epsilon E_0 e^{i(\mathbf{k}\cdot\mathbf{r}-\omega t)} \tag{2.21}$$

with $\mathbf{k}$ being the wavevector (a vector along the propagation direction of the wave with the magnitude $2\pi/\lambda$ with λ being the wavelength), ω being the radial frequency ($\omega = 2\pi\nu$ with ν being the frequency of the wave), and ϵ being a unit vector along the polarization direction. Scattering involves a momentum transfer of the incident to the scattered wave. The scattering vector (sometimes also called wavevector transfer) $\mathbf{Q}$ is defined as

$$\mathbf{Q} = \mathbf{k} - \mathbf{k}' \tag{2.22}$$

with $\mathbf{k}$ and $\mathbf{k}'$ being the wavevectors of the incident and the scattered wave respectively. The scattering is assumed to be elastic, meaning that the scattered radiation is of the same wavelength λ as the incident radiation (and hence $|\mathbf{k}| = |\mathbf{k}'|$). The derivation of the intensity scattered from molecules to a given scattering vector $\mathbf{Q}$ (at scattering angle 2Θ) is based on a classical model which builds up on the scattering strength of a single electron. At a given point $\mathbf{R}$ (corresponding to a certain $\mathbf{Q}$) in space, the (time-averaged) ratio of scattered electric field (scattered by a single electron) $E_{\mathrm{sc}}(\mathbf{Q})$ to incident electric field E_0 can be written as

$$\frac{E_{\mathrm{sc}}(\mathbf{R})}{E_0} = -r_0 \frac{e^{i\mathbf{kR}}}{R} P^{\frac{1}{2}} \tag{2.23}$$

with the so-called "Thomson scattering length" r_0

$$r_0 = \left(\frac{e^2}{4\pi\epsilon_0 mc^2} \right) = 2.82 \cdot 10^{-5} \mathring{\mathrm{A}} \tag{2.24}$$

which is regarded as the classical radius of an electron. $e^{i\mathbf{kR}}/R$ describes the falloff of the intensity of a spherical wave and P is the polarization factor which depends on the x-ray source used in the particular experiment. For linearly polarized x-ray radiation, $P = \cos^2\psi$ in the plane of polarization and $P = 1$ in the plane perpendicular to the polarization of the x-ray light. The general form of P is given by $P(\mathbf{k}') = 1 - |\hat{\mathbf{u}} \cdot \hat{\mathbf{k}}'|^2$ where the unit vector $\hat{\mathbf{u}}$ is along the polarization in the case of linearly polarized incident radiation [126].

2.3.3. Photon Scattering from Atoms, Molecules and Crystals

To calculate the ratio given in eq. (2.23) for a single atom, the electron distribution $\rho(\mathbf{r})$ within the single atom has to be considered (the atomic nucleus doesn't have to be considered since it is much heavier than the electrons and hence, in the classical picture, is by far not accelerated as well). Then, the scattered radiation field is a superposition of contributions from different volume elements of this charge distribution. The determination of the scattered field involves consideration of the phase of the wave as it interacts with volume elements at different positions. A volume element $\mathrm{d}\mathbf{r}$ at $\mathbf{r}$ contributes an amount $-r_0\rho(\mathbf{r})\mathrm{d}\mathbf{r}$ to the scattered field with a phase factor $e^{i\mathbf{Qr}}$. Thus, the total scattering amplitude of a single atom is

$$-r_0 \cdot f^{(0)}(\mathbf{Q}) = -r_0 \cdot \int \rho(\mathbf{r}) e^{i\mathbf{Qr}} \mathrm{d}\mathbf{r} \tag{2.25}$$

$f^{(0)}(\mathbf{Q})$ is the atomic form factor (or: atomic scattering factor). The right side of eq. (2.25) can be readily identified as a Fourier transform, i. e., the atomic form factor is the Fourier

transform of the electronic charge distribution in the atom. In the limits, $f^{(0)}(\mathbf{Q} \to 0)$ and $f^{(0)}(\mathbf{Q} \to \infty)$ behaves like

$$f^{(0)}(\mathbf{Q}) = \begin{cases} Z & \text{for } \mathbf{Q} \to 0 \\ 0 & \text{for } \mathbf{Q} \to \infty \end{cases} \tag{2.26}$$

where Z is the atomic number (total number of electrons) of a given atom. Atomic scattering factors can be calculated using a parametrization given in [127], where $f^{(0)}$ is obtained by the sum of five Gaussians and a constant c

$$f(s) = \sum_{i=1}^{5} a_i e^{-b_i s^2} + c \tag{2.27}$$

s represents the often used reduced scattering vector $s = \sin\Theta/\lambda$ [3]. At x-ray energies within the range of atomic absorption edges, corrections to the atomic scattering factor (the so-called dispersion corrections) $f'(\hbar\omega)$ and $f''(\hbar\omega)$ have to be considered, which account for the fact that electrons in the atom are bound and their behaviour is governed by quantum mechanics. Intuitively it is clear that the behaviour of bound electrons should be different to the behaviour of free electrons and the scattering strength of bound electrons should be smaller than the scattering strength of free electrons. The behaviour of the dispersion corrections is dominated by the tightly bound inner shell electrons and hence they depend mostly on the energy $\hbar\omega$ of the incident photons and don't have any remarkable dependence of $\mathbf{Q}$. Including dispersion corrections, the total atomic scattering factor is

$$f(\mathbf{Q}, \hbar\omega) = f^{(0)}(\mathbf{Q}) + f'(\hbar\omega) + i f''(\hbar\omega) \tag{2.28}$$

The dispersion correction diminish the scattering strength of an atom, and hence, with our sign convention, $f'(\hbar\omega)$ is negative. $f''(\hbar\omega)$ accounts for a phase shift, predominantly in the vicinity of a resonance. With increasing photon energy, the dispersion corrections vanish and $f(\mathbf{Q}, \hbar\omega) \to f^{(0)}(\mathbf{Q})$. Energy dependent and element-specific atomic scattering factors, implicitely including dispersion corrections f' and f'', are given in terms of f_1 and f_2 and are tabulated in ref. 128. In order to include dispersion corrections, the constant c in eq. (2.27) can be replaced by $f_1(\hbar\omega) + i f_2(\hbar\omega) - \sum_{i=1}^{5} a_i$.

As an example, fig. 2.3 shows the scattering factor f_{Iodine} of iodine ($Z = 53$) in dependence of the scattering vector s. The blue line depicts $f_{\text{Iodine}}(s)$ for the energy-independent

[3] The notation $s = \sin\Theta/\lambda$ according to ref. 127 is used rather than $s = 2\sin\Theta/\lambda$.

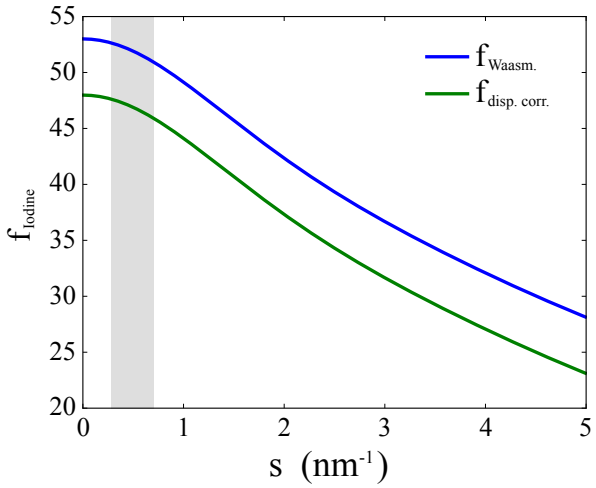

Figure 2.3.: Scattering factor f_{Iodine} of iodine ($Z = 53$) in dependence of the scattering vector $s = \sin\Theta/\lambda$. $f_{\text{Iodine}}(s)$ is shown for the energy-independent approximation by five Gaussians plus a constant, given by Waasmaier and Kirfel [127] (blue) and for the energy-dependent case involving dispersion-corrections, given by Henke et al. [128] (green, only the real part of f_{Iodine} is shown). The grey-shaded area marks the region of s-values covered in the experiment ($s = 0.28 - 0.7 \cdot \text{nm}^{-1}$).

approximation by five Gaussians plus a constant, which is given by Waasmaier and Kirfel in [127]. The green line shows $f_{\text{Iodine}}(s)$ for the energy-dependent case, involving dispersion-corrections (at a photon energy of 2 keV) given by Henke et al. [128]. The difference between both is merely a shift by an offset. The grey-shaded area marks the region of s-values covered in the experiment (where s is in the range $s = 0.28 - 0.7\ \text{nm}^{-1}$).

Considering the ideas mentioned above for the atomic scattering factor, the scattering amplitude of a molecule, which is composed of j atoms at positions $\mathbf{r}_j$, is simply obtained by adding up the contributions by the different atoms in the molecule and keeping track of the phases. Hence, the molecular scattering factor is given by

$$F_{\text{mol}}(\mathbf{Q}) = \sum_j f_j(\mathbf{Q}) \cdot e^{i\mathbf{Q}\mathbf{r}_j} \tag{2.29}$$

and hence the ratio of the amplitudes of the scattered to the incident electric field for a single molecule is given by

$$\frac{E_{\mathrm{sc}}(\mathbf{R},\mathbf{Q})}{E_0} = -r_0 \left(\cdot \sum_j f_j(\mathbf{Q}) \cdot e^{i\mathbf{Q}\mathbf{r}_j} \right) \frac{e^{i\mathbf{k}\mathbf{R}}}{R} P^{\frac{1}{2}} \tag{2.30}$$
$$= -r_0 \cdot F_{\mathrm{mol}}(\mathbf{Q}) \frac{e^{i\mathbf{k}\mathbf{R}}}{R} P^{\frac{1}{2}}$$

The goal of every experiment then would be the determination of $F_{\mathrm{mol}}(\mathbf{Q})$ for sufficiently many values of $\mathbf{Q}$ followed by fitting a model to the data to determine the positions $\mathbf{r}_j$ of the individual atoms. Since the expected scattering signal from a single molecule is very weak, not even at todays 3$^{\mathrm{rd}}$ generation x-ray sources (i. e., synchrotrons, equipped with undulator beamlines) one is able to record a measurable signal above experimental noise levels in a reasonable amount of time. But if many identical molecules get assembled into a crystal, a huge increase in the scattered signal can be obtained. The reason is the interference of scattered x-rays reflected from different lattice planes of the crystal. In a crystal, the site $\mathbf{r}_{\mathrm{atom}}$ of each atom can be written as the sum of the position $\mathbf{r}_j$ of the atom within a single unit cell of the lattice (which could be one single molecule) plus the lattice vector $\mathbf{R}_n$, the latter giving the position of a unit cell and reflecting the periodicity of the lattice. Hence, because $\mathbf{r}_{\mathrm{atom}} = \mathbf{r}_j + \mathbf{R}_n$, the scattering amplitude can be written as

$$F_{\mathrm{crystal}}(\mathbf{Q}) = \underbrace{\sum_j f_j(\mathbf{Q}) e^{i\mathbf{Q}\mathbf{r}_j}}_{\text{Unit cell structure factor}} \cdot \underbrace{\sum_n e^{i\mathbf{Q}\mathbf{R}_n}}_{\text{Lattice sum}} \tag{2.31}$$

where the lattice sum is evaluated for all n unit cells of the lattice. Assembling identical molecules into a crystal lattice serves as a means for amplification of the molecular scattering by a huge amount for the following reason: The lattice sum contains phase factors located on the unit circle in the complex plane. Therefore, the lattice sum will be of order unity for many scattering vectors $\mathbf{Q}$. Only if $\mathbf{Q}$ coincides with a reciprocal lattice vector $\mathbf{G}$ of the crystal lattice (i. e., $\mathbf{Q} = \mathbf{G}$), the phase factors will be multiple integers of 2π and the lattice sum becomes equal to the number n of unit cells of this crystal. This is known as Bragg diffraction and the resulting Bragg spots in the diffraction pattern are usually very sharp and well above noise levels. Hence, x-ray crystallography, based on Bragg diffraction, serves as the method of choice in structure determination at synchrotrons if the single molecular constituents of a sample of interest can be assembled to a crystal.

The scattering amplitude for a crystal is only given for the sake of completeness and to illustrate the huge advantages of crystallography compared to single-molecule diffraction at x-ray lightsources like, e. g., synchrotrons. In contrast, this thesis presents and discusses results from an experiment utilizing ultrashort and highly intense x-ray pulses from the

x-ray free-electron laser LCLS diffracting from a non-crystalline gas-phase sample. In this novel, so-called "diffract-before-destruct" approach, the x-ray pulses are used in order to circumvent the necessary crystallization of molecules for structure determination by x-ray diffraction, as discussed above.

3. Experimental Setup

This chapter describes the experimental setups utilized in this work. The first section is concerned with the setup used at DESY for measuring molecular beam deflection profiles of indole, indole-water clusters and 2,5-diiodobenzonitrile (DIBN) while the second section explains the setup for the coherent x-ray diffraction experiment on an ensemble of isolated molecules in the gas phase which was performed at the Linac Coherent Light Source (LCLS), an x-ray free-electron laser at the SLAC National Accelerator Laboratory. The molecular beam setup utilized at LCLS is identical to the molecular beam used in the deflection experiments at DESY except for small modifications, which will be mentioned separately in the section describing the setup at LCLS.

3.1. Molecular Beam Deflection Experiments at DESY

The molecular beam experimental setup used in the laboratory at DESY for measuring deflection profiles is depicted in fig. 3.1. As mentioned above, the same molecular beam setup was used at LCLS to provide the target molecules for the x-ray diffraction experiment of aligned DIBN molecules.

The experiment was conducted under ultrahigh vacuum conditions in a vacuum-chamber system consisting of three chambers, connected at the sites of the molecular beam skimmers. Inside vacuum, the chambers are separated by walls and the only connection between the chambers is through molecular beam skimmers. In this way, differential pumping of the three chambers ensures a low pressure in the interaction region ($p = 6 \cdot 10^{-9}$ mbar) while the pressure in the chamber housing the molecular beam valve is in the 10^{-6} mbar region when the valve is operated. The pumping system consists of three turbomolecular pumps (HiPace series, Pfeiffer Vacuum) with pumping speeds of 2000 l/s

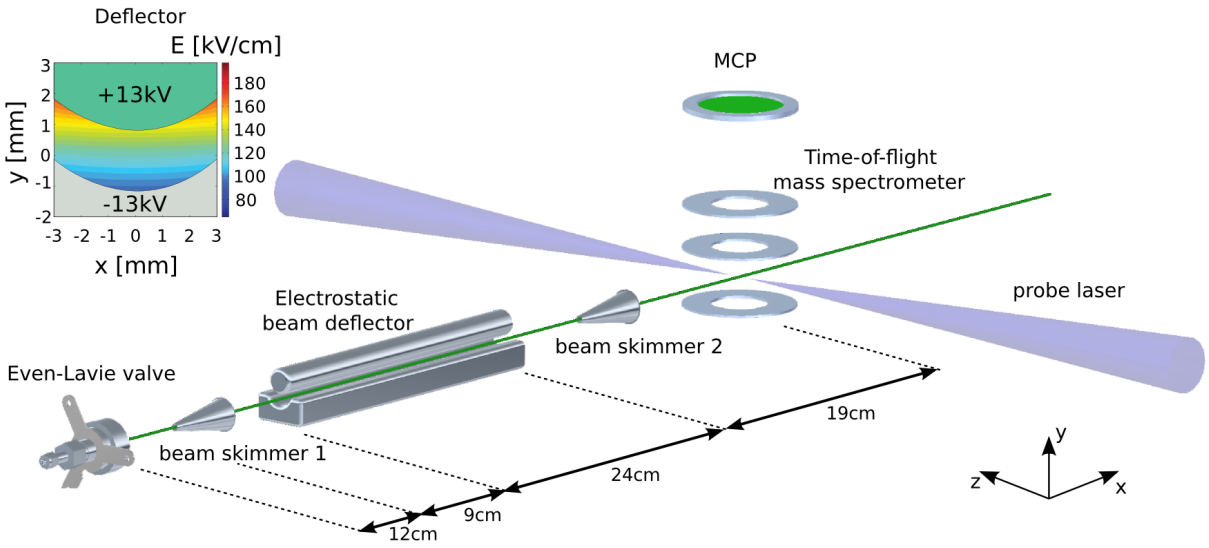

Figure 3.1.: Schematic layout of the experimental setup used for measurements of spatial molecular beam profiles; see text for details.

(molecular beam source chamber), 400 l/s (deflection chamber) and 700 l/s (interaction chamber) backed by either a booster pump (Ontool Booster, Pfeiffer Vacuum, pumping speed 130 m^3/h) or a scroll pump (Edwards XDS, pumping speed 35 m^3/h).

The molecules for deflection measurements were provided in a cold (typically around 1 K) molecular beam [55], which is formed by a supersonic expansion of a mixture of a few mbar of either indole (C_8H_7N) and water (H_2O) or 2,5-diiodobenzonitrile ($C_7H_3I_2N$, DIBN) seeded in helium at high pressure by using a pulsed Even-Lavie valve (EL valve) [129] inside the first chamber (source chamber). A small heatable reservoir inside the valve contains the molecules (indole or DIBN), while the water for the (indole-water experiment) is provided by connecting the gasline to a small reservoir filled with a few ml of de-ionized water. The molecules form a mixture with the helium backing gas, in which the ratio of the constituents depend on the vapor pressures of the molecules, while the pressure of He always was set to $\approx$ 50 bar. For indole, the temperature of the valve was set to 35–40°C while for DIBN it was set to 170°C.

The EL valve, the deflector, and both skimmers were mounted to z-y-translation stage systems (Feinmess Dresden for the EL valve and the deflector; PI,Physikinstrumente Karlsruhe for the skimmers). Fine adjustment of the molecular beam axis was achieved using the y-z-translation stages of the valve, the deflector and the two skimmers. The translation stages were also used for spatial movement of the whole molecular beam, which was applied for measurements of spatial molecular beam profiles by scanning the molecular

beam in y-direction while keeping the detection laser path fixed. The last skimmer was adjusted in order to maximize the transmission through the skimmer when the molecules are deflected.

The skimmers not only confine the molecular beam but also serve as the only orifice from the previous chamber to the next vacuum chamber, allowing for strong differential pumping, typically by two orders of magnitude. Even with a pressure of 10^{-6} mbar within the source chamber, a pressure of 10^{-8} to 10^{-9} mbar in the detection chamber (separated by two differential pumping stages) is achieved.

During the experiment, the valve is opened by a strong, short (10–11 μs) current pulse. The co-expanded molecules (DIBN or indole) are rotationally cooled by collisions with the seed gas helium. When using indole, clusters of indole and H_2O (indole$(H_2O)_n$) are formed in the early part of the expansion due to three-body collisions. After passing a skimmer (Beam Dynamics, model 50.8) with orifice diameter of 2 mm (typically placed 12 cm downstream of the valve), the molecular beam enters the chamber housing the electrostatic deflector (deflector chamber), which provides spatial quantum-state selection of molecules according to their dipole-moment-to-mass ratio. The deflector consists of two polished stainless steel electrodes, a rod and a trough, which are isolated with respect to ground and mounted at a vertical distance (see inlet of fig. 3.1) of 2.3 mm via ceramic holders (material: Macor). High static electric potentials can be applied to both electrodes via HV-feedthroughs connected to HV-power supplies (Bertram) outside vacuum, thus creating an inhomogenous electric field on the molecular beam axis of the deflector. The electric field gradient exerts a force on neutral polar molecules and clusters, which forces them to deflect towards the deflector rod, if they are in high-field seeking (hfs) states[1]. The maximum voltage difference applied across the deflector for the indole-water experiment was 26 kV (rod at +13 kV, trough at -13 kV), resulting in a electric field strength of 120 kV/cm and an electric field gradient of 250 kV/cm^2 in the center of the deflector. However, to investigate the electric field dependence of the molecular beam deflection, also voltage differences in between 0 and 26 kV were applied during the indole-water experiments. For DIBN, the maximum voltage difference was 20 kV.

After propagating through the deflector and passing a second skimmer of orifice diameter 3 mm (Beam Dynamics, model 50.8), the molecular beam enters the interaction chamber, which is equipped with a time-of-flight (TOF) mass spectrometer (Jordan). The molecular beam is crossed in the center of the TOF mass spectrometer by either a pulsed dye laser (Fine Adjustment) for the indole-water experiment or a pulsed Ti:Sa laser sys-

[1]For the electric fields used, the rotational quantum states populated by the molecules are all high-field seeking.

tem (Spectra Physics Spitfire Ace) for the DIBN experiment. The dye laser system (Fine Adjustment, Pulsare Pro) was pumped by a frequency-doubled Nd:YAG laser (Innolas, Spitlight 600-20). The dye laser pulse length was 10 ns and the pulse energy typically was in the range of 2–3 mJ. The dye laser was focussed by a UV-lens ($f = 75$ cm) in the center of the TOF mass spectrometer. The lens was mounted on a translation stage and can be moved along the y axis in order to spatially scan the molecular beam via moving the laser focus along this axis. The dye laser was operated with the dye Rhodamin 6G and can be tuned in the wavelength range 280–290 nm. Indole and indole(H_2O) clusters were ionized via one-color resonance-enhanced multi-photon ionization (REMPI). While indole is ionized at 4.369 eV (35231.42 cm^{-1}, 283.728 nm) [130], indole$(H_2O)_1$ is ionized at 4.353 eV (35099.42 cm^{-1}, 284.802 nm) [131]. Since ionization was achieved via a resonant excitation step involving distinct laser frequencies, the ionization is sensitive to the distinct species.

For the DIBN experiment, the UV-lens was exchanged in favor of a lens focussing the Ti:Sa laser ($f = 70$ cm). The pulse length t_{pulse} of the Ti:Sa laser pulse is $t_{\text{pulse}} \approx 45$ fs (FWHM). The focus size was measured with a beam profiler as $\omega_0 = 50$ μm. The pulse energy was 3 mJ, resulting in a peak power of $1.6 \cdot 10^{15}$ W/cm^2. The distinction whether ionization is due to multi-photon or field ionization can be made by estimation of the Keldysh parameter γ, which has to be < 1 for field-ionization. The Keldysh parameter for He (with ionization energy 24.6 eV) is estimated to $\gamma = 0.359$. The Keldysh parameter for DIBN cannot be estimated exactly, since the ionization energy for DIBN is not known. In any case it is assumed to be less than the ionization energy of the He atom, i. e., less than 24.6 eV, which would lead to $\gamma < 0.359$ anyway. Considering the ionization energy of 1,4-diiodobenzene ($C_6H_4I_2$) with an ionization energy of 8.6 eV [132] results in $\gamma = 0.212$. Hence, both DIBN and He are ionized exploiting strong field ionization.

The TOF mass spectrometer was operated in a Wiley-McLaren configuration [133]. The created ions are extracted from the interaction zone and accelerated towards a multi channel plate detector (MCP). By measuring the time of flight t of the different ions starting from t_0=0 (time of laser hitting the molecular beam) to the time t of impact of the ions on the MCP, the mass-to-charge ratio of the impinging ions can be obtained given by $t \propto \sqrt{m/q}$. Assuming singly charged ions, the time axis can be converted to a mass axis giving a mass spectrum. Relative indole densities were obtained from the mass 117 u (measuring at the indole$^+$ signal) while indole$(H_2O)_1$ densities were determined by adding the signals for mass 117 u (indole) and 135 u (indole$(H_2O)_1$), because after ionization, indole$(H_2O)_1$ can fragment to indole$^+$ + H_2O. Molecular densities were not determined in absolute values due to the unknown cross sections. Relative DIBN intensities were obtained from either the signal of I^+ (mass 127 u) or DIBN$^+$ ions (mass 355 u). The

signal was amplified by the MCP and recorded with a digitizer (Acqiris DC440). The data was read out by a VxWorks SBC and sent to the running data acquisition software KouDa [134] for further processing.

The whole experiment was conducted at 20 Hz. For indole-water, the limitation of 20 Hz was given by the maximum repetition rate of the pumped dye laser system. Although the Ti:Sa laser system, used for the DIBN experiment, was not limited to 20 Hz, the repetition rate of 20 Hz was kept for this experiment as well. The experiments were synchronized using an external trigger card (FHI Berlin, DG3008) for the indole-water experiment or a delay generator (Stanford Research systems, DG645) for the DIBN experiment, respectively.

3.2. Coherent X-ray Diffraction Experiments at LCLS

This section is concerned with the experimental setup used for the coherent x-ray diffraction experiment on an ensemble of laser-aligned isolated gas-phase molecules conducted at the x-ray free-electron laser LCLS. The experiment was performed at the Atomic, Molecular and Optical Physics (AMO) beamline of LCLS [135] using the CAMP experimental chamber [136], which has been attached to the High Field Physics (HFP) chamber at the AMO beamline. The section summarizes the most relevant features of the free-electron laser LCLS, the experimental setup and detection devices used in the CAMP chamber, and the data acquisition system.

3.2.1. The Linac Coherent Light Source LCLS

The Linac Coherent Light Source (LCLS) is a x-ray free-electron laser (XFEL) located at the SLAC National Accelerator Laboratory. LCLS is considered to be the worlds first real XFEL with photon pulses at hard x-ray wavelengths in the range of 0.12–2.2 nm, delivering ultrashort (fs-range) x-ray pulses with a peak brightness that extends the one obtained at synchrotrons by nearly ten orders of magnitude.

A FEL uses the interaction of an electromagnetic wave and a bunch of relativistic electrons for amplification of this electromagnetic wave in a periodic magnetic array equipped with permanent magnets of alternating polarity as the wave and the electron bunch travel through the undulator[21]. LCLS is a so-called SASE-FEL, it starts from self-amplified spontaneous emission from the electron shot noise, which then gets amplified in the undulator (in contrast to the concept of a seeded FEL, where a laser seed pulse from an external laser is fed into the undulator with which the electron bunch starts to interact with right at the beginning). Figure 3.2 shows a schematic layout of LCLS.

At LCLS, the injector produces electron bunches of 0.25 nC, a peak current of 35 A. The following steps between the linear accelerator (linac) sections involve using pairs of bunch compressors, which shorten the electron bunch in order to increase the peak current to ≈ 3.5 kA at the end of the linac sections. The pulse repetition rate in May 2010, when the reported experiment was performed, was limited to 60 Hz (it was increased to 120 Hz at a later stage). The x-ray wavelength is tunable in the range 0.12–2.2 nm by varying the electron energy in the range of 3.5–15 GeV. With a new low-charge mode of operation (20 pC) available, LCLS was also designed to deliver ultrashort pulses even below 10 fs (with a pulse energy of 0.1–0.2 mJ at any of the wavelengths given above) [135].

In the undulator, the electron bunches get exposed to magnetic fields of spatially alternating polarity as the bunch travels the undulator and hence the electron bunch gets

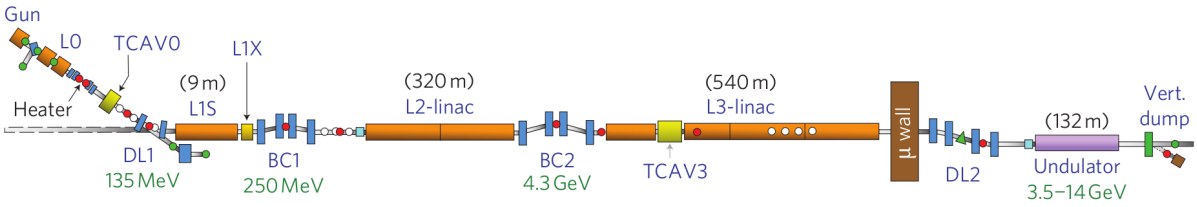

Figure 3.2.: Schematic layout of LCLS from the electron gun to the main beam dump with the accelerators (linac), bunch compressors (BC) and the undulator. The kinetic energy of the accelerated electrons after each acceleration step is given. The x-ray pulses created in the undulator are delivered to one of the six beamlines (AMO, CXI, MEC, SXR, XCS, and XPP)and experimental endstations at the right end of this picture. Image taken from ref. 135

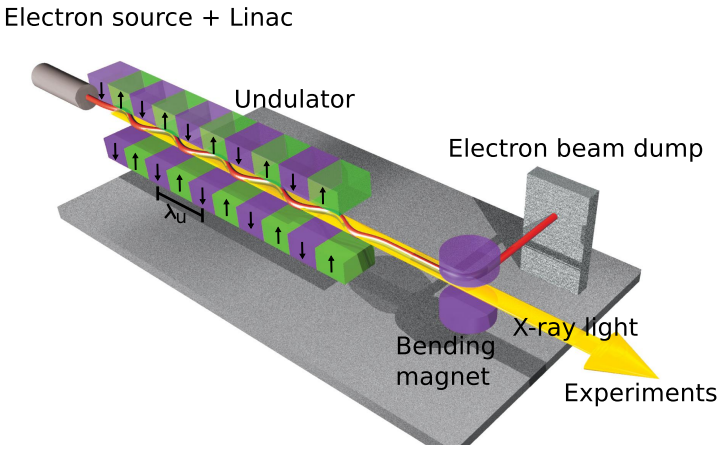

Figure 3.3.: Schematic layout of an undulator segment with permanent magnets of alternating polarity with a undulator period λ_u. The electron beam (red) is dumped after travelling the full undulator while the created X-ray radiation (yellow) is delivered towards the experimental beamlines and endstations at the right end of this picture. Image taken from ref. 137

forced onto a sinusoidal path which results in emission of electromagnetic radiation. A detailed description of the principles underlying radiation from the undulator can be found in, e. g., ref. 15. Figure 3.3 shows a schematic picture of an undulator.

The emitted radiation from the relativistic electron bunch is confined to a narrow cone and is strongly blue shifted in the laboratory frame due to the relativistic Doppler effect. At FELs, a high gain is reached via getting a large number of electrons radiating coherently, exploiting the so-called microbunching process. In this case, the radiation field

grows quadratically with the number of particles, i. e., electrons [15].

Downstream of the undulator, several photon beam diagnostic devices and attenuators are located. The devices for measuring several x-ray pulse parameters (like pulse energy and -length) together with attenuation devices were designed and fabricated at the Lawrence Livermore National Laboratory (LLNL) and are located in a tunnel downstream of the electron beam dump (right end in fig. 3.2) which is called the Front End Enclosure (FEE). A detailed description of these devices is given in [138]. Here, only the most important parts are introduced briefly.

An x-ray attenuator system can be used to attenuate the photon beam. It consists of gas (a 4.5 m long gas pipe filled with nitrogen, mainly used for attenuation in the soft x-ray range) and solid (a system of beryllium disks, used in the hard x-ray range) attenuators.

The x-ray pulse length is estimated by measuring the electron bunch length using a RF S-band deflecting cavity ('TCAV3' in fig. 3.2) in a setup similar to a streaking camera [139]. With this setup, a pulse length determination of electron bunch lengths as short as 25 fs (FWHM) is possible [135]. However, determination of ultrashort pulses shorter than 10 fs, as proposed to be delivered by LCLS operating in low-charge mode [140], is difficult and was achieved only recently with measurement of the temporal profile of individual FEL pulses at LCLS with 5 fs accuracy, using a laser-based THz-streaking setup [141]. In future experiments, such short pulses are foreseen to be utilized together with ultrashort pulses from optical lasers in optical-pump/x-ray-probe experiments, which require high accuracy in the pump-probe delay in order to achieve a good time resolution. Recently, a timing tool utilizing the ultrafast reflectivity change of silicon-nitride (Si_3N_4) membranes has proven to provide sub-10 fs time resolution for such pump-probe experiments and is now available on a routine basis at LCLS [142].

The x-ray pulse energy at LCLS is measured on a shot-to-shot basis by two gas detectors, exploiting fluorescence of nitrogen. The small gas chambers comprising the nitrogen are located up- and downstream of the attenuation section. The gas detectors don't provide absolute but relative measurement of the x-ray pulse energy (i. e., by which amount the x-ray pulse energy was diminished by the attenuators). Eventually, the absolute x-ray pulse energy is estimated by the energy loss of the electrons in the undulator, which can be exploited for absolute calibration of the gas detectors. The jitter of the x-ray pulse energy was determined to be about 8 % (rms). The spatial intensity distribution of the FEL pulse can be imaged by the so-called direct imager, which consists of a set of YAG:Ce scintillator crystals, providing a maximum spatial resolution of 20 μm [138].

Further downstream, the x-ray beam is delivered to the experimental endstations. At LCLS, the x-ray pulses can be delivered to one of six beamlines at a time. The beamlines

(in order of their respective start of operation) are: AMO (Atomic, Molecular, and Optical Physics), SXR (Soft X-ray Materials Science), XPP (X-ray Pump-Probe), CXI (Coherent X-ray Imaging), XCS (X-ray Correlation Spectroscopy), and MEC (Matter in Extreme Conditions). Information about specifications, available instrumentation at the distinct beamlines, and their scientific scope can be found in refs. 143–148.

The experiment was performed at the Atomic, Molecular, and Optical Physics (AMO) beamline using the CAMP experimental chamber [136], which was attached to the High Field Physics (HFP) chamber at the AMO beamline. The scientific scope of the AMO beamline is the investigation of fundamental light-matter interaction of intense x-ray radiation by an XFEL with atoms, small molecules, and molecular clusters [143], although it was used for coherent x-ray imaging experiments as well [27, 28]. The photon energy available at AMO is limited to the range of 560 eV to 2 keV and the beamline transmission (due to the KB mirror system, which focusses the x-ray pulses into CAMP) is ≈ 0.35, i. e., 35 % of the intensity impinging on the KB mirrors are estimated to propagate to the beamline [23]. For the experiment described here, the maximum available x-ray photon energy of 2 keV ($\lambda = 620$ pm) was utilized.

3.2.2. The CAMP Endstation

The CAMP experimental chamber was designed and built by the Max-Planck Advanced Study Group (ASG) at the Center for Free-Electron Laser Science (CFEL), Hamburg in 2009. It was intended to be used at a variety of proposed experiments at the new XFEL light sources such as, e. g., FLASH, LCLS, SSCS, and the European XFEL. CAMP is an acronym for **C**FEL-**A**SG-**M**ulti-**P**urpose Chamber. Detailed information about the CAMP instrument can be found in refs. 136, 149, 150.

In fig. 3.4, a picture of the CAMP chamber is shown. The CAMP chamber is equipped with detection devices to detect photons and charged particles (ions and electrons) simultaneously. CAMP is intended to obtain the most complete datasets possible of experiments probing atoms, molecules, droplets, clusters, nanocrystals or even solid targets with the FEL pulses. Therefore, the chamber is equipped with detectors for momentum imaging of charged particles using either a reaction microscope (REMI) or a velocity map imaging spectrometer (VMI). In addition, two CCD detectors called “pnCCDs” can be mounted in CAMP, mainly, but not exclusively, dedicated to photon detection, e. g., in fluorescence or diffraction measurements.

Figure 3.5 shows a schematic picture of the experimental setup, including the main experimental devices and detectors inside CAMP as well as the molecular beam setup attached to the CAMP chamber. The molecular sample is provided by a molecular

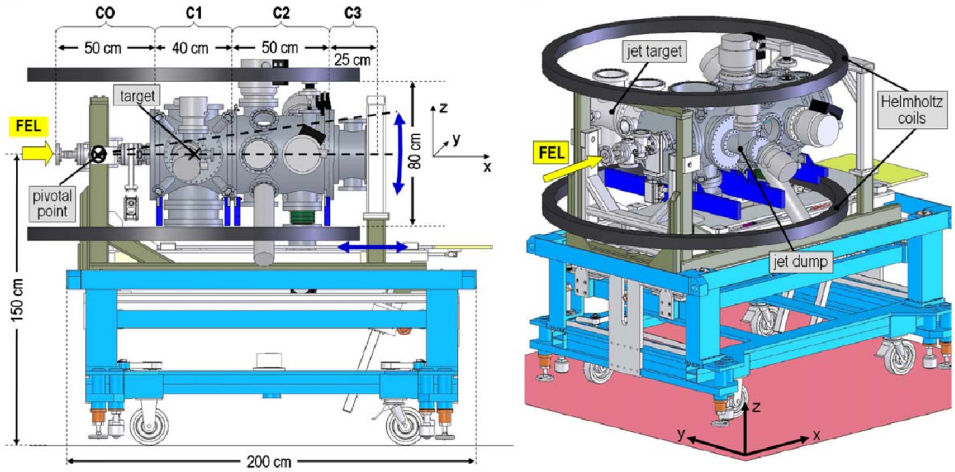

Figure 3.4.: The CAMP experimental chamber used at LCLS. CAMP is divided into four sections, labelled C0, C1, C2, and C3. C0 contains the differential pumping sections and valves to seperate CAMP from the beamline. C1 is the main (interaction) chamber. C2 houses the front pnCCD detector, while inside C3 the back pnCCD detector is installed. The whole chamber is mounted on a movable frame to adjust it to the FEL. On the outside of CAMP, Helmholtz coils could be mounted for generation of a defined magnetic field (not done in the experiment presented here). Image taken from ref. 136

beam (named "jet target" in fig. 3.4 (b)), entering the CAMP chamber perpendicularly to the FEL and optical lasers. The molecular beam setup was described before in section 3.1). The molecular sample (DIBN plus the backing gas He) gets intersected by a pulsed Nd:YAG laser (providing adiabatic laser alignment), a pulsed Ti:Sa laser (for strong-field ionization) and the FEL (providing the x-ray pulses for x-ray diffraction). Laser alignment is probed by the observation of the spatial velocity distribution of I^+ ions (from Coulomb explosion following multiple ionization of DIBN) recorded at a phosphor screen with a CCD camera after the ions were extracted from the interaction region by a velocity-map-imaging mass spectrometer with conically shaped electrodes. In front of the phosphor screen, an MCP provides signal enhancement. X-ray diffraction data from 2 keV x-ray pulses impinging on the target molecules was recorded using the pnCCD photon detectors [151, 152], which can be moved inside the chamber to cover large scattering angles. The setup will be described in detail throughout the following sections.

The Vacuum Setup

As the CAMP experimental chamber was designed to be used for a variety of different experiments studying fundamental light-matter interactions of x-ray radiation with in-

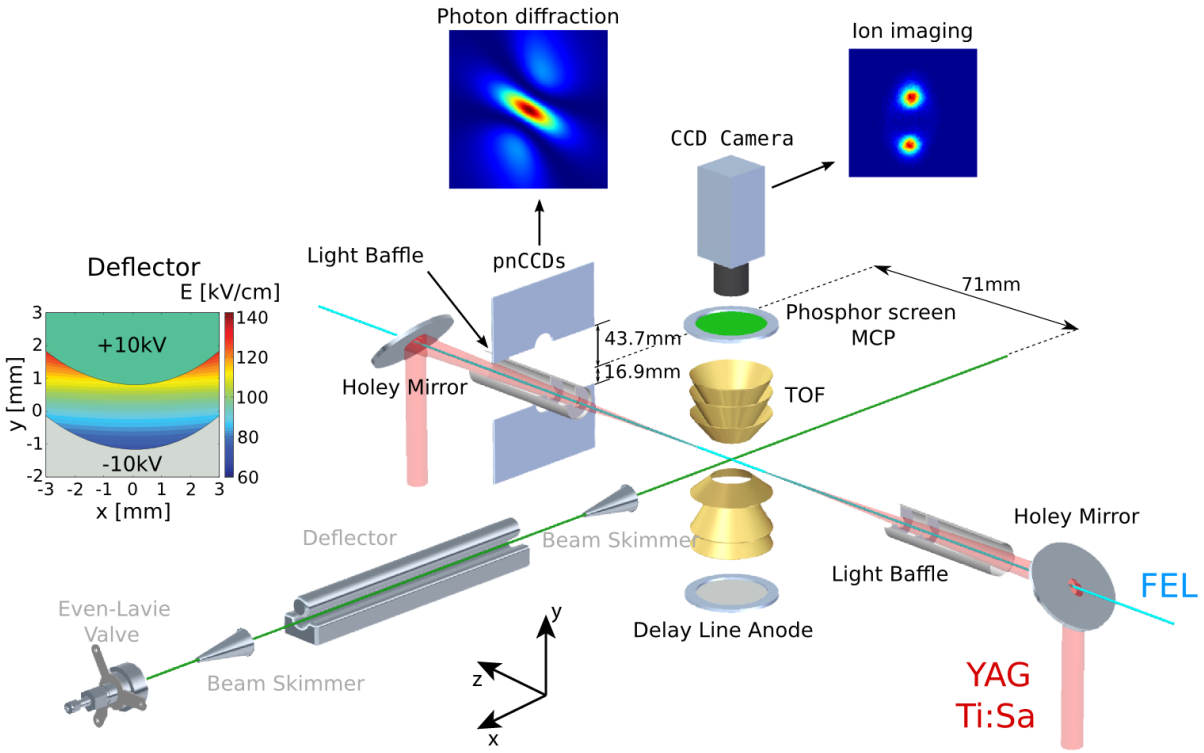

Figure 3.5.: Schematic layout of the experimental setup used at LCLS

dividual atoms and molecules, ultra-high vacuum (UHV) is a key requirement for these experiments, where usually low signal levels have to be expected.

Therefore, the CAMP chamber is equipped with four turbo-molecular pumps (TMPs, Pfeiffer Vacuum, pumping speed 700 l/s) to reach UHV. The TMPs are backed by several roughing pumps to provide a good pressure in the pre-vacuum range (10^{-4}–10^{-5} mbar). In addition, the pumps can be backed by the SLAC Roots-blower pumping system improving the pre-vacuum. The turbo-molecular pumps provide a low pressure in the 10^{-7} mbar range during the experiment described here. The final pressure reached is basically limited by the large surface area of the pnCCD-related electronical devices inside the chamber, where (during occasional venting) water and other impurities accumulate.

The vacuum requirements of the AMO beamline itself are at least 10^{-8} mbar for every experimental chamber to be connected to the beamline. As this pressure was not reached in the main CAMP chamber, the CAMP chamber was connected to the AMO beamline via several differential pumping sections. In front of the CAMP chamber, three differential pumping sections were installed, separated by 5 mm apertures to create a pressure gradient from 10^{-6} mbar at the maximum in the CAMP chamber to the required 10^{-8} mbar of the AMO beamline. The differential pumping sections could be separated from the beamline by two valves, e. g., at the occasions when the CAMP chamber had to be vented to change

parts of the setup inside CAMP. A flexible steel bellow connecting the differential pumping stage sections with the AMO beamline provides flexibility in adjusting the chambers position and alignment with respect to the FEL beam. Facing the molecular beam, a cryo pump was installed in order to trap molecules and particles from the molecular beam (and from the residual gas in the CAMP chamber) by cooling them on a liquid nitrogen cooled surface. The pressure was monitored by several pressure gauges (Pfeiffer vacuum). A residual gas analyzer (RGA) was used to analyze the composition of the remaining gas in the chamber [149]. The vacuum setup of the molecular beam connected to the CAMP chamber was described in the previous section concerning the molecular beam setup.

The Molecular Beam

The molecular beam setup is identical to the setup used in the experiments conducted at DESY to measure spatial molecular beam profiles of deflected or undeflected molecules. It was comprehensively described in the previous section (see section 3.1) except for the following modifications: For the experiments at LCLS, the skimmer sizes (i. e., orifices) were changed to 3 mm (first skimmer, between valve and deflector) and 4 mm (second skimmer, between deflector and CAMP chamber). The repetition rate of the valve was set to 60 Hz, (which was the repetition rate of the free-electron laser LCLS) and the current pulses applied to the valve were set to 14–16 μs (resulting in longer opening times of the valve) in order to maximize the number of target molecules in the interaction zone. The valve was heated to a temperature of 170°C due to the low vapor pressure of DIBN at room temperature. The deflector was used up to voltages of 20 kV. At LCLS, in the interaction zone the molecular beam is crossed by an Nd:YAG (YAG) laser, providing laser alignment of the target molecules, the free-electron laser LCLS, and/or a Ti:Sa laser as will be explained in the following.

The Laser Setup

Three different lasers were used at LCLS. An injection-seeded Nd:YAG laser (YAG) provided laser alignment of the target molecules in the interaction zone (YAG: $\lambda = 1064$ nm, 11 ns (FWHM), $E_I = 200$ mJ, $\omega_0 = 63$ μm, $I_0 \approx 2.5 \times 10^{11}$ W/cm^2). The second laser, a fs-Ti:Sapphire (Ti:Sa) laser, is used to ionize DIBN and thus to optimize the molecular beam and the alignment offline (Ti:Sa: $\lambda = 800$ nm, 50 fs (FWHM), $E_I = 400$ μJ, $\omega_0 = 40$ μm, $I_0 \approx 2.5 \cdot 10^{14}$ W/cm^2). The third beam consists of the 100-fs (FWHM)[2] x-ray pulses (LCLS: $\lambda = 620$ pm, $E_I = 4$ mJ, $\omega = 30$ μm, $I_0 \approx 1.9 \cdot 10^{15}$ W/cm^2). The

[2]The given pulse length of 150 fs is estimated from the electron bunch length. The corresponding FEL pulse length is ≈ 100 fs (FWHM) [153].

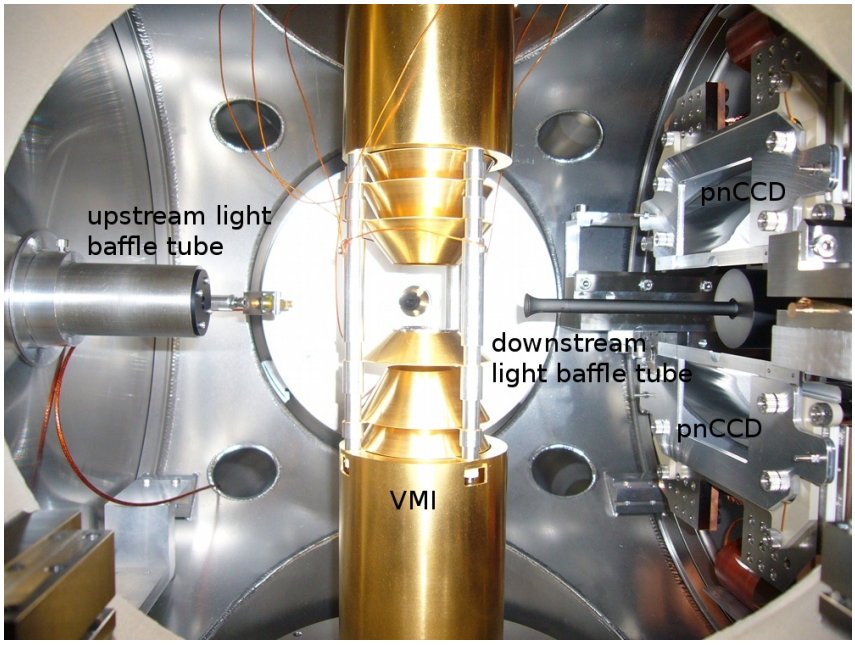

Figure 3.6.: Photograph inside the main CAMP chamber C1, facing the molecular beam. The FEL, YAG and Ti:Sa lasers enter from the left via a light-baffling tube, equipped with apertures and after impinging on the target in the center of the VMI electrodes exit via another light-baffling tube between the two panels of the front pnCCD detector. In this image, the pnCCDs cannot be seen as they were covered with Al-coated filters already; see text for details.

FEL focus was moved out of the interaction zone in order to not initiate multi-photon processes by too high FEL intensities. In the interaction zone, the width is readily described by $\omega = 30$ μm. As mentioned before, about 35 % of the generated $1.25 \cdot 10^{13}$ x-ray photons/pulse are estimated to be transported to the experiment [23].

All laser beams enter the CAMP chamber collinearly. The YAG and Ti:Sa laser were incoupled from outside vacuum into the beamline through a coated, broadband, high-reflectivity window and were overlapped with the FEL using a dichroic (1064 nm and 800 nm) mirror with a 2 mm hole in center to let the FEL pulses pass through. Eventually, the YAG and Ti:Sa laser beams exit the setup through a gap between the two panels of the pnCCD detector and another holey mirror to separate the laser beams again. The FEL pulses were dumped behind the CAMP chamber.

While straylight from outer parts of the FEL pulses was reduced via some aperture windows upstream the incoupling mirror, straylight from the optical lasers was reduced using a set of aperture holes mounted in a small tube directly in front of the interaction zone (light baffling tube, see fig. 3.5 and the photograph in fig. 3.6). To cover larger

scattering angles, the two panels of the pnCCD detector were opened by a significant amount (see fig. 3.5). Another light baffling tube was mounted directly downstream the interaction zone, reaching between the two pnCCD panels, and containing a similar set of apertures to suppress straylight from optical or x-ray photons impinging from the back of the CAMP chamber onto the back of the pnCCD panels. In addition, the front side (towards the interaction zone) of each pnCCD panel was covered using filters in order to further suppress straylight from the optical lasers. The filters consist of a Parylene-N layer (thickness 2.9 μm), coated from both sides with a layer of high purity Al (thicknesses 100 nm) [154]. Taking into account the transmittance of 0.94 (100 nm Al) and 0.914 (2.9 μm Parylene-N) together with the quantum efficiency of the pnCCD of 0.878 (at 2 keV), this results in an effective detection efficiency of 71 % (at scattering angle of $2\Theta = 0$) for the detection of an x-ray photon at a photon energy of 2 keV [155].

Velocity Map Imaging Spectrometer

Perpendicular to the horizontal plane of the molecular and laser beams a velocity-map-imaging (VMI) spectrometer was installed in order to investigate the ion- and electron-momentum distributions resulting from the Coulomb explosion of the target molecules. 2d-mapping of the momentum distributions of the I^+ ions from DIBN is used to confirm molecular alignment of DIBN as will be outlined in chapter 5.

Figure 3.7 shows the velocity map imaging spectrometer (VMI) spectrometer. The FEL beam and the optical lasers enter the chamber from the left side of the picture, intersecting the molecular beam at the center of the VMI (the axis of the molecular beam is out of the plane of the picture). The VMI is able to extract charged particles created in the interaction zone and accelerate and focus them via electrostatic lenses towards a detector at the top of fig. 3.7. The detector used was an MCP backed by a phosphor screen, which was viewed by a CCD camera.

The VMI can also serve as an ion time-of-flight mass spectrometer in a Wiley-McLaren configuration and allows for mass selective detection of individual ionic fragments. Hence, in focussing mode the full momentum vector of the ionic fragments can be retrieved. A full description of the VMI can be found in refs. 149, 150. On the right side of the VMI in fig. 3.7, facing the FEL beam, the two pnCCD panels of the front pnCCD detector are shown in the fully closed (dark blue) and fully opened position (light blue). The conically shaped electrodes of the VMI permit high scattering angles in x-ray diffraction experiments.

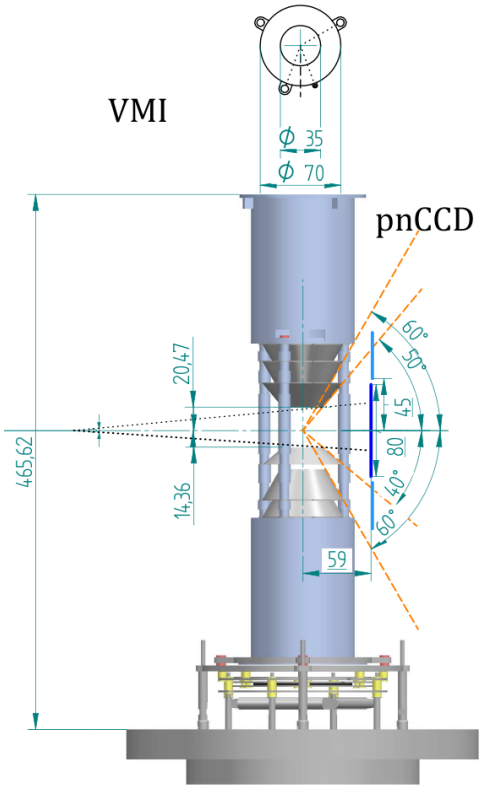

Figure 3.7.: Velocity-map-imaging (VMI) spectrometer inside the CAMP experimental chamber, facing the direction of the molecular beam. Linear dimensions given in mm, angles in degrees. The high-voltage electrostatic lens system is conically shaped in order to permit large scattering angles for the pnCCD detector. The lasers enter the center of the VMI from the left side. The two panels of the pnCCD detector can be moved independently in vertical direction and are depicted at fully closed (dark blue) and fully opened (light blue) positions. Image taken from [149].

pnCCD Photon Detectors

For photon detection, so-called pnCCD detectors were installed inside the CAMP chamber to record scattered (in diffraction experiments) or emitted (in, e. g., fluorescence measurements) photons. PnCCD detectors were developed the 1990s and have proven to exhibit a high quantum efficiency over a broad range of photon energies [151, 152]. These characteristics are key requirements for the pnCCD photon detectors developed for the CAMP instrument, due to the broad photon energy range that is covered by the new XFELs. Additional requirements include a fast readout to collect data shot-by-shot, a high dynamic range, low noise for single photon counting capability and a large area to cover a wide range of scattering angles [136].

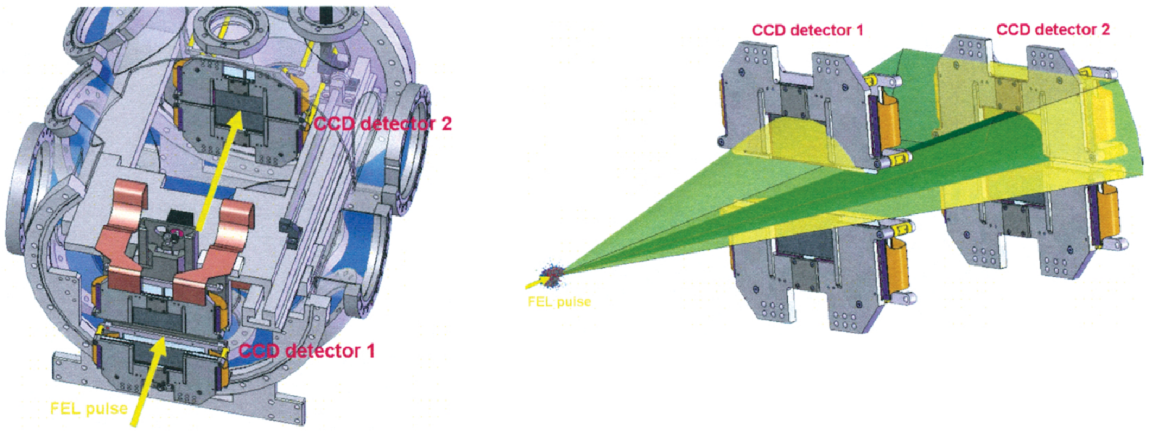

Figure 3.8.: Setup of the pnCCD detectors in the C2 (front pnCCD) and C3 (back pnCCD) chambers (left) and schematic picture of scattering angles covered by the front pnCCD (high scattering angles) and back pnCCD (small scattering angles) (right). Images taken from [156]

Figure 3.8 shows the setup of the pnCCD detectors in the CAMP instrument. The CAMP instrument is able to house two pnCCD detectors. A single pnCCD detector is composed of two chips/panels, each of which contains 512 × 1024 pixel. The size of a single pnCCD panel is 38 × 76 mm^2 and one single pixel has the size of 75 ×75 μm^2. The back pnCCD is fixed and its scope is mainly to record small angle scattering. The front pnCCD is mounted on a frame, which can be moved up- and downstream (250 mm along the z-axis with the closest distance to the interaction point being 50 mm) as well as along the x and y axis in order to cover a broad range of scattering angles. For the experiment described here, only the front pnCCD was used.

Tests of the pnCCDs performance under experimental conditions were performed at FLASH and BESSY over a wide range of energies (30 eV – 35 keV) [136] for pnCCD modules similar to the ones used at LCLS. Practical experience with the pnCCDs during the first experimental beamtimes at LCLS was outlined in [157]. The results of all these measurements are summarized briefly in the following. The energy spread at distinct photon energies (with the pnCCDs operating at -70°C) was given in ref. 158: For 1486 eV it is 66 – 74 eV (FWHM) while at 5894 eV it is 123 – 131 eV (FWHM). For 2 keV, it can be assumed to be in the range 70 – 90 eV at 2 keV [159]. Further characteristics of the pnCCD such as, e. g., a maximum possible frame readout rate of 200 Hz (LCLS was running at 60 Hz at that time), a high quantum effiency at 2 keV paired with a exceptional long term stability (reported in ref. 151) are specifications which make single photon counting experiments with very weakly scattering gas-phase samples feasable.

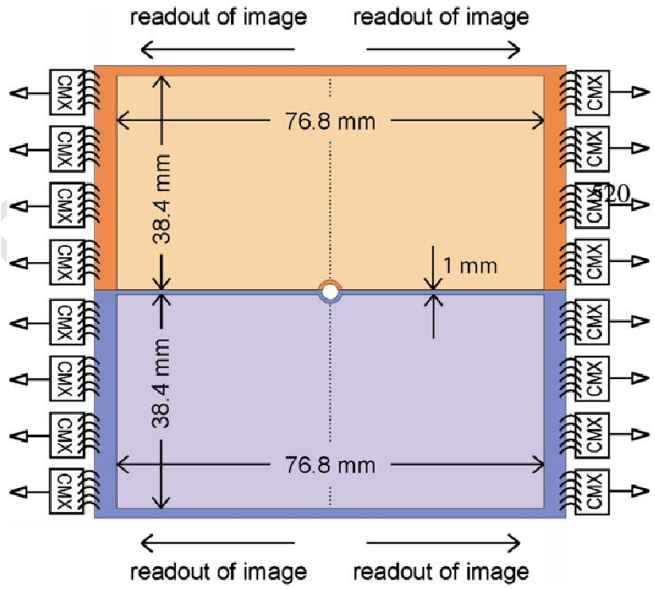

Figure 3.9.: Schematic view of the pnCCD detector. The detector consists of two chips/panels, which can be moved independently in y-direction to cover a different range of scattering angles. Channels are horizontally oriented, pixels in vertical direction will be referred to as "rows". Each panel consist of eight modules. Each module consist of 128 channels. During read-out of the acquired signal, the signals get transferred along each channel, i. e., along the horizontal direction, towards an amplifier called CAMEX (CMX). Image taken from ref. 136

3.2.3. Data Acquisition and Data Analysis

The data acquired in measurements at LCLS is processed via the LCLS DAQ system and stored in binary format in so-called xtc-files ("extended tagged container" [160]). The xtc-files contain the recorded data of multiple detectors operated by the beamline user along with some LCLS-beamline-data (e. g., FEL pulse length, FEL pulse energy,...), commonly called "machine data", either measured by the beamline detection devices (e. g., gas detector, etc.) on a shot-to-shot basis or estimated by the settings that were used. The datasets from each single FEL shot contains a unique number for unique identification of disctinct shots. For data analysis, xtc-files were accessed by the CFEL-built **C**FEL-**A**SG **S**oftware **S**uite (CASS). CASS is able to acquire and process all data recorded by the different detectors in CAMP, ranging from Acqiris analogue-to-digital- converters (ADC), commercial CCD cameras (e. g., for recording ion images from the illuminated Phosphor screen) to the pnCCD detectors. In the following, CASS will be explained briefly, for details see [161].

CASS was programmed in order to view, process, and analyse experimental data ac-

quired at LCLS and other x-ray beamline facilities. One key feature of CASS is, that it can be used either in "online" or "offline" mode. In the former, the program connects to the LCLS DAQ data stream and retrieves data while an experiment is running (e.g. for fast response to changing parameters during the experiment). In the latter case, CASS is able to read the xtc-files stored, access the data and perform analysis tasks on the data as specified by the user. By using post-processors of CASS, the user is able to perform a variety of operations to the data, e. g., threshold a histogram, collect just histograms meeting certain conditions etc. During the experiment, CASS was used to perform "semi-online" analysis (by means of the viewers "jocassview" or "lucasview" connecting to CASS and retrieving the data stored in the histograms) in order to optimize, e. g., the degree of molecular alignment by the YAG laser in dependence of, e. g., the molecular beam position or the laser parameters. The LCLS DAQ software was used as well on a semi-online basis, e. g., to view single-shot VMI data (or VMI data from running-average of the last shots) in order to overlap the lasers and the molecular beam, to optimize the degree of alignment of DIBN by the YAG laser, or to obtain molecular beam deflection profiles by measuring the I^+ ion signal in dependence of the molecular beam position.

For data analysis after the experiment, CASS was used for accessing the xtc data files in order to retrieve data measured by the VMI (to determine molecular alignment), time-of-flight data, and, most importantly, the single shot pnCCD data. For the latter, CASS was utilized to perform various operations (specified by CASS' post-processors) in order to clean the pnCCD single shot diffraction data from pnCCD based artifacts as well as from experimental backgrounds and to extract single x-ray photon hits from the data. The process of using CASS for data cleaning and single-photon counting is explained in appendix A in detail.

4. Deflection of Cold Molecular Beams

4.1. Introduction

As mentioned before, quantum-state selected molecular samples allow for very efficient manipulation techniques by, e. g., static electric fields [88, 162, 163], strong laser fields [83, 89, 96] or a combination of both [100, 164]. In experiments involving alignment and/or orientation of molecular samples with respect to a space fixed axis, preparing samples in a small set of populated quantum states, preferably the lowest states, is a highly valued prerequisite for achieving a good degree of alignment [42, 116] in novel experiments like, e. g., ultrafast x-ray diffraction experiments on single molecules [40], which is the topic of this thesis. Due to the supersonic expansion in the molecular beam, all molecules are practically in the electronic and vibronic ground state, but are distributed over many rotational states, even at the low temperatures (≈ 1 K) in the molecular beam. Quantum-state dependent deflection of neutral molecules and/or clusters in a strong inhomogenous static electric field provides a means to spatially separate molecules in a molecular beam according to their dipole-moment-to-mass ratio. Since the dipole moment of a molecule is a property of its quantum state, molecules from the same molecular sample (i. e., constant mass) in different quantum states can be spatially separated.

The second section of this chapter presents results from molecular beam deflection experiments performed on indole and indole-water complexes/clusters (indole$(H_2O)_n$). Following that, results from deflection experiments of 2,5-diiodobenzonitrile (DIBN), the target molecule for the coherent x-ray diffraction experiment, are shown. A summary concludes this chapter.

4.2. Deflection of Indole and Indole$(H_2O)_n$-clusters*

4.2.1. Introduction

Indole is the chromophore of the essential amino acid tryptophan and widely used in fluorescence studies of proteins. Protein-solvent interactions can lead to spectral shifts depending on the environment of the chromophore [166]. Especially water solvation shows a strong influence on the electronic states of indole as is discussed in, e. g., [167] where unusual large shifts of fluorescence in the presence of polar solvents are found to be due to an interchange of the order of the lowest electronically excited states. The structure of indole$(H_2O)_n$ in the ground and electronically excited state, involving a reorientation of the water moiety with respect to indole, is given in [131].

The strong deflection of indole in a cold molecular beam and the feasibility of the spatial separation of the prototypical molecule indole (C_8H_7N) and indole$(H_2O)_n$ clusters is presented here. In particular, the large dipole moment of indole$(H_2O)_1$[168] was exploited in order to prepare a pure sample of indole$(H_2O)_1$, spatially well separated from the various other species in the molecular beam. It is *a priori* not clear, whether the deflection technique can be applied to such complex molecules and clusters. Due to their large size and correspondingly small rotational constants, these molecules and clusters possess a high density of states with complex Stark energy curves, containing many real and avoided crossings. It was proposed before, that such complex systems may not be amenable to such manipulation techniques like electrostatic deflection due to their rapidly changing (in terms of the Stark energy curve) dipole moments and may exhibit "chaotic rotational behaviour" [115]. The experimental results presented here demonstrate that at low rotational temperatures on the order of a few K and at the relevant electric field strengths in the deflector, strong spatial deflection of even such complex systems like indole$(H_2O)_n$ clusters can be achieved and can be well understood by simulated molecular beam deflection profiles.

The results were obtained during two distinct experiments, one performed with indole alone and one with an indole-water mixture, illustrating different expansion properties such as the achieved rotational temperature in the cold molecular beam. The experimental molecular beam setup was explained in chapter 3. A quantitative explanation of the results is given by molecular trajectory simulations. These simulations do not only explain the spatial separation of the molecular beam as a whole, but also illustrate the

*Based on: Spatial separation of state- and size-selected neutral clusters, S. Trippel, Y.-P. Chang, S. Stern, T. Mullins, L. Holmegaard, and J. Küpper, *Phys. Rev. A* **86**, 033202 (2012) [165]

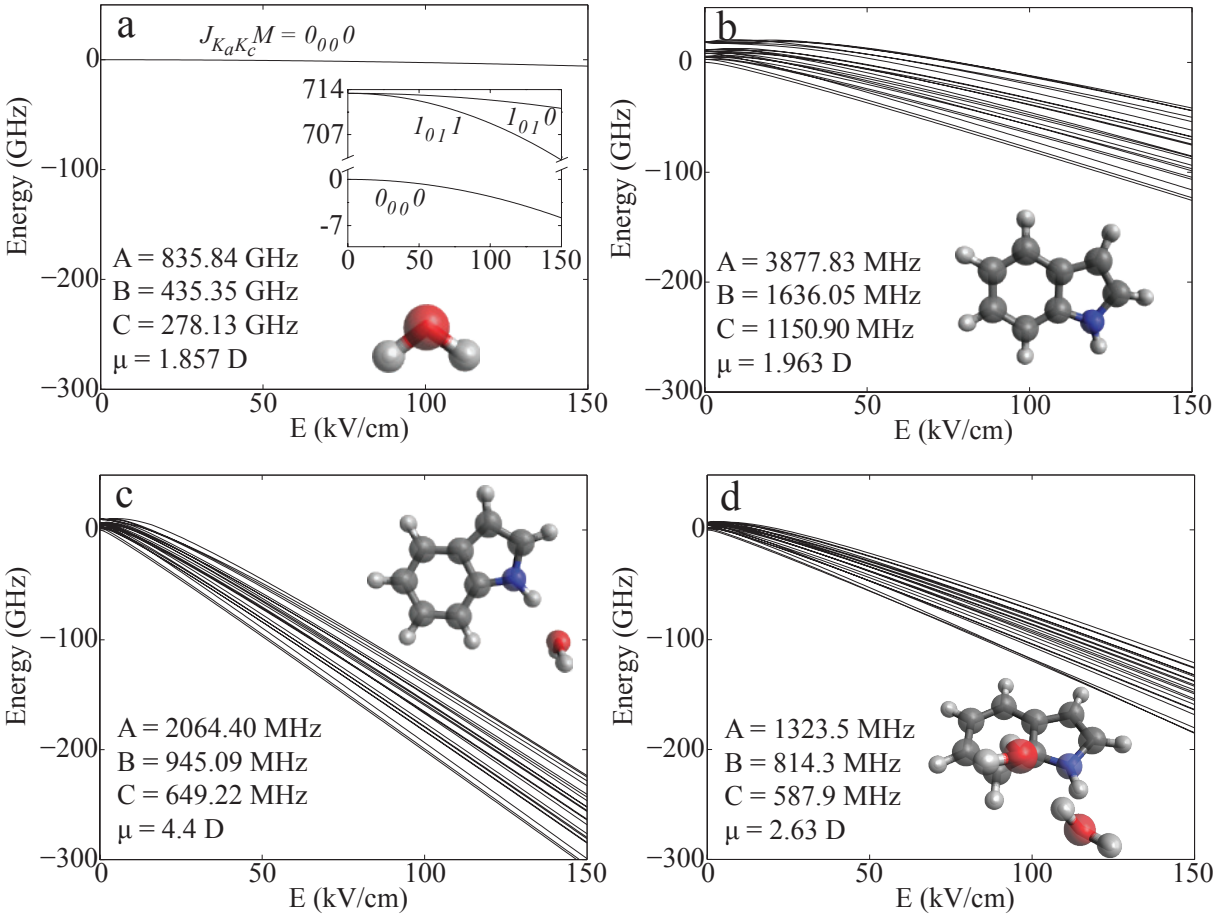

Figure 4.1.: Stark curves for H_2O (a), indole (b) and the complexes indole$(H_2O)_1$ (c) and indole$(H_2O)_2$ (d), plotted for the lowest rotational states.

quantum-state selectivity of the deflection resulting in the spatial separation of molecules in high- and low-lying rotational states.

In fig. 4.1, the Stark energies of the relevant species are presented along with their respective structures, permanent dipole moments and rotational constants. These were experimentally determined for H_2O [169, 170], indole [168, 171], and indole$(H_2O)_1$ [168, 172] and are based on ab initio calculations for indole$(H_2O)_2$ (GAMESS-US [173];B3LYP/6-31+G*)The calculated structure and dipole moments are the same as reported in refs. 174, 175. The inset of fig. 4.1 (a) visualizes the small Stark shifts of H_2O. Due to the large rotational constants and hence the large separation of rotational states in water, only the three states shown in the figure were populated and are included in the trajectory simulations. For indole, indole$(H_2O)_1$ and indole$(H_2O)_2$, the states are plotted up to $J_{\max} = 5$.

Experimental quartic centrifugal distortion constants [112, 176] were used in the cal-

culations [116]. However, the calculated deflection profiles using the rigid-rotor and the semi-rigid-rotor (the latter including centrifugal distortion) approximations are identical and hence, only the calculated deflection profiles using the semi-rigid-rotor approximation are presented in the following.

At the conditions of the experiment (i. e., the electric field strengths inside the deflector, compare fig. 3.1), all states populated by the molecules and clusters exhibit a decrease in energy with increasing electric field strength. Hence, the molecules and clusters are in high-field seeking states. This is due to mixing of closely-spaced states of the same symmetry (common to asymmetric top molecules), where avoided crossings turn all states of the same symmetry into high-field seeking states at the electric field strengths of the experiment. Figure 4.1 shows, that the Stark effect decreases with increasing rotational quantum number J and the largest change in energy is obtained for the rotational ground states, which will be deflected the most. The biggest change of the molecular whole beam profile is expected for indole$(H_2O)_1$, exhibiting the strongest change in potential energy as can be seen directly from the Stark energies.

4.2.2. Experimental Results

Deflection of Indole

A mixture of a few mbar indole is provided by a supersonic expansion from a pulsed Even-Lavie valve (EL valve), along with 50 bar Helium as a backing gas. Indole is ionized via a 1+1 REMPI transition by a UV-laser, probing the electronic ground state S_0 of indole at 4.369 eV (35231.42 cm^{-1}). The gasline was cleaned thouroughly by pumping and the absence of indole$(H_2O)_n$ clusters was confirmed by time-of-flight measurements of the ionic fragments.

In fig. 4.2, molecular beam density profiles of indole at different voltages are presented. The profiles were obtained by scanning the focus of the probe laser along the vertical direction (y-axis), see fig. 3.1. Molecular beam density profiles measured in this way will be called deflection profiles in the following. The deflection profiles of fig. 4.2 were obtained with different potentials applied to the deflector electrodes.

The solid lines are the simulated deflection profiles. The first skimmer, i. e., the one in front of the deflector, was set in a way in order to cut the molecular beam at the side of the deflector rod. By this, the molecular beam enters the deflector near the trough. This was done in order to avoid collisions of the molecular beam with the rod and to increase the sensitivity of detection of deflected molecules. All molecules are deflected upwards (i. e., towards the rod, corresponding to the right side, i. e., positive y-values

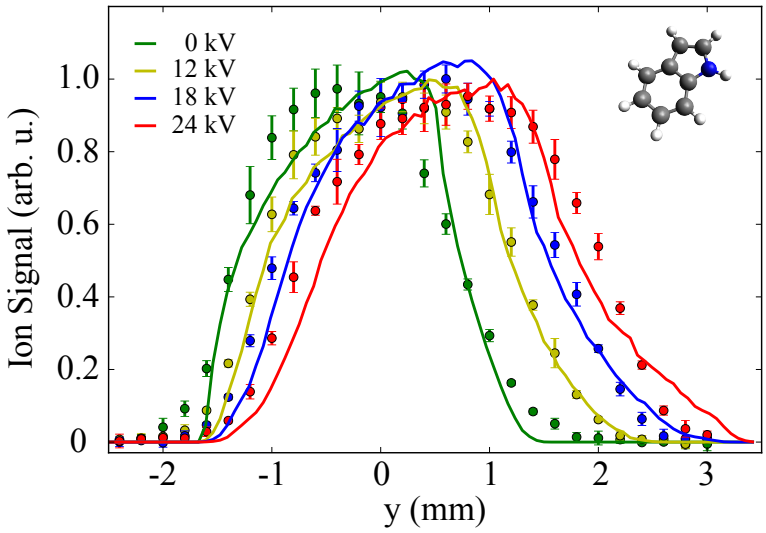

Figure 4.2.: Molecular beam deflection curves for indole for different deflector voltages. Solid lines represent simulated molecular beam profiles while the measured data is expressed by points. The obtained deflection is strong (1.3 mm for 24 kV at 50 % intensity) and best fitted with trajectory simulations with the original ensemble of indole molecules at a rotational temperature of 0.6 K.

in fig. 4.2) and are dispersed as the voltage is increased. This can be attributed to all quantum states of indole being high-field seeking at the experimental conditions used. The undeflected part of each beam profile (towards the left side in fig. 4.2) shows a rather steep cutoff, caused by the aperture of the skimmer and the deflector trough. The last skimmer (i. e., the one behind the deflector) was adjusted for maximum transmission at each deflector voltage and the deflected part of the beam shows a "tail" (based on the different dispersion of different quantum states). The deflection for cold indole without any indole$(H_2O)_n$ clusters is very strong. E. g., at 50 % intensity the beam at 24 kV is seperated by about 1.3 mm from the undeflected (0 kV) beam. The molecular beam profiles are best fitted by trajectory simulations with the ensemble of indole molecules being at a rotational temperature of 0.6 K. While the simulations of the deflected part of the beam are in quite good agreement with the experimental results, the undeflected part exhibits a broadening towards the trough axis which could not be simulated well. This broadening may be caused by secondary collisions, either within the deflector or even at the skimmer behind the deflector, resulting in a broader beam than would be simply set by the mechanical aperture of the deflector and the skimmers. This was not be accounted for in the trajectory simulations, in which molecules colliding with any aperture are neglected and not propagated further towards the interaction region.

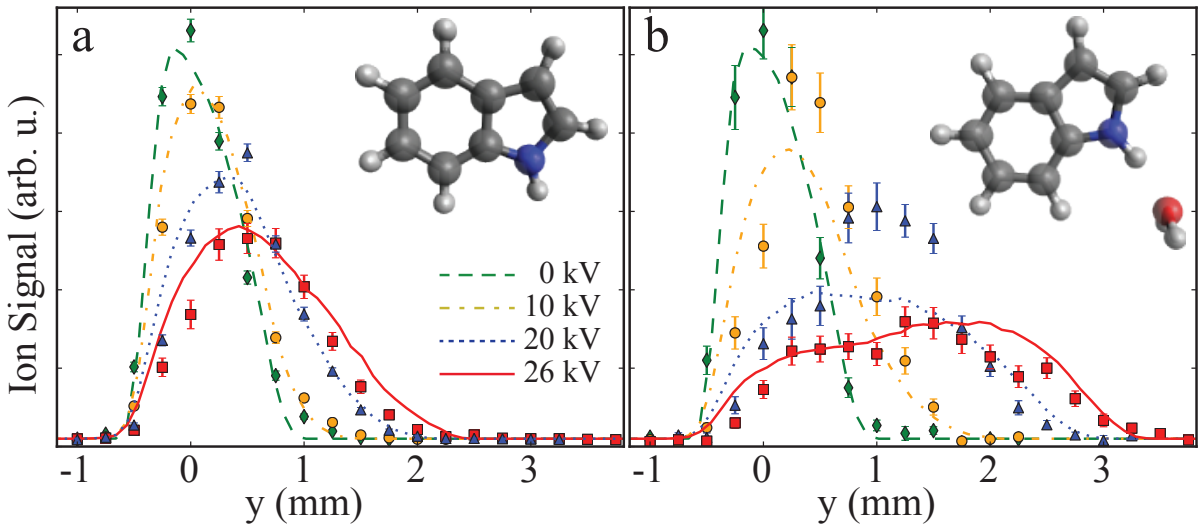

Figure 4.3.: Molecular beam deflection curves for indole (a) and indole$(H_2O)_1$ (b) for different deflector voltages. The deflector voltages are 0 (green, diamonds), 10 keV (yellow, circles), 20 keV (blue, triangles) and 26 keV (red, squares).

Deflection of Indole and Indole$(H_2O)_n$-clusters

For creation of indole$(H_2O)_n$-clusters, a small water-reservoir was connected to the gasline (the latter providing the seed gas He to the Even-Lavie valve). A mixture of a few mbar indole and water molecules is then provided by a supersonic expansion from the pulsed EL valve, along with 50 bar He as a backing gas. While indole is ionized at 4.369 eV (35231.42 cm^{-1}), as mentioned above, indole$(H_2O)_1$ is ionized at 4.353 eV (35099.42 cm^{-1}).

Figure 4.3 shows the molecular beam density profiles for indole and indole$(H_2O)_1$. The width (FWHM) of the undeflected beam is about 1 mm, limited by the mechanical aperture between the first skimmer and the deflector trough. The first skimmer again was lowered (i. e., moved towards the trough axis) and cuts the molecular beam for the same reasons given above. All molecules and clusters are again deflected upwards as all quantum states of the molecules/cluster are high-field seeking. The points in fig. 4.3 correspond to measured data while the lines correspond to simulated deflection profiles. All profiles are normalized to the peak intensity of each species under field-free conditions, thereby accounting for the unknown (relative) ionization cross sections and unknown number densities of the molecules/clusters.

In fig. 4.4, deflection profiles of the distinct species present in the molecular beam are shown at a deflector voltage of 26 kV. For indole$(H_2O)_2$ (green, triangles), the data (and simulation) is multiplied by 0.2 for illustrative reasons in order to not interfere too much

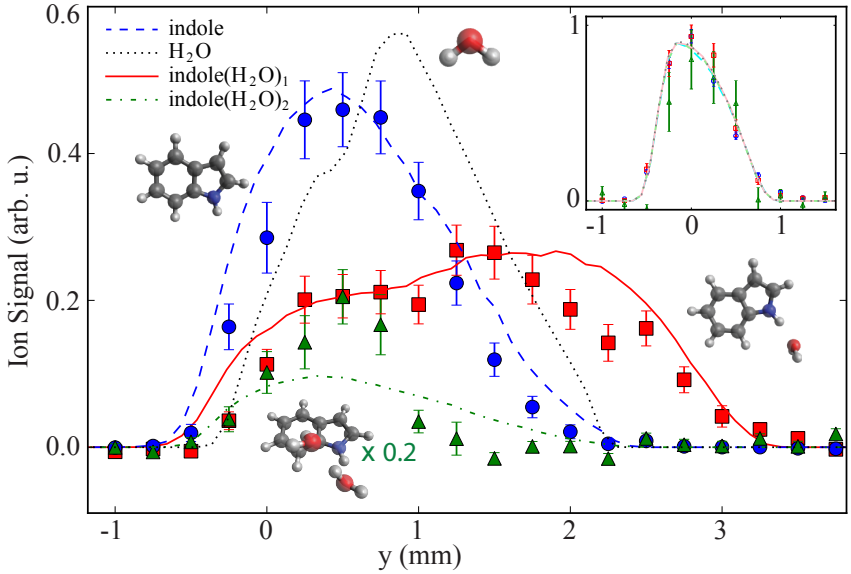

Figure 4.4.: Molecular beam deflection curves for H_2O (dotted line), indole (blue, circles), indole$(H_2O)_1$ (red, squares) and indole$(H_2O)_2$ (green, triangles) at a deflector voltage of 26 kV.

with the indole data. The inset shows profiles of the species at field-free conditions. Comparing the two conditions (field-free and deflector at 26 kV), the spatial dispersion of molecules/clusters in different (rotational) quantum states is again visible by the broadening of the deflection profiles. The deflection is strongest for indole$(H_2O)_1$when compared to the profiles of the other species. This was expected from calculations of the Stark energy shifts, see fig. 4.1. From the trajectory simulations, rotational temperatures of 4 K (indole) and 6 K (indole$(H_2O)_1$and indole$(H_2O)_2$) can be assigned to the distinct species.

In the range of y $\approx$ 2.3 – 3.3 mm, the measured density of all species but indole$(H_2O)_1$ is greatly reduced compared to the undeflected beam densities. By positioning the probe laser in this region, an almost pure sample of the single species indole$(H_2O)_1$ is accessible. In addition, this part of the deflected molecular beam offers the possibility of strong alignment and orientation of the sample, since only the clusters in low-lying rotational quantum states can be probed: At y = 2.75 mm (3.0 mm), the signal is 10 % (4 %) of the undeflected peak intensity and only the lowest 290 (110) rotational quantum states are populated (instead of the 4600 states of indole$(H_2O)_1$in the original molecular beam), which is very beneficial for alignment and orientation control.

The obtained rotational temperatures (derived from simulations of the spatial beam profiles) point at a much more efficient cooling inside the supersonic expansion in case no clusters are present in the molecular beam. In the latter case, the temperature deduced from the simulation is 0.6 K while in the case of indole$(H_2O)_n$ clusters being present in

the molecular beam, temperatures in the range 4 – 6 K are obtained. Cluster formation is a heating mechanism and upon the formation of clusters, the condensation energy of the clusters is released to the random motion of all particles in the propagating molecular beam, resulting in less cooling of molecules towards low rotational temperatures [177].

4.2.3. Torsional States in Indole$(H_2O)_1$

At this point it is noted that, in general, the torsional motion of the water moiety in indole$(H_2O)_1$ introduces the complication that the indole$(H_2O)_1$-cluster cannot be treated as a (semi)rigid rotor. However, under the achieved experimental conditions, i. e., the low temperature of the sample in the molecular beam, the large rotational constant of the internal rotation of water, and the (dis)allowed symmetry couplings of the populated torsional states, the cluster remains rigidity, as will be argued in the following. The symmetry properties of the torsional and subtorsional levels of indole$(H_2O)_1$ and the couplings between these leves in an external dc electric field have to be considered. The argumentation follows the ideas of the case of phenol$(H_2O)_1$, given in [178] and is also given in the appendix of [165].

The indole and water moieties of indole$(H_2O)_1$ are connected by a single hydrogen bond at the position close to the N-atom in indole (see [131]). The moieties are able to rotate with respect to each other about this bond. The internal motion of the water moiety with respect to the indole moiety can be described using the principal axis method (PAM) [49]. Here, the pricipal axis of the cluster is used as the coordinate system, combined with an internally rotating symmetric top moiety ($(H_2O)_1$). The axis of internal rotation of the symmetric top moiety coincides with its symmetry axis. Therefore, the moments of inertia of the overall rotation as well as the clusters principal axes are not changed by the internal rotation of the water moiety. Strictly speaking, this condition is not fullfilled in the case of indole$(H_2O)_1$, as the water moiety is an asymmetric top. However, the moment of inertia of the rotating water molecule about its pseudosymmetry axis is small and hence, the moments of inertia of the whole cluster are only slightly and insignificantly altered by the rotation of the water moiety. This is justified by spectroscopic studies of indole$(H_2O)_1$[131, 168].

This torsional motion is restricted by a twofold potential as shown in fig. 4.5. The angle α denotes the angle between the molecular plane of indole and the molecular plane of the water moiety. The twofold potential results in torsional energy levels (denoted by the torsional quantum number v_t) occuring as pairs of distinct symmetry due to tunneling splitting. The sub-torsional levels for each v_t are denoted as $\sigma = 0, 1$. The twofold potential for the rotation in first approximation is given by $V(\alpha) = \frac{V_2}{2}(1 - \cos(2\alpha))$ [49].

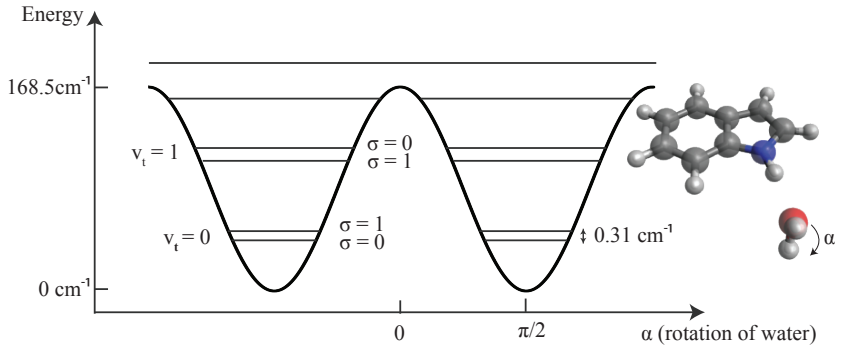

Figure 4.5.: The torsional potential and energy level scheme of indole$(H_2O)_1$in its vibronic ground state.

The height of the potential barrier ($V_2 = 168.5$ cm^{-1}), the angle of the rotation axis of the water moiety in the bc symmetry plane of the cluster (corresponding to the ab plane of the bare indole) with respect to the b axis ($\beta = 55°$), and the rotational constant of water for the internal rotation (339 GHz) were taken from ref. 131. Following the procedure outlined in chapter 12 of ref. 49, the one-dimensional Schrödinger equation was solved, yielding a splitting of the subtorsional levels of $v_t = 0$ of 0.30 cm^{-1}. This value agrees well with the value of 0.31 cm^{-1}, given in ref. 131.

G_4	E	(12)	E*	(12)*
A_1	1	1	1	1
A_2	1	1	-1	-1
B_1	1	-1	-1	1
B_2	1	-1	1	-1

G_2	E	(12)
A	1	1
B	1	-1

Table 4.1.: Character tables for the molecular symmetry groups G_4 and G_2 [178, 179]

Now the symmetry properties of the distinct states have to be derived in order to distinguish possible couplings of the states. Under field-free conditions, indole$(H_2O)_1$ belongs to the molecular symmetry group G_4 [179], the corresponding character table is given on the left side of table 4.1. Since the total wavefunction must be antisymmetric with respect to the exchange (by internal rotation) of the two protons of the water moiety (operation (12)), the symmetry Γ_{tot} of the total wavefunction is of B_1 or B_2 symmetry.

Table 4.2 summarizes the symmetry properties of the electronic, vibrational, torsional, rotational, and nuclear spin states of indole$(H_2O)_1$ in the field-free case. Due to the low temperatures in the supersonic expansion, indole$(H_2O)_1$ resides in its respective electronic

σ	K_a	K_c	Γ_e	Γ_v	Γ_t	Γ_r	$\Gamma_t \otimes \Gamma_r$	Γ_{ns}	Γ_{tot}	nssw
0	e	e	A_1	A_1	A_1	A_1	A_1	B_2	B_2	1
0	o	e	A_1	A_1	A_1	A_1	A_1	B_2	B_2	1
0	e	o	A_1	A_1	A_1	A_2	A_2	B_2	B_1	1
0	o	o	A_1	A_1	A_1	A_2	A_2	B_2	B_1	1
1	e	e	A_1	A_1	B_2	A_1	B_2	$3A_1$	B_2	3
1	o	e	A_1	A_1	B_2	A_1	B_2	$3A_1$	B_2	3
1	e	o	A_1	A_1	B_2	A_2	B_1	$3A_1$	B_1	3
1	o	o	A_1	A_1	B_2	A_2	B_1	$3A_1$	B_1	3

Table 4.2.: The symmetry classification of eigenstates of field-free indole$(H_2O)_1$ and the respective nuclear spin statistical weights.

and vibrational ground states, which are totally symmetric. The nuclear spin statistical weights of the wavefunctions of distinct symmetry are given in the last column of table 4.2. They have to be considered in the (relative) population of the distinct levels during calculation of the single-state deflection profiles.

σ	K_a	K_c	Γ_e	Γ_v	Γ_t	Γ_r	$\Gamma_t \otimes \Gamma_r$	Γ_{ns}	Γ_{tot}	nssw
0	e	e	A	A	A	A	A	B	B	1
0	o	e	A	A	A	A	A	B	B	1
0	e	o	A	A	A	A	A	B	B	1
0	o	o	A	A	A	A	A	B	B	1
1	e	e	A	A	B	A	B	3A	B	3
1	o	e	A	A	B	A	B	3A	B	3
1	e	o	A	A	B	A	B	3A	B	3
1	o	o	A	A	B	A	B	3A	B	3

Table 4.3.: The symmetry classification of eigenstates of indole$(H_2O)_1$ in a dc electric field and the respective nuclear spin statistical weights.

The molecular symmetry group of indole$(H_2O)_1$ is reduced to G_2 when entering the electric field of the deflector. The character table of G_2 is provided on the right side of table 4.1. In table 4.3, the symmetry properties of the distinct states in a dc electric field are summarized. The torsional sublevels at a given torsional quantum number v_t have the same symmetry when their quantum number σ is the same (A for all levels with $\sigma = 0$

and B for all levels with $\sigma = 1$). In an electric field, only states having the same quantum number σ are mixed and hence, the subtorsional levels of a given v_t do not mix. The contribution of the the states $v_t \geq 1$ due to the initial state population prior to entering the strong field of the deflector is estimated assuming a Boltzmann distribution of the energy states. The energy difference of $|v_t, \sigma\rangle = |0, 0\rangle$ and $|v_t, \sigma\rangle = |1, 1\rangle$ is 70.9 cm^{-1} and difference between $|v_t, \sigma\rangle = |0, 1\rangle$ and $|v_t, \sigma\rangle = |1, 0\rangle$ 76.5 cm^{-1}, which results in a relative population of less than 1 % of $v_t = 1$ with respect to $v_t = 0$ at vibrational temperatures of 20 K or below, which is expected in the supersonic expansion. Hence, population of $v_t \geq 1$ can be neglected in the calculation of the Stark energies. Coupling of $v_t = 0$ to $v_t \geq 1$ in the deflector can be neglected as the energy separation is too large. Therefore it is justified to treat indole$(H_2O)_1$ as a (quasi)rigid molecule, comfirmed by the results of fitting of the experimental deflection profiles.

It is noted that nuclear spin statistical weights, which affect the population of the distinct rovibronic states, don't have to be considered for the case of indole and indole$(H_2O)_2$, since there are no identical nuclei in these and the nuclear spin wave functions are all of the same symmetry. Hence, no weighting (based on nuclear spin statistics) of the distinct states is necessary and the states can be populated in a straigthforward manner.

4.3. Deflection of 2,5-Diiodobenzonitrile

4.3.1. Introduction

The prototypical molecule 2,5-diiodobenzonitrile ($C_7H_3I_2N$, DIBN) was considered a good candidate for the proof-of-principle x-ray diffraction experiment, testing the feasibility of single-molecule diffraction of aligned gas-phase molecules. DIBN was chosen, because it comprises two heavy atoms (i. e., the two iodine atoms), which serve as the main scatterering centers and are located at a distance of 700 pm from each other, very appropriate for an x-ray diffraction experiment at a photon energy of 2 keV (620 pm)[2]. In addition, DIBN can be aligned at an axis which almost coincides with the iodine-iodine axis: the inclination of the most-polarizable axis of DIBN to the iodine-iodine axis is about 7°. The permanent dipole moment of DIBN, which makes DIBN amenable to electrostatic deflection, is $\mu = 3.817$ D, determined by ab-initio calculations (GAMESS-US MP2/6-311G** [124]). However, the large mass of DIBN is an obstacle in for the spatial deflection, since the spatial separation by the deflector depends on the ratio μ/m. The rotational constants of DIBN are $A = 1.39$ GHz, $B = 1.54$ GHz, and $C = 1.38$ GHz. The two heavy

[2]The photon energy at the AMO beamline is limited to 2 keV.

iodine atoms cause a significant alteration of the rotational energy levels due to nuclear hyperfine splitting. For, e. g., iodobenzene, the nuclear quadrupole coupling constants are $\chi_{aa} = 1.89$ GHz, $\chi_{bb} = 0.97$ GHz, and $\chi_{cc} = 0.91$ GHz [180] and the order-of-magnitude is expected to be in the same range for DIBN. For this reason, nuclear quadrupole coupling will have a significant influence on the energy of each state and since these effect was not implemented in the CMIstark software package [106], Stark energies and hence state-specific spatial deflection was not simulated for DIBN.

Deflection of DIBN was tested in a lab experiment at DESY and was utilized during the x-ray diffraction experiment at LCLS. Deflection of DIBN serves two purposes: First, spatial selection of the lowest-lying rotational quantum states is important in order to select molecules best suited for laser alignment and secondly, a certain degree of separation from the He seed gas of the molecular beam is desirable in order to reduce scattering background from He.

4.3.2. Experimental Results

A mixture of a few mbar DIBN was provided by a supersonic expansion from a pulsed Even-Lavie valve in the same molecular beam setup as for the indole$(H_2O)_n$ experiment. The EL valve was heated up to 170° C, due to the low vapor pressure of DIBN at room temperature. The backing pressure of the seed gas He was set to 50 bar. DIBN was ionized either via the FEL (at LCLS) or via the fs-pulses of an 800 nm Ti:Sa laser (at LCLS and in the test experiment at DESY). At DESY, spatial beam profiles of DIBN along with the beam profiles of the seed gas He were obtained, exploiting strong-field ionization of He. Due to limited beamtime at LCLS, no He beam profiles were obtained at LCLS. The Keldysh parameter γ, which enables a distinction between the regime of multi-photon- to strong-field ionization, for the test experiment performed at DESY was estimated to be $\gamma = 0.359$ for He with ionization potential 24.6 eV, hence He (and also DIBN) are ionized by strong-field ionization. At LCLS, the molecular beam machine providing DIBN for the x-ray diffraction experiment, was the same as used at the test experiment at DESY.

In fig. 4.6, the spatial beam profile of DIBN at two different deflector voltages (0 kV and 20 kV) is shown, measured by recording the density of I^+ ions of fragmenting DIBN upon ionization by the Ti:Sa laser in dependence of the molecular beam position y prior to the x-ray diffraction experiment performed at LCLS. The deflection of hfs states is towards the right of fig. 4.6. Only the deflected part of the spatial beam profile was measured and the intensities are normalized to the maximum intensity of the undeflected beam (at position $y = 0.6$ mm. The lines are merely shown to guide the eye and don't correspond to simulated beam profiles.

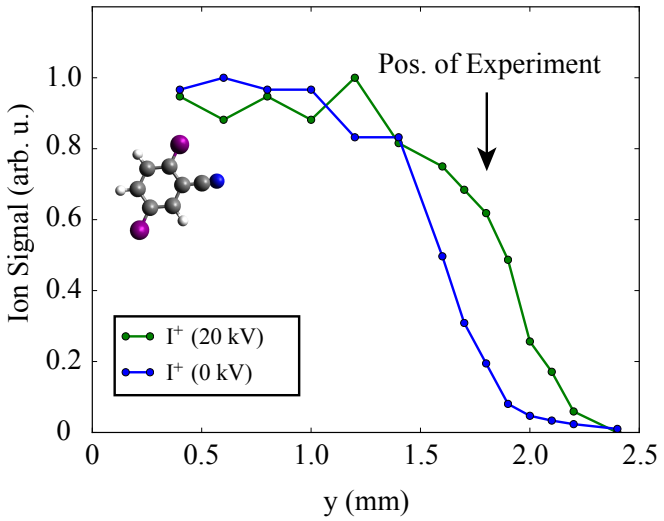

Figure 4.6.: Molecular beam deflection curves for DIBN obtained at LCLS with deflector voltages of 0 kV (blue) and 20 kV (green). Only the deflected part of the spatial molecular beam profiles was measured. The spatial separation at 50% intensity is ≈ 0.3 mm.

A separation of about 0.3 mm can be observed between the undeflected (0 kV) and deflected (20 kV) molecular beam at 50 % of the undeflected beam density. The coldest DIBN molecules are located in the deflected part, and these are well suited for laser alignment as will be shown in chapter 5. Due to limited experimental beamtime at LCLS, deflection of DIBN was not investigated thouroughly and only a few deflection measurements of DIBN were obtained. The graph shown in fig. 4.6 corresponds to the only measurement at the optimized final molecular beam positions used for the x-ray diffraction experiment. The deflection of DIBN serves for estimating the molecular beam position best suited for laser alignment. The degree of alignment was probed subsequently to recording the deflection profiles as will be outlined in the next chapter. The position marked by the arrow indicates the position to which the molecular beam was set for the x-ray diffraction experiment. At this position, a good degree of alignment was obtained in the deflected part of the beam, while the beam density has just dropped to 60 % of the peak intensity. In case one assumes the spatial profile of the He seed gas being of the same shape as the undeflected DIBN profile, an increase in the ratio DIBN/He of 60 %/ 20 %, hence by a factor of 3 is derived. However, the expansion of the seed gas He differs from the expansion of undeflected DIBN as will be shown below.

For comparison, the deflection of DIBN was investigated in a follow-up test experiment in the lab at DESY. This was performed in order to also address another important purpose of molecular beam deflection, namely the seperation of the target molecules from

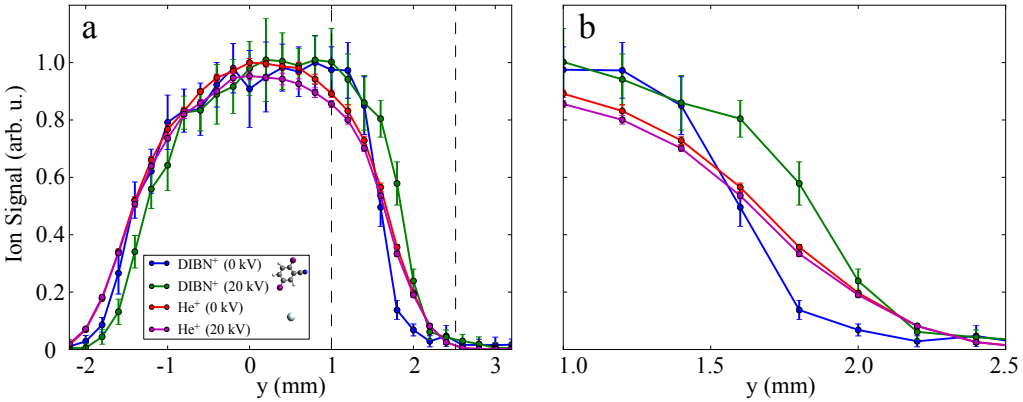

Figure 4.7.: Molecular beam deflection curves for DIBN and He obtained at DESY with deflector voltages of 0 kV and 20 kV. (a) shows the the full molecular beam profile while (b) shows a cut of the region y = 1 – 2.5 mm (marked with dashed lines in (a)). The deflection of DIBN at 20 kV is very similar to the one obtained at LCLS (≈ 2.5 mm separation at 50 % intensity). He is unperturbed by the deflector, however, its beam profile is slightly broader than the DIBN profile.

the He seed gas. In fig. 4.7, the spatial beam profiles of DIBN at two different deflector voltages (0 kV and 20 kV) are presented, measured via either recording the density of I^+ or the parent ion $DIBN^+$upon ionization by the Ti:Sa laser. The deflection profiles of I^+ and the parent ion $DIBN^+$ are identical, therefore only the profile of $DIBN^+$ is shown along with the profile for He^+. The deflection of DIBN confirms the results obtained at LCLS. The undeflected and deflected DIBN curves are separated by ≈ 0.25 mm at 50 % intensity (see fig. 4.7 (b)). Comparing the intensities at $y = 1.8$ mm, the intensity in the deflected beam has dropped to 60 % of its peak intensity while at this position the intensity of the undeflected beam is reduced to 13% of its peak intensity. The undeflected beam profile of DIBN was assumed to "mimic" the He profile as explained above. The obtained ratio (at DESY) of 60 %/ 13 % = 4.6 is slightly different to the ratio obtained at LCLS, infact, it looks even better (at LCLS, the ratio was only 60 %/ 20 % = 3, and not 4.6). However, the spatial separation of DIBN from the He seed gas is not as good as could be expected by comparing only the deflected and undeflected DIBN profiles as will be explained in the following, since the molecular beam profile of He differs from the undeflected DIBN profile.

He is completely unaffected by the deflector, as expected. However, the spatial profiles indicate that the He profile in the interaction region is slightly broader than the DIBN profile. The intensity of He at $y = 1.8$ mm has just dropped to 35 %, giving an increase in the DIBN/He ratio of 1.7 (i. e., less than the increase by factor of 3 and 4.6 as would

be deduced from the spatial profiles of the undeflected DIBN beam). This experimental finding partly counteracts the effort of using the deflector for spatial separation of the target molecules from the He seed gas, at least for these weakly deflecting molecules. The separation might be much more pronounced for the case of lighter molecules such as indole and indole$(H_2O)_1$, as indicated by the measured deflection profiles shown in section 4.2. In general, significant deflection from the He seed gas requires a significant dipole-moment-to-mass ratio, i. e., preferably light molecules with high permanent dipole moment. On the other hand, x-ray scattering requires heavy atoms/molecules in order to obtain a decent scattering signal, hence these two requirements counteract each other. However, for light molecules, the separation from the He seed gas would be much more important for x-ray diffraction experiments while for heavy molecules, more He scattering background would be tolerable as this might be compensated for by having much stronger scattering signals from heavy target molecules.

The observed behaviour has been described before and was explained to occur due to the distinct masses of the target molecule and the backing gas [55, section 2.3.8]. The species of lower mass in the gaseous mixture has a larger transversal velocity component whereas "transversal" means perpendicular to the molecular beams' propagation direction. Since in this case the backing gas is He, the effect causes more lateral spreading of the He beam profile compared to the DIBN profile. In principle, this effect should be more or less suppressed by placing skimmers at large distances as was done in the setup, where the last skimmer was placed at a distance of ≈ 50 cm from the valve. However, simulations in the indole case suggest (see above) that secondary collisions of the molecules at the skimmers and essentially at the deflector again lead to a broadening of the molecular beam profile which would be more pronounced in the case of the backing gas as this has a larger lateral velocity spread.

4.4. Summary

In this chapter, experimental results were presented demonstrating the feasibility of the spatial separation of molecules and molecular clusters in distinct rotational quantum states in an inhomogenous dc electric field of an electrostatic deflector.

Section 4.2 was concerned with electrostatic deflection of the various species present in the molecular beam of a mixture of indole, water and the backing gas He. The presented results show that a spatial separation of indole and indole$(H_2O)_n$ clusters in distinct rotational quantum states of a cold molecular beam is feasable. Most importantly, indole$(H_2O)_1$ exhibits a much stronger deflection than the indole monomer and

the indole$(H_2O)_2$ clusters. A full spatial separation of indole$(H_2O)_1$ clusters from the other species present in the molecular beam can be achieved and was demonstrated. Creation of a clean molecular sample in a small set of states is highly desirable for accessing the properties of individual samples, and for investigations of stereodynamics and stereochemistry of these samples. The experimental data was quantitatively simulated using trajectory simulations. These trajectory simulations show, that the lowest-lying rotational quantum states exhibit the strongest Stark shift and, therefore, are deflected the most. At the low temperatures due to the supersonic expansion, the deflection can be well simulated and understood. An increased amount of spatial deflection in a molecular beam of indole alone (i. e., no indole$(H_2O)_n$ clusters present) is ascribed to more efficient cooling in the absence of clustering.

In section 4.3, deflection profiles of the prototypical molecule 2,5-diiodobenzonitrile (DIBN) are presented. These were obtained in order to select a decent fraction of the coldest states best suited for laser alignment in the coherent x-ray diffraction experiment on isolated DIBN molecules. In addition, deflection was exploited to spatially separate the target as much as possible from the He seed gas. Usually, the density of He in such molecular beams is three to four orders of magnitude higher than the target density and scattering background from He at these ratios is a major obstacle in the x-ray diffraction experiment. Due to the large mass of DIBN and the increased lateral spread of the light He atoms, only a slight spatial separation of the target molecules from He was achieved. The different lateral spread of the beam profiles of the light He and the heavy DIBN was explained to be due to the combination of the increased lateral velocity of lighter gases, i. e., He, combined with secondary collisions of the molecular beam at skimmers and essentially the deflector. However, state-selection of colder states was important for laser alignment as will be outlined in the following chapter.

The deflection technique can be applied to a variety of molecular systems. It is in particular useful for quantum-state selection of large asymmetric top molecules in high-field seeking states for which other techniques such as, e. g., hexapole focussing are not applicable. Regarding the coherent x-ray diffraction experiment presented in this thesis, the purpose of the deflector is to provide quantum-state selection (for selection of the states best-suited for laser alignment) as well as spatial separation from the inert seed gas in a molecular beam. In general, these applications will be highly valued for many novel experiments making use of molecular beams at the new x-ray free-electron laser sources.

5. Laser-Induced Alignment of 2,5-Diiodobenzonitrile

5.1. Introduction

In order to investigate molecular properties of an ensemble of gas-phase molecules in the molecular frame, the interaction of a strong ac electric field from an off-resonant laser with the anisotropic molecular polarizability can be used to create directional superpositions of field-free states (so-called pendular states) and hence induce alignment of the molecules. For a linearly polarized laser field, a molecule will align with the most-polarizable axis pointing preferably along the laser polarization. This is called 1d-alignment. By using elliptically polarized laser fields, fixing of all three molecular axes in the laboratory frame, i. e., 3d-alignment, can be achieved [83]. The theory of laser alignment and the explanation of the spatial anisotropic distribution of the molecules upon the interaction with a strong laser field was given by Friedrich and Herschbach [89, 96] and Seideman [101]. Orientation, i. e., breaking of the up-down symmetry along the space fixed alingment axis, cannot be achieved in the rapidly varying ac laser fields but can be induced with additional dc electric fields [42, 100, 181]. Exploiting laser alignment has become an important tool in many experiments studying molecular properties and/or following molecular dynamics directly in the molecular frame, such as, e. g., time-resolved imaging of electronic dynamics by measuring molecular frame photoelectron angular distributions of aligned molecules [68, 182, 183].

Laser induced alignment strongly benefits from a good preparation and quantum-state selection of the molecular sample, as the angular confinement of molecules is strongest for the lowest-lying rotational quantum states. For coherent x-ray diffraction imaging of

isolated molecules in the gas-phase, a high degree of alignment of the target molecules DIBN is required in order to observe an anisotropic scattering signal on top of a strong isotropic background from atomic scattering. Therefore, quantum-state selection by electrostatic deflection was applied in order to select the states best suited for laser induced alignment during the x-ray diffraction experiment. In this chapter, results of the laser-induced alignment of 2,5-diiodobenzonitrile (DIBN) for the x-ray diffraction experiment performed at LCLS are presented.

5.2. Laser-Induced Alignment of 2,5-Diiodobenzonitrile (DIBN)

Adiabatic laser alignment of DIBN was achieved using 11 ns-pulses (FWHM) from a Nd:YAG laser (YAG) in the near-infrared regime. The laser specifications are outlined in section 3.2. DIBN molecules are aligned along the most-polarizable axis which is inclined by $\approx 7°$ with respect to the iodine-iodine axis. When Coulomb explosion of DIBN is initiated by either the fs-long Ti:Sa or FEL pulses, the spatial distribution of I^+ to be observed on the phosphor screen (i. e., the 2d-p_x-p_z momentum distribution of I^+) can be used as a direct measure of the alignment at the time of the probe, since I^+ ions recoil along the iodine-iodine axis of the molecule.

Figure 5.1 sketches the detection method for probing alignment. The YAG pulse is linearly polarized and the direction of the YAG polarisation with respect to the horizontal axis (x-axis) is given by the angle α. The FEL is, by design, always polarized horizontally, i. e., along the x-axis. A DIBN molecule aligned along $\alpha = 0$ is sketched in the interaction point. However, for the diffraction experiments, α will be varied. The Ti:Sa laser was used for measurements to probe and optimize alignment when the FEL was turned off. The Ti:Sa was linearly polarized in vertical direction in order to not cause any bias when probing alignment, since the ionization of DIBN depends on the Ti:Sa polarisation. By this, it was ensured that the degree of alignment is rather underestimated than overestimated.

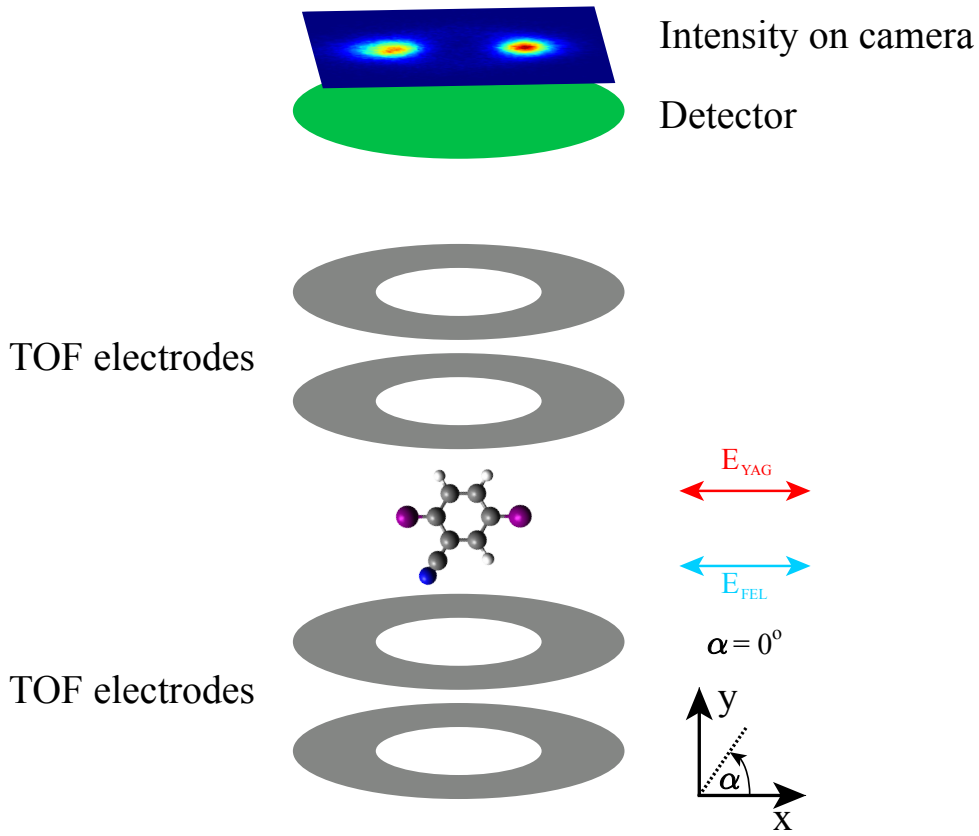

Figure 5.1.: Schematic image of the detection method for probing alignment. The DIBN molecules get aligned along the YAG laser polarisation and the alignment is by probed a second laser (either the Ti:Sa or the FEL), inducing ionization of DIBN via Coulomb explosion. The coordinate system at the bottom right sketches, how the angle α marks the inclination of the YAG polarisation with respect to the horizontal axis (x-axis, along the FEL-polarisation). Upon ionization, positive ions are accelerated towards the detector at the top. With the detector gated to I^+ ions, the 2d-momentum distribution (p_x,p_z) is resolved spatially on the phosphor screen and recorded by a camera. The, in reality conically-shaped, VMI-electrodes are simplified to disc-like electrodes.

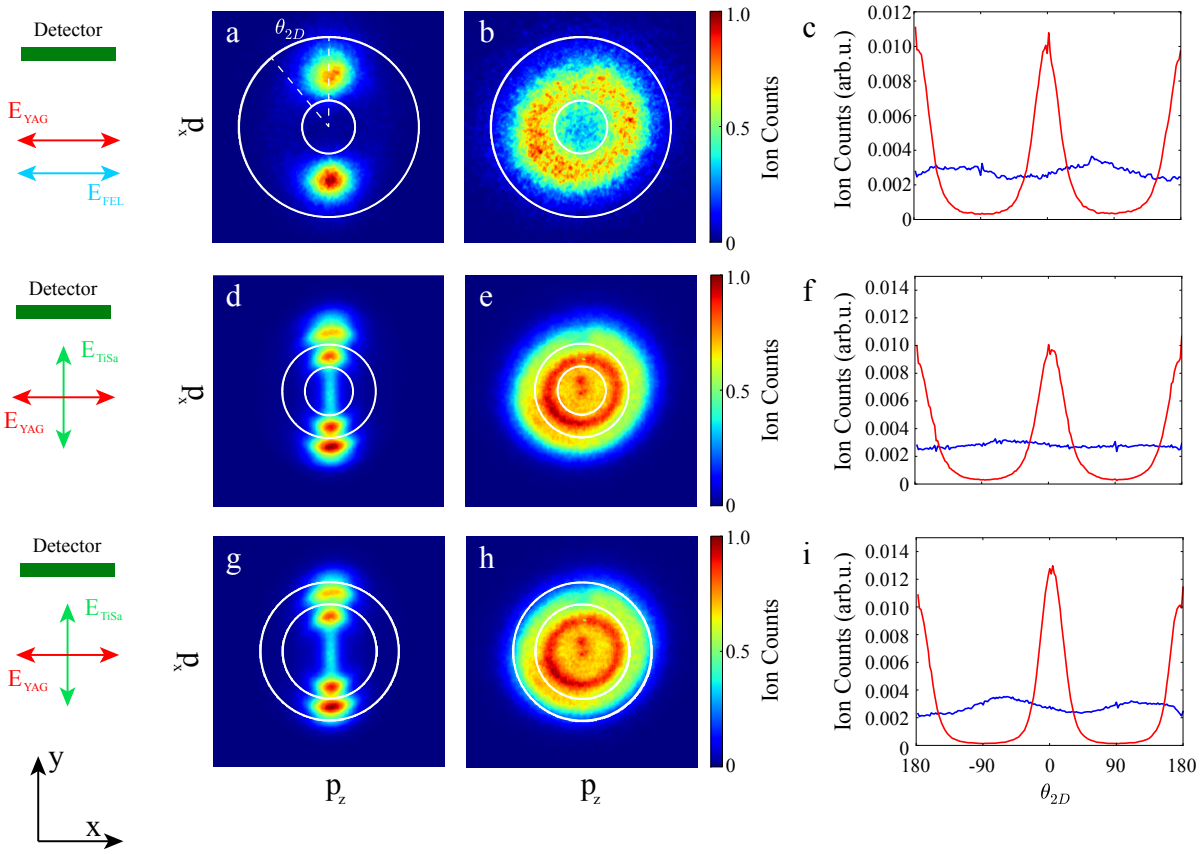

Figure 5.2.: Molecular alignment of an ensemble of DIBN molecules by the YAG laser, probed by the FEL (a-c) and the TiSa (d-i). The FEL and the YAG are horizontally polarized, i. e., in the plane of the detector, whereas the Ti:Sa is polarized perpendicular to it. When the YAG is used for alignment, strong angular confinement of the I^+ ions is observed (first column, a,d,g), whereas the I^+ momentum distribution are circularly symmetric when the YAG was not used. (second column, b,e,h). The two pairs of peaks, when the Ti:Sa is used as a probe, correspond to two different fragmentation channels, releasing different kinetic energy to the I^+ ions (see text). The azimuthal angle θ_{2D} is shown in (a) and the azimuthal histograms (c,f,i; averaged radially over the values between the two radii marked by white circles) were used to quantify the degree of alignment by calculation of $\langle \cos^2 \theta_{2D} \rangle$.

In fig. 5.2, some example images of I^+ ion momentum distributions recorded by the CCD camera on top of the phosphor screen are shown. The polarizations of the three lasers are sketched in the x-y plane on the very left along with the detector. For the images in the first row (a,b,c), the FEL was used to probe alignment. The second and third row show images recorded with the Ti:Sa being used as the probe laser. The first column

(a,d,g) shows 2d-momentum distributions of I^+-ions with the YAG turned on, polarized horizontally. The scale of intensity is the number of ion counts, normalized to its maximum value. This scaling will be applied for all 2d-momentum distributions that are shown in the following. The difference in the intensity between the two (four in the Ti:Sa case) peaks is due to a different detection efficiency of the camera and does not refer to orientation of DIBN (orientation would not be observable anyway in I^+ momentum distributions as DIBN consists of two iodines at opposite ends). A strong angular confinement along the x-axis can be directly seen in the momentum distributions. While in the FEL case, there is just a pair of two single peaks visible, two pairs, each containing two peaks, are obtained with the Ti:Sa being used a probe laser. This corresponds to two distinct fragmentation channels of DIBN, with I^+-ions from the outer pair of peaks having more kinetic energy than the inner pair of peaks. The inner peak is assigned to double ionization ($I^+ + C_7H_3NI^+$) and the outer peak to triple ionization ($I^+ + C_7H_3NI^{2+}$) of DIBN.

It is noted, that the FEL polarization is parallel to the plane of the ion detector but the momentum distribution is circularly symmetric. This demonstrates an isotropic interaction of the far-off resonant x-ray radiation with the molecule, independent of the relative angle between the molecular axis and the x-ray polarization direction. It can be concluded, that there is no detection bias due to, e. g., selective photoionization. Hence, the FEL with 2 keV x-ray radiation can be considered as an unbiased, almost ideal probe of angular confinement of the molecules. This is not the case when the Ti:Sa is used to probe molecular alignment. The Ti:Sa polarization always was set perpendicular to the detector plane, which ensures that the degree of alignment in this case is rather underthan overestimated as would be the case if Ti:Sa and YAG polarization would be parallel [184].

The angular confinement is quantified by calculating the $\langle \cos^2 \theta_{2D} \rangle$ expectation value from the images. The angle θ_{2D} is illustrated in fig. 5.2 (a). The angular distributions (along θ_{2D}) of the number of ion counts within the sketched radial regions between the two white rings are shown in the third column (c,f,i). The angular distributions of I^+ ions in the YAG (NoYAG) case are depicted by the red (blue) solid line. It can be seen, that the outer peak of the momentum distributions for aligned DIBN, probed with the Ti:Sa (g) shows a stronger angular confinement than the inner peak (d), compare fig. 5.2 (f) and (i). This is due to I^+ ions with higher velocity recoiling faster from the fragmenting DIBN molecule and are less influenced by motion of the molecule after ionization. Hence, the outer fragmentation channel provides a more accurate means of estimation of the alignment at the time of fragmentation. The degree of alignment, quantified by $\langle \cos^2 \theta_{2D} \rangle$, was calculated from the angular distribution of I^+ ions from the outer fragmentation channel when using the Ti:Sa as a probe.

5.3. Laser Alignment in the Deflected Molecular Beam

In order to achieve strong molecular alignment of DIBN molecules for the x-ray diffraction experiment, spatial quantum-state selection was exploited as explained in chapter 4. The degree of alignment was probed at distinct positions in the deflected molecular beam.

Figure 5.3 shows I^+ momentum distributions probed with the Ti:Sa at different positions of the molecular beam with the deflector turned on to 20 kV. The y-coordinate corresponds to the coordinate of the molecular beam as given in fig. 3.5. The alignment was quantified from $\langle\cos^2\theta_{2D}\rangle$ of the outer fragmentation channel at distinct positions of the molecular beam, ranging from the most-deflected part (a) to the least deflected part (h) of the beam. The strongest alignment ($\langle\cos^2\theta_{2D}\rangle = 0.894$) is obtained at y = 2.0 mm, a position close to the very edge of the deflected part of the molecular beam. This is significantly better than the degree of alignment in the undeflected part of the molecular beam which is $\langle\cos^2\theta_{2D}\rangle \approx 0.82$ (at $y \approx 0.5$ mm, see fig. 5.3 (g,h)).

Figure 5.4 shows the derived $\langle\cos^2\theta_{2D}\rangle$-values (red) along with the deflection curve from chapter 4 (green). The alignment was probed with the deflector at 20 kV, the undeflected molecular beam profile (blue) is just shown for convenience. The points marked with letters a–h in fig. 5.4 correspond to the I^+ momentum distributions shown in fig. 5.3. The left axis gives the normalized molecular beam density, while the right axis gives the degree of alignment in dependence of the probe position in the molecular beam. The lines just

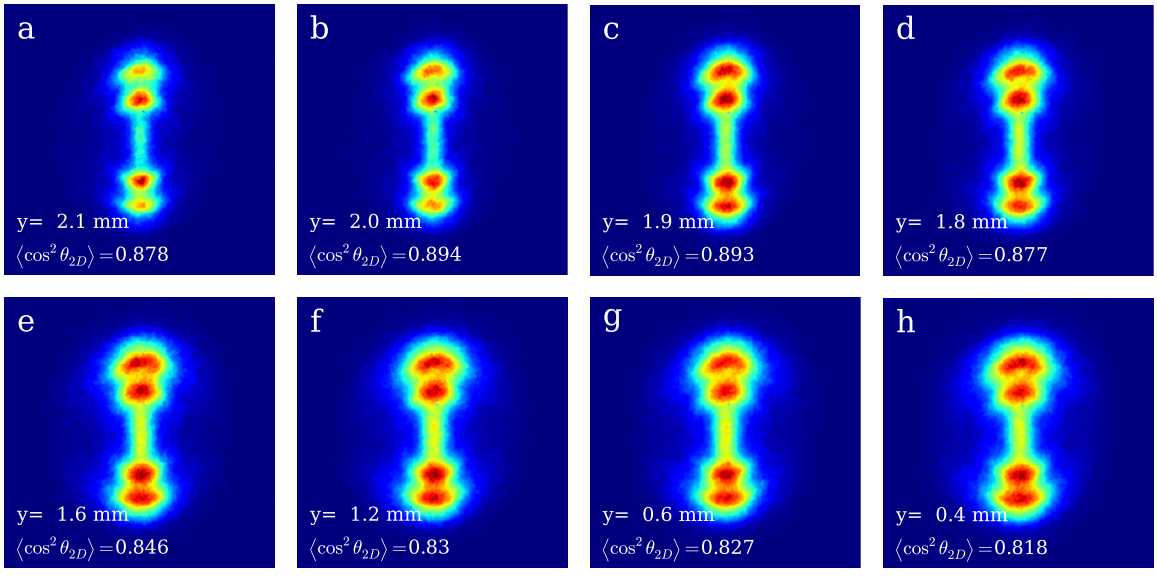

Figure 5.3.: VMI images of aligned DIBN at distinct positions of the molecular beam, ranging from the most-deflected (a) to the least deflected part (h) of the beam, compare fig. 5.4.

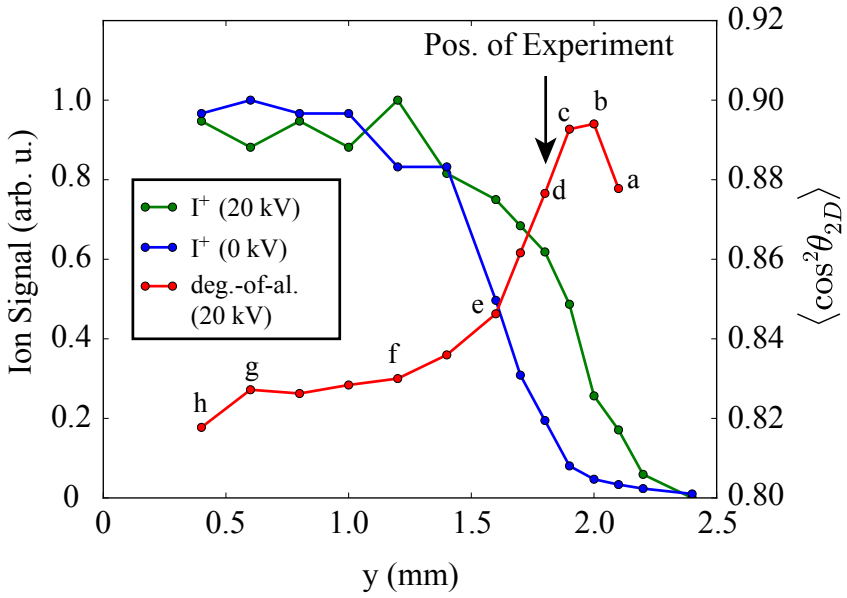

Figure 5.4.: Alignment, in terms of $\langle\cos^2\theta_{2D}\rangle$ (red), of DIBN at distinct positions of the molecular beam along with the deflection curve (green). The alignment was probed with the deflector at 20 kV. The marked points (a–h) correspond to the ion images from fig. 5.4. Considering the best compromise between degree of alignment and sufficient molecular beam density of target molecules, the x-ray diffraction experiment was performed at y = 1.8 mm ($\langle\cos^2\theta_{2D}\rangle = 0.877$), not at the position where the highest degree of alignment was estimated (i. e., $\langle\cos^2\theta_{2D}\rangle = 0.894$ at y = 2 mm).

serve to guide the eye (i. e., they don't correspond to, e. g., simulations). In general, it is clearly visible in fig. 5.4, that the degree of alignment is systematically stronger in the deflected part of the molecular beam, hence, the spatial quantum-state selection of lower rotational states nicely enhances the degree of alignment. The highest degree of alignment ($\langle\cos^2\theta_{2D}\rangle = 0.894$) was obtained at y = 2.0 mm. However, the molecular beam density at this position was considered to be too low for sufficient diffraction signal in the x-ray diffraction experiment on aligned DIBN. Therefore, for the x-ray diffraction experiment, the position of the molecular beam was set to y = 1.8 mm (fig. 5.3 (d)). At this position, the degree of alignment is still strong ($\langle\cos^2\theta_{2D}\rangle = 0.877$), while the molecular beam density is only reduced to about 60 % of the density in the center (i. e., at y = 0 mm) and not to about 25 % like it would be at y = 2 mm (fig. 5.3 (b)).

5.4. Laser Alignment of DIBN in the X-ray Diffraction Experiment

During the x-ray diffraction experiment, the polarization of the YAG was altered in order to collect x-ray diffraction data from aligned DIBN at scattering vectors $\mathbf{Q}$, for which a decent angular anisotropy of the x-ray scattering can be expected (as will be explained in chapters 6 and 7).

Figure 5.5 schematically sketches the geometry used during the x-ray diffraction experiment. The YAG polarisation was rotated to $\alpha = -60°$. This is reflected in the I^+ momentum distributions, which will be the projection of the distribution at $\alpha = 0$ to the distribution at $\alpha = -60°$. The momentum distributions were recorded together with the x-ray diffraction data (the latter by the pnCCD detector). With $\alpha = -60°$, the two I^+ peaks merge on the phosphor detector and the radii of the peak positions are reduced by a factor of 2, depicting the reduction of p_x by $\cos(60°) = 0.5$.

Figure 5.6 shows I^+ momentum distributions for the isotropically DIBN (NoYAG, a) and DIBN aligned at $\alpha = -60°$ (YAG, b). Since a reasonable estimation of the degree of alignment couldn't have been performed of momentum distributions like fig. 5.6 (b), the degree of alignment was checked with horizontal YAG polarisation at various times during the long (i. e., several hours) measurement of the x-ray diffraction data.

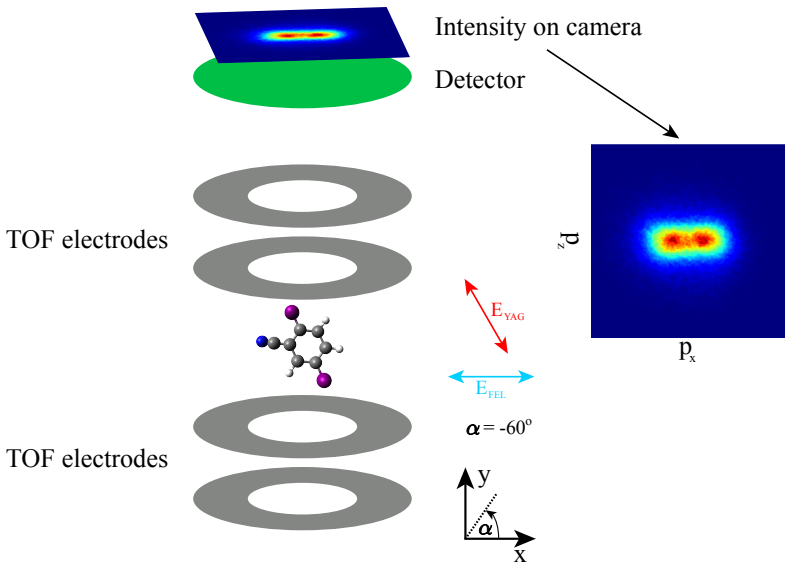

Figure 5.5.: Schematic image of the detection method for probing alignment during the time of recording x-ray diffraction data from aligned DIBN. The polarization of the YAG was altered to $\alpha = -60°$.

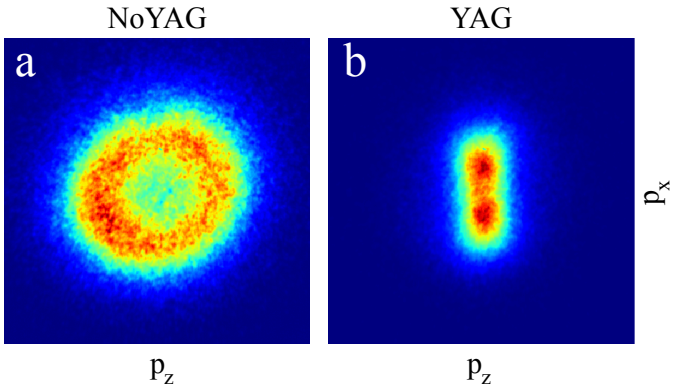

Figure 5.6.: I^+ momentum distributions probed by the FEL during the x-ray diffraction data acquisition for the isotropic (NoYAG, a) and aligned (YAG, b) sample, the latter obtained at YAG-polarisation of $\alpha = -60°$.

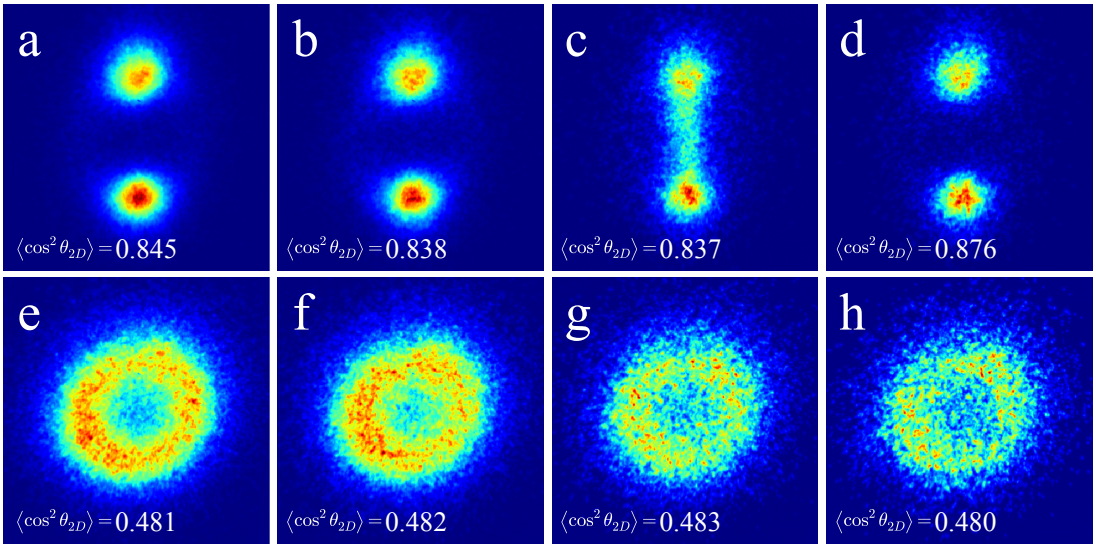

Figure 5.7.: I^+ momentum distributions for the four datasets taken in between the diffraction-data-acquisition in order to check the alignment. The YAG-polarisation was $\alpha = 0°$(horizontal), the alignment was probed by the FEL. The degree of alignment changes during the long time ($\approx$ 9 hours) for data acquisition of the x-ray diffraction data, hinting at changing laser parameters and/or changing spatial and temporal overlap of the YAG and the FEL.

In fig. 5.7, I^+ momentum distributions recorded for four datasets in between the x-ray diffraction experiment are shown. In (c), the YAG polarisation was rotated during acquisition of this dataset, resulting in some I^+ ions recorded in the center of the detector. Therefore, I^+ ions used for calculation of $\langle\cos^2\theta_{2D}\rangle$, were restricted to a slighly more narrow range, i. e., the inner radius (compare fig. 5.2) was slightly moved outwards. The

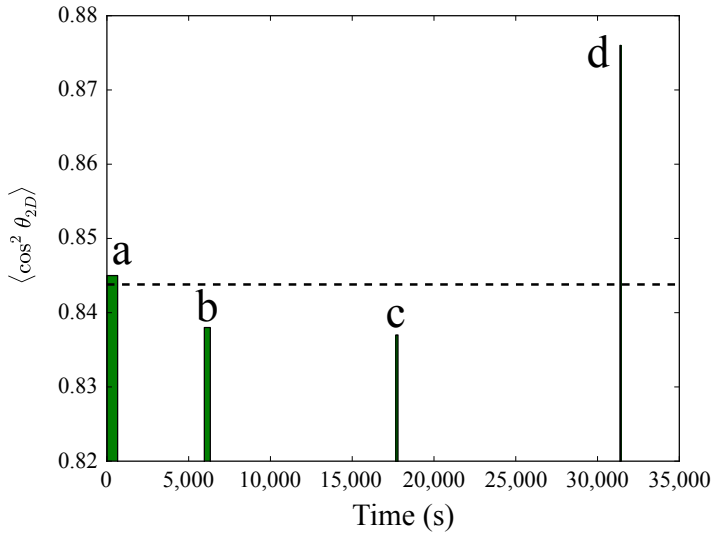

Figure 5.8.: Time-dependence of the alignment during the four datasets taken in between the diffraction-data-acquisition time in order to check the degree of molecular alignment at horizontal YAG-polarisation. The letters refer to the subfigures of fig. 5.7. The dashed horizontal line marks the average degree of alignment of $\langle\cos^2\theta_{2D}\rangle = 0.844$.

degree of alignment changes during the long time ($\approx$ 9 hours) for data acquisition of the x-ray diffraction data. This points to changing molecular beam and/or laser parameters. It is assumed that the spatial and temporal overlap of the YAG and the FEL was slightly changed during this time.

Figure 5.8 shows the degree of alignment estimated from the four datasets shown in fig. 5.7 during the complete x-ray diffraction experiment. Right at the beginning (i. e., before starting to collect x-ray diffraction data at all), $\langle\cos^2\theta_{2D}\rangle = 0.845$. The degree of alignment was checked again for two times during the x-ray diffraction measurement and right at the end (at $\approx$ 32,000 s). The width of the bars corresponds to the data acquisition time of these four datasets. The height of the bars represents the $\langle\cos^2\theta_{2D}\rangle$-values, calculated from fig. 5.7. The data acquisition times for collecting I^+ momentum distributions were different in the four cases. An average degree of alignment was obtained by the mean of the four $\langle\cos^2\theta_{2D}\rangle$-values, weighted by the respective data acquisition time (i. e., number-of-shots). This average value of $\langle\cos^2\theta_{2D}\rangle = 0.844$ is depicted in fig. 5.8 by the dashed horizontal line. It is noted that the weighted average only considers the number of shots for each of the four runs. A possible systematically changing time-dependent overlap function in between these four runs is not known. Therefore, it is assumed that the average value derived from these four datasets indeed represents the average degree of alignment during the whole x-ray diffraction experiment.

5.5. Ionization of DIBN

This section is concerned with taking a closer look at the ionization of DIBN due to Coulomb explosion caused by the FEL. Interest in the ionization of DIBN is twofold: First of all, final charge states of the I^{n+} ions created by the FEL allow to estimate, whether multi-photon processes play an important role at the experimental conditions used. Moreover, the molecular beam density M may be deduced from ion measurements such as the estimation of the number of I^{n+} created in a single FEL shot. As will be pointed out in chapter 6, the absolute number of molecules interacting with the FEL-pulses doesn't have to be known but rather the number density M of molecules in order to perform photon-accurate simulations of x-ray diffraction intensities from DIBN. In addition, the molecular beam density M of DIBN represents a parameter responsible for the contrast in diffraction-difference images (i. e., the difference of the diffraction patterns of aligned (I_{YAG}) and not-aligned (I_{NoYAG}) DIBN, named "I_{YAG}-I_{NoYAG}" in chapter 7) [1]. Since the actual density of target molecules (DIBN) in the molecular beam is not known, ion measurements in combination with considerations involving photoabsorption cross-sections can be utilized for an estimation of M.

Figure 5.9 shows a time-of-flight spectrum, obtained by probing the molecular beam with the FEL. The spectrum is dominated by H^+ and He^+. A zoom into the y-axis (see inlet) reveals much more fragments, many of which originate from DIBN. Iodine ions with increasing charge ($I^+ \ldots I^{7+}$) appear in the spectrum with decreasing intensity. In particular, singly-charged iodine I^+ is most abundant in the spectrum.

When DIBN is ionized by 2 keV photons from the FEL, predominantly the M-shell of iodine is accessed and ionization from 3s, 3p, and 3d orbitals of iodine occurs. Table 5.1 gives the subshell photo-ionization cross sections for iodine at a photon energy of 2 keV [185], obtained by calculations using the XATOM software [186]. The sum of of the values from table 5.1 (i. e., the total photo-ionization cross-section of iodine at 2 keV) of 0.42068 Mbarn is in good agreement with the cross-section given in the NIST database [187], which is 0.4192 Mbarn. The total photo-ionization cross-section of iodine at 2 keV is dominated by the cross-section of the 3p and 3d subshells. Now, the final charge states arising from ionization of predominantly the 3p and 3d subshells have to be considered.

Since the electronic decay processes do not strongly depend on the atomic number Z, for iodine, a similar behaviour to Xe is expected. This is supported by the fact, that the

[1] The degree of alignment of DIBN is a second parameter changing the contrast in I_{YAG}-I_{NoYAG} diffraction-difference images, but as this could be estimated from the I^+-momentum distributions, the only free parameter changing the contrast of diffraction-difference images remains the molecular beam density M of target molecules.

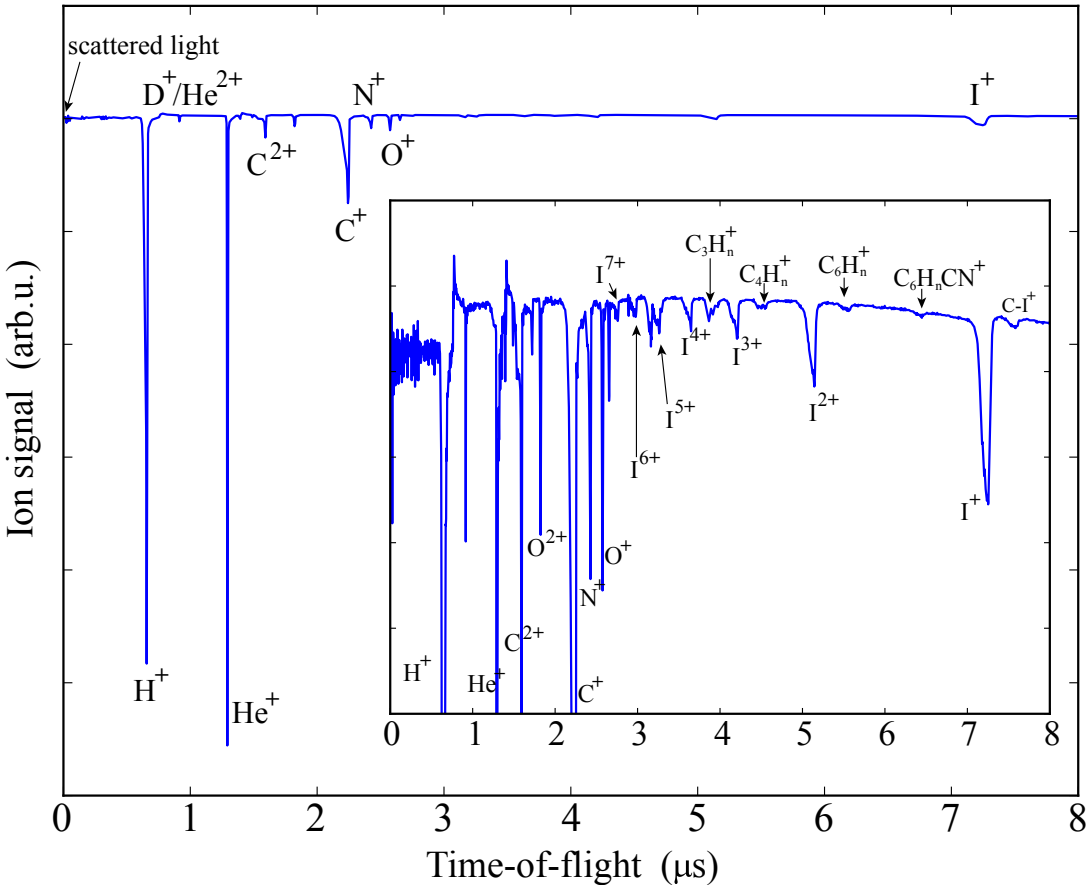

Figure 5.9.: Time-of-flight spectrum, obtained by probing the molecular beam with the FEL. The inlet is a zoom into the y-axis in order to show the various iodine ions.

Subshell	Cross-section (Mbarn)
5p	0.00218
5s	0.00114
4d	0.0259
4p	0.0256
4s	0.00796
3d	0.196
3p	0.129
3s	0.0329

Table 5.1.: Subshell photo-ionization cross sections of iodine at photon energy of 2 keV [185], obtained by calculations using the XATOM software [186]

photon energy of 2 keV is far from the electron binding energy in the next lower shell (i. e., the 2p subshell), which is 4,557 eV (iodine) and 4,786 eV (Xe), respectively [188]. For Xe, electronic decay cascades and probabilities for final yields of multiply charged Xe^{n+} ions upon creation of inner-shell vacancies were calculated, see ref. 189. For an initial 3d vacancy, the most probable final charge state is Xe^{4+}, while for a 3p vacancy, the charge-state distribution is shifted upwards and peaks around Xe^{7+}. The most-probable final charge state in both cases has a probability of $\approx 50\%$. Assuming similar ionization pathways for Xe and I (for the arguments given above), absorption of a single 2 keV photon by DIBN results in a charge state distribution of DIBN peaking at $DIBN^{4+}$ or higher charged DIBN ions. After the initial ionization and subsequent charge transfer within the DIBN, eventually Coulomb explosion sets in and destroys the molecule. Supported by the considerations given above, iodine charge states of $I^+ \ldots I^{7+}$ can be entirely due to single-photon absorption only. Two- (or higher) photon absorption is considered to be highly unlikely and is neglected in the following.

An estimation of M requires the determination of the number of iodine atoms that are ionized per shot. First of all, the number of I^+ ions per FEL-shot can be derived from single-shot VMI images. The average number of I^+ was determined for ≈ 400 shots from various datasets for which also the x-ray diffraction data was recorded. This yields an average number of 25.28 ($\pm$ 6.03) I^+/FEL-shot. Taking into account fig. 5.9, the relative intensities of all iodine ions, $I^+ \ldots I^{7+}$(the I^{8+}-peak is very weak and already hidden in the much stronger O^+-peak), in combination with the average number of 25.28 I^+/FEL-shot yield an average number of 44.01 iodine ions from a single FEL-shot.

The next step involves the calculation of the probability p_{abs} of a single iodine absorbing a 2 keV photon and subsequently getting ionized during a single FEL shot. The probability p_{abs} is given by $p_{\text{abs}} = \frac{\sigma_{\text{abs}} \cdot N_{\text{photons}}}{A_0}$ with σ_{abs} being the photoabsortion cross-section of iodine at 2 keV, N_{photons} the number of photons, impinging on the interaction area A_0. Values for photoabsorption cross-sections are taken from ref. 187. For iodine, $\sigma_{\text{abs}} = 0.4192$ Mbarn. With the FEL-pulse energy in the interaction region of 1.4 mJ (remind: only 35 % of the 4 mJ pulse is transported to the interaction zone of the experiment, see section 3.2), the number of 2 keV photons in the interaction region is $N_{\text{photons}} = 4.375 \cdot 10^{12}$. For simplicity, the FEL beam waist ω is considered to be the diameter of the interaction area A_0, hence $A_0 = \omega^2 \cdot \pi/4$. With $\omega = 30\mu$m, $A_0 = 7.068 \cdot 10^{-6}$ cm^2. Hence, the probability for a single iodine atom to absorb a 2 keV photon from the FEL pulse comprising N_{photons} photons is $p_{abs} = 0.25$. With the observed number of ≈ 44 iodine ions from a single FEL-shot, this corresponds to 176 iodine atoms in the interaction volume, which in turn corresponds to 88 DIBN molecules (a single DIBN molecule contains two iodines). With

the interaction volume $V_0 = A_0 \cdot l$, with $l = 0.4$ cm being the width of the molecular beam, the interaction volume is $V_0 = 2.827 \cdot 10^{-6}$ cm^3. Taking into account V_0, the molecular beam density would be $M = 3.1 \cdot 10^7$ cm^{-3}.

This value of M corresponds to an ion detection efficiency of 1. However, considering the real experimental setup, the ion detection efficiency is < 1. The MCP detection efficiency is assumed to be in the range 30 – 50 %. In front of the MCP, two meshes were mounted in order to apply retardation voltages in electron measurements. Each mesh has a transmission of 80 – 85 % [190]. Considering these values, the overall detection efficiency is in the range 19.2 – 36 %. This leads to molecular beam densities in the range M= 0.87 – 1.56 $\cdot$ 10^8cm^{-3}, which corresponds to 244 – 440 DIBN molecules in the interaction region. This, of course, rather underestimates the amount of DIBN, since only single-photon absorption was considered.

5.6. Summary

This chapter is concerned with the results of adiabatic laser alignment of DIBN, the target molecule for the x-ray diffraction experiment. It was shown, that a high degree of alignment can be obtained when using cold molecular beams. The effect of the initial rotational temperature was discussed, e. g., in ref. 191. Furthermore, it was demonstrated that quantum-state selection of the most-polar states by using the electrostatic deflector results in an enhanced degree of alignment as the most polar states are the lowest rotational states. During adiabatic alignment, the field-free rotational states evolve into pendular states the energy-wise ordering of which is still the same, i. e., the lowest rotational state evolves into the lowest pendular state, etc.. The lowest pendular states, however, experience a more narrow angular confinement in the laser field than the higher pendular states, hence a good quantum-state selection of the lowest-lying (field-free) rotational states prior to adiabatic laser alignment significantly enhances the obtained degree of molecular alignment. This is in agreement with previous investigations of laser alignment from quantum-state selected samples, see, e. g., refs. 42, 116. Therefore, the x-ray diffraction experiment profits from using the deflector and the degree of alignment for DIBN in the deflected part of the molecular beam is at best $\langle \cos^2 \theta_{2D} \rangle = 0.894$, in contrast to $\langle \cos^2 \theta_{2D} \rangle \approx 0.82$ in the undeflected part.

However, in order to maintain a sufficient molecular beam density for x-ray diffraction, the x-ray diffraction experiment was performed at a position in the deflected part of the molecular beam, where the alignment was determined to be $\langle \cos^2 \theta_{2D} \rangle \approx 0.87$ (measured with the Ti:Sa). The alignment was recorded at distinct times during the long (i. e., several

hours) x-ray diffraction experiment as well (using the FEL as a probe). The degree of alignment was not constant with time, but varied between $\langle\cos^2\theta_{2D}\rangle = 0.838$ and 0.876. This can be assigned to changing laser and/or molecular beam parameters such as, e. g., shifts in the spatial/temporal overlap of the FEL and the YAG laser.

A strong degree of alignment is crucial for the approach of recording x-ray diffraction data of aligned molecules, utilizing the incoherent superposition of single-molecule diffraction intensity distributions (i. e., diffraction patterns) to gain better statistics. This will be confirmed in chapter 6 where quantitative simulations of x-ray diffraction intensities for DIBN at different degrees of alignment are presented. These simulations demonstrate that the blurring of the diffraction pattern due to non-perfect alignment of DIBN significantly washes out the interference of the main scattering centers of DIBN (i. e., the two iodine atoms) even at quite high degrees of alignment of, e. g., $\langle\cos^2\theta_{2D}\rangle = 0.90$. In an experiment where the diffraction data will be used to eventually deduce the structure of the specimen of interest by phase-retrieval methods [192], limited alignment significantly hampers the resolution of the reconstructed structure of even very simple molecules as was discussed before [193, 194].

Regardless of whether phase retrieval is performed on the experimental diffraction data, a strong degree of alignment first and foremost increases the degree of angular anisotropy in the diffraction pattern of aligned molecules and the contrast in the diffraction-difference pattern, i. e., the difference pattern of aligned (YAG) and isotropic (NoYAG) pattern, see chapter 7. This is very crucial as a first result, i. e., confirmation of the feasibility of the incoherent superposition approach for a laser-aligned molecular ensemble. In any case, the weak diffraction signal even from an ensemble of aligned DIBN will be overshadowed by the abundant amount of helium seed gas (and the isotropic atomic scattering from all atoms in DIBN), as the deflection of DIBN is weak (see chapter 4) and the density of DIBN in the molecular beam, although not exactly known, is assumed to be quite low due to the low vapor pressure of DIBN. Hence, a strong degree of alignment is absolutely crucial to observe a significant anisotropy in the diffraction difference pattern, see chapter 7.

6. Simulation of X-ray Diffraction Intensity Patterns

This chapter is concerned with the simulation of x-ray diffraction intensities of 2,5-diiodobenzonitrile (DIBN) and helium. The theory given in section 2.3 is used as a starting point. By taking into account experimental details such as, e. g., the density of molecules in the molecular beam and the finite, i. e., non-perfect degree of alignment, the quantitative calculation of the number of photons scattered to certain detector elements (i. e., pixels) was performed, as will be outlined in this chapter. The simulated diffraction patterns will be compared to the experimental results in chapter 7.

The scattering signal from DIBN will be dominated by the contributions from the two iodine atoms. The charge distribution within the iodine atom, bound in the DIBN molecule, will not be altered much compared to the charge distribution of a single isolated iodine atom, as only the valence electrons take part in the molecular bond and the lower electronic shells are not affected. It is assumed that the electronic charge distribution of a particular atom is not affecting the charge distribution of the other atoms, i. e., molecular orbitals were not taken into account. In general, x-ray scattering is dominated by the inner-shell electrons (which are closely bound to the "parent atom") of an atom rather than by the valence electrons (which contribute to covalent bonds between atoms in the molecule). For this reasons, the target molecule DIBN is modelled by single atoms. These single atoms are placed at fixed distances which were estimated by ab-initio calculations (GAMESS-US MP2/6-311G** [124]). The most relevant lengthscale of the experiment is the distance of the two iodine atoms (700 pm), as diffraction will be dominated by the iodine-iodine-interference. This resembles a "double-slit" diffraction experiment on the

atomic level. Scattering by other atoms (C, H, and N) will be orders of magnitude weaker than the scattering signals from iodine and, due to the smaller interatomic distances, will mostly contribute to an isotropic background. Incoherent scattering is neglected, as the cross sections for incoherent scattering at 2 keV are two to three orders of magnitude smaller than the coherent scattering cross sections. E. g., for iodine, the coherent scattering cross section is 560 times as large as the incoherent cross section [187].

While the ratio of the scattered to the incident electric field $E_{\mathrm{sc}}(\mathbf{Q})/E_0$ involves the calculation of the molecular scattering factor $F_{\mathrm{mol}}(\mathbf{Q})$ for a set of given scattering vectors $\mathbf{Q}$, during the experiment a discrete number of photons is measured by the pnCCD detector on pixels of finite size. This discrete nature of the scattering signal, i. e., photons/pixel, is even further emphasized as the expected signals are very low, i. e., the number of scattered x-ray photons/FEL-shot is small, which is justified by the experiment where a hit rate of ≈ 0.2 photons/shot was measured on the pnCCDs, see chapter 7. The ratio $I(\mathbf{R})_{\mathrm{sc}}/I_0$ of scattered to incident intensity (both given simply in terms of number-of-photons), scattered to a certain pixel at $\mathbf{R}$) can now be expressed as [125]:

$$\frac{I_{\mathrm{sc}}(\mathbf{R})}{I_0} = \frac{|\mathbf{E}_{\mathrm{sc}}(\mathbf{R})|^2 \; R^2 \Delta\Omega}{|\mathbf{E}_0|^2 \; A_0} \tag{6.1}$$

$\mathbf{E}_{\mathrm{sc}}(\mathbf{R})/\mathbf{E}_0$ is the ratio of electric fields given in section 2.3. The cross sectional area of a certain pixel at $\mathbf{R}$ is $R^2\Delta\Omega$, where $\Delta\Omega$ is the solid angle subtended by the pixel. The solid angle is measured in the dimensionless unit steradian (sr), the full surface of a 3d sphere subtends the solid angle of 4π sr. The cross sectional area of the incident FEL laser beam is A_0 and the intensities $I_{\mathrm{sc}}(\mathbf{R})$ and I_0 are given in terms of photon counts [125]. Note that the coordinates in eq. (6.1) are given in terms of the real-space coordinates $\mathbf{R}$ whereas before the Fourier-space coordinates $\mathbf{Q}$ were used. The choice is arbitrary, either one can be used as there is an unambigous relationship between $\mathbf{R}$ and $\mathbf{Q}$.

Rather than having a single molecule in the interaction volume, the FEL is impinging at an ensemble of molecules. Hence, eq. (6.1) has to be multiplied by the number N of molecules in the interaction volume [1]. When the FEL focus is much smaller than the molecular beam (see fig. 6.1), the number density M of molecules in the molecular beam can be utilized rather than the absolute number of molecules [2]: The interaction volume V_0

[1] The relative positions of different molecules in the gas-phase ensemble are uncorellated. Hence, the diffraction pattern of the whole ensemble is assumed to be be the incoherent superposition of single-molecule diffraction patterns. Furthermore, the distances between different molecules are so large compared to the interatomic distances of the atoms within a particular molecule that interference between different molecules would result in sub-pixel interference features as will be argued below.

[2] The density M_{DIBN} of DIBN molecules is assumed to be around $M_{\mathrm{DIBN}} \approx 10^8$ cm^{-3} [195].

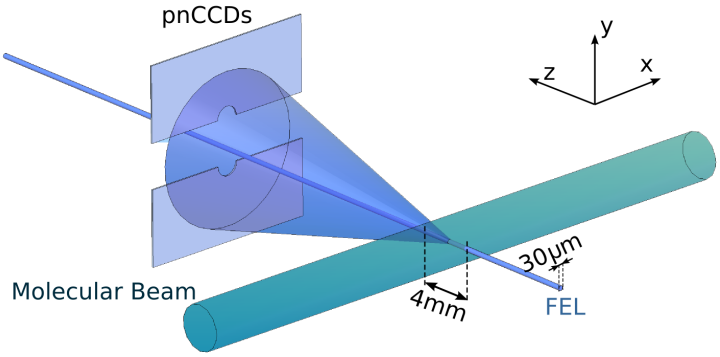

Figure 6.1.: Schematic layout of the scattering geometry used; see text for details.

of the x-rays and the molecular beam is given by the cross-sectional area of the incident FEL-beam A_0 times the length l of the interaction volume. A_0 is given by the beam waist of the FEL, which is $\omega = 30$ μm in the interaction point. The length l of the interaction volume is given by the diameter of the molecular beam, which is 4 mm, determined by the orifice of the last skimmer. Then, the number of molecules is $N = MV_0 = MlA_0$. Hence, the number of scattered x-ray photons into a single pixel at position $\mathbf{R}$ on the detector is

$$I_{sc} = \frac{|\mathbf{E}_{sc}|^2}{|\mathbf{E}_0|^2} \cdot M \cdot l \cdot R^2 \cdot \Delta\Omega \cdot I_0 \tag{6.2}$$

This can be easily understood by the following considerations. If the cross sectional area of the FEL is increased by a factor F and hence the total number of molecules in the FEL focus increases by F (while keeping the pulse energy, i. e., number of photons, constant), the x-ray flux and hence the scattering-probability-per-molecule decreases by F. Of course, this assumption breaks down, when multi-photon processes have to be considered at high intensities. Considerations about the ionization of DIBN in section 5.5 have shown, that multi-photon absorption is unlikely in this experiment. Since multiple scattering of a single 2 keV photon is even more unlikely than multi-photon absorption, the diffraction data can safely be assumed to be entirely due to single-scattering events.

Simulation of the diffraction pattern according to eq. (6.2) would yield the diffraction pattern of an ensemble of perfectly aligned molecules. However, the experimental diffraction pattern will be blurred with respect to the single-molecule diffraction pattern due to the finite degree of molecular alignment of the DIBN molecules. The diffracted intensity from a non-perfectly aligned molecular ensemble is obtained by the convolution of diffraction patterns of possible orientations with an alignment angular distribution $n(\theta)$. Here, θ is the angle between the most-polarizable axis of the molecule and the polarization of

the YAG laser. The exact form of $n(\theta)$ requires knowledge about the exact populations of all the pendular states populated in the laser field, which is very difficult to obtain. For strong alignment, however, an approximation of $n(\theta)$ is given by a gaussian [89]:

$$n(\theta) = \exp\left(-\frac{\sin^2\theta}{2\sigma^2}\right) \tag{6.3}$$

As a simplification, in the following the angle θ is taken to be the angle between the laser polarization and the iodine-iodine axis of the molecule, i. e., the small deviation of 7°, by which the most-polarizable axis deviates from the iodine-iodine axis was not considered. The rotation around the iodine-iodine axis as well as the rotation around the axis of the YAG laser polarization is assumed to be unhindered. As explained in chapter 5, the expectation values $\langle\cos^2\theta_{2\mathrm{D}}\rangle$ and $\langle\cos^2\theta_{3\mathrm{D}}\rangle$ characterize the degree of alignment. The approximation $\sigma^2 = 1 - \langle\cos^2\theta_{3\mathrm{D}}\rangle$, given in ref. 89, is only valid at high degrees of alignment. For the simulations described here, different angular distributions were obtained by utilizing different σ^2 values. The expectation values of $\langle\cos^2\theta_{2\mathrm{D}}\rangle$ and $\langle\cos^2\theta_{3\mathrm{D}}\rangle$, however, were obtained afterwards from the distribution $n(\theta)$ rather than being given as an input value to $n(\theta)$.

This results in a diffraction-intensity-per-molecule pattern which then is scaled with the molecular beam density M and the number of photons I_0, yielding the expected diffraction pattern for an ensemble of molecules with the parameters $M$and I_0 at a given degree of alignment. The simple approach of superposition of single-molecule diffraction patterns is justified by considering that the molecules in the molecular beam are in the gas phase and their positions are uncorellated. Hence, the total measured diffraction intensity $I_{\mathrm{sc}}(\mathbf{Q})$ on the pnCCD will be the incoherent superposition of single molecule diffraction events. Considering the interference of diffraction between two distinct molecules, one has to be aware that, on the one hand, the molecules are at many different distances with respect to each other, and, on the other hand, the intermolecular distances are so large compared to the interatomic distances within one molecule, that interference from two different molecules would result in very weak diffraction features at sub-pixel resolution on the pnCCD detector [3].

Considering all the issues mentioned above, simulations of diffraction patterns at the given

[3]Here, the term "resolution" is used in a different context than usual and means "resolution on the pnCCD detector", i. e., in reciprocal space. Interference of scattering from two different molecules is, in principle, possible as the transverse coherence length should be in the ≈ 10 μm-range (as measured at the SXR beamline [196], which is comparable to the AMO beamline at LCLS). However, as already stated this would result in very weak (due to the many different molecule-molecule distances), sub-pixel resolution interference features.

experimental geometry were performed in the following way: first, the ratio $(|\mathbf{E}_{sc}(\mathbf{R})|/|\mathbf{E}_0|)^2$ is calculated for 500 individual molecules, spatially distributed with $n(\theta)$. These ratio patterns were averaged in order to give the single-molecule ratio pattern. Then, this ratio pattern $(|\mathbf{E}_{sc}(\mathbf{R})|/|\mathbf{E}_0|)^2$ is multiplied by the factors M, l, R^2, $\Delta\Omega(\mathbf{R})$, and I_0, compare eq. (6.2).

Furthermore, the quantum efficiency of the pnCCD detector and the attenuation of the signal by the filters mounted in front of the pnCCD have to be considered. The quantum efficiency QE at a photon energy of 2 keV is QE = 0.87 [155]. Considering the pnCCD filters, as specified in chapter 3, the attenuation of x-rays derived from Lambert-Beer law depends on the scattering angle and is given by $F_{\text{Filter}} = \exp(-0.2139/\cos(2\Theta))$, where 2Θ is the angle between the FEL beam axis and the given position on the detector. The simulated intensities were multiplied by QE and F_{Filter}. I_0 were obtained from the beamline data at LCLS and the beamline transmission. Given $I_0 = 1.25 \cdot 10^{13}$ (4 mJ/pulse at 2 keV) and the beamline transmission of $\approx 35\%$, $4.375 \cdot 10^{12}$ photons/shot are expected in the interaction volume for the datasets that were evaluated in the data analysis. Eventually, one obtains the expected number of scattered photons in a given detector element at $\mathbf{R}$.

Figure 6.2 shows the expected number of scattered photons, scattered to a plane detector at a camera length of 71 mm for different degrees-of-alignment [4], for 565,000 shots ($4.375 \cdot 10^{12}$ photons/shot), and a molecular beam density of $M = 1.2 \cdot 10^8 \text{cm}^{-3}$. Each pixel is of size 75×75 μm^2. White rectangles mark the position of the pnCCDs in the experiment, each pnCCD panel contains 512×1024 pixels. Images a–d correspond to DIBN aligned with $\langle \cos^2 \theta_{2\text{D}} \rangle = 0.99$ (a), 0.83 (b), 0.71 (c), 0.5 (i. e., isotropic, d). The signal for 5,580 He (e) is the same as the DIBN signal at $\mathbf{Q} = 0$ [5]. The second row (f–j) shows the images of the first row, but at a different colorscale to illustrate interference features. The intensities are normalized to their maximum value and the fifth root is taken. The main interference feature, originating in the interference of the two iodines, is clearly visible in fig. 6.2 (f). However, the intensity of the first scattering maximum from the iodine-iodine interference drops to only $\approx 4\%$ of the scattering intensity at $\mathbf{Q} = 0$. Distances between all other pairs of atoms in DIBN are already smaller than the x-ray wavelength of 620 pm. Non-perfect alignment (g,h) significantly washes out the interference features at high angles and would limit the resolution in structure determination. A simple estimate of the alignment-limited resolution in dependence of the degree of alignment, the latter

[4] The schematic images of DIBN molecules at non-perfect alignment above fig. 6.2 (b–d) were created using a software application written by Mike Wesemann, FHI Berlin.

[5] The scattering intensity at $\mathbf{Q} = 0$ is simply the squared sum of the atomic scattering factors of all j atoms in DIBN, i. e., $I(\mathbf{Q} = 0) = (\sum_j f_j(\mathbf{Q} = 0))^2$.

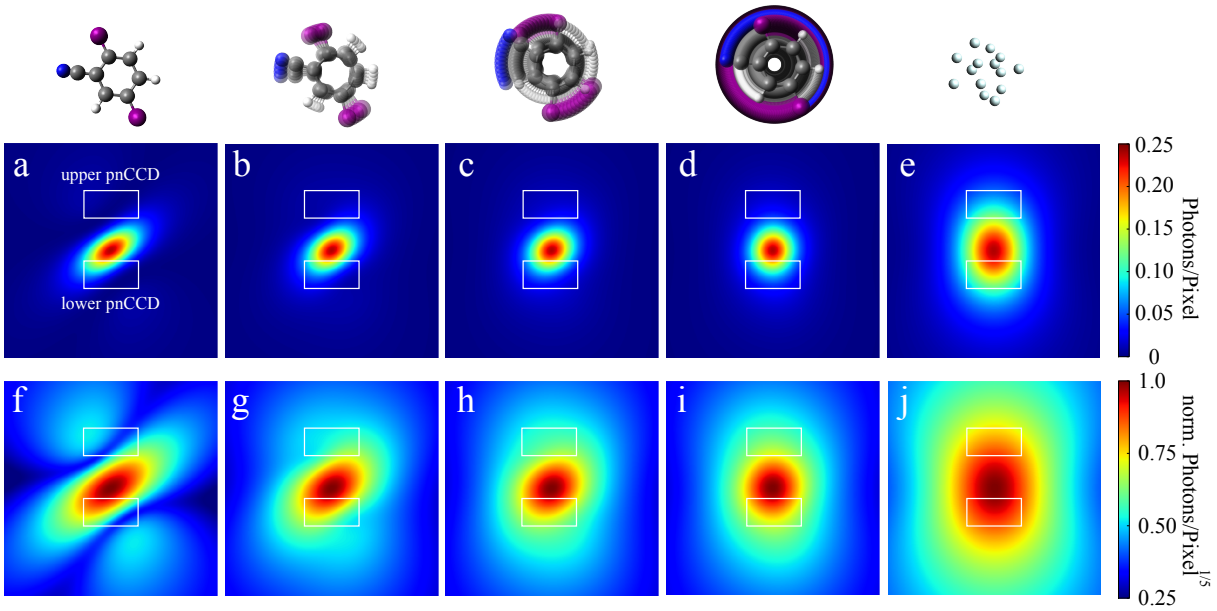

Figure 6.2.: Simulated scattering intensities for different degrees-of-alignment, scattered to a plane detector at a camera length of 71 mm for different degrees-of-alignment, for 565,000 shots ($4.375 \cdot 10^{12}$ photons/shot), and a molecular beam density of $M = 1.2 \cdot 10^8$ cm^{-3}. a–d correspond to DIBN aligned with $\langle\cos^2\theta_{2D}\rangle$= 0.99 (a), 0.83 (b), 0.71 (c), 0.5 (isotropic,d). The signal for 5,580 He (e) is the same as the DIBN signal at $\mathbf{Q} = 0$. To illustrate interference features, the second row (f–j) shows the fifth root of the normalized intensities of the first row.

measured in terms of $\langle\cos^2\theta_{3D}\rangle$, was given by Pabst et al. [193]. There, it is assumed that a non-perfectly aligned molecule librates within a cone and the opening angle of the cone is determined by $\langle\cos^2\theta_{3D}\rangle$, see [193, fig. 2]. The uncertainty of the atomic positions in the molecule and hence the alignment-limited resolution d_{coh} is simply given by $d_{\mathrm{coh}} \approx 2R\sqrt{1-\langle\cos^2\theta_{3D}\rangle}$ [193, eq. 43]. In this case, R is the distance from the center of the molecule to a certain atom. In the case of the iodine atom of DIBN, R = 350 pm, $\langle\cos^2\theta_{3D}\rangle$ =0.72 [6] and hence d_{coh} = 370 pm, which would be the best (alignment-limited) resolution of the iodine position when the diffraction data would be used for reconstructing the DIBN molecule.

In order to estimate, whether the main feature of the diffraction pattern, i. e., the iodine-iodine (I-I) interference, can be used to fit the I-I distance from the measured diffraction data, diffraction from DIBN was simulated involving different I-I distances. Figure 6.3 shows examples of simulated intensities for DIBN for the same parameters (M,

[6] The measured value of $\langle\cos^2\theta_{2D}\rangle = 0.84$, see chapter 5, corresponds to a value of $\langle\cos^2\theta_{3D}\rangle \approx 0.72$, assuming the gaussian approximation given in eq. (6.3).

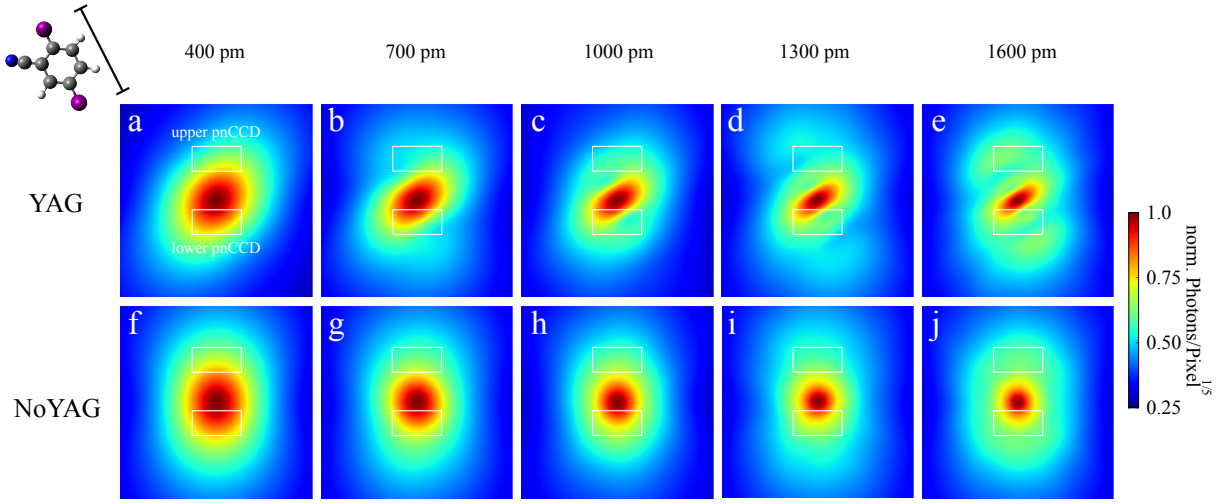

Figure 6.3.: Simulated scattering intensities for different I-I distances. Diffraction intensities are given for an aligned DIBN sample (upper row (a–e), "YAG", $\langle\cos^2\theta_{2D}\rangle = 0.83$) and an isotropic sample (lower row (f–j), "NoYAG", $\langle\cos^2\theta_{2D}\rangle = 0.5$).

number of shots, pixel size, geometry) as in fig. 6.2. The colorscale is the same as used in fig. 6.2 (f–j) to visualize the weak interference features. The rows labelled "YAG" and "NoYAG" correspond to two fixed degrees of alignment (YAG: $\langle\cos^2\theta_{2D}\rangle = 0.83$, NoYAG: $\langle\cos^2\theta_{2D}\rangle = 0.5$), but now at distinct I-I distances. The real distance is 700 pm (see, e. g., appendix B). These models were used for fitting the I-I distance from the measured diffraction data, see chapter 7.

7. X-ray Diffraction of Controlled Gas-Phase Molecules at LCLS

This chapter presents the results obtained from the coherent x-ray diffraction experiment on an ensemble of isolated 2,5-diiodobenzonitrile (DIBN) molecules in the gas phase performed at the Linac Coherent Light Source (LCLS). Details about the setup were explained in chapter 3. Here, only a brief description of the experimental setup is repeated. For the experiment, a few mbar of gas-phase DIBN, seeded in 50 bar of He, were supersonically expanded from a pulsed Even-Lavie valve into vacuum. An electrostatic deflector is used to spatially disperse molecules in distinct rotational quantum states and thereby select molecules in low rotational quantum states best suited for laser alignment. Laser alignment was achieved using the ns-long pulses from a Nd:YAG laser. Results from the spatial quantum-state selection and laser alignment of DIBN were presented in chapters 4 and 5. The ultrashort (100 fs (FWHM)) x-ray pulses of LCLS intersect the molecular beam and 2 keV x-ray photons, scattered from aligned DIBN molecules, from the backing gas He, from background gas, and from experimental devices such as, e. g., apertures, etc., were recorded by the pnCCD detector. The data evaluation of the x-ray diffraction data, and the presentation and discussion of the results is the content of this chapter.

7.1. Data Acquisition and Single Photon Counting

Single shot x-ray diffraction data was recorded by the pnCCD detector and saved to xtc-files. The xtc-files were accessed by the CFEL-ASG Software Suite (CASS) [161]. The diffraction images in this chapter presenting experimental results will be assigned the label "YAG" if the YAG was switched on (and DIBN molecules were aligned) or "NoYAG" in

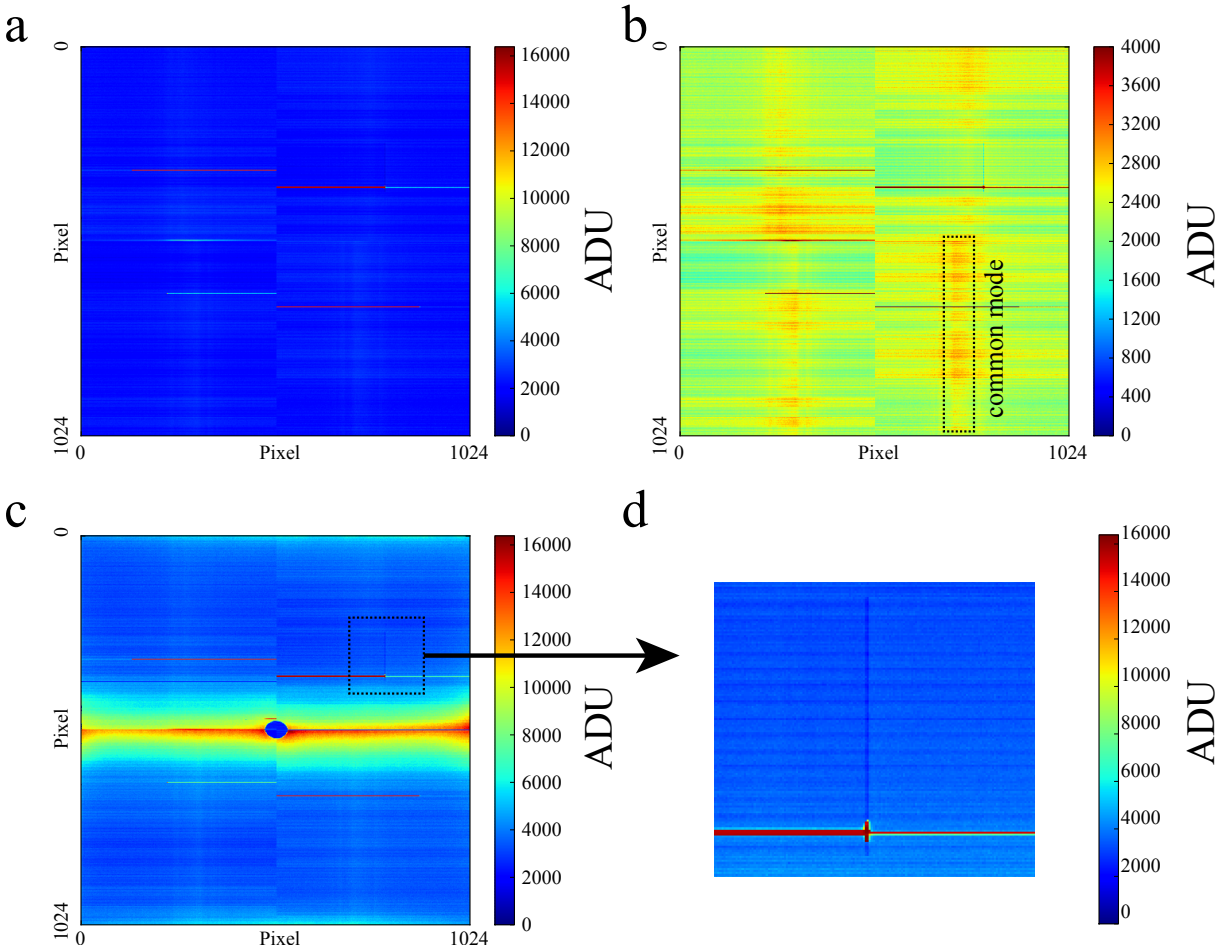

Figure 7.1.: Single shot raw data frames of an example dataset for the NoYAG case (a,b) and the YAG case (c,d). Subfigure b (d) shows details of a (c) to illustrate the various artifacts like common mode, bad pixel channels and gain variation of the 16 distinct CAMEX modules; see text for details.

case the YAG laser was switched off and DIBN molecules were randomly, i. e., isotropically distributed.

Figure 7.1 shows single shot pnCCD frames from an example dataset with YAG off (a) and on (c), respectively. The subfigures (b,d) illustrate details of the single shot frames. The single shot frames contain artifacts, which obviously don't originate from 2 keV photons scattered at the molecules from the molecular beam. Therefore, the single shot data frames have to be cleaned before single 2 keV photons can be extracted from them. As can be seen in fig. 7.1, a channel-to-channel variation along the horizontal direction as well as some broad stripes along the rows in vertical direction are visible. The former correponds to a channel-specific offset and gain variation. The latter is based on time-dependent

variations during the read-out of the signals, i. e., during the time when the charges are shifted from the center towards the corresponding CAMEX at the left and right edges (compare the pnCCD scheme shown in fig. 3.9). This is called "common mode" and best visualized at a different colorscale, see fig. 7.1 (b). Additional artifacts like channels with unusual high or even saturated values are visible. E. g., Figure 7.1 (d) shows a region of the YAG frame, where a channel of saturated values is visible along with a vertival row of unusual low signal. These "bad pixel" rows/channels were excluded from the analysis. A distinct feature of the YAG data is the severe background level, mainly concentrated within a broad horizontal stripe at the center and more narrow stripes at the outer edges of the pnCCD detector. These are based on insufficient shielding to NIR photons from the strong YAG laser, because the YAG laser propagates collinearly with the FEL and some regions of the pnCCDs were not thoroughly covered by filters.

The **C**FEL-**A**SG **S**oftware **S**uite (CASS) was used to access and "clean" the single shot pnCCD data, i. e., to correct for all artifacts and the background from the YAG. The procedure is described in a comprehensive way in appendix A, where figures of merit are given to judge the performance of each cleaning step. In the following, it will be outlined briefly.

First, the single shot data frames were corrected for the channel-dependent offset. This was done by subtracting an averaged data frame, acquired under "dark" conditions, i. e., with all lasers and the molecular beam turned off, from the individual single shot data frames. The subtracted frame will be referred to as "offset map". During the next step, the common mode correction was performed. Following that, after distinguishing YAG from NoYAG shots, i. e., single shot pnCCD data frames with YAG on and off respectively, the data was corrected for the YAG background scattering. This was done by subtracting a frame, obtained by averaging 1000 shots with YAG switched on, from the individual single shot YAG frame. Since the intensity from the YAG laser varied on a shot-to-shot basis, this background has to be scaled to match the total signal level of the individual single shot YAG frame it was subtracted of.

After this correction step, the single shot data in principle was cleaned for all artifacts but "bad pixel regions". In the following, CASS was used to find individual x-ray photon hits in the cleaned single shot data, considering the spreading of charge created by a 2 keV photon over more than a single pixel. This was taken into account by performing event-recombination, which works as follows: an algorithm in postprocessor-212 of CASS searched the single shot data row/column-wise. In case a single pixel exceeding the threshold of 500 ADU is encountered, a sub-procedure is started: adjacent pixels exceeding the same threshold are combined with the first pixel. I. e., their signal values are added to

the value of the first pixel while keeping track of the number of pixels that contributed to the hit so far. The number of pixels able to be combined to a single hit was limited to 6 and the sub-procedure terminated after this step at the latest. Then, the algorithm continoued searching the remaining rows/columns and performed the same sub-procedure in case it found a pixel exceeding 500 ADU. Photon hits, joined via this procedure, were written to an ASCII-list, containing the pnCCD coordinates (x,y) of the hit, its value in ADU and the number of pixels that the hit was combined of. Assignment of individual shot numbers to the photons hits is possible. The lists will be referred to as photon lists.

The photon lists were sorted according to whether the data was acquired with YAG on (YAG) or YAG off (NoYAG). All of the photon hits from the lists were histogrammed in order to give the 2d diffraction patterns for YAG and NoYAG, respectively. Based on these patterns, some additional processing of the photon lists was performed.

First, hits from some regions of the pnCCD had to be neglected for two reasons: Despite most of the bad pixel lines (channels/rows) were identified and subtracted by the offset map right at the beginning of the cleaning process, some pixels adjacent to these bad pixel lines show up with unusual high number of photon counts only after histogramming of the photon hits into 2d diffraction patterns (i. e., not in the single shot data). These channels/rows were neglected. Furthermore, even subtraction of the scaled averaged YAG frame in order to subtract the YAG background is, of course, not entirely successful and even the completely cleaned frames have a pixel-to-pixel variation mainly based in this YAG background subtraction. The pixel-to-pixel standard deviation σ_{Pixel} was calculated from ≈ 1000 completely cleaned frames. Pixels, where $3\sigma > 500$ ADU (i. e., the threshold from the event-recombination process, see above) were neglected, because hits in these pixels may originate from statistical fluctuations and may not be due to real photon hits. A map, showing all channels, rows, and regions that were excluded from the data analysis is shown in appendix A.

Secondly, only hits made up of at most 2 pixels were kept, as pixel hits made up of 3–6 pixels were concentrated to bad pixel lines. In the regions used for data analysis, 65 % are single pixel hits, 34 % are double pixel hits. The number of of 3-pixel-hits not concentrated in bad pixel lines is very small, i. e., < 1 %. 4–6 pixel hits are entirely concentrated in bad pixel lines. After considering all this, single- and double-pixel hits were corrected for channel-wise gain and charge transfer efficiency (CTE) and were histogrammed into 2d diffraction patterns as will be shown in the following.

7.2. Experimental Results

Data from coherent x-ray diffraction from aligned (condition "YAG") and randomly-distributed (condition "NoYAG") DIBN molecules was analyzed for 563,453 (YAG) and 842,722 shots (NoYAG) respectively. The YAG data was obtained with YAG polarization of α = -60° with respect to the horizontal plane. The duration of the FEL pulses was 100 fs (FWHM), its pulse energy in the interaction region was 1.4 mJ, corresponding to $4.375 \cdot 10^{12}$ photons/shot. In order to reduce multi-photon effects (such as radiation damage effects) to the diffraction data, the power was limited by moving the focus out of the interaction volume. In the interaction volume, the FEL beam waist is given by $\omega = 30$ μm resulting in a pulse power of $I_0 \approx 6.6 \cdot 10^{14}$ W/cm^2.

Figure 7.2 (a,b) show histograms of the single- and double-pixel photon hits in dependence of their pnCCD signal value (in ADU). The ADU value corresponds to the energy of

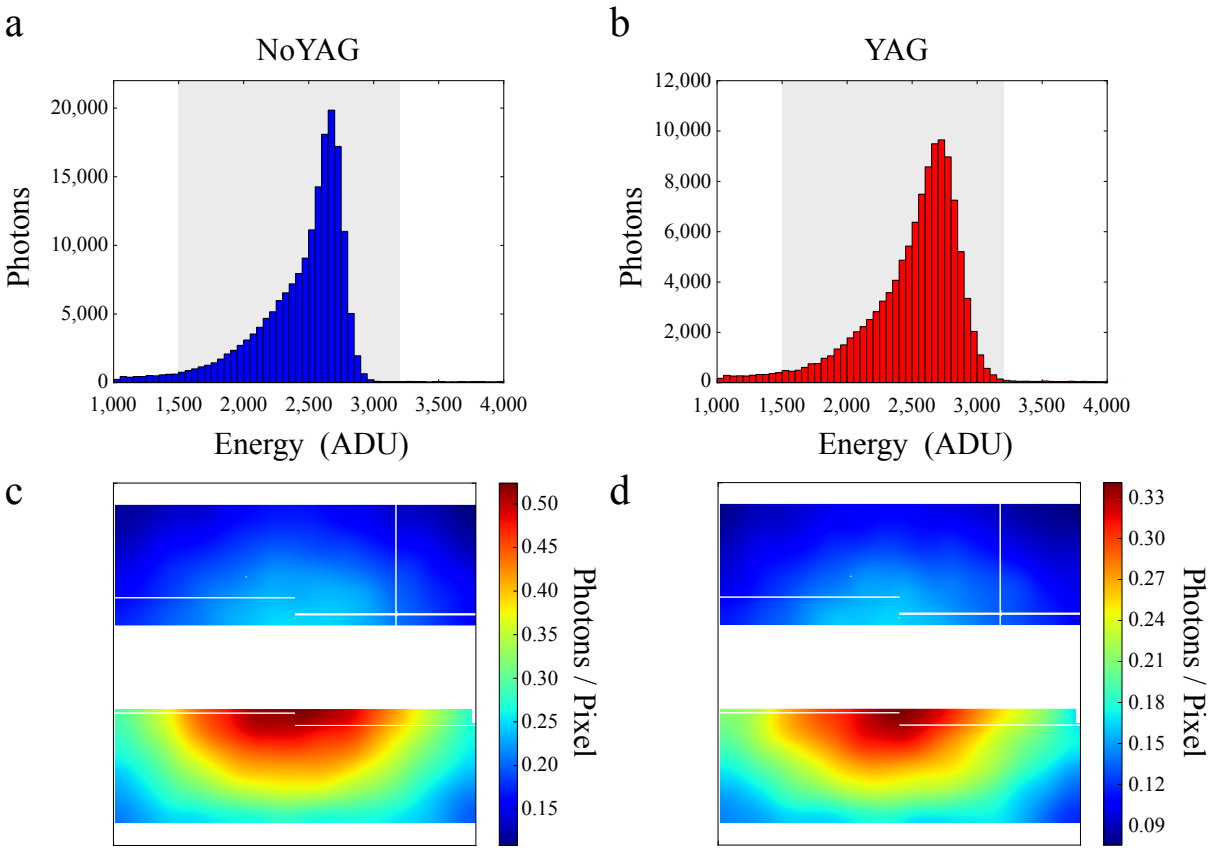

Figure 7.2.: Spectra of photon hits (a,b). Spatial distributions (I_{NoYAG}, I_{YAG}) of photon hits in the range of 1,500 – 3,200 ADU on the pnCCD, shown for the NoYAG (I_{NoYAG}, c) and YAG (I_{YAG}, d) case; see text for details.

the photon hits and therefore the histograms will be referred to as spectra. 2 keV photons are expected at a value of around 2,600 ADU and, as is obvious from fig. 7.2 (a,b), the spectra peak around this value. The width of the spectrum is determined by the photon energy jitter of LCLS, the energy resolution of the pnCCDs, the event-recombination process and the pixel-to-pixel variation of even fully cleaned frames. The latter is bigger for the YAG data frames (see appendix A), therefore the x-ray peak in the YAG case (fig. 7.2 (b) is broader than in the NoYAG case (a).

The semi-transparent boxes mark the energy intervall 1,500 – 3,200 ADU. The spatial distributions of all photon hits on the pnCCD detector for the NoYAG and YAG case in the energy range 1,500 – 3,200 ADU are shown in fig. 7.2 (c,d) in terms of photons-per-pixel. These images are the diffraction patterns and will be referred to by the terms "I_{NoYAG}" and "I_{YAG}" respectively. As mentioned above, the data was obtained from 842,722 shots (NoYAG) and 563,453 shots (YAG) respectively. It contains 172,499 (I_{NoYAG}) and 111,560 photons (I_{YAG}), hence the average hit rate was 0.204 photons/shot (NoYAG) and 0.198 photons/shot (YAG). Since many pixels don't contain any photon hit at all, the data frames shown in fig. 7.2 (c,d) were obtained by convolution of the photon distributions with a gaussian kernel of the width $\sigma_s = 0.07$ nm^{-1}.

The scattered photons don't entirely originate from scattering off DIBN or He in the molecular beam, but also from background scattering. Background scattering is due to scattering of 2 keV photons from either the residual gas in the chamber (i. e., mainly O_2, N_2, CO_2, and H_2O) or scattering of 2 keV photons from hardware devices in the chamber, such as, e. g., apertures inside the front light-baffle.

In fig. 7.3 (a) shows the measured background diffraction, obtained for 113,619 shots at a FEL pulse energy of 0.6335 mJ/shot ($1.98 \cdot 10^{12}$ photons/shot) with the molecular beam and all lasers but the FEL turned off. The data contains only 3,745 photons and hence is not a good approximation of the real background in the experiment exploiting diffraction from aligned DIBN. However, the contribution of the background is significant: scaled to the same FEL pulse energy and the same number of shots such as during recording of the diffraction data from aligned DIBN this would result in a background signal of 41,043 photons in the YAG case which corresponds to a background contribution of 36.7 %. With the same argument, one derives a contribution of 35.5 % in the NoYAG case. In principle, the background scattering from residual gas, i. e., from O_2, N_2, CO_2, and H_2O in the CAMP chamber can be simulated. Figure 7.3 (b) shows the simulated background from residual gas, considering the beampath from the front light baffle to the entrance of the back light baffle for the same FEL parameters as for the measured background. The density of the residual gas was obtained from the concentrations measured by the residual

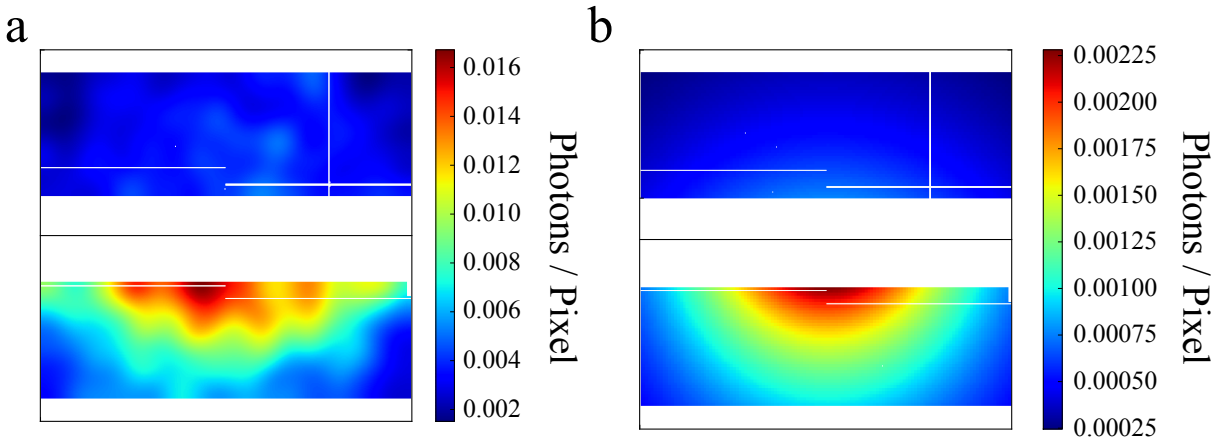

Figure 7.3.: (a) Measured background scattering of 2 keV photons recorded for 113,619 shots at a FEL pulse energy of 0.6335 mJ (photons/shot = $1.98 \cdot 10^{12}$) with the molecular beam and all lasers but the FEL turned off. (b) Simulated background (for the same FEL pulse energy and number of shots as in (a)), originating in scattering from residual gas along the beampath from the front light baffle to the entrance of the back light baffle.

gas analyzer (RGA). The simulated background contains only 516 photons, which is much less than the measured background (3,745 photons). In addition, the spatial distribution of the measured background is broader than the simulated background, which can be seen in particular on the bottom pnCCD panel. Hence, it can be concluded, that the experimental background doesn't entirely originate in scattering from residual gas only but may be also due to scattering from, e. g., apertures such as the apertures in the front light-baffle.

Since the background measurement is considered to be insufficient for a reasonable model of the background during the experiment, the strong contribution of the background to the YAG and NoYAG data and the fact, that the background cannot be simulated from residual gas scattering, the only reasonable way for the diffraction data to be analysed is in terms of the difference of the YAG and NoYAG data, i. e., I_{YAG} - I_{NoYAG}. This is named "diffraction difference", e. g., in ref. 46 and visualizes the interference features of coherent diffraction from aligned DIBN. It will be explained in the following.

7.3. Analysis of X-ray Diffraction Data

In order to analyse the experimentally obtained diffraction patterns, diffraction of aligned and not-aligned DIBN in combination with a strong background from the He seed gas was simulated. Figure 7.4 shows simulated diffraction patterns for the parameters of the experiment, i. e., for 563,453 shots like in the YAG case, and $4.375 \cdot 10^{12}$ incident photons/shot. The molecular beam density of DIBN is $M = 10^8$ cm^{-3}. The degree of alignment of DIBN in the YAG case was $\langle \cos^2 \theta_{2D} \rangle = 0.83$ with the YAG polarisation at $\alpha = -60°$. The first row (a,b) shows the scattering intensity for DIBN only. White rectangular frames mark the position of the top and bottom pnCCD panel in the experiment. The second row (c,d) shows the scattering intensity of DIBN (like in a,b), but with a strong background of He added. The ratio is He/DIBN = 14,000. This amount of He was chosen to match the total measured intensity while keeping the molecular beam density M of DIBN at $M = 10^8$ cm^{-3}. In the experiment, the amount of He is certainly lower, compare the discussion about the background given above. The value of 14,000 He/DIBN was chosen in order to mimic an isotropic background contribution by He. In the lower row (e,f), the simulated intensities in the NoYAG and YAG case in the regions covered by the pnCCD panels are shown. The alignment of DIBN with $\langle \cos^2 \theta_{2D} \rangle = 0.83$ results in a slight shift of the 0$^{\text{th}}$-order scattering maximum towards the left with respect to the center. However, the shift is hardly visible due to the strong He background. The anisotropy in the YAG case can be visualized best by plotting the difference of both diffraction patterns, i. e., I_{YAG}-I_{NoYAG}. In this case, the exact amount of He and the background becomes obsolete as these are assumed to be the same in the YAG and NoYAG case and cancel out by calculating I_{YAG}-I_{NoYAG}.

Figure 7.5 shows the diffraction difference I_{YAG}-I_{NoYAG} of the simulated scattering intensities I_{YAG} ($\langle \cos^2 \theta_{2D} \rangle = 0.83$) and I_{NoYAG} ($\langle \cos^2 \theta_{2D} \rangle = 0.5$) for different molecular beam densities M of DIBN, i. e., $M = 0.8 \cdot 10^8$ cm^{-3} (left column), $M = 1.0 \cdot 10^8$ cm^{-3} (center column), $M = 1.2 \cdot 10^8$ cm^{-3} (right column). The first row (a–c) shows the I_{YAG}-I_{NoYAG} image for a large part of reciprocal space while the second row only shows the regions covered by the pnCCDs. The most prominent interference features are the 1$^{\text{st}}$-order minima along the YAG alignment axis of $\alpha = -60°$ and the 0$^{\text{th}}$-order maximum perpendicular to them. These interference features are most pronounced on the bottom pnCCD panel (which is closer to the interaction point than the top pnCCD). The lower row (g–i) visualizes the angular anisotropy along the azimuthal angle α in the I_{YAG}-I_{NoYAG} images of the lower pnCCD panel (d–f). Comparing the distinct columns, it can be seen, that the molecular beam density M changes the contrast in the I_{YAG}-I_{NoYAG} images, but does not alter the spatial distribution.

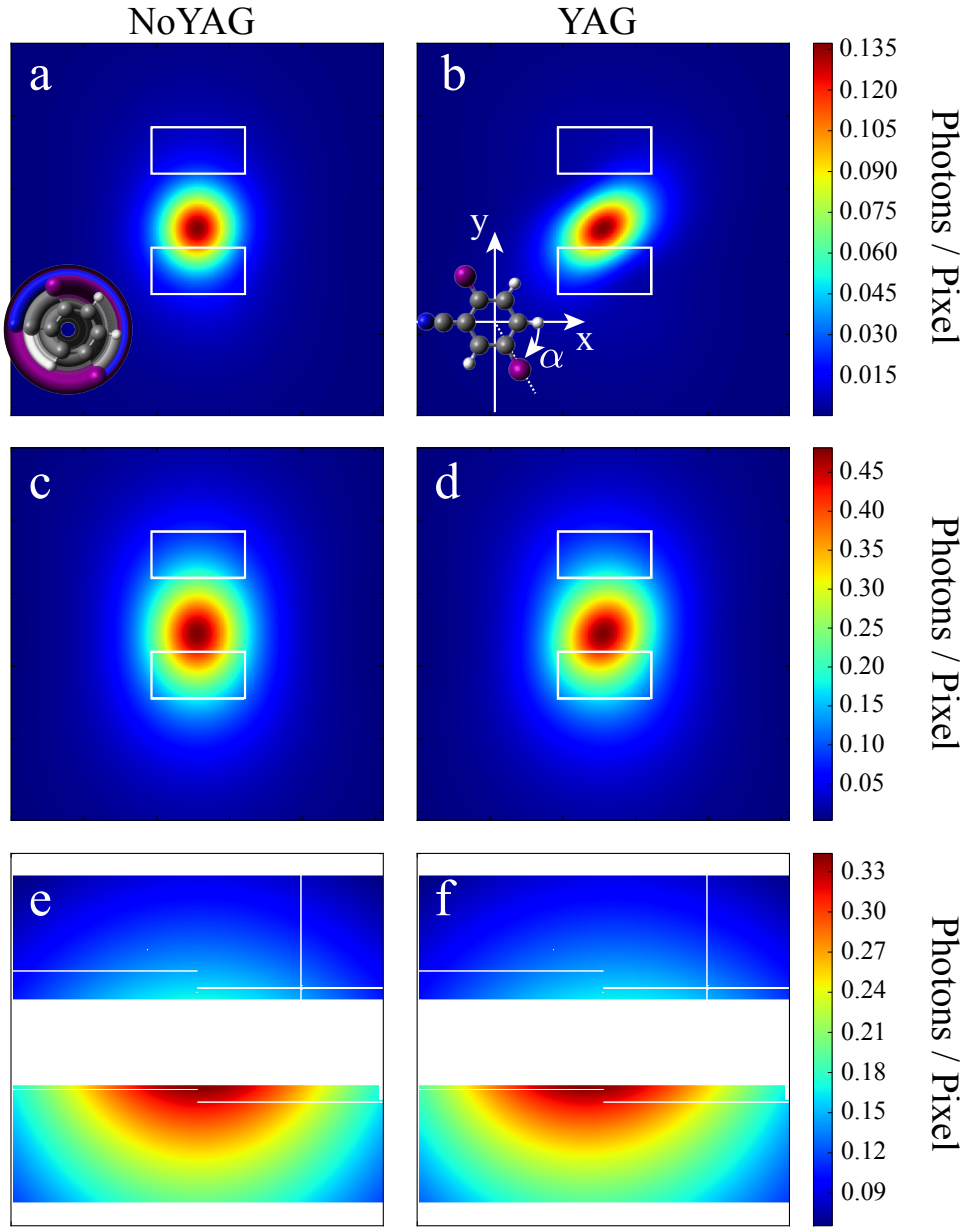

Figure 7.4.: Simulated data of DIBN for not-aligned (NoYAG) and aligned molecules (YAG, $\langle\cos^2\theta_{2D}\rangle = 0.83$, YAG-polarisation $\alpha = -60°$) with FEL parameters as in the experiment (563,453 shots, $4.375 \cdot 10^{12}$ incident photons/shot). The molecular beam density for DIBN is $M = 10^8$ cm^{-3}. (a,b) show diffraction of DIBN only, (c,d) show diffraction of DIBN with a strong scattering background of He added to the diffraction from DIBN (He/DIBN = 14,000). The white rectangular frames mark the position of the pnCCD panels in the experiment. (e,f) show the simulated intensities in the regions covered by the pnCCD panels, i. e., the regions inside the white frames of (c,d).

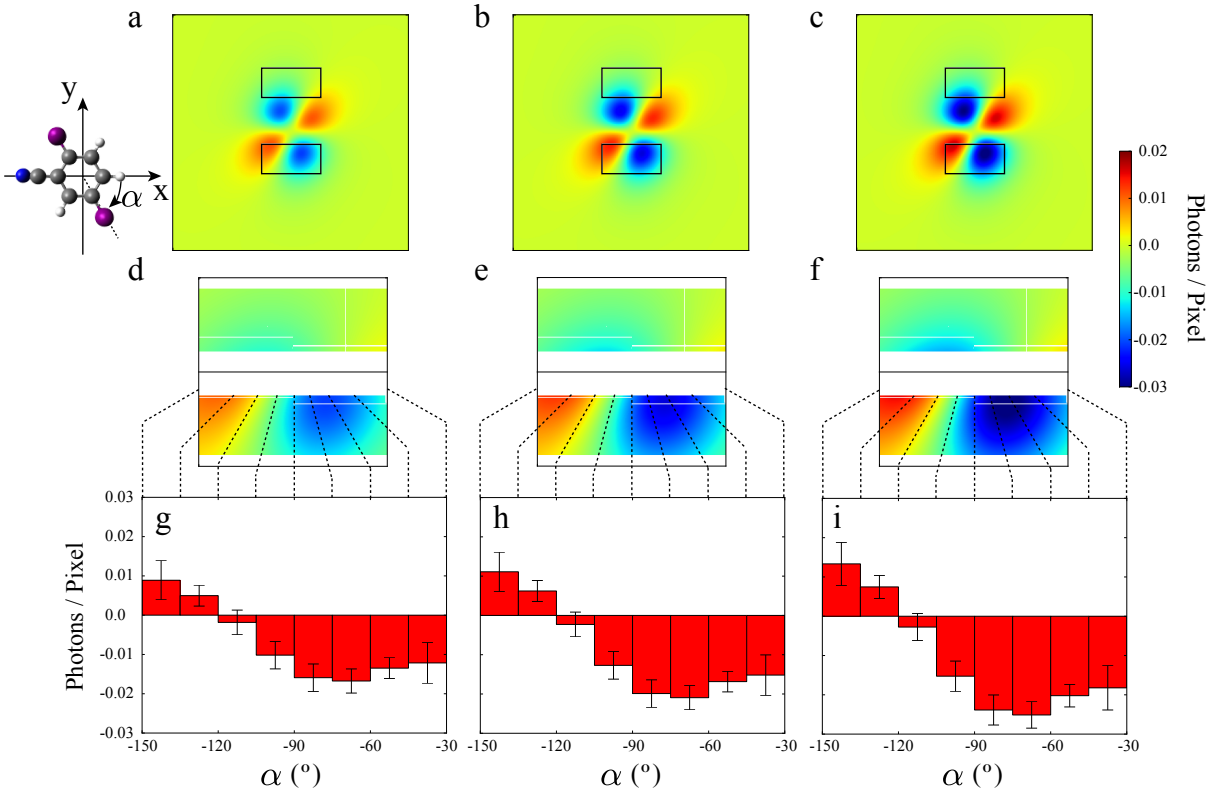

Figure 7.5.: "Diffraction difference" I_{YAG}-I_{NoYAG} of the simulated I_{YAG} ($\langle\cos^2\theta_{2D}\rangle = 0.83$) and I_{NoYAG} ($\langle\cos^2\theta_{2D}\rangle = 0.5$) scattering intensities for different molecular beam densities M of DIBN for $M = 0.8 \cdot 10^8$ cm^{-3} (left column), $M = 1.0 \cdot 10^8$ cm^{-3} (center column), $M = 1.2 \cdot 10^8$ cm^{-3} (right column). The first row (a–c) shows the I_{YAG}-I_{NoYAG} distribution for a large part of reciprocal space while the second row shows the I_{YAG}-I_{NoYAG} distribution in the regions covered by the pnCCDs. The interference features (i. e., the 0^{th}-order-maximum and 1^{st}-order minimum) are most pronounced on the bottom pnCCD panel, which is closer to the FEL beam axis than the top pnCCD. The lower row (g–i) visualizes the angular anisotropy in dependence of the azimuthal angle α in the I_{YAG}-I_{NoYAG} images.

Figure 7.6 shows the diffraction-difference I_{YAG}-I_{NoYAG} of the experimental data (right column, b,d) in comparison with theory (left column, a,c, $M = 0.8 \cdot 10^8$cm^{-3}). The errorbars correspond to the statistical error σ from the I_{YAG}-I_{NoYAG} subtraction ($\sigma = \sqrt{I_{YAG} + I_{NoYAG}}$), assuming Poisson-distributed noise. The difference is statistically significant, i. e., above experimental noise, and the contrast, compared to fig. 7.5 (g), corresponds to a molecular beam density in the range of $M \approx 0.8 \cdot 10^8$cm^{-3}.

Utilizing the difference I_{YAG}-I_{NoYAG} has the advantage that the scattering background from the seed gas He, the atomic scattering background from all individual atoms of DIBN (the "atomic scattering", which is always isotropic and hence does not change with

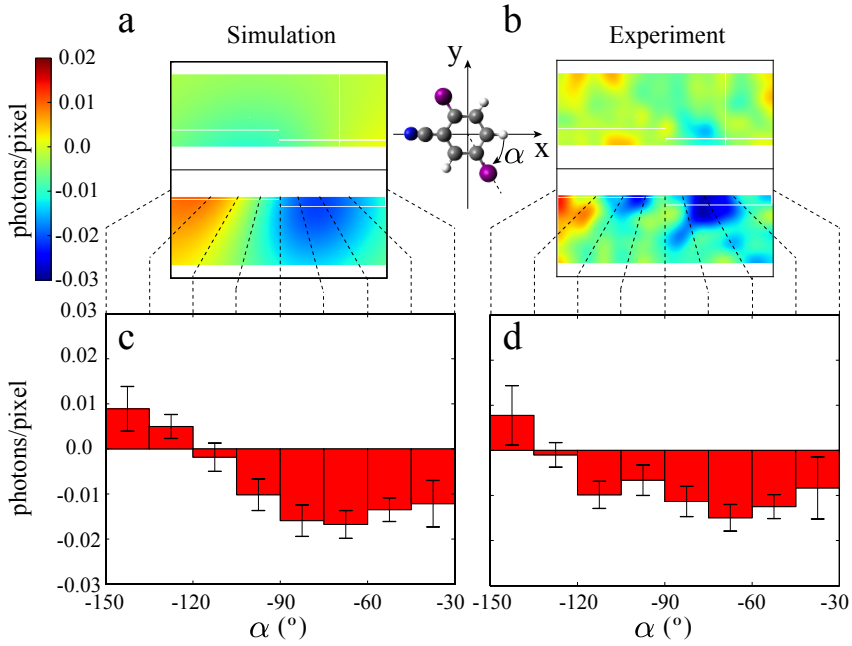

Figure 7.6.: Diffraction-difference I_{YAG}-I_{NoYAG} of the experimental data (right column) in comparison with theory (left column, $M = 0.8 \cdot 10^8 \mathrm{cm}^{-3}$). The difference I_{YAG}-I_{NoYAG} shows the same features like the simulation.

alignment) and the poorly measured experimental background (see above) are completely subtracted as these can be assumed to be identical in the YAG and NoYAG case. Hence, the diffraction-difference pattern I_{YAG}-I_{NoYAG} contains only the diffraction information from the interferences between the diffracted waves scattered at the distinct atoms, i. e., the "molecular scattering" (see ref. 46) of DIBN.

Up to here, it was confirmed, that the proposed approach of using an ensemble of quantum-state selected, and laser-aligned molecules in the gas-phase is able to produce a diffraction signal from aligned molecules, which is statistically significantly different compared to the diffraction signal of randomly (i. e., not-aligned) distributed molecules.

The strongest interference features in the diffraction pattern are due to the iodine-iodine interference. In the following it will be examined whether the obtained diffraction data can be used to reproduce the iodine-iodine (I-I) distance of $l_{iod} = 700$ pm. In fig. 7.7, the diffraction-difference I_{YAG}-I_{NoYAG} is shown for simulated data with the I-I distance l_{iod} varied while keeping the positions of the other atoms fixed. When l_{iod} is increased, the features along the alignment direction (i. e., the I-I axis) are squeezed as expected. Since the 1st scattering maximum of the I-I interference is not covered by the pnCCD (for $l_{iod} = 700$ pm) at all, shifting of the 1st-order minimum along the direction of the alignment

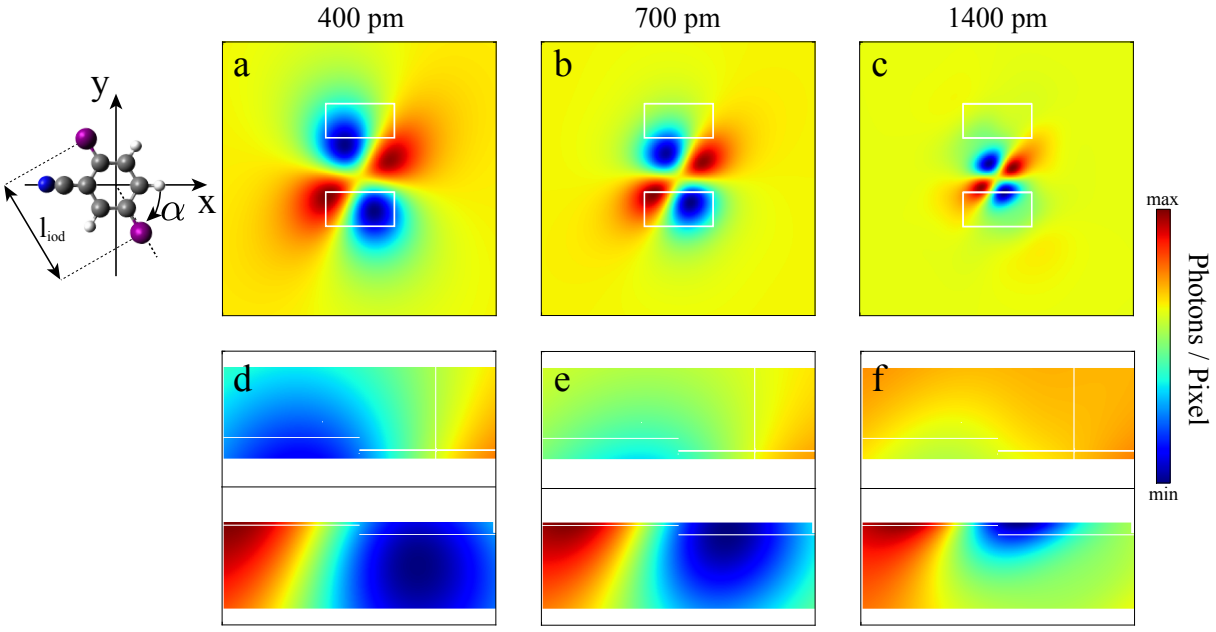

Figure 7.7.: Diffraction difference I_{YAG}-$I_{NoYAG}$of simulated data for different iodine-iodine distances l_{iod} of 400 (left column), 700 (center column), and 1400 pm (right column).

axis is the most remarkable feature changing in the diffraction-difference pattern.

Figure 7.8 shows the diffraction-difference I_{YAG}-I_{NoYAG} in a different representation. The x,y-coordinates were transformed to s, α-coordinates, where $s = \sin\Theta/\lambda$ is the scattering vector (or: wavevector transfer) and α is the azimuthal angle. Due to the twofold symmetry of the diffraction pattern for rotations about the z-axis, the upper pnCCD was rotated by 180° and "connected" to the bottom edge of the lower pnCCD, thereby extending the range of s-values. Due to the masking of pnCCD regions during the generation of photon hit lists, the regions of the two pnCCD panels, where the diffraction data is recorded, do not overlap. When varying the I-I distance, the most significant change in the I_{YAG}-I_{NoYAG} pattern is the shifting of the 1st diffraction minimum originating from the I-I interference. Since this effect is most pronounced along the alignment direction, the intensity distribution $I(s)$ of I_{YAG}-I_{NoYAG} along the alignment direction, i. e., along $\alpha = -60°$, is compared with the simulated I_{YAG}-I_{NoYAG} patterns.

Therefore, the 1-dimensional $I(s)$ curve is obtained by dividing the s-range into 20 bins and plotting the averaged intensity of the I_{YAG}-I_{NoYAG} pattern along s, averaged within each s-interval and between the azimuthal range of $\alpha \in [-70°, -50°]$. The azimuthal range is marked by dashed red rectangular frames in fig. 7.8. The range of α-values was restricted to this range (i. e., not the whole range of α-values was considered), because shifting of the 1st-order minimum along the direction of the alignment axis (i. e., along $\alpha = -60°$)

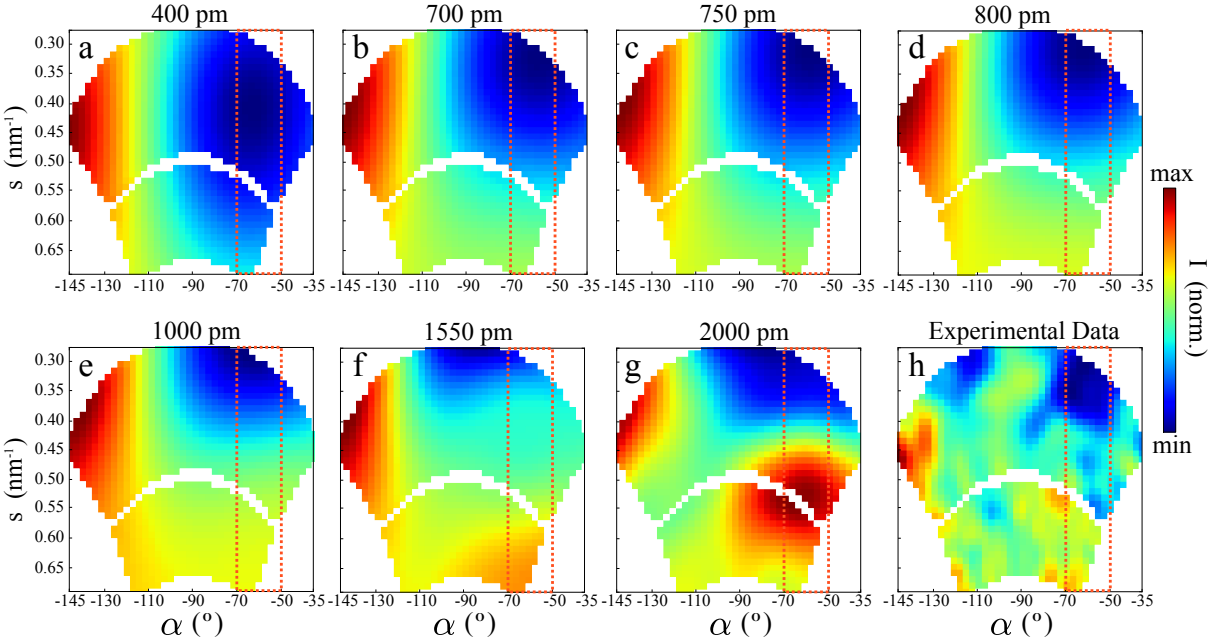

Figure 7.8.: Diffraction difference I_{YAG}-I_{NoYAG}in the s, α-representation for simulated and experimental data. The simulated data shows the diffraction-difference I_{YAG}-$I_{NoYAG}$for I-I distances of 400 (a), 700 (b), 750 (c), 800 (d), 1000 (e), 1550 (f), and 2000 pm (g). The experimental data is shown in (h). The dashed red frames mark the azimuthal range $\alpha \in [-70°, -50°]$ along which the $I(s)$ graph is obtained.

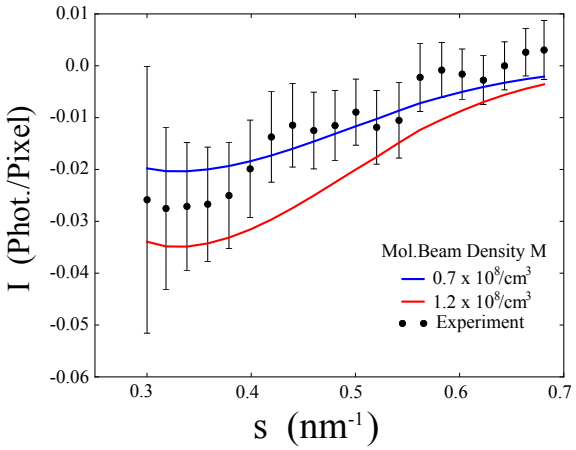

Figure 7.9.: $I(s)$ line profile of the diffraction difference I_{YAG}-I_{NoYAG} for simulated and experimental data along the alignment-direction, $\alpha = -60°$. The simulated data graphs show $I(s)$ for simulations at fixed I-I distance of $l_{iod} = 700$ pm with varying molecular beam density M, which is responsible for the contrast of the I_{YAG}-I_{NoYAG} image, but does not alter the qualitative slope of the $I(s)$ curves.

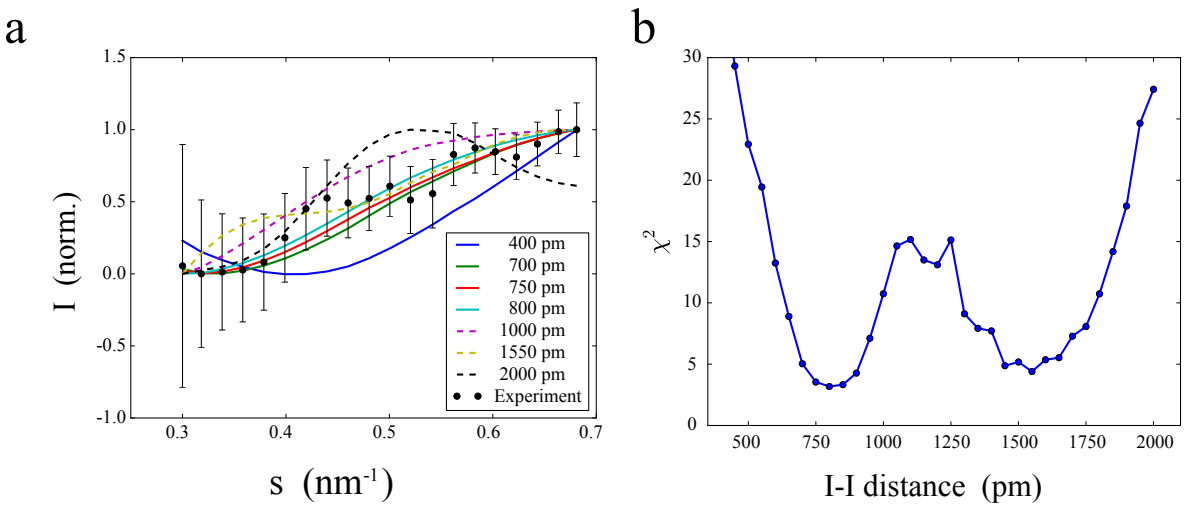

Figure 7.10.: (a) $I(s)$ line profile of the diffraction difference I_{YAG}-I_{NoYAG} for simulated and experimental data along the alingment direction (i. e., the YAG polarisation along $\alpha = -60°$). All graphs were normalized to their maxima in order to be independent of M. The simulated graphs correspond to the different I-I distances shown in fig. 7.8. (b) Test statistic χ^2 in dependence of the I-I distance. The minimum χ^2-value ($\chi^2 = 3.16$) is obtained for 800 pm.

is the most remarkable feature and shows the most significant change when changing the I-I distance. Figure 7.9 shows $I(s)$ line profiles for simulated data at fixed I-I distance of 700 pm with varying molecular beam density M along with the experimentally recorded data. Comparing the simulated data curves, it is clearly visible, that the molecular beam density M is responsible for the contrast, i. e., the "depth" of the minimum in the I_{YAG}-I_{NoYAG} image, but does not alter the qualitative shape of the $I(s)$ curves.

In fig. 7.10 (a), the $I(s)$ line profiles of the diffraction difference I_{YAG}-I_{NoYAG} for simulated and experimental data along the alingment-direction $\alpha = -60°$ are shown. All graphs were normalized to their maxima in order to be independent of the certain molecular beam density M. The simulated graphs correspond to the different I-I distances shown in fig. 7.8. The best fit of a certain simulated model to the experimental data can be found using a least-squares approach by determination of the test statistic χ^2 for each model [197]. The test statistic χ^2 is calculated for each model by summing up the squared deviations $(I_{exp} - I_{th})^2$ of a particular model $I_{th}(l_{iod})$ and the data I_{exp} for all 20 bins. Hence for a particular model of the I-I distance l_{iod}, χ^2 is obtained by the following formula:

$$\chi^2(\mathrm{l_{iod}}) = \sum_{i=1}^{20} \frac{(I_{\mathrm{exp},i} - I_{\mathrm{th},i}(\mathrm{l_{iod}}))^2}{\sigma_i^2} \tag{7.1}$$

The uncertainties σ_i^2 in each bin are given by the uncertainty of the $\mathrm{I_{YAG}}$-$\mathrm{I_{NoYAG}}$ subtraction (i. e., $\sigma_i = \sqrt{\mathrm{I_{YAG},i} + \mathrm{I_{NoYAG},i}}$). Figure 7.10 (b) shows the obtained χ^2-values in dependence of the particular model for $\mathrm{l_{iod}}$. The minimum χ^2-value ($\chi^2 = 3.16$) is obtained for 800 pm, which is close to the known I-I distance of 700 pm. For values around 1550 pm, low χ^2-values are obtained, too. A closer look to fig. 7.9 (a) reveals, that the experimentally obtained values in the range $s = 0.4 - 0.45$ nm^{-1} are higher than they should be according to, e. g., the model for $\mathrm{l_{iod}} = 700$ pm and hence are better fitted by, e. g., the models of $\mathrm{l_{iod}} = 1550$ pm, although models for 700 pm and 1550 pm are both within the statistical uncertainties. Hence, despite the left-right asymmetry being reproduced well by the data (compare figs. 7.5 and 7.6), the main structural feature, i. e., the I-I distance, could not unambigously fitted from the noisy data. This will be improved in future experiments by the collection of more diffraction data and extension of the range of s-values covered by the detector. Beside the noise, the resolution is a problem as well: The bottom pnCCD panel didn't cover the 1$^{\mathrm{st}}$ maximum at all, even the 1$^{\mathrm{st}}$ minimum is only partly covered. Hence, fitting the simulation to the model means fitting a slope without any peak to the data. Only the simulated models for very small or very large I-I distances give a very bad fit and can be ruled out, because they either fully cover peaks, i. e., either the 1$^{\mathrm{st}}$ minimum (see, e. g., fig. 7.8(a)) or the maximum (fig. 7.8(g)) and certainly neither of these peaks is present in the measured data.

In future experiments of this kind, but utilizing improved resolution which results in many more features (maxima/minima) to be present in the measured diffraction patterns, fitting to simulated models or even phase-retrieval (i. e., starting to deduce the structure without any prior knowledge from the diffraction pattern alone) will be feasible.

7.4. Radiation Damage

The question arises, whether radiation damage effects due to the intense FEL pulses influence the diffraction pattern. Recent experiments at LCLS, exploiting inner-shell ionization of the small molecule methylselenol (CH_3SeH), point at a significant (> 0.1 nm) displacement of the heavy atom (Se, Z = 34), occuring already during the fs-long XFEL-pulse [198]. Although methylselenol and DIBN cannot be compared easily, since iodine (Z = 53) is heavier than Se and the ionization pathways and XFEL pulse properties are different, radiation damage, occuring already during the XFEL pulse and its effects on

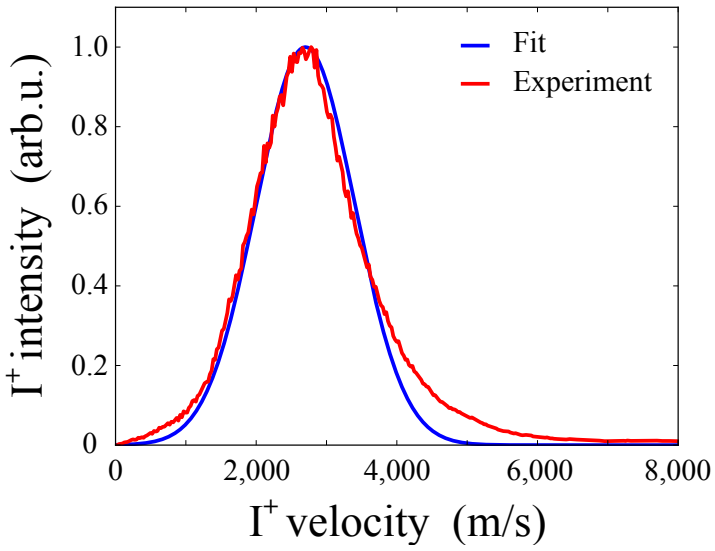

Figure 7.11.: Velocity distribution v_{I^+} of I^+ ions of upon ionization by the FEL, obtained by a 1d-cut of the 2d-momentum distributions of I^+. The distribution can be approximated with a Gaussian with mean $\overline{v}$ = 2,700 m/s and σ_v = 700 m/s.

diffractive imaging have to be considered. Here, the effect of radiation damage on diffractive imaging is discussed in terms of a purely mechanical model of atomic displacements upon ionization by the x-rays.

As pointed out in chapter 5, half of the DIBN molecules were ionized by the FEL pulse. This estimate was based on considerations involving photoabsorption cross-sections and assuming only single-photon absorption per DIBN molecule. The diffraction pattern of fragmenting DIBN looks different from the diffraction pattern of intact DIBN. Here, the influence of scattering from fragmenting DIBN on the diffraction pattern is discussed in terms of an effective spatial distribution of the two main scattering centers, i. e., the two iodine atoms, "seen" by the FEL.

Figure 7.11 shows the velocity distribution v_{I^+} of I^+ ions upon ionization by the FEL. It was obtained by a 1d-cut of the 2d-momentum distributions of I^+ shown in chapter 5. The distribution peaks at 2,700 m/s and can be approximated by a Gaussian with mean $\overline{v}$ = 2,700 m/s and σ_v = 700 m/s. Since one is interested in the relative velocity of the two iodines in the lab frame, i. e., rather than in the velocity of I^+, for simplicity it is assumed that, upon absorption of a 2 keV photon and subsequent ionization, DIBN fragments into I^+ and $C_7H_3IN^{n+}$ [1]. Since momentum conservation is valid (and considering the masses of I^+ and $C_7H_3IN^{n+}$ being 126.9 u and 228.01 u, respectively), the recoil velocity

[1] Considerations about the charge distribution of DIBN can be found in section 5.5.

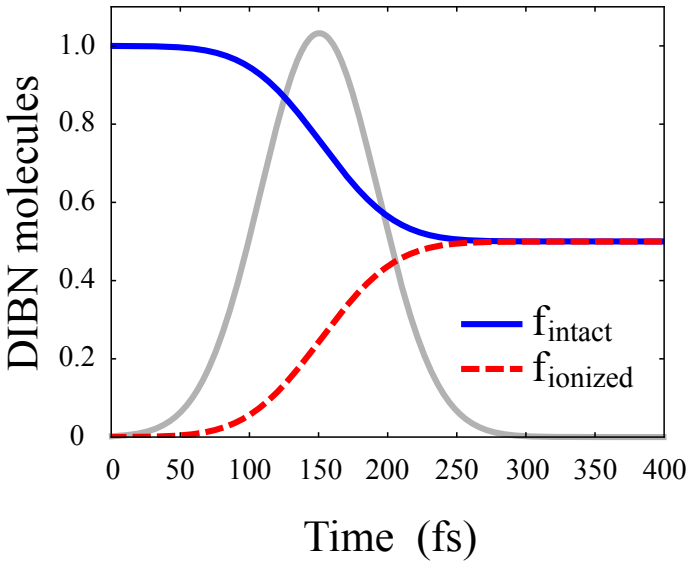

Figure 7.12.: The fractions of intact (i. e., unharmed by the XFEL pulse, solid-blue) and ionized (dashed-red) DIBN over the length of the pulse. The intensity $I_{\mathrm{FEL}}(t)$ of a 100 fs (FWHM) Gaussian pulse, which approximates the FEL pulse from the experiment, is given (without scale) by the grey solid line.

distribution of $C_7H_3IN^{n+}$ (in the center-of-mass frame) should peak at 1,500 m/s. This yields a velocity distribution v_{ions} of the relative velocity of I^+ with respect to $C_7H_3IN^{n+}$ with $\overline{v} = 4{,}200$ m/s and $\sigma_v = 1{,}090$ m/s.

This, of course, is an approximation. A detailed model of the movement of ionic fragments is very difficult to obtain. First, the time for acceleration of the fragments as well as the time for ionization (i. e., the finite delay due to Auger decay and subsequent charge rearrangement) after a 2 keV photon was absorbed by a DIBN molecule has not been taken into account; instead, instant ionization after absorption is assumed with the I^+ ions starting already with the final velocity. By this, the displacement is overestimated, i. e., in reality it is lower due to a finite ionization time and gradual velocity increase of the fragments. However, the dynamic behaviour depends a lot on where the charges are located. Assuming one fragment is I^+, then the exact location of the residual charge at $C_7H_3IN^{n+}$, which strongly influences the recoil of the ionic fragments, is not known. Furthermore, only the velocity distribution of I^+ was measured. The measurement (or modelling) of the velocity distributions of all ions/fragments would be necessary, though. For all these reasons, the following discussion is restricted to the model case given above, i. e., utilizing a constant relative velocity distribution described by a mean of $\overline{v} = 4{,}200$ m/s and a width of $\sigma_v = 1{,}090$ m/s.

In the following, the velocity distribution is utilized in order to estimate an effective spatial distribution of the I-I distance "seen" by the FEL pulse in small time steps during the pulse. In fig. 7.12, the fractions of intact (i. e., unharmed by the FEL pulse) and ionized DIBN over the length of the pulse are plotted. The intensity $I_{\mathrm{FEL}}(t)$ of the 100 fs (FWHM) Gaussian XFEL pulse is given (without scale) by the grey solid line [2]. The effective I-I distance distribution S seen by all photons in the FEL pulse is now derived in the following way: At each time t_i in fig. 7.12, the effective spatial distribution $s(t_i)$ seen by the fraction $I_{\mathrm{FEL}}(t_i)$ of photons is calculated, normalized to 1 and then multiplied by $I_{\mathrm{FEL}}(t_i)$. $s(t_i)$ at each time t_i depends on all timesteps $t_j < t_i$ before at which a fraction of molecules was ionized and started to recoil with the given velocity distribution. Therefore, $s(t_i)$ is given by the following formula:

$$s(t_i) = I_{\mathrm{FEL}}(t_i) \int_0^{t_i} v_{\mathrm{ions}}(t_i - t_j) \cdot f_{\mathrm{ionized}}(t_j) + f_{\mathrm{intact}}(t_j) dt_j \tag{7.2}$$

where $f_{\mathrm{ionized},j}$ and $f_{\mathrm{intact},j}$ are the fractions of molecules that are ionized and intact at time t_j respectively, see fig. 7.12. As mentioned above, the onset of Coulomb explosion is assumed to happen instantly upon absorption of a 2 keV photon, neglecting the finite delay due to Auger decay and subsequent charge rearrangement within the DIBN molecule. This is of course a "worst case approximation" which rather overestimates the distance of the fragmenting ions. The complete effective spatial distribution S seen by the whole FEL pulse is just the sum over all t_i:

$$S = \int s(t_i) dt \tag{7.3}$$

Figure 7.13 (a) shows a histogram of S, visualizing the fraction of molecules in different distance intervals, seen by the FEL pulse. The cumulative distribution (for smaller stepsize in I-I-distance) is given in fig. 7.13 (b), which can be understood as follows: 75 % of the elastically scattered photons originate from scattering at intact molecules (i. e., I-I-distance of 700 pm), while 90 % (95 %) of the scattered photons originate from scattering of molecules corresponding to I–I distances that are less than 200 pm (330 pm) longer than the equilibrium distance. While these damaged molecules might contribute to the experimentally determined elongated I-I distance of 800 pm in the minimum of the χ^2-fit, these effects cannot be fully resolved in the current experiment with 620 pm wavelength radiation, since the signal-to-noise ratio is not sufficient enough and the range of s-values (scattering vectors) covered is too small, i. e., the features in the diffraction pattern are

[2] Nominally 150 fs pulses (the duration was given by the LCLS machine data in the experiment presented here) rather correspond to 100 fs (FWHM) photon pulses [153], as discussed already in chapter 3

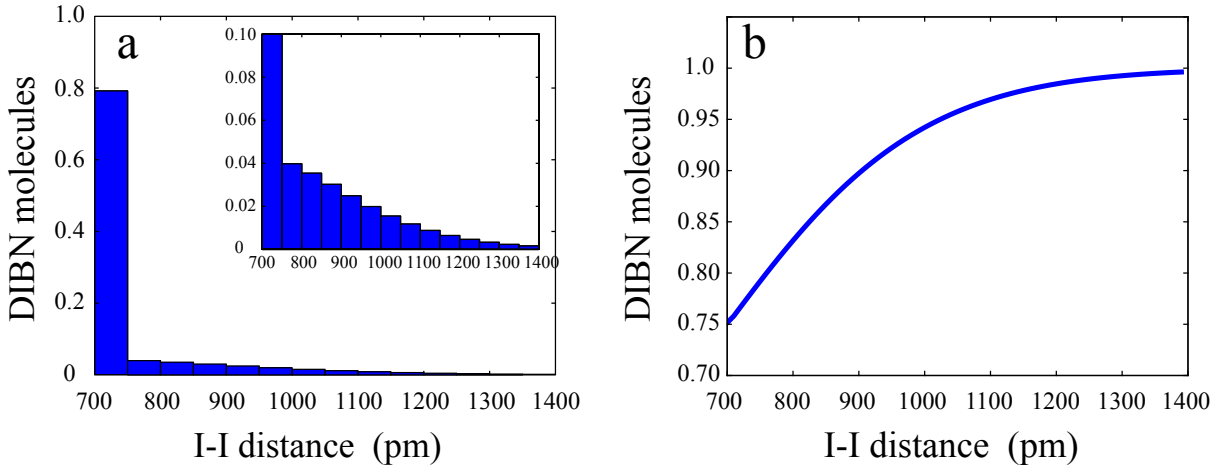

Figure 7.13.: (a) Histogram of S, visualizing the fraction of molecules in different distance intervals, seen by the FEL pulse. (b) The cumulative distribution of S, utilizing a smaller stepsize in I-I distances than in (a).

too broad over the recorded range. Nevertheless, these radiation damage considerations, which are based on the results from ion measurements (see section 5.5) and the model given above, support the general findings, i. e., damage effects do not show up in the diffraction pattern at the low resolution and the signal-to-noise ratio of this experiment. The issue of radiation damage and its possible effects on the diffraction from isolated molecules is further discussed in chapter 8.

7.5. Summary

This chapter presented the first experimental results of coherent x-ray diffraction experiments utilizing hard x-rays on aligned molecular gas-phase samples. An ensemble of quantum-state selected and strongly laser-aligned isolated molecules in the gas phase was prepared in order to record x-ray diffraction data, exploiting the unique pulse properties of the novel x-ray free-electron laser LCLS. The approach of using an ensemble of identical isolated molecules, all laser-aligned along a common axis in the lab frame results in signal enhancement by incoherent superposition of single-molecule diffraction intensities. This is in contrast to the usually proposed approach (see, e. g., ref. 12), where only a single molecule (on average) per shot is imaged and the 3d-diffraction volume in reciprocal space is reconstructed by "post-orientation", i. e., determining the molecular orientation in the lab frame from inspection of single shot diffraction data by computational methods, as discussed, e. g., in ref. 31–34. rather than imposing it prior to x-ray diffraction by laser

alignment. However, the post-orientation method is completely impossible with the weak diffraction signal from small molecules such as used in the scope of this thesis, where a count rate of only 0.2 diffracted photons/shot, even from an ensemble of many molecules, was measured.

The target molecule 2,5-diiodobenzonitrile (DIBN) was chosen to be an ideal candidate for this proof-of-principle experiment, because it consists of two heavy iodine atoms. With the most-polarizable axis almost coinciding with the I-I axis, the molecule could be aligned along this axis, thereby forming a kind of "Youngs double slit" on the atomic level. The weak scattering signals of isolated small molecules in combination with laser-alignment posed severe challenges in data collection. A high quantum efficiency, low noise, high readout rates, and a good energy resolution of the imaging detector was a strong prerequisite to allow for single-photon counting such as in the experiment described here. This conditions were met by the novel pnCCD detector of the CAMP instrument. While many artifacts in the single-shot pnCCD data like "hot-pixels", gain-, offset, and common-mode based artifacts were corrected for (owing to the low noise and high signal level of individual 2 keV photon hits on the pnCCD), the background from NIR photons by the strong alignment laser pulses of the YAG laser, propagating collinearly with the FEL, was a severe problem. Since the molecular beam was much broader ($\approx$ 4 mm) compared to the YAG focus, the co-propagating geometry was the only way of ensuring that all target molecules from the molecular beam intersected by the FEL are strongly aligned in the lab frame. Unfortunately, the filters used to block NIR photons from the YAG did not completely cover the pnCCD detector. In particular the regions at the detector edges were not thoroughly covered, resulting in very high or even saturated values in particular at the bottom (top) edge of the top (bottom) pnCCD panel, i. e., the edges where the lasers were propagating close to. Therefore, parts of the pnCCD data had to be neglected for data analysis. A detailed description of the process of data-cleaning and single-photon is given in appendix A, while a brief description is given at the beginning of this chapter.

Due to limited beamtime at LCLS, diffraction data of DIBN was obtained from 842,722 shots (NoYAG) and 563,453 shots (YAG) only, containing only 172,499 photons (I_{NoYAG}) and 111,560 photons (I_{YAG}) (average hit rate was $\approx$ 0.2 photons/shot). Since the experimental background from the chamber was not measured thoroughly, but contributes significantly by $\approx$ 35 % to the measured diffraction signal, the diffraction data is best analysed in terms of the difference of the diffraction from aligned (YAG) and randomly-oriented (NoYAG) DIBN. By this method, the experimental background as well as the isotropic scattering contribution from atomic scattering from the DIBN atoms and He is removed, preserving only the diffraction features of molecular scattering (i. e., originating

from the interference of scattering from distinct atoms in DIBN), which are different in the YAG and NoYAG case. This is confirmed by the I_{YAG}-I_{NoYAG} difference image which shows a clear and significant angular anisotropy.

With the x-ray wavelength (620 pm) only slightly smaller than the longest interatomic distance in DIBN (I-I distance: 700 pm), the diffraction features from interatomic interferences, from which mainly the I-I interference is recognized, are very broad, slowly varying on the pnCCD detector, and extending to high scattering angles 2Θ. Hence, the range of s (or: Q) values covered by the pnCCD detector is very limited, covering only parts of the 0^{th}-order maximum and 1^{st}-order minimum. The 1^{st} maxima from the I-I interference are not covered by the detector at all. This complicates analysis of the obtained diffraction pattern since at this low resolution, inverting, i. e., phasing of the obtained diffraction pattern in order to derive the molecular structure of DIBN from the diffraction data alone is infeasible. Additionaly, the resolution in structure determination would be limited by the non-perfect degree of alignment of $\langle \cos^2 \theta_{2D} \rangle = 0.84$ which washes out the I-I interference in the diffraction pattern and would hamper phase-retrieval-based structure determination as was discussed before in chapters 5 and 6. Therefore, the I_{YAG}-I_{NoYAG} data was analysed by comparing the measured I_{YAG}-I_{NoYAG} patterns with theoretical patterns, simulated with different I-I distances. The course of the 1d-$I(s)$ profile in the I_{YAG}-I_{NoYAG} difference image is best fitted by a model with extended I-I distance of 800 pm. However, when performing a goodness-of-fit test by the χ^2 method, the minimum of χ^2 values (minimal values indicate a good fit of a particular model to the data) around 800 pm is very broad and also the model with the correct value of 700 pm shows a good agreement with the data. The data contains some "outliers", which also give a good fit of the 1550 pm model. This is attributed mainly to the sparse and noisy data and will be avoided in measurements involving longer data acquisition and significantly reduced experimental background.

A second reason for the slightly extended bondlength in the fit is supported by radiation damage considerations. As estimated in section 5.5, 50 % of the target molecules are destroyed by the intense FEL pulses. Given a temporal profile of the FEL pulse, an effective spatial distribution of atomic displacements from the equilibrium geometry for iodine-iodine is derived, where all photons able to elastically scatter at a certain time t_i of the FEL pulse "see" a spatial distribution that is influenced by the fragmentation at all times prior to t_i. The model is a purely mechanical model, taking into account only the Gaussian temporal profile of the pulse, the recoil velocities of fragments in the molecular frame and the total ionization yield for a whole pulse. The onset of Coulomb explosion is assumed to happen instantly upon absorption of a 2 keV photon, neglecting

the finite delay due to Auger decay and subsequent charge reorganisation within the DIBN molecule. This is of course a "worst case approximation" which rather overestimates the distance of the fragmenting ions. By integrating over the temporal pulse profile it is derived, that 75 % of the diffraction signal originates in the scattering from completely intact DIBN, while the residual 25 % are due to scattering from increased I–I distances. However, 90 % of the diffracted signal still corresponds to I–I distances that are less than 200 pm longer than the equilibrium geometry. Due to the low resolution in the current experiment with 620 pm wavelength radiation, these effects cannot be fully resolved. If shorter x-ray pulses, i. e., with 10 fs duration, would be used practically no damage would be observed even for the same pulse energy, with > 95 % of the molecules at equilibrium distance within 40 pm. The consequences of different pulse durations and different pulse energies, i. e., different degrees of ionization to this purely mechanical radiation damage model are discussed in chapter 8.

Recent experiments [198] on inner-shell photoionization of small molecules suggest, that already during the time necessary to produce the final charge states due to Auger decay (< 10 fs), the molecular geometry has changed, i. e., bond distances have increased. This leads to lower kinetic energy release than by modelling the kinetic energy release by simply taking into account the final charge states and the equilibrium distances in the molecule, i. e., if instantaneous ionization would be assumed. In addition, x-rays scattered elastically at damaged molecules/fragments, i. e., where some electrons were removed from, will "see" a lower charge density and hence lower coherent scattering cross-sections than in the intact molecule. This can be assumed to further reduce damage effects in the diffraction pattern as damaged atoms/molecules will scatter less than intact atoms/molecules. However, the exact difference, regarding total scattered intensity and its spatial distribution, might be negligible if the ions are only of low charge, i. e., the difference in scattering from I^+ compared to the intact I atom can be assumed to be very small.

In conclusion, diffraction data of laser-aligned and randomly-distributed DIBN molecules was recorded at 620 pm wavelength radiation using the worlds first x-ray free-electron laser LCLS. The obtained single-shot diffraction patterns were carefully corrected for various background artifacts. The resulting diffraction patterns from aligned and randomly-distributed DIBN molecules were analysed in terms of the diffraction-difference image I_{YAG}-I_{NoYAG} and a clear and significant signal from aligned molecules was found. Due to the limited s-range, i. e., low resolution, phasing the diffraction pattern was not performed. Instead, the obtained I_{YAG}-I_{NoYAG} data was compared to simulations of distinct I–I distances, giving a best fit for a slightly increased I–I distance compared to the molecules equilibrium geometry. Radiation damage effects on the diffraction pattern were discussed

in terms of a purely mechanical model of the spatial distribution of fragmenting ions "seen" by the FEL.

There is room for many improvements in future coherent x-ray diffraction experiments of this kind. For better state-selection of cold molecules, along with better spatial separation from the He backing gas, improved deflector electrodes, e. g., providing stronger electric field strengths and gradients should be contrived. The design should focus on optimizations regarding the geometry and surface quality of the deflector electrodes. Improved deflection would result in better state-selection of cold molecules, increasing the degree of alignment and thereby improving resolution and enhancing the contrast in, e. g., the I_{YAG}-I_{NoYAG} image. For reducing experimental background from the alignment laser, the photon detector should be carefully covered against NIR photons. In addition, the experimental background from scattering by residual gas or apertures (i. e., the scattering not originating from the molecular beam) should be measured more comprehensively. However, in any case, the amount of measured data and the resolution (i. e., the range of s-values covered by the detector) should be increased in order to permit proper phasing of the diffraction patterns. The latter could be achieved by using shorter wavelengths, which became available at LCLS and will be available at the European XFEL from the beginning of its operation. In conclusion, since this experiment was the first x-ray diffraction experiment on quantum-state selected, strongly-aligned, isolated gas-phase molecules, important progress was achieved in order to pave the way towards follow-up coherent x-ray diffraction experiments of this kind, further ideas of which are discussed in chapter 8.

8. Conclusions and Outlook

In the framework of this thesis, coherent x-ray diffraction from laser-aligned gas-phase molecules was implemented experimentally for the first time at an x-ray free electron laser (XFEL). The prototypical molecule 2,5-diiodobenzonitrile (DIBN) was chosen to be a good candidate for this kind of experiment, where mainly the two-center interference of the two (heavy) iodine atoms was utilized for coherent x-ray diffraction, resembling a kind of "Youngs double slit" on the atomic level. Since scattering from a single small molecule such as DIBN, even at the high intensities of the x-ray free electron laser LCLS, is very weak, signal enhancement was obtained by using an ensemble of some hundreds of identical target molecules, all strongly laser-aligned with respect to a fixed direction in space. This results in an incoherent superposition of single-molecule scattering intensities and thereby resembles a single-molecule diffraction pattern, which is blurred due to the finite degree of alignment of the molecules in the ensemble.

In order to reach a high degree of alignment, the target molecules had to be provided in the preferably lowest rotational quantum states in order to achieve strong alignment by the alignment laser. Therefore, the target molecules were cooled in a supersonic expansion from a pulsed Even-Lavie valve together with helium as a backing gas. Spatial quantum-state selection of low-lying (rotational) quantum states was provided by the inhomogenous static electric field inside the electrostatic deflector. As shown in section 5.3, quantum-state selection by the deflector resulted in an improved degree of alignment in the deflected part of the molecular beam. The average degree of alignment during the diffraction experiment was $\langle \cos^2 \theta_{2D} \rangle \approx 0.84$, limited by the spatial and temporal overlap of the YAG and the FEL. Since the deflection is not very strong, the second purpose of using the deflector, namely the partial spatial separation from the helium seed gas, was not achieved successfully and will be improved in future experiments.

The single shot x-ray diffraction data from aligned and randomly-distributed DIBN was successfully cleaned for various detector-based artifacts and background, including the severe background signal from NIR photons from the alignment laser. Scattered x-ray photons were extracted from the cleaned single-shot data with a count rate of ≈ 0.2 photons/shot. All photon hits were histogrammed into 2d-histograms, i. e., diffraction patterns, according to whether the molecules were aligned (YAG) or not-aligned, i. e., randomly distributed (NoYAG) . In the obtained diffraction patterns, the molecular interference from the two main scatterers (iodine) manifests itself in regions of negative and positive intensity when taking the difference of the diffraction data from aligned and not-aligned molecules ("I_{YAG}-I_{NoYAG}"). Despite the relatively low number of photons ($\approx$ 170,000 in the NoYAG case and $\approx$ 110,000 photons in the YAG case), the I_{YAG}-I_{NoYAG} difference is well beyond noise and coherent x-ray diffraction from aligned molecules is confirmed by the results of this experiment.

8.1. Prospective X-ray Diffraction Experiments on Controlled Molecules

Although the feasibility of coherent x-ray imaging of isolated molecules was confirmed by these results, future experiments of this kind will benefit a lot from experiences of this work. One of the main issues, due to the weak scattering from non-crystalline molecular samples, is the data acquisition and single photon counting itself. As mentioned in section 7.5, having the alignment laser co-propagating with the FEL is the only way to ensure that the diffraction pattern of the target molecules will not be blurred by scattering from a (possible major) fraction of these target molecules being not-aligned, i. e., isotropically distributed . For this reason and the high laser intensity necessary for strong alignment, the photon detector should ideally be completely blocked to NIR photons from the alignment laser, i. e., thoroughly be covered by filters. The filters used in the experiment have proven to cover the detector quite well in each detector panels central region, but imperfect coverage at the edges resulted in a significant fraction of saturated regions which had to be neglected for data analysis. Ideally, the whole photon detector should be "wrapped up" almost completely by a filter, avoiding the most severe source of background in the experiment. For the front side, i. e., towards the interaction region, Al-coated parylene layers, such as already used in this experiment, should be utilized as a filter. The backside and everything not facing the interaction region could, in principle, be covered by a relatively thick Al filter. Care has to be taken at all mechanical mountings, edges, and corners.

In addition, the amount of experimental background from x-ray photons not scattered by the molecular beam, but, e. g., by residual gas, apertures, etc., should be measured comprehensively, because it can contribute significantly to the measured diffraction signal, as was shown in chapter 7. In experiments involving a molecular beam source with a backing gas, like He, the amount of scattering by the backing gas should, in principle, also be measured at the same conditions like in the following experiment, but without placing the molecular sample of interest in the reservoir of the EL valve. However, this measurement is not as crucial as the measurement of the background from scattering by, e. g., apertures, etc., because the latter is, most likely, not circularly symmetric and contributes a non-isotropic background which cannot be modelled but has to be measured for each experiment individually.

Another important point is the precise determination of the scattering geometry. Due to the weak scattering from non-crystalline molecular samples, precise determination of the scattering geometry, i. e., assigning a certain scattering vector $\mathbf{Q}$ to each point on the detector (in other words: the assignment of x-y-z coordinates to each detector pixel), cannot be performed by using the sample itself as would be possible in crystallography or by "virtual powder patterns" such as in XFEL-nanocrystallography experiments, see ref. 199. A solution would be to collect Bragg diffraction data, either from a crystalline powder sample or from a single (preferably cubic) crystal, temporarily placed in the beampath. This "calibration sample" could be placed in and removed from the interaction point by vacuum-compatible remote-controlled motorized translation stages.

In the proposed approach of using an ensemble of identical laser-aligned molecules, one always has to deal with a tradeoff between the target density and the achievable degree of alignment in the interaction region. Both parameters affect the contrast in the diffraction-difference $\mathrm{I_{YAG}}$-$\mathrm{I_{NoYAG}}$, i. e., higher degree of alignment and/or higher target density M enhace the contrast. Since a good degree of alignment can be achieved by a good spatial selection of lowest lying quantum states, the distance from the deflector to the interaction point should be large, which unfortunately in turn reduces M. Stronger deflection and hence better spatial separation from the backing gas He would be beneficial, but is counteracted by the fact that the heavier the target molecule (and hence: the better suited for diffraction due to heavy constituent atoms), the smaller the dipole-moment-to-mass ratio (for a given dipole moment). To wrap up the points mentioned here, since the degree of alignment $\langle \cos^2 \theta_{\mathrm{2D}} \rangle$ and the target density M affect the contrast in the $\mathrm{I_{YAG}}$-$\mathrm{I_{NoYAG}}$ pattern, in case the data has to be analysed in terms of the $\mathrm{I_{YAG}}$-$\mathrm{I_{NoYAG}}$ pattern (e. g., when the amount of He or other background is not known exactly),

M and/or $\langle \cos^2 \theta_{2D} \rangle$ have to be optimized in order to give a good contrast. In case a complete or partial model of the diffraction signal from the target molecule is known, the amount of data that should be taken in order to determine a (minimum) necessary contrast (which is well above the noise level) should be determined prior to the experiment.

While the repetition rate in this experiment was 60 Hz (30 Hz YAG and NoYAG, respectively), data acquisition will be significantly increased at, e. g., the European XFEL with FEL repetition rates of $\approx$ 27,000 Hz [41]. Hence, data acquisition will only limited by the repetition rate of the alignment laser and the read-out of the detector. The European XFEL utilizes a special timing scheme which has to be accomodated by the photon detector for efficient data acquisition. The European XFEL will deliver 10 pulse trains of x-ray pulses per second. Each pulse train will contain 2,700 x-ray pulses separated by 220 ns, hence the length of a single pulse train is $\approx$ 600 μs. A pulse trains is followed by 99.4 ms of idle time (see, e. g., [200, fig. 1]). The short spacing of x-ray pulses within each pulse train corresponds to a repetition rate of $\approx$ 4.5 MHz [41]. This is way too fast for, e. g., the pnCCDs which are able to handle $\approx$ 200 Hz. In order to accomodate for this challenging timing scheme, new detectors have to be developed. A promising candidate is the Adaptive Gain Integrating Pixel Detector (AGIPD) [200, 201] which is under development at DESY in collaboration with the University of Hamburg, the University of Bonn and the Paul Scherrer Institute (PSI) in Switzerland. The AGIPD detector allows for signal-based and pixel-wise dynamic gain switching resulting in a high dynamic range able to count from single photons up to 10^4 photons. The analog memory connected to each pixel of the detector is able to store up to 352 images before read-out. Hence a promising operating scheme for the detector would be to collect 352 diffraction images from a 2,700-pulse-train which are digitalized and read-out during the 99.4 ms of idle time between the x-ray pulse trains. This results in an efficient DAQ rate of 3520 Hz and thereby shortening DAQ times by a factor of $\approx$ 60 compared to the 60 Hz utilized for the experiment described in this thesis.

In case a reasonable shielding to optical and NIR photons is ensured, data acquisition involving integration of multiple shots should be considered as well, as this would even further improve data acquisition making optimal use of the European XFEL's timing scheme.

In order to accomodate this DAQ rate in terms of molecular alignment, cw molecular beams can be utilized paired with novel high-power near-infrared cw lasers able to provide molecular alignment at arbitrary repetition rates, a project currently in progress within the Controlled Molecule Imaging (CMI) group and the Center for Ultrafast Imaging (CUI) at DESY.

8.2. Phase Retrieval of Unknown Structures

In future experiments, where the purpose of coherent x-ray diffraction on isolated molecules would be the structure determination of partially or even completely unknown molecular structures, forward modelling of the diffraction pattern, as explained in chapter 6, will not be possible and the molecular structure has to be inferred from the diffraction pattern itself by phase-retrieval methods. Phase-retrieval methods represent a iterative mathematical way to the solution of the "phase-problem", i. e., the fact, that only the square-modulus, i. e., the intensity, of the diffracted wave is measured in the detector plane, but not its phase. The phase of the diffracted wave, however, is necessary for reconstruction of the object by Fourier transformation. Phase-retrieval methods work as follows: starting from an initial "guess" of the phases which can be totally random and applying constraints in real and reciprocal space such as, e. g., the known maximum possible extent of the object in real space (e. g., the "support" constraint), the phase of the diffracted wave can be reconstructed from the measured diffraction pattern. Phase-retrieval has been applied to various diffraction data from non-crystalline specimens, see, e. g., refs. 24, 202. A comprehensive description of phase-retrieval methods is given by, e. g., Marchesini [192].

The resolution in structure determination obtained from such diffraction experiments applying the proposed approach of utilizing a laser-aligned ensemble of gas-phase molecules depends on the achieved degree of alignment, the maximum momentum transfer recorded (i. e., the range of s values covered by the detector), and sample deterioration due to radiation damage effects caused by the intense XFEL pulses. Radiation damage will be dealt with in section 8.3.

Phase-retrieval is hindered significantly in the case of non-perfect molecular alignment. As the diffraction pattern is the incoherent superposition of single-molecule diffraction patterns distributed with a certain alignment angular distribution, this distribution of molecular orientations will show up in the diffraction patterns as well and interferences will be washed out compared to the diffraction pattern from a perfectly aligned molecule. It will cause an uncertainty of the atomic positions, in particular of the outermost atoms. The problem and its effects on the strucure determination by phase-retrieval have been theoretically discussed before [193]. For simple molecular systems such as, e. g., a symmetric top molecule containing a heavy atom, the data from an ultrafast electron diffraction experiment could be corrected for the finite degree of alignment. This was proven to significantly enhance the resolution in the derived structure as shown by Hensley et al. [46], following an holographic approach proposed before by Ho et al. [194].

In any case, for a successful implementation of phase retrieval, increasing the resolution by extending the range of s-values measured is absolutely necessary in order to get an interpretable image, i. e., the diffraction should be measured for high s-values in the detector plane. For the x-ray diffraction experiment presented in this thesis, the wavelength was quite long (620 pm) compared to the heavy-atom distance (700 pm) and hence the resolution was low, resulting in not even the first scattering maxima from the iodine-iodine interference being covered by the detector (see chapter 7). Higher resolution can be achieved by using shorter wavelength in the region of 200–100 pm, as became available at LCLS and will be at the European XFEL from the start of its operation [41].

However, one of the main issues envisioned to be adressed by coherent imaging experiments at XFELs is the structure determination of biological macromolecules that avoid successful crystallization and hence cannot be adressed by crystallography experiments at synchrotrons. One prominent example is the class of membrane proteins which mitigate transport between biological cells and are an important target for drug delivery. The approach proposed by Spence and Doak [11] is to use a jet of either liquid He [203] or water droplets, doped with the target molecule, which is intersected by a polarized NIR laser providing 1d- or 3d-alignment and a probe beam providing diffraction from the sample. The proposal by Spence and Doak involves a continous electron beam as a probe in order to collect electron diffraction data. However, instead of using a continous electron beam, the sample could be probed by the ultrafast XFEL pulses as proposed by Neutze et al. [12]. By rotating the polarization of alignment laser and collecting diffraction data at various orientations, a tomographic reconstruction of the 3d electron density can be achieved [11]. Laser alignment of small molecules in He droplets has recently been confirmed experimentally [105]. When using water droplets the water shell around the target molecule is expected to sublimate during the expansion from the nozzle-valve into the vacuum of the chamber thereby cooling the molecule and potentially forming a small layer of vitreous ice covering the molecule [11]. The surrounding layer will also be beneficial to reduce and delay sample damage [204].

Laser alignment of large biomolecules such as, e. g., proteins in a liquid jet of He or water/ice as described above has not been studied yet. Due to the limited resolution imposed by the limited alignment, as is described above, the degree of alignment is crucial for such experiments. However, the dielectric interaction of large biomolecules with the alignment laser can be expected to fairly exceed the values for small molecules such as, e. g., DIBN, due to the volume dependence of the anisotropic polarizability [11]. Alignment limited resolution for large biomolecules has been discussed by Spence et al.[205] where the uncertainty of the atomic positions for a given degree of alignment, i. e., angular

uncertainty of atomic positions, is described in a simple classical picture similar to the one given in ref. 193, fig. 2. The dependence of the squared r.m.s. angular deviation from perfect orientation $\langle \Delta\theta^2 \rangle$ (θ is the angle to the laser polarization axis) on temperature T, polarizability anisotropy $\Delta\alpha$, and laser power I is given by $\langle \Delta\theta^2 \rangle = 3 \cdot 10^8 \; T/(\Delta\alpha \; I)$ [205, eq: 3], where I is given in units of W cm^{-2} and $\Delta\alpha$ in units of nm^3. Hence, the angular confinement of molecules enhances (i. e., $\langle \Delta\theta^2 \rangle$ decreases) with decreasing temperature and increasing polarizability anisotropy and laser power, as expected.

The difficulty lies in determination of $\Delta\alpha$ for molecules such as proteins. Polarizability values have been calculated for separate amino acids [206] and dielectric properties of macromolecules and proteins have been modelled before [207, 208]. In the approach given by Spence et al.[205], a macromolecule is modelled by an elongated (prolate) dielectric spheroid and the anisotropic polarizability of this prolate spheroid can be written as the product of the volume V and a so-called shape factor, hence $\Delta\alpha = \gamma V$. γ depends on the shape of the spheroid and its dielectric constant. Details can be found in ref. 205. A small protein such as lysozyme may be aligned by an off-resonant NIR laser with a quite modest power of $I = 5{\cdot}10^9$ W cm^{-2} within a small angular range permitting resolution of ≈ 0.7 nm in the reconstruction of the structure. This is already sufficient to resolve, e. g., α-helices from the secondary protein structure. Therefore, the temperature should be in the range of 115–366 K (the values vary due to the uncertanity in the dielectric constant). Higher laser powers and lower temperatures will certainly enhance the resolution. Increasing the laser power by a factor of 100 to $I = 5 \cdot 10^{11}$ W cm^{-2} (similar to the power used for DIBN, see chapter 5) already enhances the alignment-based resolution by a factor of 10 to 0.07 nm. In this case, the resolution would not be limited by alignment anymore but only by the wavelength λ (which even at the upcoming XFELs is larger than 0.07 nm), the maximum momentum transfer recorded by the detector, and potentially sample deterioration due to radiation damage. Structure determination for simulated diffraction data from a stream of hydrated lysozyme molecules at 0.3 nm resolution has been conducted by Wu and Spence [209] and has been confirmed to perform quite well, i. e., promising R-factors of $R < 0.1$ have been obtained after $\approx$100 iterations.

For larger molecules or virusses with larger volumes and more elongated shapes (i. e., larger shape factors), the conditions for alignment are even more relaxed than the conditions mentioned above: E. g., 1 nm resolution at the big TMV virus is already achieved for $T = 320$ K and $I = 2.5 \cdot 10^8$ W cm^{-2}. This suggests that laser alignment for larger molecules should be possible. However, conditions for appropriate liquid jet operation when using single macromolecules inside liquid He or water droplets for such experiments should be studied in detail as soon as possible.

In general, there is a specific point in terms of total scattering signal per shot at which post-classification of the orientation of a single molecule (i. e., not an ensemble) solely based on inspection of the single-shot diffraction pattern itself would be sufficient for orientation determination [31–36] and more beneficial than pre-(laser) alignment. Additionally, for experiments where one is only interested in a 1d measurement such as, e. g., the I-I distance in DIBN, powder diffraction of an ensemble of isotropically-distributed target molecules is sufficient. This would also allow to be performed much closer to the valve providing the sample, i. e., at much higher target densities.

8.3. Radiation Damage Effects on Coherent Diffraction Data

In addition to non-perfect molecular alignment, further blurring of the diffraction pattern can be due to radiation damage effects, i. e., the scattering of x-rays by fragmenting molecules. Here, the effects of radiation damage on the diffraction pattern are investigated in terms of the purely classical mechanical model of the effective spatial distribution S, which was introduced in section 7.4.

Figure 8.1 shows the cumulative spatial distribution of S like in fig. 7.13 (b), visualizing the fraction of molecules in different I-I distance intervals, seen by the FEL pulse. The graphs have to be interpreted in the way explained in chapter 7. As an example, when looking at the cyan graph of fig. 8.1 (a), i. e., at pulse length 100 fs, 75 % of the diffraction pattern is due to diffraction from intact molecules (i. e., I-I distance at equilibrium value of 700 pm) while 80 % is due to diffraction from molecules with I-I distances of less then $\approx$ 780 pm. I. e., 5 % of the diffraction is due to destroyed molecules the I-I distance of which is still between 700 and 780 pm. The steeper the curve the less does damage show up in the diffraction pattern, most prominent for the shortest pulses. The distribution is shown for different FEL pulse lengths. The ion velocity distribution in all cases is centered around 4,200 m/s like in section 7.4.(a) and (b) correspond to realistic parameters at different LCLS beamlines. (a) AMO beamline, photon energy 2 keV, fraction of molecules ionized during the whole FEL pulse $f_{\text{ionized}} = 0.5$. (b) CXI beamline, 8 keV, $f_{\text{ionized}} = 0.04$). The different amount of ionization is given by the different photoabsorption cross sections σ_{abs} of iodine at the different photon energies as given in ref. 187. The details of the following derivation are outlined in section 5.5 [1]. At 2 keV, $\sigma_{\text{abs,iodine}} = 419$ kbarn,

[1] Only single-photon processes are considered. The experiment should be performed out-of-focus (as it was the case during the experiment described in this thesis, i. e., in chapter 7), or, more precisely, at a reasonable low photon fluence in order to avoid multi-photon processes.

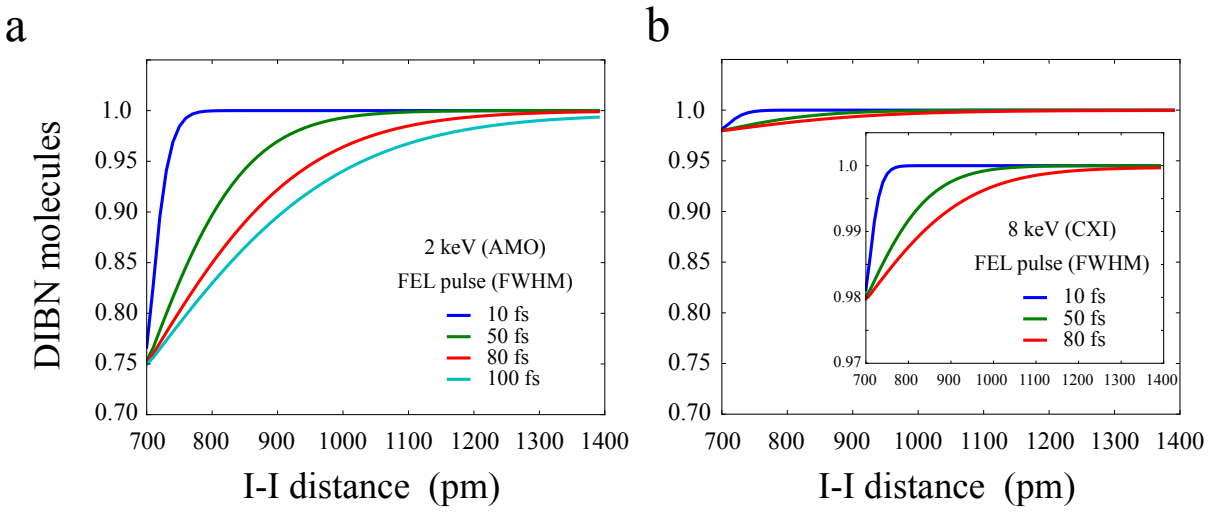

Figure 8.1.: Cumulative spatial distribution of S, visualizing the fraction of molecules in different I-I distance intervals, seen by the FEL pulse. (a) Different FEL pulse length (Gaussian pulse, width given in FWHM), total amount of molecules ionized during the whole FEL pulse $f_{\text{ionized}} = 0.5$ (AMO beamline of LCLS, 2 keV). (b) Different FEL pulse length, $f_{\text{ionized}} = 0.04$ (CXI beamline of LCLS, 8 keV). The ion velocity distribution in all cases is centered around 4,200 m/s like in section 7.4.

number of photons N = $4.317 \cdot 10^{12}$ (pulse energy 4 mJ, 35 % beamline transmission). The probability for 1-photon absorption by iodine is $p_{\text{abs,iodine}} = 0.25$, hence for a DIBN molecule (two iodines) $p_{\text{abs,DIBN}} = 0.5$. At the CXI beamline, 8 keV, $\sigma_{\text{abs,iodine}} = 60.8$ kbarn, N = $2.34 \cdot 10^{12}$ (pulse energy 3 mJ, $\approx$ 100 % beamline transmission), and $p_{\text{abs,DIBN}}$ = 0.04. The maximum pulse length at 8 keV is limited to between 50 and 80 fs [20].

It can be clearly seen in fig. 8.1 (a,b), that the amount of damage, i. e., displacement of the fragments from the equilibrium geometry "seen" by the FEL pulse, strongly depends on the FEL pulse length. At 2 keV, in the case of a pulse length of 10 fs and $f_{\text{ionized}} = 0.5$ (blue line in fig. 8.1 a), practically 95 % of the diffraction pattern are from completely unharmed molecules (displacement $\leq$ 40 pm). When taking data at 8 keV (CXI beamline), the diffraction pattern will practically be entirely due to unharmed molecules at all pulse lengths, which is due to the very low photoabsorption cross section at a photon energy of 8 keV. Of course, the low photoabsorption cross section at 8 keV goes along with a lower cross section for coherent scattering as well. Since the coherent cross section at 8 keV is 0.72 kbarn (1.56 kbarn at 2 keV), the measurement time should be at least twice as long. However, even then, utilizing a photon energy of 8 keV is more promising than 2 keV: the ratio of coherent scattering cross sections between 8 and 2 keV is 0.72/1.56 = 0.46, but the ratio of photoabsorption drops to 60.8/419 = 0.145. It should be noted, that

the number of photons used here for the 10 fs pulses is the same as for the longer pulse length', although pulses as short as 10 fs in reality require the "low charge bunch mode", which results in much less photons and hence results in even less damage (but of course, also less coherently scattered photons).

A common feature of this model is that if the fraction f_{ionized} of target molecules getting ionized during the whole FEL pulse is known, then the effective spatial distribution of molecular displacements S from the molecules equilibrium geometry "seen" (i. e., exploited for coherent elastical scattering) by the FEL pulse always starts at 1 - $f_{\text{ionized}}/2$. I. e., if in total half of the molecules are ionized by the FEL during a whole pulse (such as in the experiment presented in this thesis), S will start at 1 - $0.5/2 = 0.75$. If a fraction of 0.2 of the target molecules is ionized, 90% of the data will consist of scattering at completely intact molecules and so on. This argument is trivially justified only by the symmetric gaussian shape of the FEL pulse, which was assumed in the model. If the FEL pulse is not symmetric, the effective spatial distribution of molecular displacements S will be different. Note, that f_{ionized} is not limited to 1. If, e. g., the intensity (or the absorption cross section) is that high that already after half of the FEL pulse all molecules are ionized, than $f_{\text{ionized}} = 2$.

In conclusion, the examples given above in fig. 8.1 present a method to quickly visualize how much the obtained diffraction pattern will be blurred based on scattering from damaged molecules. As shown in section 7.4, 75 % of the scattering data from DIBN is due to unperturbed molecules and still 20 % is due to scattering from molecules less than 330 pm displaced from the equilibrium geometry. Due to the noisy data and the relatively long wavelength, these features cannot be resolved in the current experiment. But in future experiments, careful considerations of the effect of damage to scattering pattern based on FEL pulse length, photoabsorption cross sections, and velocity distributions of the recoiling ions should be taken into account. The model should be extended to include finite time delays due to Auger/electronic ralaxation processes upon photon absorption and changing coherent scattering cross sections due to changing electron densities and scattering of free electrons as considered, e. g., in ref. 210. In addition, the measurement of velocity distributions of the most important ionization channels would be useful. Ideally, measuring the velocities of recoiling fragments comprising the most important heavy atoms, i. e., which have the most significant effect on the diffraction patterns, would be very beneficial for modelling. In general, in addition to the work of Erk et al. [198], the response of polyatomic systems to inner-shell photoabsorption at XFELs and subsequent electronic relaxation dynamics, should be studied experimentally in more detail.

8.4. Towards Dynamical Studies

So far, only static diffraction experiments were considered. In order to collect static diffraction data following the diffract-before-destruct approach, the FEL pulses have to be short enough to suppress the effects of radiation damage in the diffraction patterns. The ultrashort pulses of XFELs, however, are also well suited to follow fragmentation and/or vibration dynamics of gas-phase molecules on fs-timescales via pump-probe experiments. In a pump-probe experiment, some process is initiated by a short laser pulse, i. e., the "pump pulse". Subsequently, the induced dynamics is probed by another laser pulse, i. e., the "probe pulse". The dynamic process is then followed by a sequence of snapshots with distinct pump-probe delays. The time resolution is determined by the accuracy to which the pump-probe delay can be adjusted and the pulse duration and jitter of both laser pulses. The unique pulse properties of XFEL pulses hold the promise to record a "molecular movie", i. e., following atomic and molecular dynamics at atomic resolution, in the fs-time domain, and at very high x-ray radiation intensities [35].

Concerning coherent x-ray diffraction experiments at XFELs, the pump pulse can be used for initiating dissociation/fragmentation of the target molecule. Extending the static diffraction experiment presented in this thesis, the fragmentation process of DIBN may be followed in real time by recording a sequence of "static" diffraction patterns at various pump-probe delays. The iodine ions in DIBN recoil along the alignment axis and the fragmentation process involving I^{n+}+$C_7H_3IN^{n+}$ can be followed by a change in the diffraction pattern, i. e., the images become "squeezed" and the fringe-spacing on the detector gets smaller with time. However, the diffraction pattern of the fragmenting molecule will be not only be blurred due to non-perfect alignment like the static diffraction patterns, but also due to the velocity distribution of the recoiling fragments. Further blurring may be due to the time-resolution of the pump-probe experiment, i. e., the finite width of the pump and probe pulses, the timing jitter of the FEL (due to the SASE process) and the accuracy of the relative pump-probe delay as mentioned above.

To illustrate the influence of the velocity distribution of the recoiling fragments, fig. 8.2 shows the spatial distribution S, visualizing the fraction of molecules in different I-I distance intervals seen by the FEL probe pulse like in fig. 7.13 (a). For simplicity, the pump pulse is assumed to ionize all DIBN molecules and the probe pulse doesn't cause any further ionization, but is only used for coherent diffractive imaging of the increasing I-I distance of the fragmenting molecule. The pulse lengths (FWHM of a Gaussian pulse) of ionizing pump- and diffracting probe-pulses are (a) 10 fs, (b) 50 fs, and (c) 10 fs respectively. The ion velocity distribution in (a,b) is centered around μ_v = 4,200 m/s, with a width of $\sigma_v = \mu_v/4$ (like in section 7.4) whereas (c) shows S for a very narrow velocity dis-

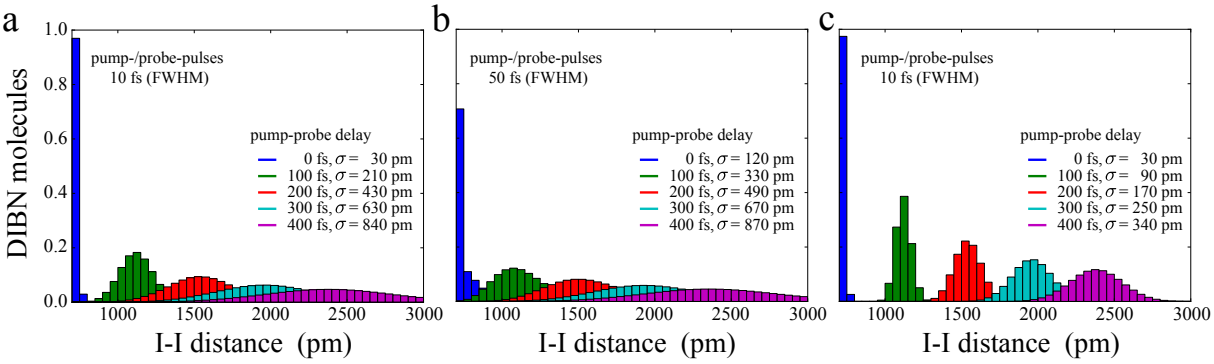

Figure 8.2.: Spatial distribution S, visualizing the fraction of molecules in different I-I distance intervals seen by the FEL probe pulse in an pump-probe experiment. The pulse lengths (FWHM of a Gaussian pulse) of ionizing pump- and diffracting probe-pulses are (a) 10 fs, (b) 50 fs, and (c) 10 fs respectively. The ion velocity distribution in (a,b) is centered around $\mu_v = 4{,}200$ m/s, with a width of $\sigma_v = \mu_v/4$ (like in section 7.4) whereas (c) shows S for a very narrow velocity distribution with $\sigma_v = \mu_v/10$. The three subfigures show S for different pump-probe delays. The σ values correspond to the 1-standard-deviation interval of each spatial distribution S.

tribution with $\sigma_v = \mu_v/10$. The three subfigures show S for different pump-probe delays. The σ values correspond to the 1-standard-deviation interval of each spatial distribution S.

When comparing the distributions at time-delay 0 fs (i. e., pump- and probe pulse exactly overlapping), in the case of a 50 fs pulse (b), the spatial distribution "seen" by the FEL already contains some damage effects, in contrast to the 10 fs pulse (a,c), where almost no damage effect may be observed, since the fragments have not moved significantly in that short time. However, in both cases (a,b), at long delays of several 100 fs, the spatial distribution seen by the FEL is significantly broaden due to the velocity distribution of the recoiling ions. The width of the spatial distribution become more and more equal at long delays and the width of the probe pulse itself does not play a significant role anymore. E. g., at a pump-probe delay of 200 fs, the diffraction pattern is due to a broad range of I-I distances. i. e., 68.2 % of the diffraction pattern is due to I-I distances comprising 430 (a) and 490 pm (b) respectively, centered roughly around ≈ 1600 pm. At a delay of 400 fs, the width of the 1-σ-interval is already 840 (a) and 870 pm (b) respectively, and the recorded diffraction pattern will be significantly blurred. If, in contrast, the velocity distribution of the ions is rather narrow (c), the blurring in the pattern will be reduced. This illustrates the difficulties in such experiments involving a broad velocity distribution of recoiling ions. Nevertheless, the resulting diffraction pattern will show

(blurred) stripes, with separations inversely proportional to the mean distance of the two heavy atoms. The amount of data taken at each time-delay will then be responsible for the confidence of how good different I-I distances, corresponding to different pump-probe delays can be resolved in dependence of the width of the ion velocity distribution.

Fragmentation dynamics could also be investigated by a holographic approach by exploiting the interference of the waves scattered from a single-atomic ion and the parent molecule to directly image this parent molecule in a type of dynamical Fourier-transform holography, called "fragmentation holography". In this type of experiment, the molecule to be investigated has to be aligned in the plane parallel to the photon detector. A pump pulse would be used to initiate fragmentation of the molecule. One of the fragments is a (preferably heavy) single-atomic ion. With a finite delay, the FEL is used to probe the fragments in order to collect scattering data. The scattered wave from the single-atomic ion would serve as a "reference wave" in this holographic approach. The diffraction pattern of both, single-atomic ion and parent molecule, could be Fourier-transformed directly to give the real-space structure, i. e., electron density of the parent molecule, sampled with the resolution given by the electron density of the reference scatterer, hence resembling a Fourier-transform holography experiment [35].

Figure 8.3 demonstrates the method of fragmentation holography, utilizing the prototypical molecule 1,4-diiodobenzene ($C_6H_4I_2$, DIB). DIB was assumed to be 3d-aligned in the plane of the detector. Upon ionization, assuming the conditions given in before in fig. 8.2 (a), DIB fragments into $C_6H_4I^{n+}$ (the "object" of the holographic experiments) and I^{n+} (the "reference scatterer"). The upper row shows the diffraction patterns for pump-probe delays of 200 fs (a) and 400 fs (b), whereas the lower row (c,d) shows the Fourier transform of these diffraction patterns. The photon energy was 8 keV (155 pm), the center of an outer edge of the diffraction pattern corresponds to $2\Theta = 54°$. Blurring of the diffraction patterns is only due to the velocity distribution of the recoiling ions, the molecular alignment is assumed to be perfect, i. e., $\langle \cos^2 \theta_{2D} \rangle = 1$ for simplicity.

The Fourier transforms (c,d) of the diffraction patterns (a,b) consist of the autocorrelations of the object and the reference and the cross-correlation of object and reference, displaced from the origin by the spatial distribution given by fig. 8.2 (a). The structure of the object, i. e., the $C_6H_4I^{n+}$ fragment, is difficult to derive from the cross-correlation term, if the velocity distribution of the fragments is not known. In case the velocity distribution is known (e. g., by VMI measurements), methods to deconvolve this velocity distribution from the cross-correlation term in (c,d), such as the Richardson-Lucy deconvolution algorithm [211–213], may be used to extract the fragments' structure. On the other hand, the holograms may be used to extract an unknown velocity distribution in

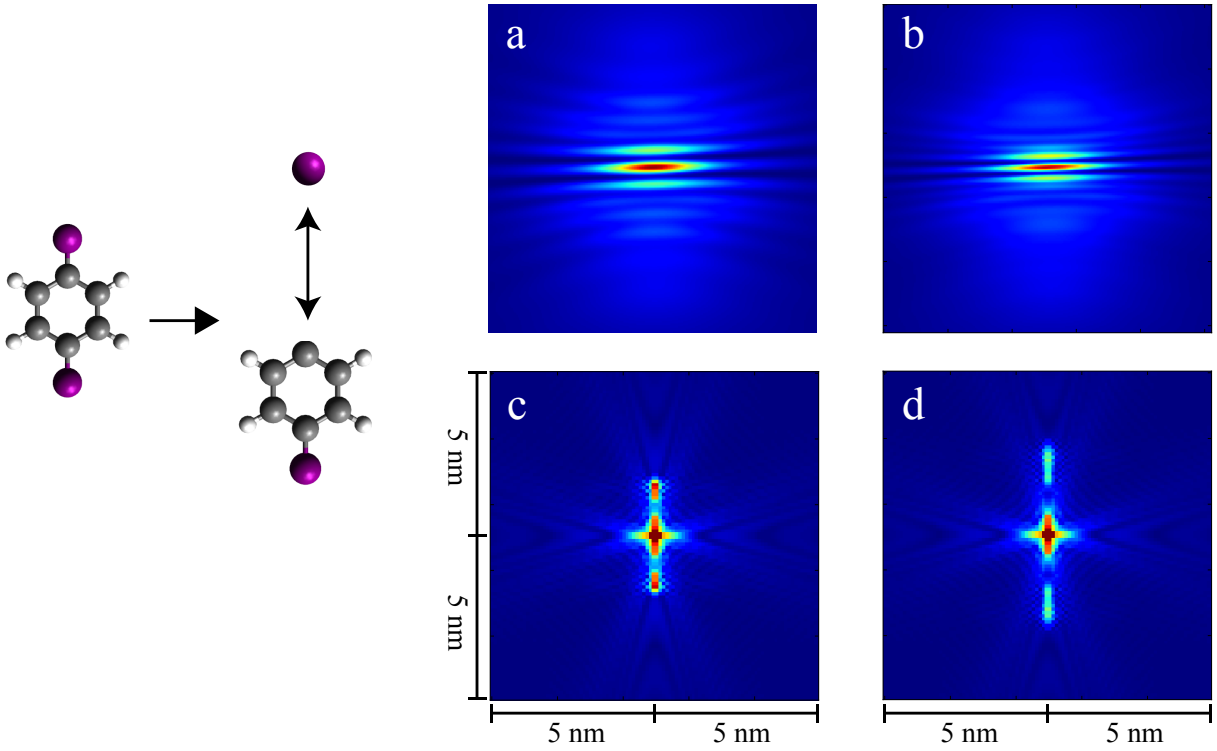

Figure 8.3.: Fragmentation holography: The picture on the left visualizes the principle of fragmentation holography and shows the molecular structure of 1,4-diiodobenzene (DIB). (a,b) are the obtained diffraction patterns with one of the iodine atoms being the reference scatterer, detached from the residual parent molecule, after pump-probe delays of 200 fs (a) and 400 fs (b). (c,d) are the Fourier transforms, i. e., the fragmentation holograms of (a,b). The molecular structure of the parent molecule, convolved with the electron density of the reference scatterer and the recoil-velocity distribution, manifests itself in the cross-correlation terms, i. e., in the terms displaced from the origin in (c,d). As can be seen in (c,d), the blurring due to the ion velocity distribution is significant. Blurring due to imperfect alignment was not taken into account.

case only x-ray diffraction data (and no ions) are measured in an experiment. In principle, information about ionization channels involving the heavy atoms may be deduced from the diffraction data, complementary to VMI measurements.

Figure 8.4 visualizes how fragmentation holography can be used to directly visualize the object structure in the cross-correlation terms. In contrast to Figure 8.3, the velocity distribution is infinitely sharp, comprising a single fragmentation channel (a,c) or two fragmentation channels (b,d) such as, e. g., shown when the Ti:Sa is utilized, compare the I^+ velocity distributions from chapter 5, e. g., fig. 5.2 (d,g). The pump-probe delay here is 400 fs in order to get a sufficient separation of the cross-correlation term from the

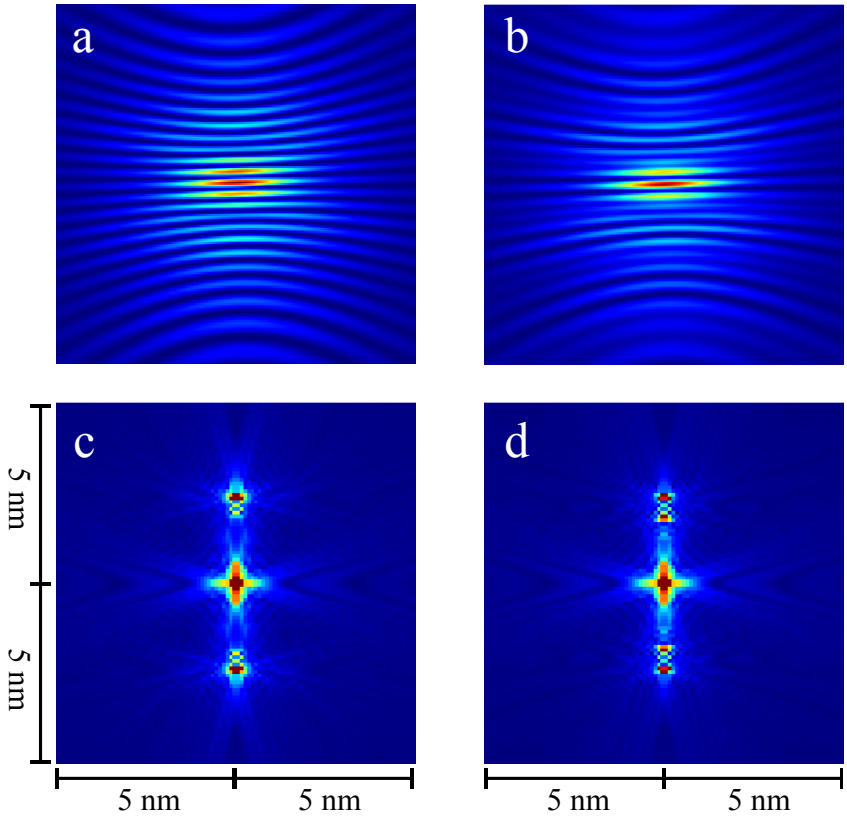

Figure 8.4.: Fragmentation holography in the case of a infinitely sharp velocity distribution, comprising a single ionization channel (left column, a,c) or two ionization channels (right column, b,d), the latter, e. g., from ionization with the Ti:Sa. Without blurring, i. e., a sharp velocity distribution, the molecular structure can be obtained from the holograms, especially in the case of a single ionization channel (c).

autocorrelation term in the center of the image. The resolution, i. e., "pixel size" at which the density is given in Figure 8.4 (c,d) is 100 pm.

In principle, the method of fragmentation holography can be applied to any molecular system, which is amenable to strong (laser) alignment and in which a well-defined site-specific fragmentation process can be initiated. Instead of utilizing an atom from the target molecule for creation of the reference wave, an external reference scatterer that is attached to the target molecule at a specific site could be used, e. g., in a molecule-atom cluster, where the atom is a noble gas atom. In principle, also the indole$(H_2O)_1$ complex could be used to test the feasibility of this approach.

8.5. Summary

To summarize, the recently build x-ray free-electron laser facilities promise to address structural molecular dynamics and thereby record "molecular movies" on ultrafast timescales as well as overcome radiation damage limits x-ray diffraction experiments for structure determination of non-crystalline samples. The latter is especially interesting to structural biology for a huge number of molecular samples which avoid forming crystals sufficient for crystallography at synchrotron sources.

However, the route towards single-molecule structure determination by x-ray diffraction experiments even at XFELs is difficult. For small molecules, such as DIBN that was utilized in this thesis, the scattering signal is very weak. The approach of increasing the scattering signal by using an ensemble of identical molecules, strongly laser aligned prior to diffraction, enhances the scattering signal but also poses the problem of motional blurring of the diffraction pattern due to imperfect alignment. Bigger molecules such as, e. g., biological macromolecules provide much stronger scattering signal and, though not studied yet, should be amenable to laser alignment as well, even at much relaxed requirements regarding laser power and molecular cooling due to the potentially highly anisotropic polarizabilities for such big molecules. In case no laser alignment is utilized, single-molecule diffraction could be applied and the orientation of the molecule is determined afterwards from the diffraction data itself by classification of the single-shot diffraction patterns. However, biological macromolecules often come in a variety of conformers which hamper orientation determination or the deduction of a clear-defined molecular structure.

As pointed out several times, optimization of all experimental parameters such as sample delivery, quantum-state selection, molecular alignment, repetition rate of the experiment, and reduction of background is absolutely crucial due to the very weak scattering signals and the long data acquisition times required. Such technical challenges will certainly be adressed and optimized in the near future when also new XFEL lightsources such as, e. g., the European XFEL in Hamburg will become operational.

A. Generation of Photon Lists

This chapter describes how single 2 keV x-ray photons were obtained from the single-shot pnCCD data and how different sources of background and pnCCD artifacts were accounted for. Single photon hits were extracted from the pnCCD data of the xtc-files, which were recorded by the LCLS data acquisition system. The xtc-files were accessed by the **C**FEL-**A**SG **S**oftware **S**uite (CASS). Details on the workflow inside CASS can be found in ref. 161.

In brief, when CASS is operated in offline mode, it accesses the data stored in the xtc-files (the list of xtc-files to be used has to be specified beforehand) and stores the data of all detectors as well as the beamline parameters of a single FEL-shot (i. e., the data of a single LCLS event) in a class called "cassevent". The datasets to be extracted from this cassevent have to be specified in an ini-file before starting CASS. The datasets specified in the inifile are stored in histograms which can be either 0d (a scalar value), 1d, or 2d. Many operations can be applied to the data in the histograms by so-called post processors. Post processors can, e. g., apply thresholds to the values of a histogram or distinguish histograms by certain criteria. In the end, there are two postprocessors designated to write processed data to either HDF5- [214] or ROOT-files [215]. For the experiment the results of which are presented in this thesis, CASS was used to extract single 2 keV x-ray photons from the individual pnCCD data frames. The post processing necessary for this purpose is described here.

A.1. Single Shot Raw Data

A single shot image acquired by the pnCCD detector, to which no correction was applied is called "raw data" or "raw data frame" in the following. Figure A.1 shows raw data frames when the YAG laser was off (a,b, condition "NoYAG") and on (c,d, condition "YAG") respectively. The pnCCD permits energy-resolved photon measurements. Although photon energies are not of interest for the diffraction pattern (where only the spatial distribution of the 2 keV photons matter), they are important during the cleaning process, e. g., for thresholding the signal and distinction from background, etc.. The measured pnCCD signals are given in ADU (analog-digital converting unit). The pnCCDs analog-digital converters operated in full gain mode in order to give a good separation of 2 keV and optical and NIR photons (the latter from the YAG laser). The ADU values range from 0

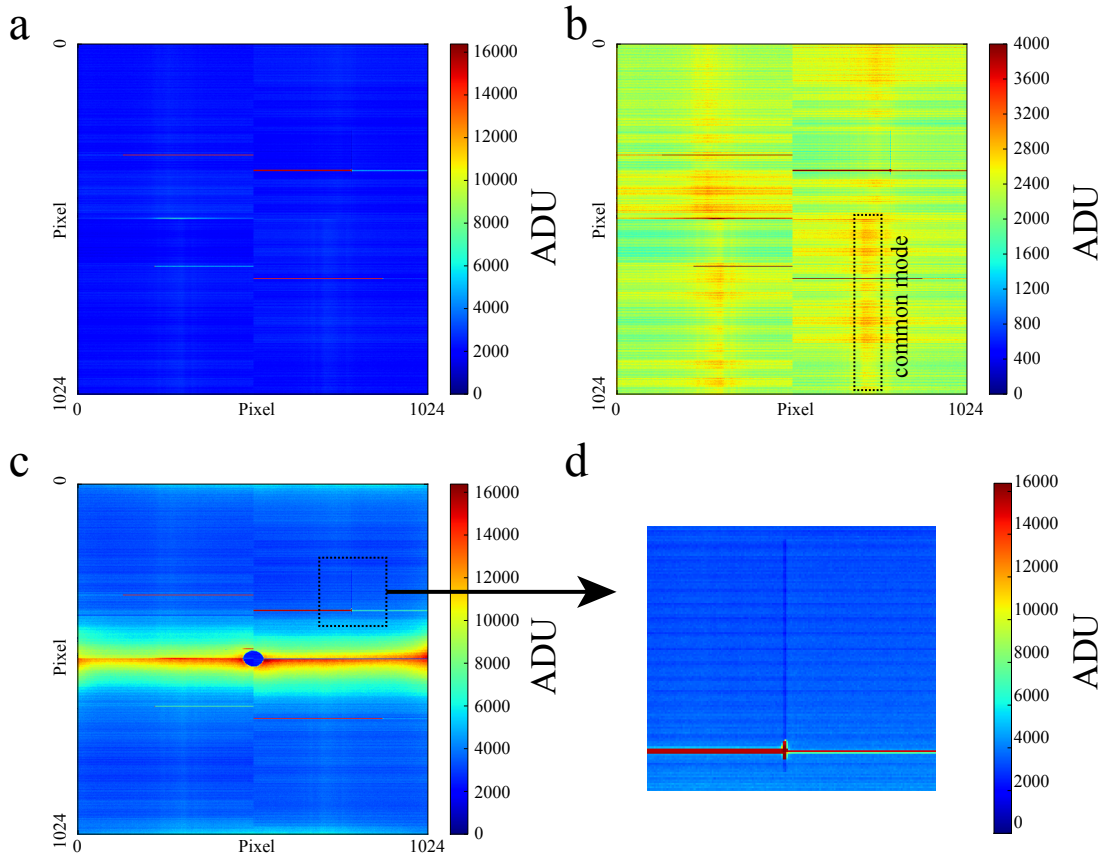

Figure A.1.: Single shot raw data frames of an example dataset for the NoYAG case (a,b) and the YAG case (c,d). Subfigure b (d) shows details of a (c) to illustrate the various artifacts like common mode, bad pixel channels and gain variation of the 16 distinct CAMEX modules; see text for details.

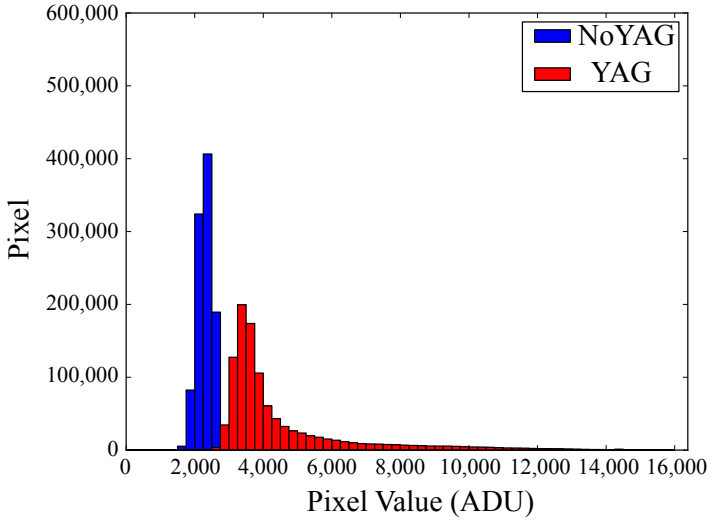

Figure A.2.: Spectra (histogram for the 1024×1024 pnCCD values) for the single shot data frames given in fig. A.1 (a,c); see text for details.

to $2^{14} - 1 = 16,383$. A single 2 keV photon creates 548 electron/hole pairs, corresponding to an ADU-value of 2,600 ADU, while an optical/NIR photon creates 1 electron/hole pair, resulting in a signal of 4.75 ADU [216].

Many artifacts were contained in the single shot raw data frames, which obviously didn't originate from 2 keV photons scattered at the molecules from the molecular beam. A distinct feature of the YAG data was the high signal levels within a broad horizontal stripe at the center and within stripes at the outer edges of the detector. They were based on insufficient shielding to NIR photons from the YAG laser, because the YAG laser was propagating collinearly with the FEL. Other pnCCD-based artifacts included a channel-to-channel variation (horizontally) as well as some broad stripes in vertical direction. The former correponds to a channel-specific offset and gain variation, while the latter was based on time-dependent variations during the read-out of the signals. This is called "common mode", see inlet in fig. A.1 (b). Additional artifacts are visible like channels (horizontal lines) with unusual low/high or even saturated values. Figure A.1 (d) shows a region of the YAG frame, where a channel of saturated values is visible along with a row (vertical) of unusual low signal. These "bad pixel" rows/channels were excluded from the analysis, as will be described later. In addition, fig. A.1 (b) shows clearly the distinct offset and gain in each of the 16 distinct CAMEX modules that the pnCCD detector is made of (for a description of the CAMEX modules, see section 3.2 and/or [136]). Although there is a channel-wise offset and gain variation, all channels within the same CAMEX have similar gain and the difference of the channel-wise gain between distinct CAMEX is more pronounced than the gain variation within one CAMEX.

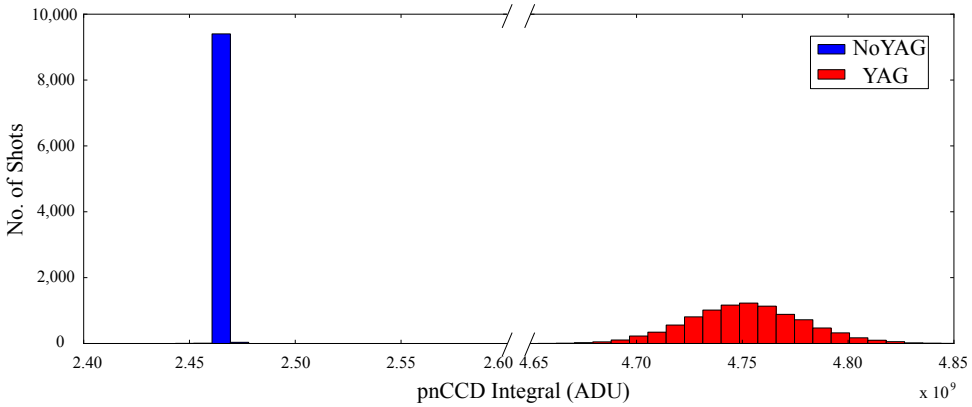

Figure A.3.: Histogram of the total integrated value of individual YAG/NoYAG data for an example dataset containing 9,451 shots with YAG off (NoYAG) and 9,449 shots with YAG on (YAG).

Figure A.2 shows histograms for the 1024×1024 pnCCD values of the single shot data frames given in fig. A.1 (a,c). The width of each bin is 250 ADU. The constant offset of most pixels of ≈ 2,400 ADU in the NoYAG case is obvious. In the YAG case, in addition to the pnCCD-based offset, there is the huge background at the inner (and outer edges) of the two pnCCD panels, resulting in a shift of the spectrum towards higher values. The YAG based "offset" will be called "YAG background" from now on while the channel-wise pnCCD-based offset will simply be called "offset".

Figure A.3 shows a histogram of the total integrated value for individual YAG/NoYAG shots for an example dataset. Offset-based, the mean of the total integrated signal for NoYAG is $2.46 \cdot 10^9$ ADU ±0.04 % while for the YAG shots it is $4.75 \cdot 10^9$ ADU ±0.5 %. The variation in the YAG case is due to the YAG intensity, varying on a shot-to-shot level. The YAG saturates the pnCCD detector in some regions, hence the standard deviation given here (0.5 %) depicts a lower limit of the variation of the YAG intensity. YAG and NoYAG shots are clearly separated regarding the totally integrated pnCCD signal. This will be used to differentiate between YAG and NoYAG shots.

A.2. Offset and Common Mode Correction

The channel-wise offsets were corrected for by subtracting an offset map, which was obtained from averaging many single shot pnCCD frames (some 1,000) while no laser nor the molecular beam was running (a so-called "dark run"). The common mode was corrected for by subtracting the median value along each vertical row from this row, separately for the upper and lower pnCCD panel.

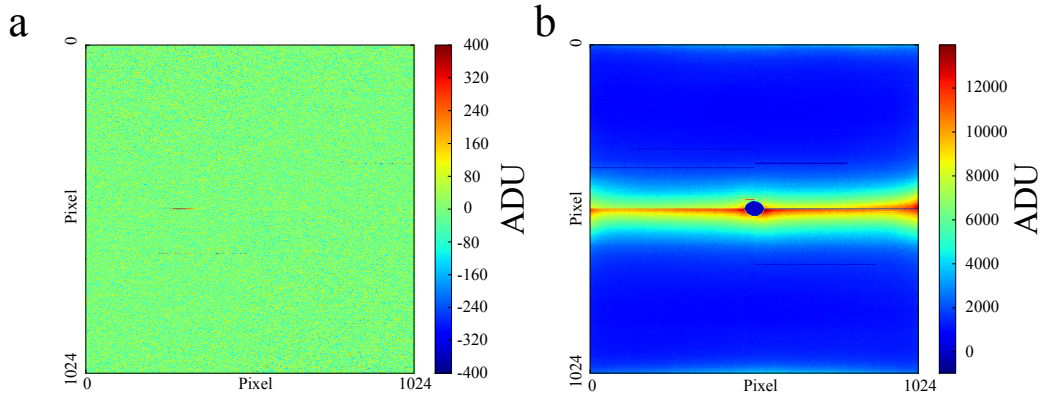

Figure A.4.: Single shot data frames, corrected for channel-dependent offset and common mode.

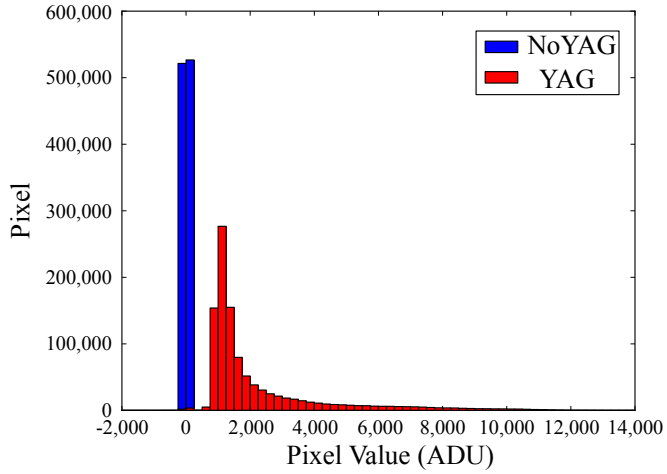

Figure A.5.: Spectra for the single shot data frames given in fig. A.4

Figure A.4 shows an example of the resulting frames for YAG and NoYAG. The data frames look much cleaner now. The NoYAG data is shown with a much narrower colorscale while the YAG data still contains the high signal from the YAG background. The channel-wise signal variation was succesfully corrected for and some regions with unusual high/low intensity ("bad pixels/bad pixel rows/lines") were set to 0 value. Regarding bad pixel lines: Some of the bad pixel lines don't vary in time, they always show unusual very low/high values. However, neighboring channels can show time-wise varying behaviour and hence, cannot be handled with the offset correction. Handling of bad pixels will be described later.

Figure A.5 shows the single shot spectra of the pnCCD values for the example data shown in fig. A.4. The NoYAG data is close to 0 at most pixels, the YAG data still contains higher values based on the YAG background.

A.3. Distinction YAG/NoYAG

The distinction whether the YAG was switched on or off during a certain single shot was crucial to the whole analysis, since the data from many shots had to be averaged due to the very low count rates. The shot-by-shot YAG/NoYAG distinction was made by estimation of the integral value of the individual pnCCD frame. Since the YAG laser was responsible for a strong background on the pnCCDs, this distinction was easily made by comparing the totally integrated signal of the whole pnCCD detector for each shot. As mentioned above, a single YAG photon doesn't create as much charge in the pnCCD as a single 2 keV x-ray photon. However, due to the high YAG intensity, many YAG photons could pile up in a single pixel, especially in the regions which were not shielded thoroughly by the pnCCD filters due to gaps between the filter frame and the frame on which the pnCCD panels are mounted. In addition, in front of and behind the interaction point, steel tubes containing apertures of different size were mounted to reduce straylight as much as possible. Unfortunately, due to their position close to the interaction point and in case of not optimal laser beam alignment, scattering at these apertures may result in straylight from the apertures/light-baffle edges.

The distinction of YAG and NoYAG shots was made by comparing the total integrated CCD values of individual shots and, as pointed out above, this value clearly separates YAG and NoYAG shots. Figure A.6 shows the histogram of the total integral value for the same example dataset used above for fig. A.3. Still, after the offset and common mode correction, YAG and NoYAG shots are well separated by the total intensity measured on the pnCCD for a single shot. The total integrated pnCCD value is centered around 0 ADU

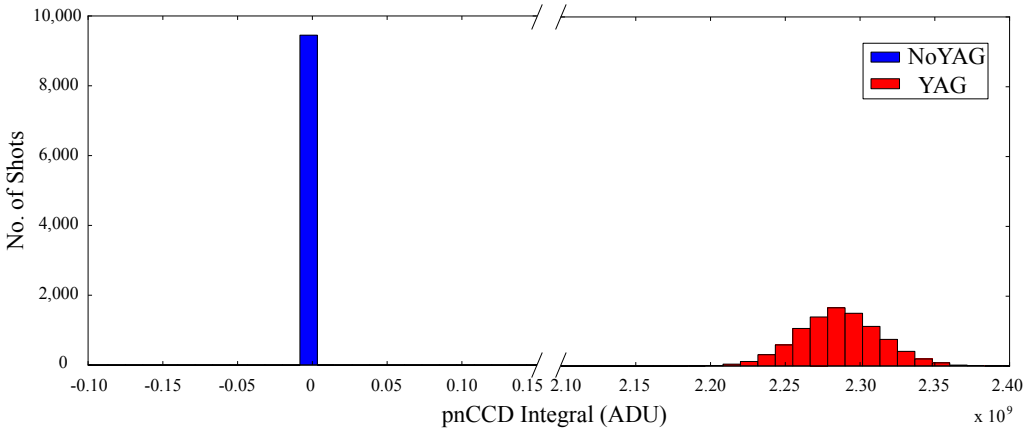

Figure A.6.: Histogram of the total integrated value of individual YAG/NoYAG data for an example dataset containing 9,451 shots with YAG off (NoYAG) and 9,449 shots with YAG on (YAG) after the offset and common mode correction was applied.

for NoYAG shots and around $2.28 \cdot 10^9$ ADU for YAG shots. The distinction of YAG and NoYAG shots, which was used in the graphs before, is now justified and each single shot data with an total integral between -1 $\cdot$ 10^9 and 1 $\cdot$ 10^9 ADU is regarded as a NoYAG shot while each shot with a total integral between 2 $\cdot$ 10^9 and 4 $\cdot$ 10^9 ADU is regarded as a YAG shot. This allows to be independent from a second parallel measurement such as, e. g., a measurement by an additional photodiode. Due to the clear separation of the integral pnCCD values, the distinction works reliably as was confirmed by the VMI data, see chapter 5.

A.4. YAG Background

During the next step, the YAG background scattering was subtracted from the YAG frames. The background from the YAG was obtained by averaging of 1,000 data frames when the YAG was on. The total YAG intensity is varying on a shot-to-shot level but the spatial distribution of the YAG on the pnCCD is independent of a certain shot, i. e., it can be scaled by a single number. Hence, the YAG background of a single frame was obtained by scaling the averaged YAG frame to match the total intensity of a certain single individual shot. This method worked reliably well except for the first shots of each dataset. Therefore, the photon hits extracted from the first 100 shots (extraction of single photon hits will be explained below) were neglected. The same procedure, i. e., subtracting the scaled averaged data from the individual shot data, was applied to NoYAG data as well, despite being not of much additional benefit as the NoYAG data is already "clean" after the offset and common mode corrections were applied.

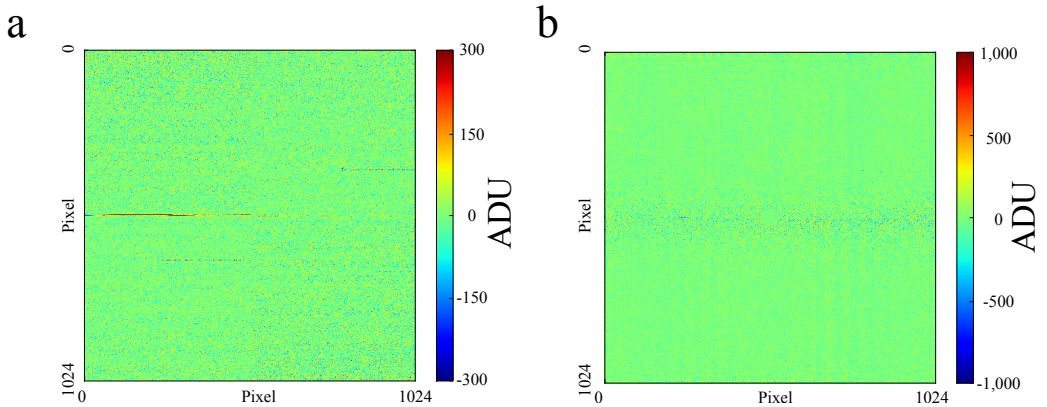

Figure A.7.: Individual single shot data frames for NoYAG (a) and YAG (b) after the scaled averaged background (in the YAG case: the YAG background) was succesfully subtracted from the individual shot data.

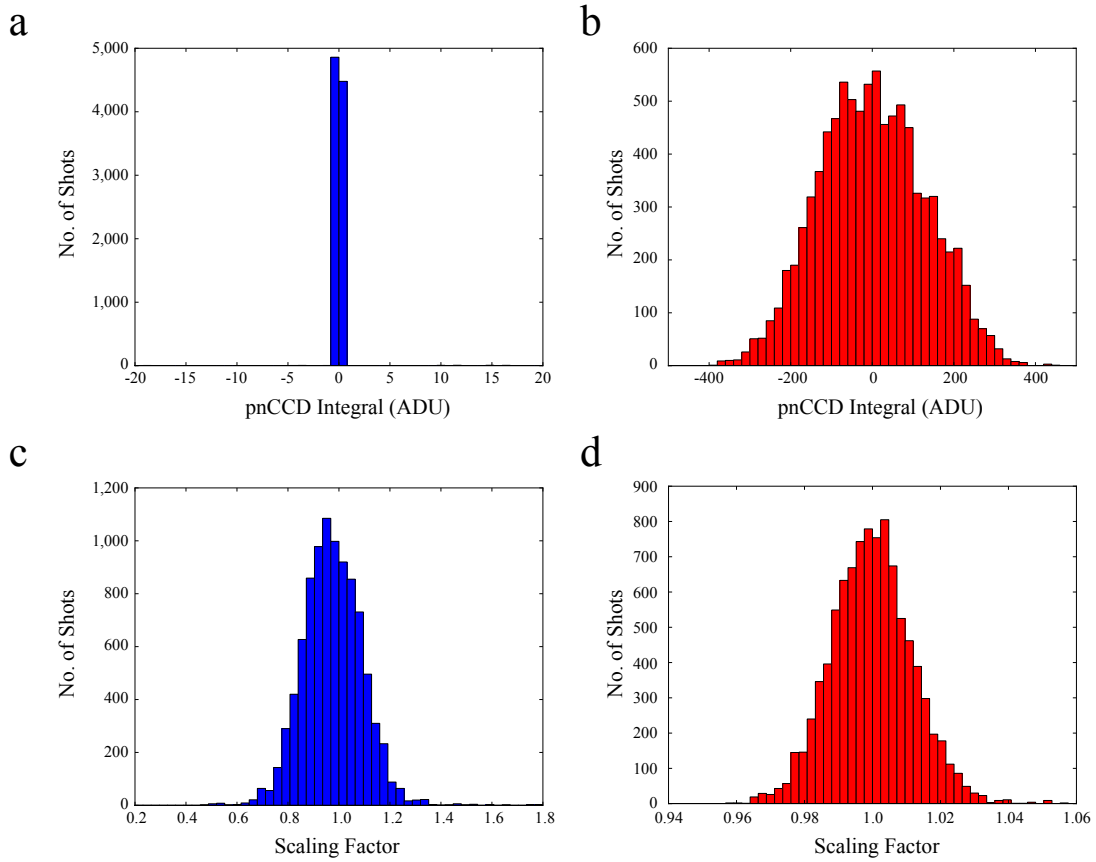

Figure A.8.: Histograms for the total integrated pnCCD value for NoYAG (blue, left column) and YAG (red, right column) after subtraction of the scaled averaged background (a,b) and variation of the scaling factors (c,d) used to scale the averaged background to the same total intensity of an individual shot data frame.

Examples of the resulting single shot data frames are shown in fig. A.7. The colorscales are different to illustrate certain features: First, a line of unusual high intensity is visible in the center of the cleaned NoYAG data. Secondly, in the YAG data the variation in the center part (i. e., in the area which was saturated by the YAG) is higher than in the outer parts of the pnCCD, which can be explained by higher Poisson noise due to higher total signal in this region.

Figure A.8 shows histograms for the total integrated pnCCD value for NoYAG (a) and YAG (b) after subtraction of the scaled averaged background. The variation of the scaling factors, used to scale the averaged background to match the total intensity of an individual shot data frame, is shown in (c,d). For the example dataset used here, the total integrated pnCCD value is centered around zero for NoYAG and YAG respectively. The YAG values (b), however, vary more than the NoYAG values (a). The scaling factor in the YAG case

(d) depicts the shot-to-shot variation of the total YAG intensity. In the NoYAG case (c), the scaling factor has a larger variation, based on the fact, that the NoYAG was almost zero before already and slight deviations are weighted much more than in the YAG case.

A.5. Photon Hits and Event Recombination

During the next step, individual x-ray photons were extracted from the cleaned single-shot data. Single 2 keV photons are expected to be around a signal of 2,600 ADU. The whole procedure described before relies on the assumption that the x-ray photons impinge very rarely on the pnCCD and hence the whole data cleaning procedure, i. e., averaging data frames and subtracting them from a single individual frames, didn't affect single x-ray photons. It has to be considered, that a 2 keV photon in the pnCCD creates a charge cloud which can cross the barrier of a single pixel. Hence, a single photon can lead to a signal in two or more neighboring pixels which have to be added and counted as a single hit, i. e., simple thresholding of the individual cleaned data frames is not sufficient. At 2 keV, the probability to get a single or a double pixel hit, i. e., the charge cloud diffuses into a single neighboring pixel in the latter case, is close to 1 and it is highly unlikely to get hits made up of 3 or more pixels [217]. This is justified by the experimental results (shown later), where 64 % of all x-ray attributed hits are single-pixel hits, 35 % are double-pixel hits while < 1 % make up for the rest.

For finding x-rays in the individually cleaned single-shot data frames, postprocessor 212 of CASS was applied. The algorithm of postprocessor 212 is illustrated in fig. A.9: The whole fully cleaned individual pnCCD frame is examined pixel-by-pixel. If a pixel is found

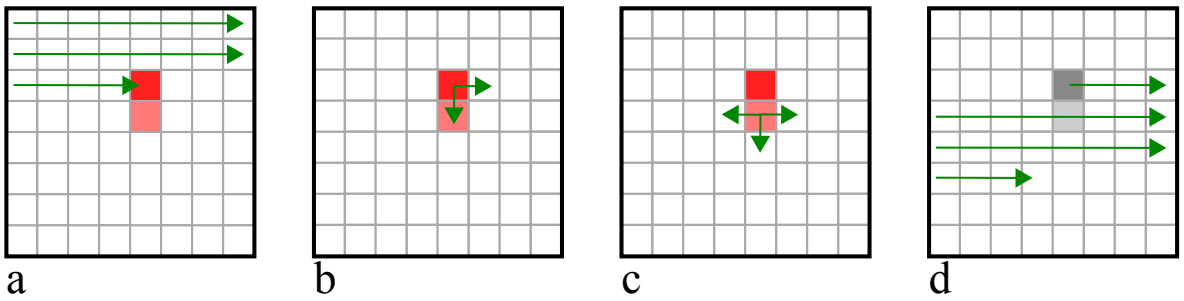

Figure A.9.: Principle of photon hit finding and event recombination performed by CASS' postprocessor 212 for the example of a double-pixel hit: The 1024×1024 single shot data frame is searched channel-wise for pixels exceeding the threshold value of 500 ADU. After such a pixel was found, adjacent pixels exceeding the same threshold will be added to the initial pixel to make up a "single photon hit" event; see text for details.

to be above a certain threshold (a), the so-called "pre-gate" (a threshold of 500 ADU was chosen), then the algorithm checks if any of the adjacent pixels is above this threshold, too (b). Adjacent pixels above the pre-gate value will be added to the value of the original pixel and the algorithm starts again (actually it works in a recursive manner) looking in the neighboring pixels for values above the pre-gate value (c) while keeping track of the number of pixels that have contributed to this single photon hit so far. The algorithm terminates after a user-defined maximum number of pixels that a photon hit can be made of (which was chosen to be 6) or in case no adjacent pixels exceed the pre-gate threshold value. All hits exceeding a total value 1,000 ADU ("main-gate value") were written to a list (an ASCII-file) containing the coordinates, the signal value (in ADU) and the number-of-pixels that have contributed to this hit. Then, the algorithm continues searching the pnCCD dataframe (d). The lists will be called "photon-hits" from now on (although they may not contain solely photons as will be discussed in the following).

Figure A.10 (a,b) show histograms of the hits from the photon lists derived from the example dataset (the same which was used for all previous examples) for NoYAG and YAG respectively, limited to single- and double-pixel hits. The histogram shows the number of hits in certain ADU intervals, hence it is an "energy spectrum" of the obtained hits. One is interested in the spatial distribution, i. e., the diffraction pattern of the x-ray hits with values around 2,600 ADU. The spectra show a huge "tail" at energies below 2,600 ADU. In the NoYAG case, a peak at 2,600 ADU is visible, while in the YAG case it may be completely "buried" in the huge tail. The spatial distribution of single- and double-pixel hits is shown in fig. A.10 (c – f), where 16×16 pixels were binned together. Figure A.10 (c,d) show the spatial distribution in the energy interval of 1,000 – 2,000 ADU of the "histogram tail". It is clearly seen, that the hits in 1,000 – 2,000 ADU are almost entirely limited to the edges of the pnCCD panels or bad pixel lines on the CCD. In the YAG case there is a huge concentration of these hits in the center part which collected a huge amount of YAG photons, up to saturation, indicating problems with the YAG background subtraction. On the other hand, the 2,000 – 4,000 ADU hits are distributed over the whole CCD despite some bad pixels that are left. Further bad pixel corrections are explained below.

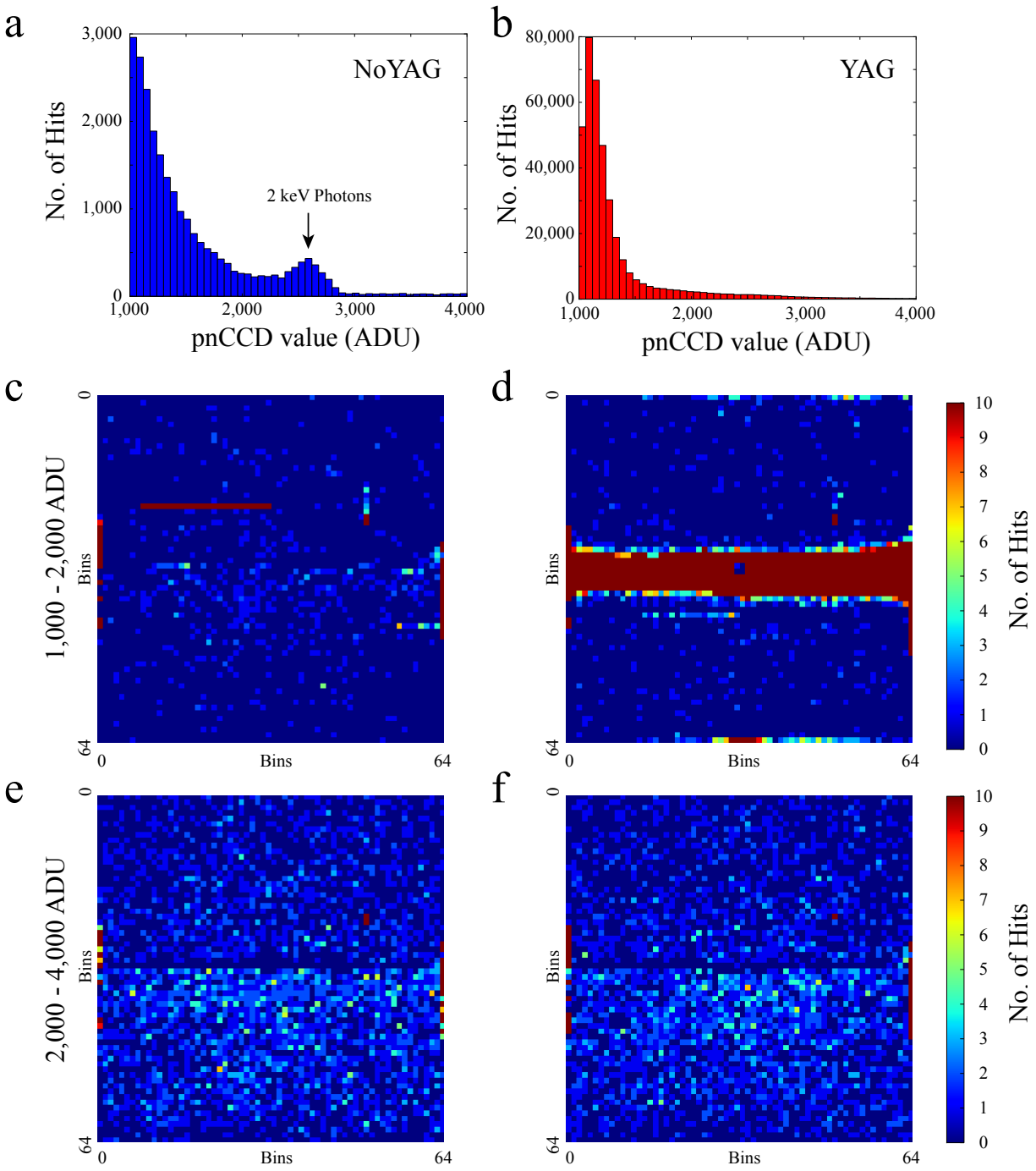

Figure A.10.: Spectra of the hits from photon lists for NoYAG (a) and YAG (b) for hits made up out of 1-2 pixels (single- and double-pixel hits); spatial distribution of these hits in distinct energy intervals: 1,000 – 2,000 ADU (c: NoYAG, d: YAG), and 2,000 – 4,000 ADU (e: NoYAG, f: YAG); see text for details

Figure A.11 shows spectra and spatial distributions for hits made up of 3 – 6 pixels. The NoYAG spectrum looks strange and there is no clear peak at 2,600 ADU anymore. The YAG spectrum shows the big "tail" again. The hits are either concentrated at the saturated center or along bad pixel lines, with only a small amount of pixels distributed in the rest of the pnCCD as can be seen in the spatial distributions (c – f). Both spectra contain only hits with energies > 1,500 ADU. This is, because a 3-pixel hit was at least made up of 3 pixels exceeding the pre-gate value of 500 ADU, hence the lowest value in the spectrum has to be 1,500 ADU.

As a result, only single- and double-pixel hits were considered for the final analysis and 3–6-pixel hits were thrown out of the lists. In addition, a so-called "bad pixel map" was made up which marks all bad pixels which have to be thrown away. The final bad pixel map will be explained below.

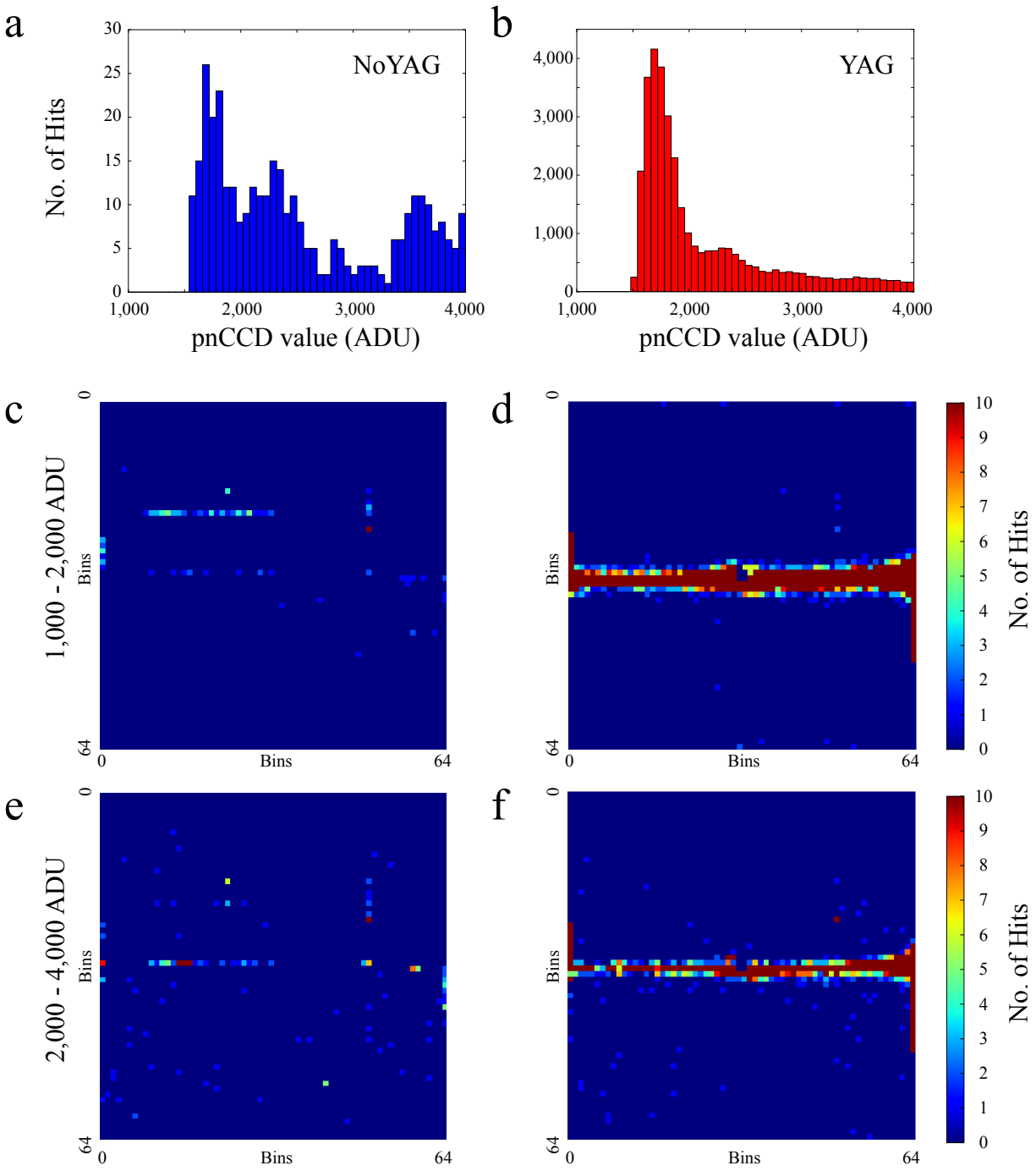

Figure A.11.: Spectra of the hits from photon lists for NoYAG (a) and YAG (b) for hits made up out of 3 – 6 pixels; spatial distribution of these hits in distinct energy intervals: 1,000 – 2,000 ADU (c: NoYAG, d: YAG), and 2,000 – 4,000 ADU (e: NoYAG, f: YAG); see text for details

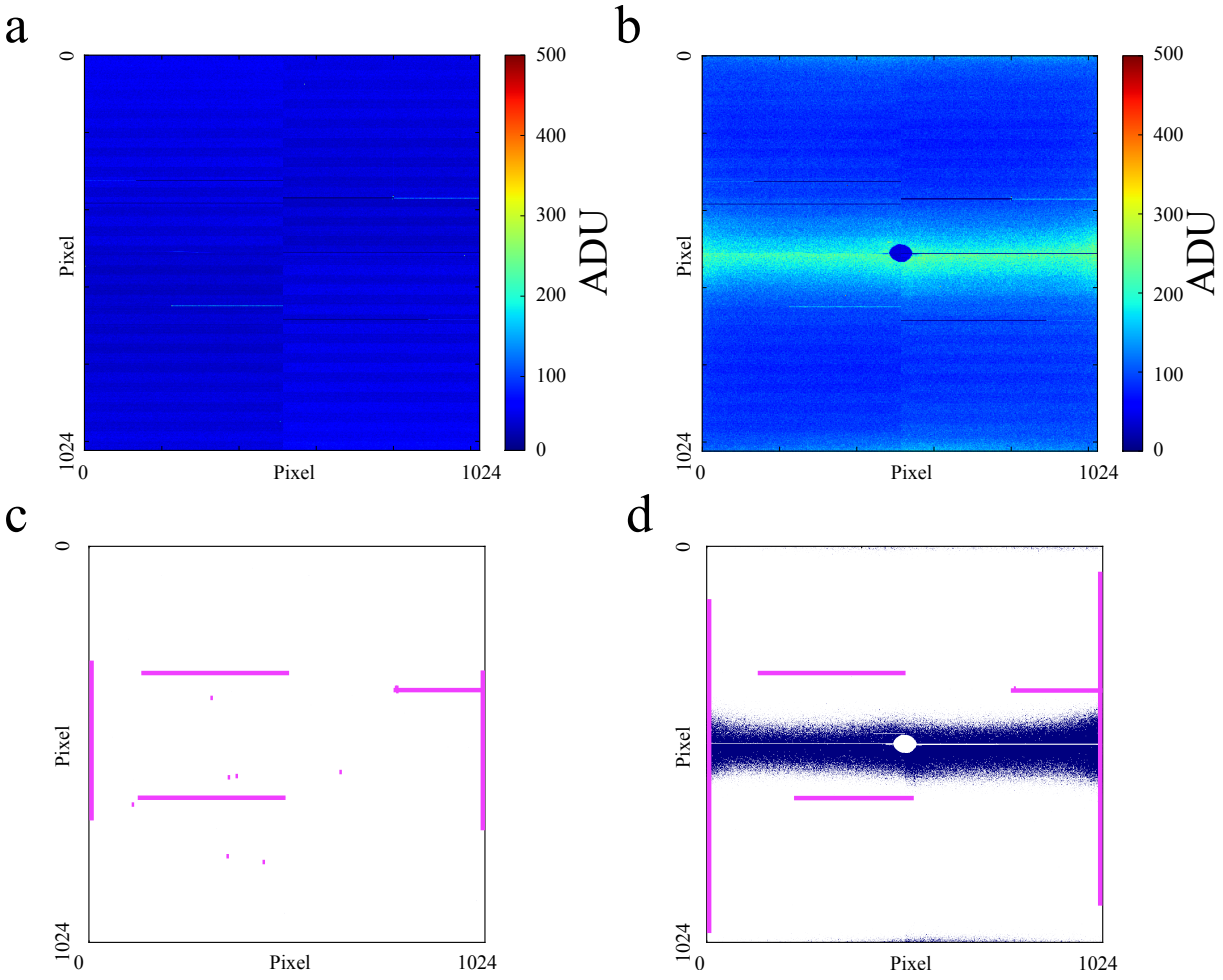

Figure A.12.: Pixel-to-pixel standard deviation σ_{pixel} of fully cleaned frames for NoYAG (a) and YAG (b). Regions, where $3\sigma_{\text{pixel}} > 500$ ADU (and therefore had to be masked for further analysis) for NoYAG (c) and YAG (d); see text for details.

The concentration of many hits in the center part of the pnCCD in the YAG case can be explained by the YAG background subtraction. Even after the subtraction of the scaled averaged YAG frame, there is a variation in this region. Now, the pre-gate threshold has to be higher than the noise (i. e., error) based on this variation. Figure A.12 shows the pixel-to-pixel standard deviation σ_{pixel} of the NoYAG (a) and YAG (b) data after all cleaning was performed (i. e., after the scaled averaged YAG- or NoYAG-background was subtracted). It was obtained from averaging 1,000 completely cleaned single shot data frames in the YAG and NoYAG case respectively. Regions of comparably high standard deviation in the NoYAG case (a) are entirely limited to certain lines (i. e., bad pixel lines). Additionally to bad pixel lines, the center part of the pnCCD shows increased standard deviation around 200 ADU the YAG case (b). Figure A.12 (c,d) show the regions, where

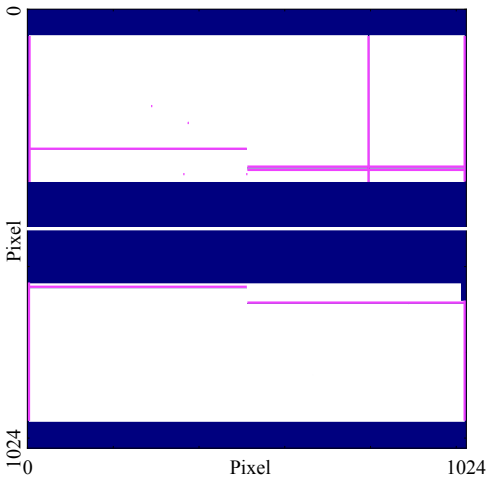

Figure A.13.: "Bad Pixel Map", schematically showing regions of the pnCCD which cannot be trusted and the photon hits extracted in these areas have to be neglected; see text for details.

$3\sigma_{\text{pixel}} > 500$ ADU (dark blue, magenta) and where $3\sigma_{\text{pixel}} < 500$ ADU (white). Magenta areas mark regions, which are, in reality, just very thin lines, rows or even single pixels and were exagerrated for illustrative reasons. I. e., the magenta horizontal lines comprise actually just a few pnCCD channels; the same goes for the single "points", the latter just being single pixels exceeding $3\sigma_{\text{pixel}}$. Areas marked in dark blue are not exagerrated. In the center part of the YAG frame, $3\sigma_{\text{pixel}}$ is exceeding 500 ADU and hence the hits obtained from this region (with a pre-gate value of 500 ADU, see above) cannot be trusted. Of course, the saturated parts of the innermost center part have to be neglected in any case (they also show up in fig. A.12 d). By plotting the hits from all photon lists together and carefully checking their spatial distribution on the pnCCDs for lines/rows of unusual low/high intensity, bad pixel lines were identified which, together with the center part of the pnCCD, have to be thrown out of the lists. Eventually, a map of all pixels that cannot be trusted (i. e., a "bad pixel map") is derived and hits in pixels marked as bad pixels were thrown out of the photon lists.

Figure A.13 shows the schematic bad pixel map. Areas that "can be trusted", i. e., where photon hits were derived from, are shown in white. Bad pixel areas are marked in dark blue. Magenta areas mark bad pixel areas, which are, in reality, just very thin lines/rows or even single pixels and, for illustrative reasons are exagerrated in the image. E. g., the four magenta horizontal lines comprise actually just a few pnCCD channels; the same goes for the three vertical lines and the single magenta "points", the latter just being single pixels with unusual high signal.

A.6. Final Data Cleaning

Despite the data cleaning steps explained so far, further processing of the photon lists that were written by CASS was necessary. Further cleaning was performed by self-written Python-scripts.

First, all hits in pixels marked as bad pixels were thrown out of the photon lists. Secondly, only single- and double-pixel-hits were kept. All 3–6-pixel-hits were thrown out of the lists. During the third step, a correction for channel-dependent gain was applied to the ADU-values of each pixel hit. Although, this is not 100% correct for hits made up of two pixels, because the hits extracted from the data by CASS are already "combined"[1], it works sufficiently as neighboring channels have similar gain and bigger differences in gain are only between different CAMEX modules. Overall, channel-dependent gain variation is < 10 % for all channels. The fourth step involves correction for charge-transfer efficiency ("CTE correction"). During readout, the charges (i. e., the "signal") are transferred along each channel horizontally towards the analogue-digital-converting unit of each CAMEX. Shifting of charges from one pixel to the other during read-out results in a loss of charges, characterized by the so-called "charge transfer efficiency" (CTE). The CTE was 0.999921/pixel [218], resulting in a maximum loss of signal of 4 % for charges created in the center of the pnCCDs, i. e., charges that have to be shifted by 512 pixels for readout from the center towards the left and right pnCCD edges.

Figure A.14 (a,b) show spectra for the completely cleaned lists, combined of all runs that were considered for the data analysis of diffraction by aligned DIBN molecules. Only single and double pixels hits were taken into account as mentioned above. The spectrum is nicely peaking at 2,600 ADU, indicating that the correct 2 keV photons were extracted from the raw data. The peak has a certain width attributed to the event recombination of double pixel hits which is easily explained: Imagine an x-ray hit is redistributed over 2 pixels with one pixel containing the value of 499 and the other one the value of 2,101. Then, the first pixel does not exceed the threshold and doesn't contribute to the hit. Hence, thresholding of the cleaned single shot dataframes (by the pre-gate value) together with event recombination is responsible for the width of the peak. In addition, the cleaned frame obtained by subtraction of averaged YAG and NoYAG data is not exactly zero everywhere but exhibit a certain variation, see fig. A.12, which results in broadening of the peak. Further broadening of the peak is due to the energy resolution of the pnCCDs. The energy spread at distinct photon energies (with the pnCCDs operating at -70°C) was

[1] The gain- and CTE correction was implemented in CASS just very recently.

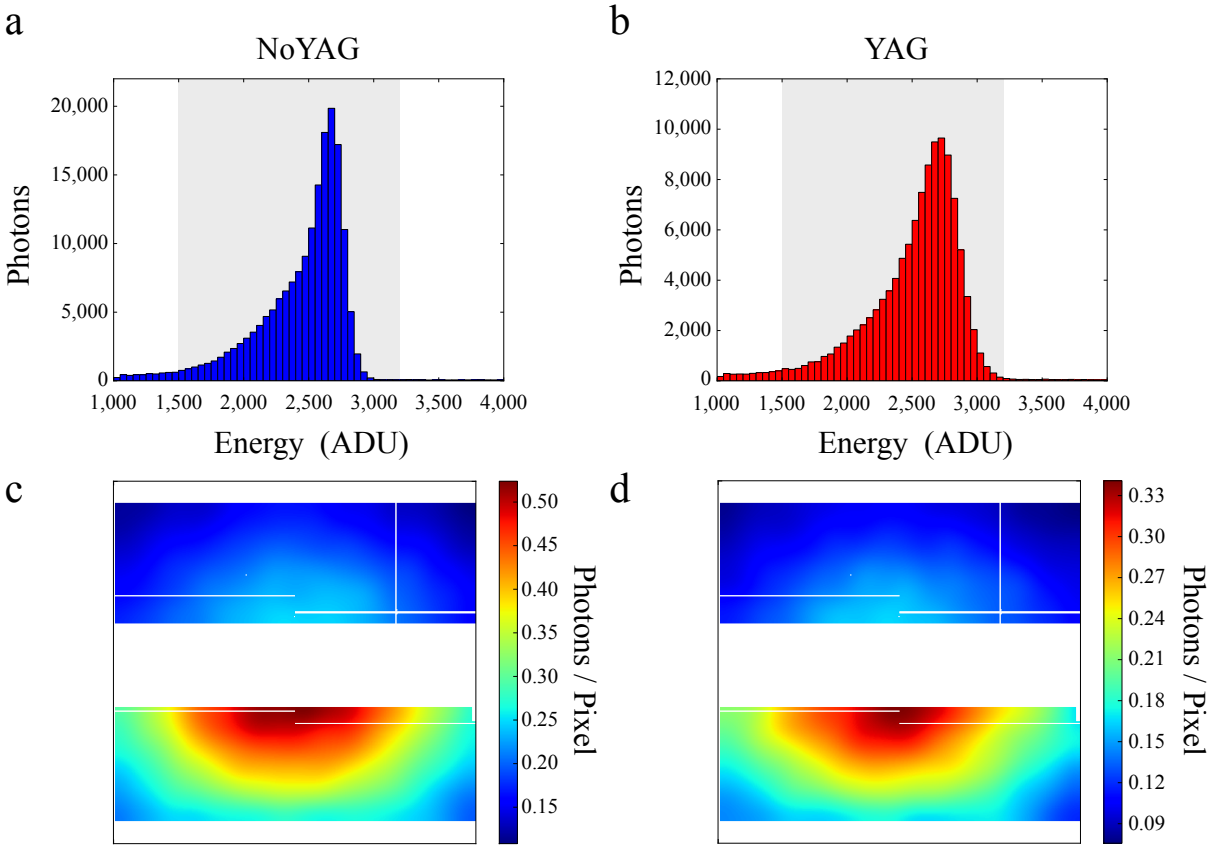

Figure A.14.: Spectra of the hits from completely cleaned photon lists for NoYAG (a) and YAG (b) for hits made up out of 1 – 2 pixels; spatial distribution of these hits in the energy interval 1,500 – 3,200 ADU (c,d). The raw data was convoluted with a gaussian kernel.

determined, e. g., by Meidinger et al. [158]: For 1,486 eV it is 66 – 74 eV (FWHM) while at 5,894 eV it is 123 – 131 eV (FWHM). For 2 keV, it can be assumed to be in the range 70 – 90 eV at 2 keV [159], (i. e., 3.5 – 4.5 % corresponding to a spread of 91 – 117 ADU at 2,600 ADU), an effect much smaller than the effect mentioned above.

In the energy interval 1,500 – 3,200 ADU there are 172,499 photons for the NoYAG and 111,560 photons for the YAG data which are used for data analysis. The data was obtained from 842,722 shots (NoYAG) and 563,453 shots (YAG) respectively. Hence the average hit rate was 0.204 photons/shot (NoYAG) and 0.197 photons/shot (YAG). The results from the data analysis of the diffraction data shown in fig. A.14 (c,d) are presented and discussed in chapter 7.

B. Properties of 2,5-diiodobenzonitrile

Here, the properties of 2,5-diiodobenzonitrile, ($C_7H_3I_2N$, DIBN), the target molecule of the x-ray diffraction experiment are summarized. The molecule is depicted in fig. B.1, the scale bar depicts the lengthscale most relevant to the diffraction experiment, i. e., the

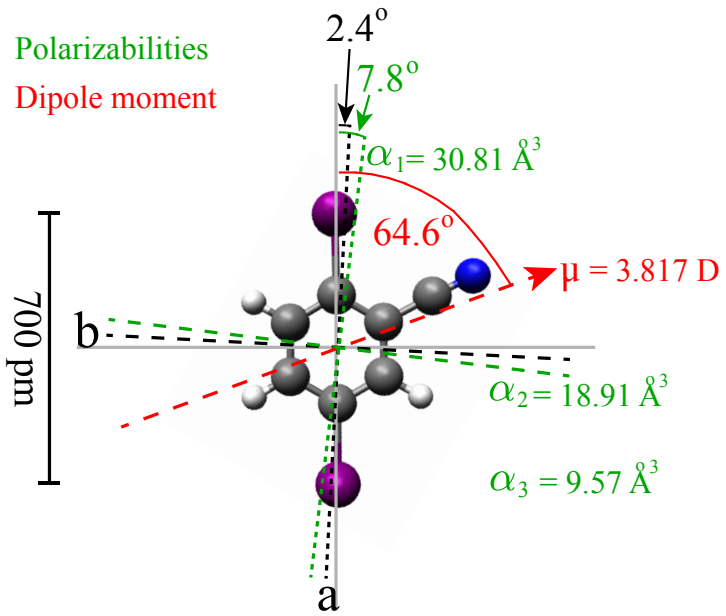

Figure B.1.: Molecular structure of 2,5-diiodobenzonitrile along with the axes of the relevant properties such as rotational constants (A, B, C, along axes a,b,c), dipole moment (μ), and polarizabilities ($\alpha_{1,2,3}$). The grey lines represent a coordinate system centered in the center-of-mass with one axis pointing along the iodine-iodine axis. The angles are given with respect to the iodine-iodine axis. See text for details.

iodine-iodine (I-I) distance which is almost exactly 700 pm (the exact value is 698.4 pm, obtained by ab-initio calculations as explained in the following). The geometry as well as the permanent dipole moment μ and the components of the polarizability tensor $\alpha_{1,2,3}$ have been obtained by ab-initio calculations (GAMESS-US MP2/6-311G** [124]). The rotational constants can be directly inferred from the geometry. The orientations of the relevant properties such as rotational constants (A, B, C, along axes a, b, c), dipole moment (μ), and polarizabilities $\alpha_{1,2,3}$ are given in fig. B.1 with respect to a coordinate system centered in the center-of-mass and represented by the grey lines. One of the grey axes is pointing along the iodine-iodine axis and the angles are given with respect to that axis.

Crucial for the diffraction experiment, which mainly exploits the I-I interference, is the orientation of the most-polarizable axis (MPA). The MPA lies in the molecular plane, inclined by 7.8° with respect to the I-I axis. The values of the components $\alpha_{1,2}$ are given in fig. B.1 ($\alpha_1 = 30.81$ Å^3, $\alpha_2 = 18.91$ Å^3). The smallest component of the polarizability, oriented perpendicular to the molecular plane, is $\alpha_3 = 9.57$ Å^3. The permanent dipole moment μ lies in the molecular plane, its value is given in fig. B.1. The rotational constants of DIBN are $A = 1.39$ GHz, $B = 1.54$ GHz, and $C = 1.38$ GHz. The rotational constants, however, have not been utilized for, e. g., calculation of Stark shifts because the large nuclear-spin quadrupolar coupling constants, which are of the the same order of magnitude as the rotational constants, have not been considered yet in the CMIstark software, as has been argued in chapter 4.

Bibliography

[1] W. C. Röntgen, *Über eine neue Art von Strahlen*, Annalen der Physik **300**, 12 (1898).

[2] International Union of Crystallography, *Nobel Prize Winners associated with Crystallography* (2013), `http://www.iucr.org/people/nobel-prize`, from 05/04/2013.

[3] W.-L. Bragg, *The Specular Reflection of X-rays*, Nature **90**, 410 (1912).

[4] W.-L. Bragg, *The Structure of Some Crystals as Indicated by Their Diffraction of X-rays*, Proc. R. Soc. Lond. A **89**, 248 (1913).

[5] B. Rupp, *Biomolecular Crystallography: Principles, Practice, and Application to Structural Biology* (Garland Science, Taylor & Francis Group, 270 Madison Avenue, New York NY 10016, USA, 2009), 1st ed.

[6] D. Harker and J. S. Kasper, *Phases of Fourier coefficients directly from crystal diffraction data*, Acta Cryst. **1**, 70 (1948).

[7] D. Sayre, *The squaring method: a new method for phase determination*, Acta Cryst. **5**, 60 (1952).

[8] R.E. Franklin, R.G. Gosling, *Molecular configuration in sodium thymonucleate*, Nature **171**, 740 (1953).

[9] J. Watson and F. Crick, *Molecular structure of nucleic acids: A Structure for Deoxyribose Nucleic Acid*, Nature **171**, 737 (1953).

[10] R. Henderson, *The Potential and Limitations of Neutrons, Electrons and X-Rays for Atomic-Resolution Microscopy of Unstained Biological Molecules*, Quart. Rev. Biophys. **28**, 171 (1995).

[11] J. C. H. Spence and R. B. Doak, *Single molecule diffraction*, Phys. Rev. Lett. **92**, 198102 (2004).

[12] R. Neutze, R. Wouts, D. van der Spoel, E. Weckert, and J. Hajdu, *Potential for biomolecular imaging with femtosecond X-ray pulses*, Nature **406**, 752 (2000).

[13] J. Solem, *High-intensity x-ray holography: an approach to high-resolution snapshot imaging of biological specimens*, Tech. Report LA-9508-MS (1982).

[14] J. C. Solem, *Imaging biological specimens with high-intensity soft x rays*, J. Opt. Soc. Am. B **3**, 1551 (1986).

[15] P. Schmüser, M. Dohlus, and J. Rossbach, *Ultraviolet and Soft X-Ray Free-Electron Lasers*, Springer Tracts in Modern Physics (Springer Verlag, Berlin Heidelberg, 2008), 1st ed.

[16] H. Motz, *Applications of the Radiation from Fast Electron Beams*, J. Appl. Phys. **22**, 527 (1951).

[17] R. W. H. Motz, W. Thon, *Experiments on Radiation by Fast Electron Beams*, J. Appl. Phys. **24**, 826 (1953).

[18] R. M. Phillips, *History of the ubitron*, Nucl. Instrum. Meth. A **272**, 1 (1988).

[19] J. Madey, *Stimulated emission of Bremsstrahlung in a Periodic Magnetic Field*, J. Appl. Phys. **42**, 1906 (1971).

[20] LCLS, *LCLS-FAQ* (2013), `https://portal.slac.stanford.edu/sites/lclscore_public/Lists\/LCLS_FAQ/FAQ.aspx`, from 05/04/2013.

[21] B. W. J. McNeil and N. R. Thompson, *X-ray free-electron lasers*, Nat. Photon. **4**, 814 (2010).

[22] L. Young, et al., *Femtosecond electronic response of atoms to ultra-intense x-rays*, Nature **466**, 56 (2010).

[23] B. Rudek, et al., *Ultra-efficient ionization of heavy atoms by intense x-ray free-electron laser pulses*, Nat. Photon. **6**, 858 (2012).

[24] H. N. Chapman, et al., *Femtosecond diffractive imaging with a soft-x-ray free-electron laser*, Nat. Phys. **2**, 839 (2006).

[25] A. Barty, et al., *Ultrafast single-shot diffraction imaging of nanoscale dynamics*, Nat. Photon. **2**, 415 (2008).

[26] D. P. DePonte, U. Weierstall, K. Schmidt, J. Warner, D. Starodub, J. C. H. Spence, and R. B. Doak, *Gas dynamic virtual nozzle for generation of microscopic droplet streams*, J. Phys. D Appl. Phys. **41**, 195505 (2008).

[27] M. M. Seibert, et al., *Single mimivirus particles intercepted and imaged with an x-ray laser*, Nature **470**, 78 (2011).

[28] H. N. Chapman, et al., *Femtosecond x-ray protein nanocrystallography*, Nature **470**, 73 (2011).

[29] L. Redecke, et al., *Natively Inhibited Trypanosoma brucei Cathepsin B Structure Determined by Using an X-ray Laser*, Science **339**, 227 (2013).

[30] J. C. H. Spence, U. Weierstall, and H. N. Chapman, *X-ray lasers for structural and dynamic biology*, Rep. Prog. Phys. **75**, 102601 (2012).

[31] N.-T. D. Loh and V. Elser, *Reconstruction algorithm for single-particle diffraction imaging experiments*, Phys. Rev. E **80**, 026705 (2009).

[32] R. Fung, V. Shneerson, D. Saldin, and A. Ourmazd, *Structure from fleeting illumination of faint spinning objects in flight*, Nat. Phys. **5**, 64 (2009).

[33] D. K. Saldin, V. L. Shneerson, R. Fung, and A. Ourmazd, *Structure of isolated biomolecules obtained from ultrashort x-ray pulses: exploiting the symmetry of random orientations*, Journal of Physics: Condensed Matter **21**, 134014 (2009).

[34] G. Huldt, A. Szoke, and J. Hajdu, *Diffraction imaging of single particles and biomolecules*, J. Struct. Biol. **144**, 219 (2003).

[35] A. Barty, J. Küpper, and H. N. Chapman, *Molecular Imaging Using X-Ray Free-Electron Lasers*, Annu. Rev. Phys. Chem. **64**, 415 (2013).

[36] O. M. Yefanov and I. A. Vartanyants, *Orientation determination in single-particle x-ray coherent diffraction imaging experiments*, J. Phys. B **46**, 164013 (2013).

[37] G. von Helden, T. Wyttenbach, and M. T. Bowers, *Conformation of macromolecules in the gas-phase – use of matrix-assisted laser-desorption methods in ion chromatography*, Science **267**, 1483 (1995).

[38] F. Filsinger, U. Erlekam, G. von Helden, J. Küpper, and G. Meijer, *Selector for structural isomers of neutral molecules*, Phys. Rev. Lett. **100**, 133003 (2008).

[39] F. Filsinger, J. Küpper, G. Meijer, J. L. Hansen, J. Maurer, J. H. Nielsen, L. Holmegaard, and H. Stapelfeldt, *Pure samples of individual conformers: the separation of stereo-isomers of complex molecules using electric fields*, Angew. Chem. Int. Ed. **48**, 6900 (2009).

[40] F. Filsinger, G. Meijer, H. Stapelfeldt, H. Chapman, and J. Küpper, *State- and conformer-selected beams of aligned and oriented molecules for ultrafast diffraction studies*, Phys. Chem. Chem. Phys. **13**, 2076 (2011).

[41] M. Altarelli, et al., Tech. Rep., DESY, Hamburg, Germany (2007), `http://xfel.desy.de/technical_information/tdr/tdr/`.

[42] L. Holmegaard, J. H. Nielsen, I. Nevo, H. Stapelfeldt, F. Filsinger, J. Küpper, and G. Meijer, *Laser-induced alignment and orientation of quantum-state-selected large molecules*, Phys. Rev. Lett. **102**, 023001 (2009).

[43] H. Ihee, M. Lorenc, T. Kim, Q. Kong, M. Cammarata, J. Lee, S. Bratos, and M. Wulff, *Ultrafast x-ray diffraction of transient molecular structures in solution*, Science **309**, 1223 (2005).

[44] H. Ihee, V. Lobastov, U. Gomez, B. Goodson, R. Srinivasan, C. Ruan, and A. H. Zewail, *Direct imaging of transient molecular structures with ultrafast diffraction*, Science **291**, 458 (2001).

[45] H. Ihee, B.M. Goodson, R. Srinivasan, V.A. Lobastov, A.H. Zewail, *Ultrafast electron diffraction and structural dynamics: transient intermediates in the elimination reaction of $C_2F_4I_2$*, J. Phys. Chem. A **106**, 4087 (2002).

[46] C. J. Hensley, J. Yang, and M. Centurion, *Imaging of isolated molecules with ultrafast electron pulses*, Phys. Rev. Lett. **109**, 133202 (2012).

[47] E. B. Wilson, *Microwave spectroscopy in chemistry*, Science **162**, 59 (1968).

[48] C. H. Townes and A. L. Schawlow, *Microwave Spectroscopy* (Dover Publications, New York, 1975).

[49] W. Gordy and R. L. Cook, *Microwave Molecular Spectra* (John Wiley & Sons, New York, NY, USA, 1984), 3rd ed.

[50] J. Emsley, J. Feeney, and L. Sutcliffe, *High resolution nuclear magnetic resonance spectrocopy*, vol. 1 (Pergamon Press Ltd., Headington Hill Hall, Oxford, 1965), 1st ed.

[51] J. Emsley, J. Feeney, and L. Sutcliffe, *High resolution nuclear magnetic resonance spectrocopy*, vol. 2 (Pergamon Press Ltd., Headington Hill Hall, Oxford, 1965), 1st ed.

[52] J. Kraitchman, *Determination of molecular structure from microwave spectroscopic data*, Am. J. Phys. **21**, 17 (1953).

[53] P. M. Felker, *Rotational Coherence Spectroscopy - Studies Of The Geometries Of Large Gas-phase Species By Picosecond Time-domain Methods*, J. Phys. Chem. **96**, 7844 (1992).

[54] C. Riehn, *High-resolution pump-probe rotational coherence spectroscopy - rotational constants and structure of ground and electronically excited states of large molecular systems*, Chem. Phys. **283**, 297 (2002).

[55] G. Scoles, *Atomic and Molecular Beam Methods* (Oxford University Press, 1988).

[56] C. Schröter, K. Kosma, and T. Schultz, *CRASY: Mass- or Electron-Correlated Rotational Alignment Spectroscopy*, Science **333**, 1011 (2011).

[57] G. G. Brown, B. Dian, K. O. Douglass, S. M. Geyer, S. T. Shipman, and B. H. Pate, *A broadband fourier transform microwave spectrometer based on chirped pulse excitation*, Rev. Sci. Instrum. **79**, 053103 (2008).

[58] B. C. Dian, G. G. Brown, K. O. Douglass, and B. H. Pate, *Measuring picosecond isomerization kinetics via broadband microwave spectroscopy*, Science **320**, 924 (2008).

[59] B. C. Dian, G. G. Brown, K. O. Douglass, F. S. Rees, J. E. Johns, P. Nair, R. D. Suenram, and B. H. Pate, *Conformational isomerization kinetics of pent-1-en-4-yne with 3,330 cm^{-1} of internal energy measured by dynamic rotational spectroscopy*, PNAS **105**, 12696 (2008).

[60] J. Emsley and J. Feeney, *Forty years of Progress in Nuclear Magnetic Resonance Spectroscopy*, Progress in Nuclear Magnetic Resonance Spectroscopy **50**, 179 (2007).

[61] K. Wüthrich, *The way to NMR structures of proteins*, Nat. Struct. Mol. Biol. **8**, 923 (2001).

[62] K. Wüthrich, *NMR Studies of Structure and Function of Biological Macromolecules (Nobel Lecture)*, Angewandte Chemie International Edition **42**, 3340 (2003).

[63] K. Pervushin, R. Riek, G. Wider, and K. Wüthrich, *Attenuated T_2 relaxation by mutual cancellation of dipole-dipole coupling and chemical shift anisotropy indicates an avenue to NMR structures of very large biological macromolecules in solution.*, PNAS **94**, 12366 (1997).

[64] R. Riek, G. Wider, K. Pervushin, and K. Wüthrich, *Polarization transfer by cross-correlated relaxation in solution NMR with very large molecules*, PNAS **96**, 4918 (1999).

[65] M. Billeter, G. Wagner, and K. Wüthrich, *Solution nmr structure determination of proteins revisited*, Journal of Biomolecular NMR **42**, 155 (2008).

[66] J. Itatani, J. Levesque, D. Zeidler, H. Niikura, H. Pépin, J. C. Kieffer, P. B. Corkum, and D. M. Villeneuve, *Tomographic imaging of molecular orbitals*, Nature **432**, 867 (2004).

[67] L. Holmegaard, J. L. Hansen, L. Kalhøj, S. L. Kragh, H. Stapelfeldt, F. Filsinger, J. Küpper, G. Meijer, D. Dimitrovski, M. Abu-samha, C. P. J. Martiny, and L. B. Madsen, *Photoelectron angular distributions from strong-field ionization of oriented molecules*, Nat. Phys. **6**, 428 (2010).

[68] C. Z. Bisgaard, O. J. Clarkin, G. Wu., A. M. D. Lee, O. Geßner, C. C. Hayden, and A. Stolow, *Time-resolved molecular frame dynamics of fixed-in-space CS_2 molecules*, Science **323**, 1464 (2009).

[69] F. Krasniqi, B. Najjari, L. Strüder, D. Rolles, A. Voitkiv, and J. Ullrich, *Imaging molecules from within: Ultrafast angström-scale structure determination of molecules via photoelectron holography using free-electron lasers*, Phys. Rev. A **81**, 033411 (2010).

[70] O. Stern, *Ein Weg zur experimentellen Prüfung der Richtungsquantelung im Magnetfeld*, Z. Phys. **7**, 249 (1921).

[71] W. Gerlach and O. Stern, *Der experimentelle Nachweis der Richtungsquantelung im Magnetfeld*, Z. Phys. **9**, 349 (1922).

[72] H. Kallmann and F. Reiche, *Über den Durchgang bewegter Moleküle durch inhomogene Kraftfelder*, Z. Phys. **6**, 352 (1921).

[73] E. Wrede, *Über die Ablenkung von Molekularstrahlen elektrischer Dipolmoleküle im inhomogenen elektrischen Feld*, Z. Phys. **44**, 261 (1927).

[74] O. Stern, *Zur Methode der Molekularstrahlen I*, Z. Phys. **39**, 751 (1926).

[75] J. P. Gordon, H. J. Zeiger, and C. H. Townes, *Molecular microwave oscillator and new hyperfine structure in the microwave spectrum of NH_3*, Phys. Rev. **95**, 282 (1954).

[76] T. Maiman, *Stimulated optical radiation in ruby*, Nature **187**, 493 (1960).

[77] H. L. Bethlem, G. Berden, and G. Meijer, *Decelerating neutral dipolar molecules*, Phys. Rev. Lett. **83**, 1558 (1999).

[78] S. Y. T. van de Meerakker, H. L. Bethlem, and G. Meijer, *Taming molecular beams*, Nat. Phys. **4**, 595 (2008).

[79] F. Filsinger, *Manipulation of large neutral molecules with electric fields*, Ph.D. thesis, Radboud Universiteit, Nijmegen, The Netherlands (2010).

[80] S. Putzke, F. Filsinger, H. Haak, J. Küpper, and G. Meijer, *Rotational-state-specific guiding of large molecules*, Phys. Chem. Chem. Phys. **13**, 18962 (2011).

[81] K. Wohlfart, F. Grätz, F. Filsinger, H. Haak, G. Meijer, and J. Küpper, *Alternating-gradient focusing and deceleration of large molecules*, Phys. Rev. A **77**, 031404(R) (2008).

[82] S. Putzke, F. Filsinger, J. Küpper, and G. Meijer, *Alternating-Gradient Focusing of the Benzonitrile-Argon Van der Waals Complex*, J. Chem. Phys. **137**, 104310 (2012).

[83] H. Stapelfeldt and T. Seideman, *Colloquium: Aligning molecules with strong laser pulses*, Rev. Mod. Phys. **75**, 543 (2003).

[84] P. M. Chaikin and T. C. Lubensky, *Principles of Condensed Matter Physics* (Cambridge University Press, 2000).

[85] V. Aquilanti, D. Ascenzi, D. Cappelletti, and F. Pirani, *Velocity Dependence Of Collisional Alignment Of Oxygen Molecules In Gaseous Expansions*, Nature **371**, 399 (1994).

[86] V. Aquilanti, D. Ascenzi, M. Vitores, F. Pirani, and D. Cappelletti, *A quantum mechanical view of molecular alignment and cooling in seeded supersonic expansions*, J. Chem. Phys. **111**, 2620 (1999).

[87] F. Pirani, D. Cappelletti, M. Bartolomei, V. Aquilanti, M. Scotoni, M. Vescovi, D. Ascenzi, and D. Bassi, *Orientation of Benzene in Supersonic Expansions, Probed by IR-Laser Absorption and by Molecular Beam Scattering*, Phys. Rev. Lett. **86**, 5035 (2001).

[88] B. Friedrich and D. R. Herschbach, *Spatial orientation of molecules in strong electric fields and evidence for pendular states*, Nature **353**, 412 (1991).

[89] B. Friedrich and D. Herschbach, *Alignment and trapping of molecules in intense laser fields*, Phys. Rev. Lett. **74**, 4623 (1995).

[90] T. Seideman and E. Hamilton, *Nonadiabatic alignment by intense pulses. concepts, theory, and directions*, Adv. Atom. Mol. Opt. Phys. **52**, 289 (2005).

[91] R. N. Zare, *Optical Preparation Of Aligned Reagents*, Berichte der Bunsengesellschaft für physikalische Chemie **86**, 422 (1982).

[92] M. S. de Vries, V. I. Srdanov, C. P. Hanrahan, and R. M. Martin, *Orientation dependence in the reaction of Xe^* with photodissociation polarized IBr*, J. Chem. Phys. **78**, 5582 (1983).

[93] B. A. Zon and B. G. Katsnelson, *Nonresonant scattering of intense light by a molecule*, Sov.Phys. JETP **42**, 595 (1976), `http://www.jetp.ac.ru/cgi-bin/dn/e_042_04_0595.pdf`.

[94] B. Friedrich, D. P. Pullman, and D. R. Herschbach, *Alignment and orientation of rotationally cool molecules*, J. Chem. Phys. **95**, 8118 (1991).

[95] D. Normand, L. Lompre, and C. Cornaggia, *Laser-induced molecular alignment probed by a double-pulse experiment*, J. Phys. B **25**, 497 (1992).

[96] B. Friedrich and D. Herschbach, *Polarization of molecules induced by intense nonresonant laser fields*, J. Phys. Chem. **99**, 15686 (1995).

[97] W. Kim and P. Felker, *Spectroscopy of pendular states in optical-field-aligned species*, J. Chem. Phys. **104**, 1147 (1996).

[98] H. Sakai, C. P. Safvan, J. J. Larsen, K. M. Hilligsøe, K. Hald, and H. Stapelfeldt, *Controlling the alignment of neutral molecules by a strong laser field*, J. Chem. Phys. **110**, 10235 (1999).

[99] J. J. Larsen, H. Sakai, C. P. Safvan, I. Wendt-Larsen, and H. Stapelfeldt, *Aligning molecules with intense nonresonant laser fields*, J. Chem. Phys. **111**, 7774 (1999).

[100] B. Friedrich and D. Herschbach, *Manipulating molecules via combined static and laser fields*, J. Phys. Chem. A **103**, 10280 (1999).

[101] T. Seideman, *Rotational excitation and molecular alignment in intense laser fields* , J. Chem. Phys. **103**, 7887 (1995).

[102] F. Rosca-Pruna and M. Vrakking, *Experimental observation of revival structures in picosecond laser-induced alignment of I_2*, Phys. Rev. Lett. **87** (2001).

[103] F. Rosca-Pruna and M. J. J. Vrakking, *Revival structures in picosecond laser-induced alignment of I_2 molecules. I. Experimental results*, J. Chem. Phys. **116**, 6567 (2002).

[104] J. Nielsen, *Laser-induced alignment and orientation of quantum-state selected molecules and molecules in liquid helium droplets*, Ph.D. thesis, University of Aarhus (2012).

[105] D. Pentlehner, J. H. Nielsen, A. Slenczka, K. Mølmer, and H. Stapelfeldt, *Impulsive laser induced alignment of molecules dissolved in helium nanodroplets*, Phys. Rev. Lett. **110**, 093002 (2013).

[106] Y.-P. Chang, F. Filsinger, B. G. Sartakov, and J. Küpper, *CMIstark: Python package for the Stark-effect calculation and symmetry classification of linear, symmetric and asymmetric top wavefunctions in dc electric fields*, Comp. Phys. Comm. (2013).

[107] J. Küpper and F. Filsinger, *libcoldmol: A particle trajectory calculation framework (2003-2008)* (2008), `http://libcoldmol.cold-molecules.info`, from 10/10/2013.

[108] M. Born and R. Oppenheimer, *Zur Quantentheorie der Molekeln*, Ann. Physik **84**, 457 (1927).

[109] W. Demtröder, *Molekühlphysik, Theoretische Grundlagen und experimentelle Methoden* (Oldenbourg Verlag München Wien, 2003).

[110] B. S. Ray, *Über die Eigenwerte des asymmetrischen Kreisels*, Z. Phys. **78**, 74 (1932).

[111] G. W. King, R. M. Hainer, and P. C. Cross, *The asymmetric rotor I. Calculation and symmetry classification of energy levels*, J. Chem. Phys. **11**, 27 (1943).

[112] J. K. G. Watson, *Determination of centrifugal distorsion coefficients of asymmetric top molecules*, J. Chem. Phys. **46**, 1935 (1967).

[113] S. C. Wang, *On the asymmetrical top in quantum mechanics*, Phys. Rev. **34**, 243 (1929).

[114] J. Stark and G. Wendt, *Beobachtungen über den Effekt des elektrischen Feldes auf Spektrallinien. II. Längseffekt*, Ann. Phys. **348**, 983 (1914).

[115] M. Abd El Rahim, R. Antoine, M. Broyer, D. Rayane, and P. Dugourd, *Asymmetric top rotors in electric fields: Influence of chaos and collisions in molecular beam deflection experiments*, J. Phys. Chem. A **109**, 8507 (2005).

[116] F. Filsinger, J. Küpper, G. Meijer, L. Holmegaard, J. H. Nielsen, I. Nevo, J. L. Hansen, and H. Stapelfeldt, *Quantum-state selection, alignment, and orientation of large molecules using static electric and laser fields*, J. Chem. Phys. **131**, 064309 (2009).

[117] Comsol, *Multiphysics 3.4* (2007), `http://www.comsol.com/products/news/3.4`.

[118] C. Z. Bisgaard, *Laser induced alignment*, Ph.D. thesis, University of Aarhus, Aarhus, Denmark (2006).

[119] R. N. Zare, *Angular Momentum* (John Wiley & Sons, New York, NY, USA, 1988).

[120] E. Hamilton, T. Seideman, T. Ejdrup, M. D. Poulsen, C. Z. Bisgaard, S. S. Viftrup, and H. Stapelfeldt, *Alignment of symmetric top molecules by short laser pulses*, Phys. Rev. A **72**, 043402 (2005).

[121] J. J. Larsen, K. Hald, N. Bjerre, H. Stapelfeldt, and T. Seideman, *Three dimensional alignment of molecules using elliptically polarized laser fields*, Phys. Rev. Lett. **85**, 2470 (2000).

[122] J. J. Larsen, *Laser induced alignment of neutral molecules*, Ph.D. thesis, Aarhus University, Aarhus, Denmark (2000).

[123] L. Holmegaard, *Laser-induced alignment and orientation; photoelectron angular distributions from strong field ionization*, Ph.D. thesis, Aarhus University, Aarhus, Denmark (2010).

[124] M. W. Schmidt, et al., *General atomic and molecular electronic structure system*, J. Comput. Chem. **14**, 1347 (1993).

[125] J. Als-Nielsen and D. McMorrow, *Elements of Modern X-ray Physics* (John Wiley & Sons, Chichester, West Sussex, United Kingdom, 2001).

[126] R. A. Kirian, X. Wang, U. Weierstall, K. E. Schmidt, J. C. H. Spence, M. Hunter, P. Fromme, T. White, H. N. Chapman, and J. Holton, *Femtosecond protein nanocrystallography; data analysis methods*, Opt. Express **18**, 5713 (2010).

[127] D. Waasmaier and A. Kirfel, *New analytical scattering-factor functions for free atoms and ions*, Acta Cryst. A **51**, 416 (1995).

[128] B. Henke, E. Gullikson, and J. Davis, *X-Ray Interactions: Photoabsorption, Scattering, Transmission, and Reflection at E = 50-30,000 eV, Z = 1-92*, Atomic Data and Nuclear Data Tables **54**, 181 (1993).

[129] U. Even, J. Jortner, D. Noy, N. Lavie, and N. Cossart-Magos, *Cooling of large molecules below 1 K and He clusters formation*, J. Chem. Phys. **112**, 8068 (2000).

[130] G. Berden, W. L. Meerts, and E. Jalviste, *Rotationally resolved ultraviolet spectroscopy of indole, indazole, and benzimidazole: Inertial axis reorientation in the $S_1(^1L_b) \leftarrow S_0$ transitions*, J. Chem. Phys. **103**, 9596 (1995).

[131] T. M. Korter, D. W. Pratt, and J. Küpper, *Indole-H_2O in the gas phase. structures, barriers to internal motion, and $S_1 \leftarrow S_0$ transition moment orientation. solvent reorganization in the electronically excited state*, J. Phys. Chem. A **102**, 7211 (1998).

[132] A. W. Potts, M. L. Lyus, E. P. F. Lee, and G. H. Fattahallah, *High resolution ultraviolet photoelectron spectra of C_6H_5X and p-$C_6H_4X_2$ where X = Cl, Br or I*, J. Chem. Soc., Faraday Trans. 2 **76**, 556 (1980).

[133] W. Wiley and I. Mclaren, *Time-of-flight Mass Spectrometer With Improved Resolution*, Rev. Sci. Instrum. **26**, 1150 (1955).

[134] J. Küpper, U. Hoppe, H. Junkes, C. Tschentscher, C. Kuhlisch, and A. Stanik, *KouDa - Cold Molecules Data Acquisition* (2013), `http://kouda.cold-molecules.info`, from 12/01/2013.

[135] P. Emma, et al., *First lasing and operation of an angstrom-wavelength free-electron laser*, Nat. Photon. **4**, 641 (2010).

[136] L. Strüder, et al., *Large-format, high-speed, X-ray pnCCDs combined with electron and ion imaging spectrometers in a multipurpose chamber for experiments at 4th generation light sources*, Nucl. Instrum. Meth. A **614**, 483 (2010).

[137] HASYLAB, *FEL Basics* (2013), `http://hasylab.desy.de/facilities/sr_and_fel_basics/fel_basics/index_eng.html`, from 12/01/2013.

[138] S. Moeller, et al., *Photon beamlines and diagnostics at LCLS*, Nucl. Instrum. Meth. A **635**, S6 (2011).

[139] P. Emma, J. Frisch, and P. Krejcik, in *Proceedings Particle Accelerator Conference* (2001), pp. 18–22, `www-ssrl.slac.stanford.edu/lcls/technotes/lcls-tn-00-12.pdf`.

[140] Y. Ding, et al., *Measurements and Simulations of Ultralow Emittance and Ultrashort Electron Beams in the Linac Coherent Light Source*, Phys. Rev. Lett. **102**, 254801 (2009).

[141] I. Grguras, et al., *Ultrafast x-ray pulse characterization at free-electron lasers*, Nat. Photon. **6**, 852 (2012).

[142] M. Harmand, R. Coffee, M. R. Bionta, M. Chollet, D. French, D. Zhu, D. M. Fritz, H. T. Lemke, N. Medvedev, B. Ziaja, S. Toleikis, and M. Cammarata, *Achieving few-femtosecond time-sorting at hard X-ray free-electron lasers*, Nat. Photon. **7**, 215 (2013).

[143] J. D. Bozek, *AMO instrumentation for the LCLS X-ray FEL*, Eur. Phys. J. Special Topics **169**, 129 (2009).

[144] P. Heimann, et al., *Linac Coherent Light Source soft x-ray materials science instrument optical design and monochromator commissioning*, Rev. Sci. Instrum. **82**, 093104 (2011).

[145] D. Fritz, in *Frontiers in Optics 2009/Laser Science XXV/Fall 2009 OSA Optics & Photonics Technical Digest* (Optical Society of America, 2009), p. LSMD2, `http://www.opticsinfobase.org/abstract.cfm?URI=LS-2009-LSMD2`.

[146] S. Boutet and G. Williams, *The Coherent X-ray Imaging (CXI) instrument at the Linac Coherent Light Source (LCLS)* , New J. Phys. **12**, 035024 (2010).

[147] A. Robert, in *Frontiers in Optics 2009/Laser Science XXV/Fall 2009 OSA Optics & Photonics Technical Digest* (Optical Society of America, 2009), p. LSThC1, `http://www.opticsinfobase.org/abstract.cfm?URI=LS-2009-LSThC1`.

[148] R. F. Boyce, R. M. Boyce, G. Haller, J. B. Hastings, G. Hays, H. J. Lee, R. W. Lee, B. Nagler, M. Scharfenstein, D. Marsh, and W. E. White, *Matter in Extreme Conditions Instrument - Conceptual Design Report*, SLAC National Accelerator Laboratory, (2009) (2009).

[149] B. Rudek, *Multiple ionization of heavy atoms by intense x-ray free-electron laser pulses*, Ph.D. Thesis, Ruprecht-Karls-Universität Heidelberg (2012).

[150] B. Erk, *Fragmentation dynamics of small molecules upon multiple ionization by x-ray free-electron laser pulses*, Ph.D. Thesis, Ruprecht-Karls-Universität Heidelberg (2013).

[151] N. Meidinger, R. Andritschke, R. Hartmann, S. Herrmann, P. Holl, G. Lutz, and L. Strüder, *pnCCD for photon detection from near-infrared to X-rays*, Nucl. Instrum. Meth. A **565**, 251 (2006).

[152] L. Strüder, et al., *The European Photon Imaging Camera on XMM-Newton: The pn-CCD camera* , Astronomy and Astrophysics **365**, L18 (2001).

[153] S. Düsterer, et al., *Femtosecond x-ray pulse length characterization at the Linac Coherent Light Source free-electron laser*, New J. Phys. **13**, 093024 (2011).

[154] S. Bajt, private communication, 04/24/2012 (2012).

[155] R. Hartmann, private communication, 10/02/2012 (2012).

[156] R. Hartmann, S. Epp, S. Herrmann, P. Holl, N. Meidinger, C. Reich, D. Rolles, H. Soltau, L. Struder, J. Ullrich, and G. Weidenspointner, in *Nuclear Science Symposium Conference Record, 2008. NSS '08. IEEE* (2008), pp. 2590–2595, `http://ieeexplore.ieee.org/xpl/articleDetails.jsp?arnumber=4774888`.

[157] G. Weidenspointner, S. Epp, A. Hartmann, R. Hartmann, G. Hauser, P. Holl, N. Kimmel, D. Rolles, L. Strüder, and J. Ullrich, *Practical experience from operating the imaging pnCCD instrument of the CAMP chamber at LCLS*, Proc. SPIE 8078, Advances in X-ray Free-Electron Lasers: Radiation Schemes, X-ray Optics, and Instrumentation p. 80780U (2011).

[158] N. Meidinger, et al., *Next generation of pnCCDs for X-ray spectroscopy and imaging*, Nucl. Instrum. Meth. A **568**, 141 (2006).

[159] S. Epp, private communication, 02/18/2013 (2013).

[160] SLAC, *Photon Controls and Data Systems Group, LCLS-pdsdata Reference Manual* (2013), `https://confluence.slac.stanford.edu/display/PCDS/pdsdata+Reference+Manual`, from 01/12/2013.

[161] L. Foucar, et al., *CASS—CFEL-ASG software suite*, Comp. Phys. Comm. **183**, 2207 (2012).

[162] H. J. Loesch and A. Remscheid, *Brute force in molecular reaction dynamics: A novel technique for measuring steric effects*, J. Chem. Phys. **93**, 4779 (1990).

[163] B. Friedrich and D. R. Herschbach, *On the possibility of orienting rotationally cooled polar molecules in an electric field*, Z. Phys. D **18**, 153 (1991).

[164] B. Friedrich and D. Herschbach, *Enhanced orientation of polar molecules by combined electrostatic and nonresonant induced dipole forces*, J. Chem. Phys. **111**, 6157 (1999).

[165] S. Trippel, Y.-P. Chang, S. Stern, T. Mullins, L. Holmegaard, and J. Küpper, *Spatial separation of state- and size-selected neutral clusters*, Phys. Rev. A **86**, 033202 (2012).

[166] J. T. Vivian and P. R. Callis, *Mechanisms of tryptophan fluorescence shifts in proteins*, Biophys J **80**, 2093 (2001).

[167] H. Lami and N. Glasser, *Indole solvatochromism revisited*, J. Chem. Phys. **84**, 597 (1986).

[168] C. Kang, T. M. Korter, and D. W. Pratt, *Experimental measurement of the induced dipole moment of an isolated molecule in its ground and electronically excited states: Indole and indole–H_2O*, J. Chem. Phys. **122**, 174301 (2005).

[169] F. C. De Lucia, P. Helminger, R. L. Cook, and W. Gordy, *Submillimeter Microwave Spectrum of* $H_2{}^{16}O$, Phys. Rev. A **5**, 487 (1972).

[170] S. L. Shostak, W. L. Ebenstein, and J. S. Muenter, *The dipole moment of water. I. Dipole moments and hyperfine properties of H_2O and HDO in the ground and excited vibrational states*, J. Chem. Phys. **94**, 5875 (1991).

[171] W. Caminati and S. Dibernardo, *Microwave-spectrum and amino hydrogen location in indole*, J. Mol. Struct. **240**, 253 (1990).

[172] S. Blanco, J. Lopez, J. Alonso, P. Ottaviani, and W. Caminati, *Pure rotational spectrum and model calculations of indole-water*, J. Chem. Phys. **119**, 880 (2003).

[173] M. S. Gordon and M. W. Schmidt, in *Theory and Applications of Computational Chemistry: the first forty years*, edited by C. E. Dykstra, G. Frenking, K. S. Kim, and G. E. Scuseria (Elsevier, Amsterdam, 2005).

[174] J. R. Carney and T. S. Zwier, *Infrared and ultraviolet spectroscopy of water-containing clusters of indole, 1-methylindole, and 3-methylindole*, J. Phys. Chem. A **103**, 9943 (1999).

[175] K. R. F. Somers, E. S. Kryachko, and A. Ceulemans, *Theoretical study of indole: protonation, indolyl radical, tautomers of indole, and its interaction with water*, Chem. Phys. **301**, 61 (2004).

[176] J. K. G. Watson, in *Vibrational Spectra and Structure*, edited by J. R. Durig (Marcel Dekker, 1977), vol. 6, p. 1.

[177] M. Hillenkamp, S. Keinan, and U. Even, *Condensation limited cooling in supersonic expansions*, J. Chem. Phys. **118**, 8699 (2003).

[178] G. Berden, W. L. Meerts, M. Schmitt, and K. Kleinermanns, *High resolution UV spectroscopy of phenol and the hydrogen bonded phenol-water cluster*, J. Chem. Phys. **104**, 972 (1996).

[179] P. R. Bunker and P. Jensen, *Fundamentals of Molecular Symmetry*, Series in Chemical Physics (Institute of Physics Publishing, Bristol, UK, 2005).

[180] O. Dorosh, E. Białkowska-Jaworska, Z. Kisiel, and L. Pszczółkowski, *New measurements and global analysis of rotational spectra of Cl-, Br-, and I-benzene: Spectroscopic constants and electric dipole moments*, J. Mol. Spec. **246**, 228 (2007).

[181] O. Ghafur, A. Rouzee, A. Gijsbertsen, W. K. Siu, S. Stolte, and M. J. J. Vrakking, *Impulsive orientation and alignment of quantum-state-selected NO molecules*, Nat. Phys. **5**, 289 (2009).

[182] A. Rouzee, F. Kelkensberg, W. K. Siu, G. Gademann, R. R. Lucchese, and M. J. J. Vrakking, *Photoelectron kinetic and angular distributions for the ionization of aligned molecules using a HHG source*, J. Phys. B **45**, 074016 (2012).

[183] J. Hansen, H. Stapelfeldt, D. Dimitrovski, M. Abu-Samha, C. Martiny, and L. Madsen, *Time-resolved photoelectron angular distributions from strong-field ionization of rotating naphthalene molecules*, Phys. Rev. Lett. **106**, 073001 (2011).

[184] M. Poulsen, E. Skovsen, and H. Stapelfeldt, *Photodissociation of laser aligned iodobenzene: Towards selective photoexcitation*, J. Chem. Phys. **117**, 2097 (2002).

[185] S.-K. Son, private communication, 07/11/2013 (2013).

[186] S.-K. Son and R. Santra, *Monte Carlo calculation of ion, electron, and photon spectra of xenon atoms in x-ray free-electron laser pulses*, Phys. Rev. A **85**, 063415 (2012).

[187] M. J. Berger, J. H. Hubbell, S. M. Seltzer, J. Chang, J. S. Coursey, R. Sukumar, D. S. Zucker, and K. Olsen, *XCOM: Photon Cross Sections Database* (2010), available at `http://physics.nist.gov/xcom`, National Institute of Standards and Technology, Gaithersburg, MD.

[188] J. A. Bearden and A. F. Burr, *Reevaluation of x-ray atomic energy levels*, Rev. Mod. Phys. **39**, 125 (1967).

[189] A. Kochur, A. Dudenko, V. Sukhorukov, and I. Petrov, *Direct Hartree-Fock calculation of multiple Xe(i+) ion production through inner shell vacancy de-excitations*, J. Phys. B **27**, 1709 (1994).

[190] D. Rolles, private communication, 04/23/2013 (2013).

[191] V. Kumarappan, C. Z. Bisgaard, S. S. Viftrup, L. Holmegaard, and H. Stapelfeldt, *Role of rotational temperature in adiabatic molecular alignment*, J. Chem. Phys. **125**, 194309 (2006).

[192] S. Marchesini, *A unified evaluation of iterative projection algorithms for phase retrieval*, Rev. Sci. Instrum. **78**, 011301 (2007).

[193] S. Pabst, P. J. Ho, and R. Santra, *Computational studies of x-ray scattering from three-dimensionally-aligned asymmetric-top molecules*, Phys. Rev. A **81**, 043425 (2010).

[194] P. J. Ho, D. Starodub, D. K. Saldin, V. L. Shneerson, A. Ourmazd, and R. Santra, *Molecular structure determination from x-ray scattering patterns of laser-aligned symmetric-top molecules*, J. Chem. Phys. **131**, 131101 (2009).

[195] L. Holmegaard, private communication, 01/14/2013 (2013).

[196] I. A. Vartanyants, et al., *Coherence Properties of Individual Femtosecond Pulses of an X-Ray Free-Electron Laser*, Phys. Rev. Lett. **107**, 144801 (2011).

[197] K. Nakamura (Particle Data Group), *Review of particle physics*, J. Phys. G **137**, 075021 (2010), section 33 (Statistics).

[198] B. Erk, et al., *Ultrafast charge rearrangement and nuclear dynamics upon inner-shell multiple ionization of small polyatomic molecules*, Phys. Rev. Lett. **110**, 053003 (2013).

[199] A. Barty, et al., *Self-terminating diffraction gates femtosecond x-ray nanocrystallography measurements*, Nat. Photon. **6**, 35 (2012).

[200] G. Potdevin, U. Trunk, and H. Graafsma, *Performance simulation of a detector for 4th generation photon sources: The AGIPD*, Nucl. Instrum. Meth. A **607**, 51 (2009).

[201] B. Henrich, et al., *The adaptive gain integrating pixel detector AGIPD a detector for the European XFEL*, Nucl. Instrum. Meth. A **633**, S11 (2011).

[202] S. Marchesini, H. He, H. N. Chapman, S. P. Hau-Riege, A. Noy, M. R. Howells, U. Weierstall, and J. C. H. Spence, *X-ray image reconstruction from a diffraction pattern alone*, Phys. Rev. B **68**, 140101 (2003).

[203] M. N. Slipchenko, S. Kuma, T. Momose, and A. F. Vilesov, *Intense pulsed helium droplet beams*, Rev. Sci. Instrum. **73**, 3600 (2002).

[204] S. P. Hau-Riege, R. A. London, H. N. Chapman, A. Szoke, and N. Timneanu, *Encapsulation and Diffraction-Pattern-Correction Methods to Reduce the Effect of Damage in X-Ray Diffraction Imaging of Single Biological Molecules*, Phys. Rev. Lett. **98**, 198302 (2007).

[205] J. C. H. Spence, K. Schmidt, J. S. Wu, G. Hembree, U. Weierstall, B. Doak, and P. Fromme, *Diffraction and imaging from a beam of laser-aligned proteins: resolution limits*, Acta Cryst. A **61**, 237 (2005).

[206] X. Song, *An inhomogeneous model of protein dielectric properties: Intrinsic polarizabilities of amino acids*, J. Chem. Phys. **116**, 9359 (2002).

[207] D. Porschke, *Macrodipoles: unusual electric properties of biological macromolecules*, Biophys. Chem. **66**, 241 (1997).

[208] T. Simonson, *Electrostatics and dynamics of proteins*, Rep. Prog. Phys. **66**, 737 (2003).

[209] J. S. Wu and J. C. H. Spence, *Phasing diffraction data from a stream of hydrated proteins*, J. Opt. Soc. Am. A **22**, 1453 (2005).

[210] B. Ziaja, H. N. Chapman, R. Fäustlin, S. Hau-Riege, Z. Jurek, A. V. Martin, S. Toleikis, F. Wang, E. Weckert, and R. Santra, *Limitations of coherent diffractive imaging of single objects due to their damage by intense x-ray radiation*, New J. Phys. **14**, 115015 (2012).

[211] W. Richardson, *Bayesian-Based Iterative Method of Image Restoration*, J. Opt. Soc. Am. **62**, 55 (1972).

[212] L. B. Lucy, *An iterative technique for the rectification of observed distributions*, Astronomical J. **79**, 745 (1974).

[213] D. A. Fish, A. M. Brinicombe, E. R. Pike, and J. G. Walker, *Blind deconvolution by means of the Richardson-Lucy algorithm*, J. Opt. Soc. Am. A **12**, 58 (1995).

[214] The HDF group, *HDF - Hirarchical data format* (2013), `http://www.hdfgroup.org/HDF5/`, from 01/20/2013.

[215] CERN, *ROOT - a data analysis framework* (2013), `http://root.cern.ch/`, from 01/20/2013.

[216] R. Hartmann, private communication, 08/30/2010 (2010).

[217] R. Hartmann, private communication, 02/10/2011 (2011).

[218] N. Kimmel, private communication, 11/11/2010 (2010).

Summary

This thesis is concerned with an experiment testing the feasibility of a new approach of coherent diffractive x-ray imaging. X-ray diffractive imaging is at the very heart of materials science and has been utilized for decades to solve unknown molecular structures. Nowadays, it serves as the key method of structural biology to solve molecular structures of large biological molecules comprising several thousand or even millions of atoms where spectroscopic methods such as, e. g., rotational spectroscopy fail. In x-ray diffractive imaging, the electromagnetic x-ray wave scattered from a sample to be investigated is recorded by a photon detector. This recorded image is called the "x-ray diffraction pattern" of the sample and mathematical algorithms can be applied to determine the sample structure from its diffraction pattern. Starting from a simple x-ray tube, introduced by Röntgen at the end of the 19^{th} century, huge efforts have been conducted to design and build new x-ray lightsources, delivering x-ray radiation with strongly improved properties such as, e. g., largely increased brightness, monochromaticity, or ultrashort pulse legths. This vastly extended the range of molecular structures which have been solved by x-ray diffractive imaging methods up to now.

However, x-ray diffraction from isolated molecules is very weak. If the structure of an unknown molecule has to be solved, usually many identical copies of this molecule have to be confined in a crystal lattice. By the strict and regular arrangement of these molecules at well-defined positions in a crystal into so-called unit cells, the diffraction signal is vastly enhanced and concentrated into well-defined narrow spots with huge intensity which is easily measured by photon detectors. This is called Bragg diffraction and x-ray diffraction exploiting Bragg diffraction from crystals is usually called x-ray crystallography. The major bottleneck of structural biology is that many of biologically interesting molecules refuse to form crystals of sufficient size to be used at synchrotron x-ray lightsources. In

particular, crystallization of samples of the biologically very relevant class of membrane proteins can take years and for most of them is never achieved. Addressing the demand of building an x-ray lightsource capable to perform x-ray diffraction experiments on very weakly scattering non-crystallizable molecular samples, a new generation of x-ray lightsources, the x-ray free-electron lasers (XFELs), have been designed and realized recently. The x-ray pulses provided by an XFEL can be many orders of magnitude more intense than x-ray pulses from a synchrotron source and at the same time as short as only several tens of femtoseconds. This opens up the possibility to circumvent the damage threshold of molecular samples and in principle utilize pulses of arbitrary high intensity in a "diffract-before-destruct" approach, i. e., the high intensity eventually destroys the sample but since the pulse is so short sample deterioration has not set in on that timescale and the diffraction pattern is entirely due to intact molecular samples.

In the framework of this thesis, a coherent x-ray imaging experiment on an ensemble of isolated molecules in the gas-phase was performed at the x-ray free-electron laser LCLS. The prototypical molecule 2,5-diiodobenzonitrile ($C_7H_3I_2N$, DIBN) was chosen, where mainly the two-center interference of the two (heavy) iodine atoms was utilized for coherent x-ray diffraction, which resembles a kind of "Young's double slit" on the atomic level. In order to infer the single-molecule diffraction pattern of DIBN, an ensemble of DIBN target molecules was laser-aligned with respect to a common axis in the laboratory frame by utilizing the strong ns-long pulses from an off-resonant near-infrared Nd:YAG laser. This results in a diffraction pattern which is the incoherent superposition of single-molecule diffraction patterns, convolved with an alignment-angular distribution with respect to the laser polarisation. A significant part of the work was dedicated to gaining control of the molecular degrees of freedom, namely via spatial quantum-state selection and laser-alignment prior to the x-ray diffraction experiment.

In order to reach a high degree of alignment, the target molecules had to be "cold", i. e., in the lowest possible rotational quantum states. An efficient cooling of the target molecules was achieved in a molecular beam, created via a supersonic expansion of the target molecules along with a backing gas. A strong inhomogenous static electric field of the so-called deflector was used to spatially separate molecules according to their quantum state. At the strong electric fields in the deflector (several 100 kV/cm), all quantum states of the investigated molecular systems were high-field seeking with the lowest quantum states being deflected the most by the deflector.

The results of the deflection experiments are presented in chapter 4. Deflection of molecules was applied to two different molecular systems. In the course of the first exper-

iment, the distinct deflection of the molecule indole and various indole$(H_2O)_n$-clusters was investigated. The deflection is most remarkable for the indole$(H_2O)_1$ cluster. Since its dipole moment is considerably stronger than the dipole moments of the other species in the molecular beam, a full separation of indole$(H_2O)_1$ from the other species was obtained by the deflector. Deflection profiles of all species were simulated well utilizing molecular trajectory simulations, and a rotational temperature of 4–6 K was obtained. The results show, that at the low temperatures present in the molecular beam, the Stark-curves and hence the deflection even of such complex systems like indole$(H_2O)_n$ clusters can be well understood and simulated.

Deflection of DIBN, the target molecule for the coherent x-ray diffraction experiment, was utilized in order to spatially select the molecules in the lowest rotational quantum states, as these are best suited for laser alignment. Although the spatial separation from the undeflected beam was weak, selecting molecules in the deflected part of the molecular beam resulted in a significant improvement of the degree of alignment as shown in chapter 5.

In order to compare the outcome of the x-ray diffraction experiment to theory, diffraction intensities of the target molecule DIBN and the backing gas He were simulated quantitatively, taking into account all parameters (geometry, molecular degree of alignment, incident FEL-intensity, etc.) from the experiment. These simulations are outlined in chapter 6.

The results of the coherent x-ray diffraction experiment on the ensemble of quantum-state selected and strongly laser-aligned DIBN molecules are presented in chapter 7. Diffraction data from aligned and randomly-distributed DIBN was recorded for $\approx$ 560,000 (aligned) and $\approx$ 840,000 (randomly-distributed) shots respectively. The single-shot data contained various sources of background, most notably the strong background by the alignment laser. In future experiments of this kind, better methods to shield the detectors from background have to be implemented. The process of cleaning the data in order to extract single photon hits is explained in detail in appendix A.

Single-shot diffraction data from aligned and randomly-distributed DIBN was recorded with a count rate of $\approx$ 0.2 photons/shot, which corresponds to $\approx$ 110,000 and $\approx$ 170,000 photons in the case of aligned and not-aligned DIBN respectively. All photon hits were histogrammed to 2d-diffraction patterns. The difference of the scattering from aligned and isotropical DIBN is very faint. This is due to the relatively long wavelength 620 pm, which is only slightly shorter than the longest atomic distance in DIBN (I-I distance: 700 pm) and causes very broad and slowly varying features in the diffraction pattern, and background scattering from the backing gas He in the molecular beam and a strong

background not originating in scattering from the molecular beam, but from apertures, rest gas, etc.

The asymmetry of the scattering in the case of aligned molecules is best visualized by subtracting the data of isotropic DIBN from the dataset, where DIBN was aligned. This diffraction-difference clearly reveals a statistically significant difference and hence confirmes the observation of an x-ray diffraction signal from aligned DIBN molecules. Due to the relatively long wavelength, compared to the interatomic distances in DIBN, the diffraction maximum of the most-notable interference (iodine-iodine) occurs at high scattering angles, and was not recorded by the detector. Due to this low resolution, phase-retrieval methods were not applied to the data. Nevertheless, it was investigated whether the I-I distance can be inferred from the position of the scattering minimum. By comparing simulations of different I-I distances to the data, the data is best fitted with the model for an I-I distance of 800 pm. However, the difference to the 700 pm model is minimal. While the fit is consistent with the known I-I distance, it is not a true confirmation due to the low signal-to-noise of the data. The influence of radiation damage, occuring during the FEL pulse, on the diffraction pattern was investigated and the slightly elongated I-I distance of the best-fitting model may be attributed to it. However, these these damage effects cannot be resolved in the current experiment with 620 pm wavelength radiation.

While, in principle, the detection of a measurable signal from aligned molecules was confirmed, the structural information that may be derived from this data is very limited. This is mainly due to the low signal-to-noise of the data and the limited resolution. As discussed in chapter 8, along with experimental improvements (which might include improvements in quantum-state selection and alignment), the most notable issues to be adressed in future experiments of this kind are: a sufficient shielding to background (from the alignment laser), better signal-to-noise by collecting more diffraction data, and gaining improved resolution by the application of shorter wavelengths and a higher degree of alignment. Although already proposed theoretically, the application of this method should be tested on biologically relevant macromolecules as well in the near future. Furthermore, the unique pulse properties of XFEL pulses should be exploited for investigations of ultrafast atomic and molecular dynamics in femtosecond pump-probe experiments.

Acknowledgements

When I came to Hamburg in 2009, after completing my diploma thesis in a completely different field of physics, I had to learn a lot about x-ray diffraction and cold molecules almost from the basics and fortunately I had the chance to profit from the help by many other people regarding the science and experimental techniques for this challenging project of x-ray diffraction by isolated molecules at the new X-ray Free-Electron Lasers.

Therefore, I would like to thank especially my supervisors Prof. Jochen Küpper and Prof. Henry Chapman in guiding me through this project and answering all of my questions. Everytime I was stuck with the data analysis, you provided help, motivation and many new ideas and therefore I would really like to thank you a lot for all the small and big discussions during my work for the thesis. It is amazing to watch science being pushed to new frontiers with these many new interesting projects using XFELs.

I also would like to thank Sebastian Trippel, Terry Mullins, Yuan-Pin Chang from our CMI group, Lotte Holmegaard and Prof. Henrik Stapelfeldt from the Aarhus university, and Frank Filsinger for all their help with experimental and theoretical questions, the discussions with you have been a big help for me to better understand molecular physics. At this point, also a big thanks goes out to our CMI group, Nele Müller, Daniel Horke, Thomas Kierspel, Jens Kienitz, Bastian Deppe, and Karol Dlugolecki for all their help and support during my PhD thesis. Since we have been a quite small group, I liked the fact that we often got together beside work and I think we had a quite strong identification with our group, which was really great.

Regarding data analysis and theoretical questions, I profit a lot from discussions with Andrew Martin, Tom White, Fenglin Wang, and Anton Barty and I would like to thank you very much for all your help. I am also very grateful for all the help and advice in experimental and technical issues and would like to thank Lars Gumprecht, Holger Fleckenstein, Tjark Delmas, and Helmut Mahn for their efforts and help.

A big thanks goes out to Lutz Foucar, who has always been just an Email, or phonecall, away, providing me with the best support when using CASS during my data analysis. During the FEL beamtimes, it has also been great to work with Daniel Rolles, Artem Rudenko, Carlo Schmidt, Sascha Epp, Rebecca Boll, Denis Anielski, Benjamin Erk, and Benedikt Rudek from the Max-Planck ASG group and Arnaud Rouzee from the MBI Berlin and I would like to thank you all a lot for your help and discussions.

After some issues regarding the data analysis have been solved, I really got to like the pnCCD detectors very much and I would like to thank the people from the HLL Munich, Robert Hartmann, Georg Weidenspointner, Andreas Hartmann, and Nils Kimmel a lot for our discussions about the data analysis and all of their help regarding the pnCCD detectors.

Also, I would like to thank Sang-Kil Son for our short discussions and for doing the cross-section calculations for iodine, thanks Sang-Kil.

I would like to emphasize, that I really enjoyed the nice working atmosphere in the coherent imaging division a lot and I would like to thank the whole coherent imaging group of CFEL. Finally, thanks to Carl Caleman and Prof. Janos Hajdu from Uppsala University for our discussions and for providing me with a lot of motivation.

List of Publications

1. *Multistage polar switching in bent-core mesogens*
   S. Findeisen-Tandel, M.W. Schröder, G. Pelzl, U. Baumeister, W. Weissflog, S. Stern, A. Nemes, R. Stannarius, and A. Eremin
   Eur. Phys. J. E **25**, Issue 4, 395–402 (2008)

2. *Electrically Induced Tilt in Achiral Bent-Core Liquid Crystals*
   A. Eremin, S. Stern, and R. Stannarius
   Phys. Rev. Lett. **101**, 247802 (2008)

3. *At the boundary to banana-shaped liquid crystals: polar properties of phases formed by new asymmetric achiral four-ring bent-core mesogens*
   W. Weissflog, U. Dunemann, S. Findeisen-Tandel, M.G. Tamba, H. Kresse, G. Pelzl, S. Diele, U. Baumeister, A. Eremin, S. Stern, and R. Stannarius
   Soft Matter **5**, 1840–1847 (2009)

4. *A model for a field-induced ferrielectric state in a bent-core mesogen*
   S. Stern, R. Stannarius, A. Eremin, and W. Weissflog
   Soft Matter **5**, 4136–4140 (2009)

5. *Femtosecond X-ray protein nanocrystallography*
   H. N. Chapman, P. Fromme, A. Barty, T. A. White, R. A. Kirian, A. Aquila, M. S. Hunter, J. Schulz, D. P. Deponte, U. Weierstall, B. R. Doak, F. R. N. C. Maia, A. V. Martin, I. Schlichting, L. Lomb, N. Coppola, R. L. Shoeman, S. W. Epp, R. Hartmann, D. Rolles, A. Rudenko, L. Foucar, N. Kimmel, G. Weidenspointner, P. Holl, M. Liang, M. Barthelmess, C. Caleman, S. Boutet, M. J. Bogan, J. Krzywinski, C. Bostedt, S. Bajt, L. Gumprecht, B. Rudek, B. Erk, C. Schmidt, A. Hömke, C. Reich, D. Pietschner, L. Strüder, G. Hauser, H. Gorke, J. Ullrich, S. Herrmann, G. Schaller, F. Schopper, H. Soltau, K.-U. Kühnel, M. Messerschmidt, J. D. Bozek, S. P. Hau-Riege, M. Frank, C. Y. Hampton, R. G. Sierra, D. Starodub, G. J. Williams, J. Hajdu, N. Timneanu, M. M. Seibert, J. Andreasson, A. Rocker, O. Jönsson,

M. Svenda, S. Stern, K. Nass, R. Andritschke, C.-D. Schröter, F. Krasniqi, M. Bott, K. E. Schmidt, X. Wang, I. Grotjohann, J. M. Holton, T. R. M. Barends, R. Neutze, S. Marchesini, R. Fromme, S. Schorb, D. Rupp, M. Adolph, T. Gorkhover, I. Andersson, H. Hirsemann, G. Potdevin, H. Graafsma, B. Nilsson, and J. C. H. Spence
Nature **470**, 73–77 (2011)

6. *Single mimivirus particles intercepted and imaged with an X-ray laser*
M. M. Seibert, T. Ekeberg, F. R. N. C. Maia, M. Svenda, J. Andreasson, O. Jönsson, D. Odić, B. Iwan, A. Rocker, D. Westphal, M. Hantke, D. P. Deponte, A. Barty, J. Schulz, L. Gumprecht, N. Coppola, A. Aquila, M. Liang, T. A. White, A. V. Martin, C. Caleman, S. Stern, C. Abergel, V. Seltzer, J.-M. Claverie, C. Bostedt, J. D. Bozek, S. Boutet, A. A. Miahnahri, M. Messerschmidt, J. Krzywinski, G. Williams, K. O. Hodgson, M. J. Bogan, C. Y. Hampton, R. G. Sierra, D. Starodub, I. Andersson, S. Bajt, M. Barthelmess, J. C. H. Spence, P. Fromme, U. Weierstall, R. A. Kirian, M. S. Hunter, B. R. Doak, S. Marchesini, S. P. Hau-Riege, M. Frank, R. L. Shoeman, L. Lomb, S. W. Epp, R. Hartmann, D. Rolles, A. Rudenko, C. Schmidt, L. Foucar, N. Kimmel, P. Holl, B. Rudek, B. Erk, A. Hömke, C. Reich, D. Pietschner, G. Weidenspointner, L. Strüder, G. Hauser, H. Gorke, J. Ullrich, I. Schlichting, S. Herrmann, G. Schaller, F. Schopper, H. Soltau, K.-U. Kühnel, R. Andritschke, C.-D. Schröter, F. Krasniqi, M. Bott, S. Schorb, D. Rupp, M. Adolph, T. Gorkhover, H. Hirsemann, G. Potdevin, H. Graafsma, B. Nilsson, H. N. Chapman, and J. Hajdu
Nature **470**, 78–81 (2011)

7. *In vivo protein crystallization opens new routes in structural biology*
R. Koopmann, K. Cupelli, L. Redecke, K. Nass, D. P. DePonte, T. A. White, F. Stellato, D. Rehders, M. Liang, J. Andreasson, A. Aquila, S. Bajt, M. Barthelmess, A. Barty, M. J. Bogan, C. Bostedt, S. Boutet, J. D. Bozek, C. Caleman, N. Coppola, J. Davidsson, B. R. Doak, T. Ekeberg, S. W. Epp, B. Erk, H. Fleckenstein, L. Foucar, H. Graafsma, L. Gumprecht, J. Hajdu, C. Y. Hampton, A. Hartmann, R. Hartmann, G. Hauser, H. Hirsemann, P. Holl, M. S. Hunter, S. Kassemeyer, R. A. Kirian, L. Lomb, F. R. N. C. Maia, N. Kimmel, A. V. Martin, M. Messerschmidt, C. Reich, D. Rolles, B. Rudek, A. Rudenko, I. Schlichting, J. Schulz, M. M. Seibert, R. L. Shoeman, R. G. Sierra, H. Soltau, S. Stern, L. Strüder, N. Timneanu, J. Ullrich, X. Wang, G. Weidenspointner, U. Weierstall, G. J. Williams, C. Wunderer, P. Fromme, J. C. H. Spence, T. Stehle, H. N. Chapman, C. Betzel, and M. Duszenko
Nature Methods **9**, 259–262 (2012)

8. *Lipidic phase membrane protein serial femtosecond crystallography*
L. C. Johansson, D. Arnlund, T. A. White, G. Katona, D. P. DePonte, U. Weierstall, B. R. Doak, R. L. Shoeman, L. Lomb, E. Malmerberg, J. Davidsson, K. Nass, M. Liang, J. Andreasson, A. Aquila, S. Bajt, M. Barthelmess, A. Barty, M. J. Bogan, C. Bostedt, J. D. Bozek, C. Caleman, R. Coffee, N. Coppola, T. Ekeberg, S. W. Epp, B. Erk, H. Fleckenstein, L. Foucar, H. Graafsma, L. Gumprecht, J. Hajdu, C. Y. Hampton, R. Hartmann, A. Hartmann, G. Hauser, H. Hirsemann, P. Holl, M. S. Hunter, S. Kassemeyer, N. Kimmel, R. A. Kirian, F. R. N. C. Maia, S. Marchesini, A. V. Martin, C. Reich, D. Rolles, B. Rudek, A. Rudenko, I. Schlichting, J. Schulz, M. M. Seibert, R. G. Sierra, H. Soltau, D. Starodub, F. Stellato, S. Stern, L. Strüder, N. Timneanu, J. Ullrich, X. Y. Wahlgren, X. Wang, G. Weidenspointner, C. Wunderer, P. Fromme, H. N. Chapman, J. C. H. Spence, and R. Neutze
Nature Methods **9**, 263–265 (2012)

9. *Pattern-Stabilized Decorated Polar Liquid-Crystal Fibers*
A. Eremin, U. Kornek, S. Stern, R. Stannarius, F. Araoka, H. Takezoe, H. Nadasi, W. Weissflog, and A. Jakli
Phys. Rev. Lett. **109**, 017801 (2012)

10. *Spatial separation of state- and size-selected neutral clusters*
S. Trippel, Y.-P. Chang, S. Stern, T. Mullins, L. Holmegaard, and J. Küpper
Phys. Rev. A **86**, 033202 (2012)

11. *Transitions between paraelectric and ferroelectric phases of bent-core smectic liquid crystals in the bulk and in thin freely suspended films*
A. Eremin, M. Floegel, U. Kornek, S. Stern, and R. Stannarius
Phys. Rev. E **86**, 051701 (2012)

12. *Single-particle structure determination by correlations of snapshot X-ray diffraction patterns*
D. Starodub, A. Aquila, S. Bajt, M. Barthelmess, A. Barty, C. Bostedt, J. D. Bozek, N. Coppola, B. R. Doak, S. W. Epp, B. Erk, L. Foucar, L. Gumprecht, C. Y. Hampton, A. Hartmann, R. Hartmann, P. Holl, S. Kassemeyer, N. Kimmel, H. Laksmono, M. Liang, N. D. Loh, L. Lomb, A. V. Martin, K. Nass, C. Reich, D. Rolles, B. Rudek, A. Rudenko, J. Schulz, R. L. Shoeman, R. G. Sierra, H. Soltau, J. Steinbrener, F. Stellato, S. Stern, G. Weidenspointner, M. Frank, J. Ullrich, L. Strüder, I. Schlichting, H. N. Chapman, J. C. H. Spence, and M. J. Bogan
Nature Comm. **3**, No. 1276 (2012)

13. *Spatial Separation of molecular conformers and clusters*
D. A. Horke, S. Trippel, Y.-P. Chang, S. Stern, T. Mullins, T. Kierspel, and J. Küpper
J. Vis. Exp., e51137 (2013)

14. *X-ray diffraction from isolated and strongly aligned gas-phase molecules with a free-electron laser*
J. Küpper, S. Stern, L. Holmegaard, F. Filsinger, A. Rouzée, D. Rolles, A. Rudenko, P. Johnsson, A. V. Martin, M. Adolph, A. Aquila, S. Bajt, A. Barty, C. Bostedt, J. Bozek, C. Caleman, R. Coffee, N. Coppola, T. Delmas, S. W. Epp, B. Erk, L. Foucar, T. Gorkhover, L. Gumprecht, A. Hartmann, R. Hartmann, G. Hauser, P. Holl, A. Hömke, N. Kimmel, F. Krasniqi, K.-U. Kühnel, J. Maurer, M. Messerschmidt, R. Moshammer, C. Reich, B. Rudek, R. Santra, I. Schlichting, C. Schmidt, S. Schorb, J. Schulz, H. Soltau, L. Strüder, J. Thøgersen, M. J. J. Vrakking, G. Weidenspointner, T. A. White, C. Wunderer, G. Meijer, J. Ullrich, H. Stapelfeldt, and H.N. Chapman
Phys. Rev. Lett., submitted (2013)

15. *Femtosecond Photoelectron Diffraction on Laser-Aligned Molecules: Freeze Frames of a Molecular Movie*
R. Boll, D. Anielski, C. Bostedt, J. D. Bozek, L. Christensen, R. Coffee, S. De, P. Decleva, S. W. Epp, B. Erk, L. Foucar, F. Krasniqi, J. Küpper, A. Rouzée, B. Rudek, A. Rudenko, S. Schorb, H. Stapelfeldt, M. Stener, S. Stern, S. Techert, S. Trippel, M. J. J. Vrakking, J. Ullrich, and D. Rolles
Phys. Rev. Lett., submitted (2013)